Palladium/Zeolites as Model Catalysts for Cold Start Passive NOx Adsorption

A

Dissertation

Presented to

the faculty of the School of Engineering and Applied Science

University of Virginia

in partial fulfillment

of the requirements for the degree

Doctor of Philosophy

by

Yuntao Gu

December 2020

APPROVAL SHEET

This
Dissertation
is submitted in partial fulfillment of the requirements
for the degree of
Doctor of Philosophy

Author: Yuntao Gu

Author Signature: Yuntao Gu

This Dissertation has been read and approved by the examining committee:

Advisor: William Epling

Committee Member: Robert Davis

Committee Member: Christopher Paolucci

Committee Member: Andres Clarens

Committee Member: Giri Gaurav

Accepted for the School of Engineering and Applied Science

Craig H. Benson, School of Engineering and Applied Science

December 2020

Acknowledgement

I want to first express the utmost gratefulness to my parents, Ning Gu and Yongqiong Tao, who have never hesitated to support me the best they can both materially and spiritually, starting from the minute I was born till now even though they are more than 8000 miles away from me. Their unconditional love and care have made me who I am today, and I will never be grateful enough to have them as my greatest mother and father.

I would like to deeply thank my PhD advisor Prof. William S. Epling for all the guidance, patience, encouragement, and support that he has offered, as well as the tremendous influence he has left on me as a scientific researcher. I have to say that I was fortunate enough to meet Bill in Houston and it was a life-changing decision to come to Virginia with him. To date, I am very proud to be one of his students and would love to carry the pride and embrace more challenges in the future. Thank you, Bill.

I am also thankful for having a lot of genius people around me, especially Prof. Robert J. Davis and Prof. Christopher Paolucci. I appreciate everything they have taught me, and the time they spent discussing science with me. Thanks for filling my PhD journey with a lot of enlightening moments that I am sure will have a long-lasting impact. I would also want to acknowledge Josh A. Pihl from Oak Ridge National Laboratory for all the fruitful discussions about my research project and a lot of unique input as a great reaction engineer and scientist. I want to thank Dr. Monique Shauntá Wilburn and Dr. Yasser Jangjou, two of the greatest young scholars that motivated and inspired me a lot, for your mentorship and kindness during the first two years of my PhD.

I am feeling blessed to meet all the great people that I have worked with in the past five years at the University of Houston, University of Virginia, Oak Ridge National Laboratory and Volvo Group Trucks Technology: Silvia Marino, Yu-Ren Chen, Dr. Lai Wei, Ryan Zelinsky,

Natalia Diaz Montenegro, Dr. Jiahan Xie, Dr. Gordon Brezicki, Lu Yang, Colby Whitcomb, Keka Mandal, Annalisa Tosti, Dr. Marina Cortés-Reyes, Prof. Izabela Pieta, Prof. Sung Bong Kang, Dr. Todd J. Toops, Dr. Sreshtha Sinha Majumdar, Will Miller, Ron Weaver and Dr. Nick Hansford. I want to thank all of them for the help and support they have offered and making my PhD journey wonderful and unforgettable.

I have been extremely lucky to make a lot of good friends who have made grad school and my PhD experience full of laughter and joyful memories. I want to thank my classmates: Luke Huelsenbeck, Kevin Chang, Xueying Zhao, Hongxi Luo, Joey Roberts, Lucas Kimerer, Erica Hui, Katelyn Dagnall, Saringi Agata, Devanshi Gupta and Naomi Miyake for making the chemical engineering department truly feel like a home for me. I would also like to acknowledge Dr. Mengmeng Li, Dr. Di Wang, Dr. Hui Wang for their continuous support and constructive career development advices. To Yiran Wang, Yuanyuan Ji, Hongxu Dong, Henrique Pacheco, Lisong Chen and Zhongwen Luo: thanks for exploring Virginia with me and making my stay at Charlottesville a fantastic chapter of my life.

It was very nice to meet Anan Wang and have her company during the last year of my PhD. I would like to thank her for bearing with my occasional workaholism and continuously motivating me to be a better person, and more importantly, to be a better man.

Abstract

Reducing NOx emissions is challenging during engine or aftertreatment system warm up due to the low exhaust temperatures and thus limited reaction kinetics. NOx emitted during this period is often referred to as cold start NOx emissions and represents one of the main obstacles in emissions regulations compliance. Passive NOx adsorbers (PNA) have been proposed to help address cold start NOx emissions via low temperature NOx trapping and subsequent thermal release, such that NOx generated and trapped during cold start can ultimately be converted by a downstream NOx reduction catalyst. Several groups of potential PNAs have been evaluated for low temperature NOx storage and subsequent release, of which the laboratory-scale experimental testing results appear to be promising and point to Pd/zeolites as potentially the best PNA material. In this study, the nature of Pd within the zeolite framework and Pd speciation as a function of reaction conditions were first investigated using Pd/SSZ-13 model PNAs. Results show that Pd cations are responsible for the NOx storage and tend to be solvated by H_2O under cold start conditions. Once solvated, Pd detaches from the zeolite and forms homogeneous Pd-nitrosyl species. This effect of H_2O solvation appears to be a general phenomenon regardless of zeolite topology. A similar study on a Pd/ZSM-5 commercial PNA confirmed the solvated nature of Pd and revealed key reaction and adsorption pathways under realistic NO adsorption conditions. A simplified NO adsorption and desorption mechanism that is able to capture the characteristics of NO adsorption in the presence of H_2O and CO was proposed.

Additionally, a CO-induced irreversible NOx storage degradation mode was observed on Pd/BEA model PNAs during cyclic NO adsorption and temperature programmed desorption (TPD) experiments. Characterization of the degraded catalyst indicates that the Pd migration from ion-exchanged positions to particles that reside on the external surface of the zeolite leads to the observed degradation. The degradation mechanism was further studied using in situ X-ray absorption spectroscopy (XAS) and temperature programmed reduction (TPR) experiments. Results show that CO leads to the reduction of Pd cations and high temperature accelerates the agglomeration of PdO nanoparticles to prevent them from oxidative regeneration.

As a final topic, Pd/SSZ-13 PNA was integrated with a Pt/Al_2O_3 oxidation catalyst, of which the results show enhancement in system durability and more ideal NOx release temperature. The first is due to the limited high temperature CO exposure. The more ideal NOx release temperature was found to correlate to the early onset of NO_2 formation as a result of enhanced oxidation activity.

List of Figures

2 (773 K, 3.1% H_2O, 10% O_2), and **(b)** Thermodynamic phase diagrams for 1Al and 2Al Pd-exchanged sites on a common energy scale based on HSE06-D3(BJ)vdw calculated energies. (The low and high temperature conditions are labeled accordingly on the phase diagrams with the structures shown for the corresponding minimum free energy species)

Figure 3.5. HSE06-optimized structures of **(a)** NO adsorbed on 1Al and 2Al Pd-exchanged sites, and **(b)** NO adsorbed in the presence of H_2O.

Figure 3.6. CCSD(T) calculated NBOs for B3LYP optimized geometries of **(a)** $Z_2[PdNO(H_2O)_3]$, **(b)** $Z[PdOH(NO)(H_2O)_2]$, and **(c)** $Z[PdNO(H_2O)_3]$. Red and blue isosurfaces indicate the different phases of the NBOs. NBO assigned Lewis dot structures for each species' Pd-NO moiety are beneath their NBO representations, with emphasis on the occupancy of the unbound N valence electrons. Pd-NO bond angles and distances are also displayed. The isovalues used for NBO plots are ±0.15.

Figure 3.7. (a) Thermodynamic phase diagram for $\mathrm{Z_*PdH}_x\mathrm{O}_y(\mathrm{NO})_z$ species at 1Al and 2Al Pd-exchanged sites on a common energy scale incorporating the zero-point, and vibrational free energies, and HSE06-computed energies, and **(b)** Formation free energies (ΔGform) of $\mathrm{Z_*PdH}_x\mathrm{O}_y(\mathrm{NO})_z$ species at 1Al and 2Al sites represented on a common energy scale at 403 K, 4.5% H2O, 10% O2, 200 ppm NO.

Figure 3.8. NO_x temperature programmed desorption (NO_x-TPD) profiles of Pd/SSZ-13 (Si/Al = 9, Pd/Al = 0.056) in the presence of 200 ppm NO, 10% O_2, 4.5% H_2O (red) and < 5ppm H_2O (black) at a ramp rate of 30 K/min.

List of Tables

Table of Contents

Chapter 1. Introduction

Note: a more detailed introduction to passive NOx adsorbers including literature review has been published and can be found as: Y. Gu, W.S. Epling, Passive NOx adsorber: An overview of catalyst performance and reaction chemistry, Appl. Catal. A Gen. 570 (2019) 1–14. The manuscript can be found in Appendix A.

In an internal combustion engine (ICE), the combustion of fuel is the basic chemical reaction that releases energy from a fuel and air mixture. The temperature and pressure of an internal combustion chamber increase as the energy is released, and part of the energy is then converted to work, thus driving the vehicle through the powertrain system. The spark ignition gasoline engine and the compression ignition diesel engine are the two types of most widely used ICEs, both of which consist of a four-stroke combustion cycle but have different fuel injection processes and the fuel ignition mechanisms. In a spark ignition gasoline engine, the fuel is mixed with air prior to the intake process, and a spark is used to induce combustion after the piston compresses the fuel-air mixture to an ideal pressure. In a compression ignition diesel engine, the fuel is not injected into the combustion chamber until the air is compressed, and no spark is needed to initiate the combustion since the hot compressed air ignites the fuel spontaneously. However, as a result of not using spark ignition, the pressure needed for spontaneous fuel combustion is significantly higher than the maximum pressure reached in gasoline engines, thus using a much higher compression ratio (CR). Besides the differences in the fuel injection process, compression ratio and the ignition mechanism, the air-fuel ratio (AFR) is another factor that can be used to differentiate diesel and gasoline engines. In general, diesel engines combust fuel in an excessive amount of air, which is also known and referred to as lean burn, whereas gasoline engines combust under stoichiometric conditions (Ø=1 in **Fig. 1-1**). Due to these differences, the combustion temperature of diesel engines is usually lower than gasoline engines and they are also more fuel-efficient. Additionally, the higher compression ratio of the cylinder also leads to higher torque, thus making diesel engines good candidates for heavy-duty commercial vehicles.

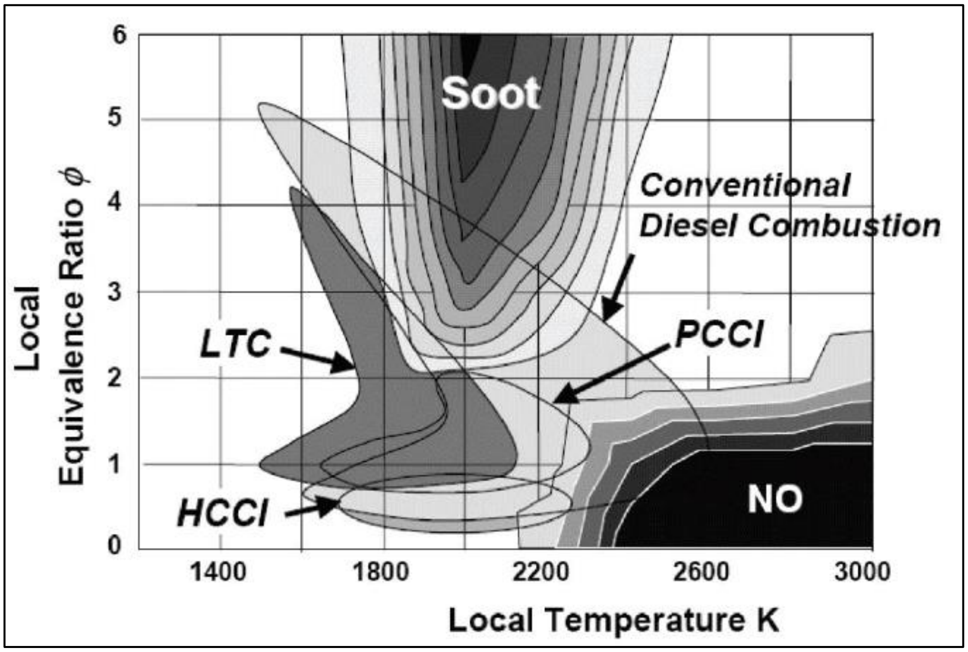

Figure 1.1 Conventional and other combustion process zone in the NOx and soot formation areas

Although the advantages of diesel engines are widely known, conventional diesel combustion inevitably generates regulated emissions because of incomplete combustion and high temperature induced NOx formation in the combustion chamber, this is shown in **Figure 1.1**. The formation of NOx and soot originates from non-ideal mixing within the combustion chamber and the existence of local hot and cold spots during combustion. Arguably, with the development of advanced combustion techniques such as low temperature combustion (LTC), homogeneous charge compression ignition (HCCI) and premixed charge compression ignition (PCCI), simultaneous reduction in the amount of NOx and soot formed in the combustion chamber can theoretically be achieved, the local inhomogeneity of the air and fuel mixing is, however, hard to eliminate. Furthermore, conventional diesel combustion suffers from the well-known trade-off between soot and NOx formation, making current regulated emission control oftentimes challenging.

Catalytic removal of regulated emissions from the exhaust after-treatment systems has proven effective for both diesel and gasoline engines. Although some platforms can differ, the diesel engine exhaust after-treatment system typically consists of a diesel oxidation catalyst (DOC), a diesel particulate filter (DPF), a selective catalytic NOx reduction catalyst (SCR) and an ammonia slip catalyst (ASC). Research into emission catalysis has led to significant progress over the last two decades, and the current state-of-the-art emission catalysts are highly efficient and can meet current emission regulations.

Based on US Environmental Protection Agency (EPA) reported data, annual highway vehicle carbon monoxide (CO), NOx, particulate matter (PM) and volatile organic compounds (VOC) emissions have been decreasing since 1970 despite the exponential growth in vehicles miles traveled (VMT). However, there is still significant effort in improved emission reductions and fuel economy. In terms of improved fuel economy, the emergence of advanced combustion techniques increases fuel efficiency and helps offset growth in vehicle energy use, but consequently the exhaust temperatures are lower and the catalytic removal of emissions under these exhaust conditions is more challenging. Thus, the need for more research in the emissions catalysis field, where there has been a growing emphasis on low temperature catalysis.

1.1 Emission regulations

The Clean Air Act of 1963 was the first established federal legislation that put emphasis on controlling air pollution, and amendments further encouraged the study of air pollution monitoring as well as emissions regulation setting. The US EPA was established as part of the 1970 amendment. To date, two sets of federal emission standards, namely, Tier 1 and Tier 2 standards have successfully phased-in starting from 1991, and Tier 3 standards were applied in 2014 to be phased-in between 2017 and 2025.California emission standards, also known as Low Emission Vehicle (LEV) standards, followed the succession of federal emission standards and is now at their LEV III stage. As is shown in **Figure 1.2**, a fleet average non-methane hydrocarbons and oxygenated hydrocarbons plus NOx (NMOG+NOx) emission level of 0.03g/mi is required for model year 2025.

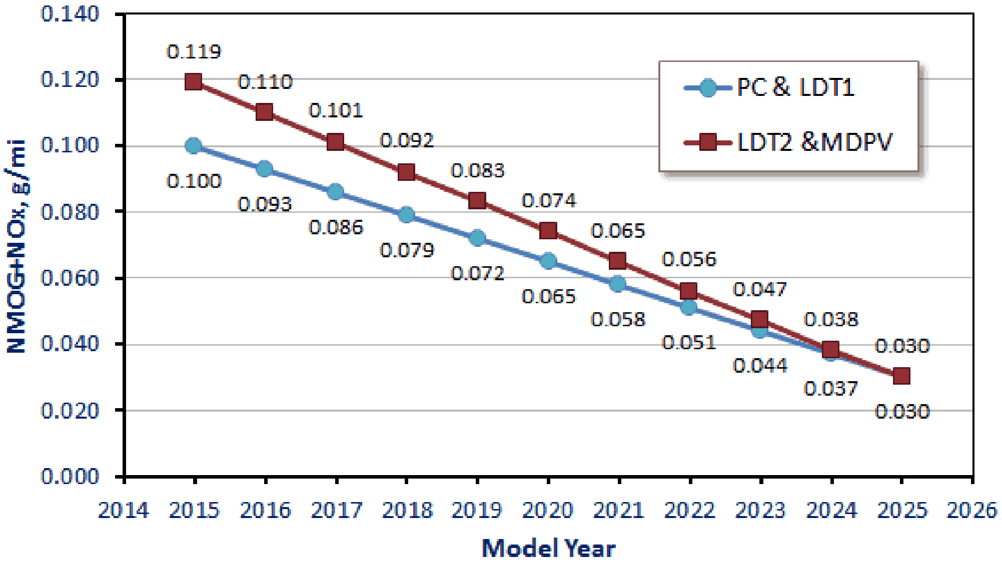

Figure 1.2 LEV III Fleet Average Emission Standards

Moreover, regulated emissions measured during a federal testing cycle do not always represent the real-world emissions due to the discrepancies between the federal testing cycle and real-world driving conditions. More specifically, the underestimated portion of cold start and low load idling represent a set of scenarios where emission catalysts are not as active due to low exhaust temperature, and will become more relevant with the adoption of more efficient combustion strategies that lead to lower exhaust temperatures. Knowing that the number of vehicles and miles traveled is projected to increase, EPA and California Air Resource Board (CARB) are actively monitoring on-road emissions. Furthermore, portable emission measurement (PEM) technologies have uncovered several emissions scandals. Hence, the development of more representative testing cycles and more accurate emission measurement methods have been developed or are under development.

1.2 Diesel after-treatment system

Lean burn diesel engines are used in heavy-duty commercial vehicles and off-road vehicles due to their better fuel economy and higher torque compare to gasoline engines. However, the excess O_2 in the exhaust makes NOx reduction significantly more challenging than for gasoline engine exhaust. In a stoichiometric burn gasoline engine, the desired ratio between oxidant and reductant is optimized for the performance of a downstream three-way catalyst where NOx reduction, hydrocarbon oxidation and CO oxidation can occur simultaneously. The after-treatment of diesel engine exhaust, however, needs to handle oxidation and reduction separately because the reduction of NOx via CO or hydrocarbons in an oxidative atmosphere is not feasible under lean conditions.

A diesel oxidation catalyst (DOC) is one of the key components in diesel after-treatment systems, and its role is to oxidize unburned hydrocarbons (HCs) and CO. In general, molecular O_2 is dissociated on platinum group metals (PGM) to react with HCs and CO. The oxidation reactions produce CO_2 and H_2O and can be written as follows:

$$C_nH_m + (n + \frac{m}{2})O_2 \rightarrow nCO_2 + \frac{m}{2}H_2O \quad ----Reaction.(1)$$

$$CO + \frac{1}{2}O_2 \rightarrow CO_2 \quad ----Reaction.(2)$$

After CO and unburned hydrocarbons are converted into CO_2 and H_2O, NOx is reduced on a downstream selective catalytic reduction (SCR) catalyst in the presence of O_2, of which the main reactions are:

$$4NO + 4NH_3 + O_2 \rightarrow 4N_2 + 6H_2O \quad ----Reaction.(3)$$

$$2NO_2 + 4NH_3 + O_2 \rightarrow 3N_2 + 6H_2O \quad ----Reaction.(4)$$

$$NO + NO_2 + 2NH_3 \rightarrow 2N_2 + 3H_2O \quad ----Reaction.(5)$$

Reaction. (3) and Reaction (5) are commonly known as the standard SCR, and fast SCR. Notably, NH_3 is used as the reductant to selectively convert NOx into N_2. In order to supply NH_3 in a continuous manner, an NH_3 injection system is usually required to facilitate NH_3-SCR. Anhydrous or aqueous urea is currently the most widely used NH_3 source since both of them can be easily stored and transported on a diesel engine powered vehicle, and decompose or hydrolyze into NH_3 and CO_2 as follows:

$$CO(NH_2)_2 + H_2O \rightarrow 2NH_3 + CO_2 \quad ----Reaction.(6)$$

Once NH_3 is generated, the current state-of-the-art SCR catalysts are reported to be able achieve more that 95% NOx conversion in most operating temperature ranges, and the durability of the catalysts are currently satisfactory. A characteristic of the exhaust after treatment system is that the catalysts are exposed to a transient gas phase mixture, of which the flow rate and exhaust temperature fluctuate with time, thus controlling NH_3 injection is non-trivial. Excess NH_3 can slip through the SCR catalyst, and to ensure that there is no NH_3 emitted from the tailpipe an ammonia slip catalyst (ASC) is present to facilitate ammonia oxidation. The ammonia oxidation reaction shown below is usually the last step before exhaust is emitted to the environment:

$$4NH_3 + 3O_2 \rightarrow 2N_2 + 6H_2O \quad ----Reaction.(7)$$

DOC, SCR and ASC are three of the key components that follow a cascaded architecture in the tailpipe downstream of the diesel engine, all of which are usually in the form of a washcoated monolith to achieve high catalytic activity while minimizing the gas phase pressure drop.

1.3 Cold start emissions

Cold start occurs when the engine is started, and the engine block, tailpipe and catalysts warm up from ambient temperature. The exhaust after-treatment system is at low temperature and emission catalysts are therefore less effective due to kinetic limitations. With emission regulations becoming progressively more stringent and the engine exhaust temperature decreasing as a result of increasing combustion efficiency, the cold start period will be further elongated and remain a major problem for emissions reduction from automotive sources [1–5]. This is especially true in the case of lean burn diesel engines where an excessive amount of air exists, thus increasing the thermal mass of the exhaust [2,5–8]. The US EPA Urban Dynamometer Driving Schedule (FTP-72 and FTP-75), as examples of typical test cycles for light-duty gasoline engines, consist of a 505 second cold start phase with a 0.43 weighing factor, whereas the counterpart for heavy-duty diesel engines (Heavy-Duty FTP transient cycle) is run with both cold and hot start tests with a weighing factor of 1/7 and 6/7 for the cold start and hot start, respectively. Furthermore, a low-load cycle (LLC), representing a scenario where an engine idles for extended time and exhaust temperatures drop, has been added to certification cycles.

An NH_3-SCR system with a state-of-the-art Cu/SSZ-13 catalyst can effectively reduce NOx generated from a lean burn engine once the exhaust temperature exceeds 200 °C [9–11]. Similarly, lean NOx traps (LNTs) and three-way catalysts (TWCs) with optimized formulations are highly effective in reducing NOx at high temperatures [10,12–15]. However, with kinetic limitations at low temperature, neither system can remediate NOx emissions effectively during cold start. Arguably, LNT and TWC low temperature activity can be further improved to minimize NOx emitted during cold start, but the inability of decomposing the currently required aqueous urea solution at low temperature (<180 °C) makes application of NH_3-SCR systems prohibitive if cold start NOx emissions cannot be successfully addressed [16].

1.4 Passive NOx adsorber

To address NOx emitted during cold start, a device with the ability to temporarily store NOx at low temperature and thermally release NOx at higher temperature has been proposed. A series of patents from the automobile and catalyst manufacturing industries indicate that this technology has been conceptually established for some time [17–19], but due to the rapid development of a variety of other deNOx technologies it apparently did not attract the same attention as it has more recently. Over the last few years there has been renewed interest in this approach with publications in the open literature by Johnson Matthey Inc., specifically referring to nitric oxide adsorbents that can be thermally regenerated as part of a cold-start concept catalyst [19,20]. Since then, different groups of materials have been extensively evaluated for NOx adsorption and release. To date, this approach has been developed into one of the more promising technologies for cold start NOx emission control, and the systems are often referred to as passive NOx adsorbers or PNAs [21–30].

As a supplemental device for currently existing after treatment systems, PNAs are designed to reduce NOx emissions during the cold start period[30]. Notably, cold start is a transient process with a relatively fixed time duration, therefore, the amount of NOx generated within such a period is finite. And because of this unique behavior, PNAs are able to overcome the catalytic reduction reaction challenge by simply adsorbing NOx at low temperatures instead of converting them immediately. The exhaust gas temperature will eventually exceed 200 °C, where a downstream

NOx reduction catalyst is efficient, and ideally in the time to reach 200 °C, all the NOx from the engine will adsorb on the PNA.

Furthermore, again ideally, as soon as the exhaust gas temperature reaches 200 °C, the temperature that triggers urea decomposition and high NOx conversion, the NOx that adsorbed during cold start would be released. The driving force of desorption will be nothing but a higher exhaust temperature. However, instead of generating a sharp NOx flux pulse in the after-treatment system that might be hard to handle, the NOx release process can be elongated in several ways, but desorption temperatures around 200 °C are favored[11]. A too high NOx desorption temperature could possibly make the device inefficient since the regeneration of the NOx storage capacity via desorption of the NOx might not be complete or significant.

The goal of this work is to understand the characteristics as well as the mechanism of the NOx adsorption and desorption process that take place on Pd/zeolite based PNAs, evaluate these potential PNAs under exhaust relevant conditions with an emphasis on understanding the chemical nature of the material and its interaction with different exhaust components, and study the existing degradation/deactivation mode(s). Furthermore, once the adsorption and desorption mechanism and the degradation are understood, rational catalyst design guidelines and an engineering solution to enable successful commercialization of this technology is proposed.

1.5 References

[1] A. Solouk, M. Shakiba-herfeh, K. Kannan, H. Solmaz, P. Dice, M. Bidarvatan, N.N.T. Kondipati, M. Shahbakhti, Fuel Economy Benefits of Integrating a Multi-Mode Low Temperature Combustion (LTC) Engine in a Series Extended Range Electric Powertrain, in: SAE 2016 Int. Powertrains, Fuels Lubr. Meet., SAE International, 2016.

[2] M. V. Twigg, Progress and future challenges in controlling automotive exhaust gas emissions, Appl. Catal. B Environ. 70 (2007) 2–15.

[3] H.C. Frey, Trends in onroad transportation energy and emissions, J. Air Waste Manage. Assoc. 68 (2018) 514–563.

[4] P.-Y. Peng, H. Nguyen, M.P. Harold, D. Luss, Spatio-Temporal Phenomena in Monolithic Reactors Measured by Combined Spatially-Resolved Mass Spectrometry and Optical Frequency Domain Reflectometry, in: Adv. Chem. Eng., 1st ed., Elsevier Inc., 2017: pp. 83–130.

[5] R. Zhang, J.-S. McEwen, M. Kollár, F. Gao, Y. Wang, J. Szanyi, C.H.F. Peden, NO Chemisorption on Cu/SSZ-13: A Comparative Study from Infrared Spectroscopy and DFT Calculations, ACS Catal. 4 (2014) 4093–4105.

[6] M.P. Harold, NOx storage and reduction in lean burn vehicle emission control: a catalytic engineer's playground, Curr. Opin. Chem. Eng. 1 (2012) 303–311.

[7] H.C. Frey, Trends in onroad transportation energy and emissions, J. Air Waste Manage. Assoc. 68 (2018) 514–563.

[8] C. Sharp, C.C. Webb, S. Yoon, M. Carter, C. Henry, Achieving Ultra Low NOX Emissions Levels with a 2017 Heavy-Duty On-Highway TC Diesel Engine - Comparison of Advanced

Technology Approaches, SAE Int. J. Engines. 10 (2017) 2017-01–0956.

[9] B.T. Johnson, Diesel Engine Emissions and Their Control, Platin. Met. Rev. 52 (2008) 23–37.

[10] T. Johnson, Vehicular Emissions in Review, SAE Int. J. Engines. 9 (2016) 2016-01–0919.

[11] V. Schmeisser, M. Weibel, L. Sebastian Hernando, I. Nova, E. Tronconi, M.P. Ruggeri, Cold Start Effect Phenomena over Zeolite SCR Catalysts for Exhaust Gas Aftertreatment, SAE Int. J. Commer. Veh. 6 (2013) 2013-01-1064.

[12] G.D. Neely, D. Mehta, J. Sarlashkar, Diesel Cold-Start Emission Control Research for 2015-2025 LEV III Emissions, SAE Int. J. Engines. 7 (2014) 2014-01-1552.

[13] K. Kamasamudram, N.W. Currier, X. Chen, A. Yezerets, Overview of the practically important behaviors of zeolite-based urea-SCR catalysts, using compact experimental protocol, Catal. Today. 151 (2010) 212–222.

[14] P. Forzatti, I. Nova, E. Tronconi, New “Enhanced NH 3 -SCR” Reaction for NOx Emission Control, Ind. Eng. Chem. Res. 49 (2010) 10386–10391.

[15] F. Gao, Y. Wang, M. Kollár, N.M. Washton, J. Szanyi, C.H.F. Peden, A comparative kinetics study between Cu/SSZ-13 and Fe/SSZ-13 SCR catalysts, Catal. Today. 258 (2015) 347–358.

[16] W.S. Epling, L.E. Campbell, A. Yezerets, N.W. Currier, J.E. Parks, Overview of the Fundamental Reactions and Degradation Mechanisms of NOx Storage/Reduction Catalysts, Catal. Rev. 46 (2004) 163–245.

[17] S. Matsumoto, Recent advances in automobile exhaust catalysts, Catal. Today. 90 (2004) 183–190.

[18] R.M. Heck, R.J. Farrauto, Automobile exhaust catalysts, Appl. Catal. A Gen. 221 (2001) 443–457.

[19] V. Schmeisser, M. Weibel, L. Sebastian Hernando, I. Nova, E. Tronconi, M.P. Ruggeri, Cold Start Effect Phenomena over Zeolite SCR Catalysts for Exhaust Gas Aftertreatment, SAE Int. J. Commer. Veh. 6 (2013) 190–199.

[20] Jarvis, M., and Adams, K.M., US Patent US6182443

[21] Feeley, J. S., Farrauto, R.J., and Deeba, M., US Patent US6471924

[22] Melville, J.E., Brisley, R.J., Keane, O., Phillips, P.R., and Mountstevens, E.H., US Paternt US8105559

[23] H.-Y. Chen, S. Mulla, E. Weigert, K. Camm, T. Ballinger, J. Cox, P. Blakeman, Cold Start Concept (CSC^{TM}): A Novel Catalyst for Cold Start Emission Control, SAE Int. J. Fuels Lubr. 6 (2013) 2013-01–0535.

[24] Ancimer, R.J., Geveci, M., Haas, M., Joshi, A., and Kamasamudram, K., US Patent US9512761

[25] Qi, G., Schmieg, S.J., Ren, S., Li, and Li, W., US Patent US9597635 [26] Rajaram, R.R., Chen, H., and Liu, D., US Patent US20150158019

[27] Kearl, B., Yin, Q., Qi, X., and Biberger, M.A., US Patent US20160045867

[28] Collier, J.E. and Yang, S., US Patent US20170001169

[29] Janssens, T.V.W., and Vennestrom, P.N.R., US Patent US20170095804

[30] Chiffey, A.F., Corps, J., Mitchell-Downie, L., Moreau, F., and O'brien, M., US Patent US20170096923

[31] Chen, H., and Mulla, S., US Patent US20170128922

[32] Biberger, M.A., Kearl, B., Yin, Q., and Qi, X., US Patent US20180093249

[33] H.-Y. Chen, D. Liu, E. Weigert, L. Cumaranatunge, K. Camm, P. Bannon, J. Cox, L. Arnold, Durability Assessment of Diesel Cold Start Concept (dCSC^{TM}) Technologies, SAE Int. J. Engines. 10 (2017) 2017-01–0955.

[34] Y. Gu, W.S. Epling, Passive NOx adsorber: An overview of catalyst performance and reaction chemistry, Appl. Catal. A Gen. 570 (2019) 1–14.

[35] Y. Gu, W.S. Epling, Passive NOx Adsorber: An Overview of Catalyst Performance and Reaction Chemistry, Appl. Catal. A Gen. 570 (2018).

[36] P. Gélin, A. Goguet, C. Descorme, C. Lécuyer, M. Primet, Catalytic Properties of Palladium Exchanged ZSM-5 Catalysts in the Reduction of Nitrogen Monoxide by Methane in the Presence of Oxygen: Nature of the Active sites, in: 1998: pp. 275–284.

[37] C. Descorme, P. Gelin, M. Primet, C. Lecuyer, Infrared study of nitrogen monoxide adsorption on palladium ion-exchanged ZSM-5 catalysts, Catal. Letters. 41 (1996) 133–138.

[38] V.I. Yakerson, V. V Rozanov, A.M. Rubinshtein, Thermodesorption studies on adsorbate-adsorbent interaction, Surf. Sci. 12 (1968) 221–246.

[39] K. Khivantsev, F. Gao, L. Kovarik, Y. Wang, J. Szanyi, Molecular Level Understanding of How Oxygen and Carbon Monoxide Improve NO x Storage in Palladium/SSZ-13 Passive NO x Adsorbers: The Role of NO + and Pd(II)(CO)(NO) Species, J. Phys. Chem. C. 122 (2018) 10820–10827.

[40] A. Vu, J. Luo, J. Li, W.S. Epling, Effects of CO on Pd/BEA Passive NOx Adsorbers, Catal. Letters. 147 (2017) 745–750.

[41] J.R. Theis, An assessment of Pt and Pd model catalysts for low temperature NO x adsorption, Catal. Today. 267 (2016) 93–109.

[42] S.T. Homeyer, W.M.H. Sachtler, Oxidative redispersion of palladium and formation of PdO particles in NaY. An Application of High Precision TPR, Appl. Catal. 54 (1989) 189–202.

[43] S. HOMEYER, Elementary steps in the formation of highly dispersed palladium in NaY I. Pd ion coordination and migration, J. Catal. 117 (1989) 91–101.

[44] T. Hamzehlouyan, C. Sampara, J. Li, A. Kumar, W. Epling, Experimental and kinetic study of SO2 oxidation on a Pt/γ-Al2O3 catalyst, Appl. Catal. B Environ. 152–153 (2014) 108–116.

[45] Y. Gu, W.S. Epling, Passive NOx adsorber: An overview of catalyst performance and reaction chemistry, Appl. Catal. A Gen. 570 (2019) 1–14.

[46] H.-Y. Chen, J.E. Collier, D. Liu, L. Mantarosie, D. Durán-Martín, V. Novák, R.R. Rajaram, D. Thompsett, Low Temperature NO Storage of Zeolite Supported Pd for Low Temperature Diesel Engine Emission Control, Catal. Letters. 146 (2016) 1706–1711.

[47] Y. Ryou, J. Lee, Y. Kim, S. Hwang, H. Lee, C.H. Kim, D.H. Kim, Effect of reduction treatments (H2 vs. CO) on the NO adsorption ability and the physicochemical properties of Pd/SSZ-13 passive NOx adsorber for cold start application, Appl. Catal. A Gen. 569 (2019) 28–34.

[48] A. Russell, W.S. Epling, Diesel Oxidation Catalysts, Catal. Rev. 53 (2011) 337–423.

[49] M.J. Hazlett, W.S. Epling, Heterogeneous catalyst design: Zoned and layered catalysts in diesel vehicle aftertreatment monolith reactors, Can. J. Chem. Eng. 97 (2019) 188–206.

Chapter 2. Experimental Methods

2.1 Bench scale reactor

A synthetic exhaust flow reactor system was used to perform NO adsorption, CO chemisorption, CO temperature programmed reduction, steady state kinetics measurements and temperature programmed desorption experiments. High purity compressed gas cylinders are the sources of different gas components. A series of mass flow controllers (MKS Instruments) was used to vary the composition of the feed, except for H_2O. H_2O vapor was introduced to the reactor with a Bronkhorst controlled evaporator mixer (CEM). Two electrically actuated four-way valves, customized by and purchased from Swagelok, were used such that at any given time one gas stream flows through the reactor and another through a bypass line. The outlet of either the bypass or reactor connects to either an MG2030 FTIR analyzer (MKS Instruments) or a vent line. A quartz tube reactor assembly was placed into a tubular furnace (Lindberg Blue/M) to facilitate temperature control and two K-type thermocouples were placed into the reactor at both the upstream and downstream of the catalyst for temperature measurements.

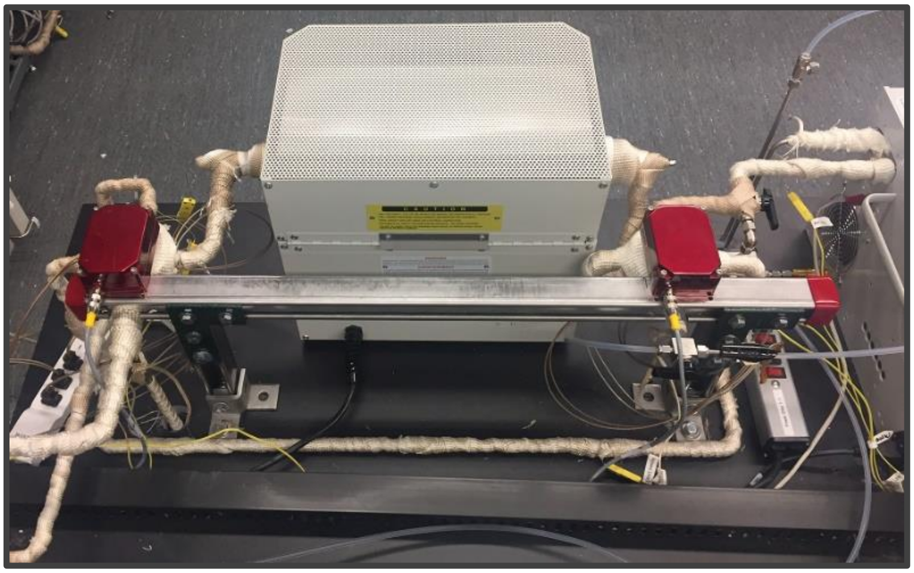

Figure 2.1 Bench scale reactor used for catalyst performance evaluation and kinetics experiments.

2.2 Diffuse reflectance infrared Fourier transform spectroscopy

In order to gain insight into the surface intermediates and reactions on the catalyst surface during NO adsorption, an Agilent Cary 670 FTIR spectrometer and Thermo Scientific Nicolet iS50 FTIR spectrometer with a Harrick Praying Mantis diffuse reflectance infrared Fourier transform spectroscopy (DRIFTS) cell and a liquid nitrogen-cooled mercury-cadmium-telluride (MCT) detector were used to collect the spectra. The DRIFTS accessory consisted of a Harrick high temperature reaction chamber with ZnSe windows. A thin layer of the washcoated sample (~0.3 cm^2) or a pellet of the powder form were placed in the center of a sample holder. A series of mass flow controllers (MKS Instruments) were used to control the composition of the gas flowing through the sample. Water was introduced to the feed using a saturator immersed in a recirculating constant temperature bath or a bubbler. 64 spectra were averaged for background collection and 32 spectra were averaged for sample spectra.

2.3 X-ray absorption spectroscopy

We collected Pd K edge (23450 eV) X-ray absorption spectra at beam 8-ID of the National Synchrotron Light Source II, Upton NY. All measurements were performed with an electron storage ring operated at 3 GeV and a beam current of 400 mA. We pelletized the catalysts to 225-425 μm and loaded them into 0.25-inch stainless steel tube placed inside an aluminum heating jacket. We collected spectra of the ambient exposed sample with no additional treatment. Pd K edge in-situ XAS experiments were performed at beam 10-ID of the Advanced Photon Source, Lemont IL. Measurements were taken in transmission mode with a stainless-steel sample holder, a quartz tube reactor and X-ray transparent windows.

2.4 X-ray diffraction

Crystallinity of the catalysts after calcination and hydrothermal aging were investigated via X-ray diffraction (XRD) using a PANalytical X'Pert Pro multi-purpose diffractometer. Cu Kα X-ray source and a vertical circle theta:theta goniometer with an incident radius of 240 mm were used.

2.5 Transmission electron microscopy

Scanning transmission electron micrographs (STEM) were collected in high-angle annular dark-field (HAADF) mode on a FEI Titan transmission electron microscope operated at 80-300kV S-Twin platform. Samples were supported on a carbon grid and loaded onto a low-background double tilt specimen holder.

Chapter 3. Condition-Dependent Pd Speciation and NO adsorption in Pd/Zeolites

This chapter is published in ACS Catalysis and can be found as: K. Mandal, Y. Gu, K.S. Westendorff, S. Li, J.A. Pihl, L.C. Grabow, W.S. Epling, C. Paolucci, Condition-Dependent Pd Speciation and NO adsorption in Pd/Zeolites, ACS Catal. (2020) 12801–12818. https://doi.org/10.1021/acscatal.0c03585

3.1 Introduction

Metal-exchanged zeolites are widely used in chemical separations, catalysis, and pollution remediation technologies. [1–4] In the limit of single metal cations, the active sites in these materials resemble their analogues in the organometallic and homogeneous catalysis literature.[5] Metal cations form bonds to the zeolite or acquire ligands via gas adsorption and can become solvated, interacting only electrostatically with the zeolite framework.[6] Solvation and mobilization of metal ions by H_2O or other adsorbates appear to be a general phenomenon of metal-exchanged zeolite systems under certain conditions, and has important consequences on catalytic function and adsorption of other gases.[7–11] However, this phenomenon has largely gone unrecognized in the Pd/zeolite literature. Here, we integrate computation at multiple levels of theory, and in-situ spectroscopic and kinetic experimental measurements, to determine the nature of Pd complexes exchanged in zeolites. We explore the molecular structure of Pd-zeolite motifs under a wide range of conditions of practical relevance for NO abatement technologies, and catalytic CO oxidation and methanol synthesis. We show that H_2O-solvation of Pd cations profoundly affects their chemical nature, catalytic performance, and complexing with NO.

Pd cations have been extensively explored in the inorganic chemistry and homogeneous catalysis literature. Similar to most group 8 and higher transition metals, Pd typically favors lower oxidation states of Pd^0 and Pd^{II}.[12–14] While Pd^I and Pd^{III} have been observed, their presence has only been confirmed in a minute number of homogeneous compounds.[13–19] Infrared (IR) evidence of carbonyl anions of binuclear Pd^I were reported by Goggin and cowork-ers,[18] and binuclear Pd^I isocyanide complexes have been synthesized by Otsuka et al.[14] Similar binuclear Pd^I complexes with various ligands have also been observed using a variety of spectroscopic characterization techniques.[12–14] However, mononuclear homogeneous Pd^I complexes have not yet been identified.[14] Even though higher oxidation states like +4, +5 and +6 have been identified for Pd in homogeneous complexes, [17,20–27] structural characterization of mononuclear Pd speciation in zeolites is wanting.

Zeolites are crystalline aluminosilicates comprised of interconnected tetrahedra of SiO_4 and AlO_4 to form a nanoporous, three-dimensional cage-like structure. Re-placement of Si^{IV} with Al^{III} at the corner-sharing aluminosilicate tetrahedra, called T-sites, induces a negative charge on the zeolitic framework that is compensated by cations. Synthetic protocols determine the framework distribution of Al and the Si/Al ratio, which influence the speciation and location of the exchanged cation.[28–32] Depending upon the Al distribution, various local Al configurations are possible, producing numerous possibilities for the charge-compensating cation, which has, hitherto not been systematically investigated for Pd ions. The commonly observed Pd^{II} oxidation state can charge-compensate one or two Al T-sites in the form of a single Pd cation or Pd with an oxidizing ligand. Despite the absence of evidence for mononuclear Pd^I in homogeneous complexes, some studies have assigned Pd^I at a 1Al T-site as a possible species.[33–38]

Pd/zeolites have been investigated for catalytic alkene hydrogenation, methane oxidation, Wacker oxidation, selective catalytic reduction of NOx with methane (CH_4-SCR) and other applications.[39–46] Recently, Pd/zeolites have been studied for low temperature NOx trapping from automotive engine exhaust.[47–55] Pd/zeolites, among all other candidates, meet the practical requirements for NO storage capacity and NO release temperature, although their resistance against different aging modes, such as CO and hydrocarbon-induced degradation, and sulfur poisoning, needs further investigation.[47,51,56] Khivantsev et al. [34] synthesized a series of atomically dispersed Pd/SSZ-13 catalysts (Pd/Al = 0.03, Si/Al = 6) and reported IR features at 1860 cm^{-1} and 1805 cm^{-1} during NO exposure in the absence of H_2O, similar to those reported by Chen et al.[47] They assigned the 1860 cm^{-1} feature to Pd^{II}-NO and the 1805 cm^{-1} feature to Pd^{I}-NO. The effect of multiple H_2O adsorption and H_2O-solvation of Pd-nitrosyl complexes is still not well-understood.

Though there are IR NO stretching assignments in the Pd/zeolite literature for PdI species,[33–36] odd oxidation states including Pd^{I} and Pd^{III} have only been directly characterized in Pd/Y and X zeolites using EPR under vacuum and following exposure to H_2 at 298 K.[57,58] Descorme et al. invoked Pd^{I} to explain NO_2 formation upon NO exposure on Pd/ZSM-5 in the absence of O_2 and assigned an IR feature at 1881 cm^{-1} to NO on Pd^{I}; however, no other characterization was provided to demonstrate the oxidation state of Pd^{I}.[33]

Literature results highlight a number of ambiguities in our understanding of Pd/zeolites. The initial Pd distribution, Pd speciation during ion-exchange, and dependency on zeolite composition are not clear. The precise nature of the effect of H_2O on Pd speciation is also unknown. The coordination environment of Pd-NO complexes in the presence and absence of H_2O, a ubiquitous and non-innocent spectator in emission technologies, requires investigation. Here, we present a combined computational and experimental study on Pd speciation under a variety of conditions, highlight the hydration effect on Pd cation structures and reveal the intrinsic difference in the sites formed in the presence and absence of H_2O. We report that Pd complexes in zeolites primarily manifest as mobile and H_2O-solvated Pd^{II} complexes under conditions of practical interest for PNA, and catalytic CO and Wacker oxidation. We show that upon exposure to either NO, or mixtures of NO and CO, mobile and H_2O-solvated Pd_{II}-NO complexes form, and these observations extend to multiple zeolite topologies and rationalize a large number of observations in the literature.

3.2 Methods

3.2.1 Details of DFT and AIMD Calculations

We performed periodic DFT calculations employing a plane-wave basis set with an energy cutoff of 400 eV, and a triclinic SSZ-13 supercell consisting of 24 T-sites for 2Al Pd-exchanged sites. We performed calculations in both 12 and 24 T-site supercells for the 1Al Pd-exchanged sites reported in supporting information and found that the energies were consistent irrespective of the supercell cell. Hence, we used the 12 T-site supercell for the 1Al Pd-exchanged sites to avoid unnecessary computational expense. Since the zeolitic system is an insulator, we considered only the point for sampling the first Brillouin zone. To determine plausible local minima of the structures studied, we carried out spin-polarized ab initio molecular dynamics (AIMD) simulations beginning with initial guess structures in the NVT ensemble using the Vienna ab initio Simulation Package (VASP),121 version 5.4.4. Simulations of at least 60 ps, with a time step of 0.5 fs, were run at temperatures of 298 K and 473 K applying the Perdew-Becke-Ernzerhof (PBE)122 generalized gradient approximation (GGA) exchange-correlation functional coupled with Becke-Johnson damping (D3(BJ)vdw) dispersion correction method.[123,124]

Thereafter, we optimized five low energy structures selected from the AIMD simulations, first with GGA-PBE functional and subsequently with the Heyd-Scuseria-Ernzerhof (HSE06)[125–128] hybrid functional for computational efficacy. All geometry optimizations were spin-polarized with the projector augmented wave (PAW) method used for computing core-valence interactions,[129,130] along with the D3(BJ)vdw correction. We used a convergence criterion of 10^{-8} eV and 0.01 eV/Å for self-consistent-field (SCF) electronic energies and atomic forces, respectively. We applied the Bader charge method[131–135] on HSE06-optimized structures to compute the oxidation state of Pd, represented as a superscript on Pd. The obtained charges were normalized to Pd^{I} and PdII using [ZPd^{I}] and [Z_2Pd^{II}] as references, and rounded to the nearest integer. All the optimized geometries have been provided in the supporting information CONTCARS attachment.

3.2.2 Calculation of Ab Initio Formation Free Energies

We expressed the formation free energies of the adsorbed species involving O and H atoms, as a function of the re-action conditions and the DFT-calculated energies using O_2 and H_2O as references:[136,137]

$$\Delta \mathrm{G}_{x,y}^{\mathrm{form}}\left(\mathrm{T},\, \Delta\mu_{O_2},\, \Delta\mu_{H_2O}\right) = \Delta \mathrm{E}_{x,y}^{\mathrm{form}} - \mathrm{T}\Delta \mathrm{S}_{x,y}^{\mathrm{ST}}\,(\mathrm{T}) - \frac{x}{2}\left(\Delta\mu_{H_2O} - \frac{1}{2}\Delta\mu_{O_2}\right) - \frac{y}{2}\Delta\mu_{O_2}$$

$$\Delta \mathrm{E}_{x,y}^{\mathrm{form}} = \mathrm{E}_{\mathrm{Z_*PdH}_x\mathrm{O}_y} - \mathrm{E}_{\mathrm{Z_*Pd}} - \frac{x}{2}\left(\mathrm{E}_{\mathrm{H_2O}} - \frac{1}{2}\,\mathrm{E}_{\mathrm{O_2}}\right) - \frac{y}{2}\,\mathrm{E}_{\mathrm{O_2}}$$

$\Delta\mu$ represents the difference in the chemical potential of the species between 0 K (μ°) and the reaction conditions (μ(P,T)), and is calculated using the ideal gas equation; P is the pressure at standard state (1 atm).

$$\mu\,(\mathrm{P},\mathrm{T}) = \mu^{\circ} + \mathrm{RT}\ln\left(\frac{\mathrm{P}}{\mathrm{P}^{\circ}}\right)$$

Translational, rotational, and vibrational contributions to the entropy and enthalpy of the gaseous species were calculated according to standard statistical mechanics ap-proximations.[138]

Previous studies have reported that sole use of the harmonic oscillator approximation underestimates adsorption free energies on zeolites, since they retain a significant component of their translational and rotational free energy.[139–144] We estimated the entropy difference between a clean and adsorbate-covered site, ΔS^{ST} from an empirical approximation validated by potential of mean force AIMD simulations, using the Sackur-Tetrode equation and assuming that the adsorbate retains 2/3 of its gas-phase translational entropy:[145,146]

$$\Delta S^{\mathrm{ST}}_{x,y} = \left(S_{\mathrm{Z_*PdH}_x\mathrm{O}_y} - S_{\mathrm{Z_*Pd}}\right) \approx \frac{2}{3}\, k_B \ln\left[\left(\frac{2\pi M_{x,y} k_B T}{h^2}\right)^{3/2} \left(\frac{k_B T}{P^\circ}\right)\frac{e^{5/2}}{N_A}\right]$$

where $M_{x,y}$ represents mass of the adsorbate.

Analogous to the expressions above, when NO is pre-sent in addition to O and H atoms, the equations can be modified to incorporate the chemical potential of NO.

$$\Delta G^{\mathrm{form}}_{x,y,z}\left(T,\, \Delta\mu_{O_2},\, \Delta\mu_{H_2O}, \Delta\mu_{\mathrm{NO}}\right) = \Delta E^{\mathrm{form}}_{x,y,z} - T\Delta S^{\mathrm{ST}}_{x,y,z}\,(T) - \frac{x}{2}\left(\Delta\mu_{H_2O} - \frac{1}{2}\Delta\mu_{O_2}\right) - \frac{y}{2}\Delta\mu_{O_2} - z\Delta\mu_{\mathrm{NO}}$$

3.2.3 Details of H_2O-solvated Pd, and Zeolite Cluster Calculations

Starting with the PBE-optimized periodic geometries of [$\mathrm{ZPd^{I}}$], [$\mathrm{ZPd^{II}OH}$], and [$\mathrm{Z_2Pd^{II}}$], we created the zeolite clusters by isolating the Pd cation in the associated 6 (or 8) MR, along with four of the neighboring 4MRs and 8 (or 6) MR, and Si T-sites bound to the terminal oxygen atoms. We replaced these terminal T-sites with a hydrogen atom while maintaining the O-H bond length of 0.97 Å and orientation of original bond angles of the periodic zeolite framework intact. We calculated single-point energies of the species considered in both the models using Gaussian 16[147] and DFT methods of GGA-PBE, and hybrid functionals of HSE06 and B3LYP.[148,149] Single-point energy calculations using the CCSD(T) method were performed only for the species considered in the H_2O-solvated Pd model. All calculations were carried out spin unrestricted with the basis set def2-TZVPP.[150,151]

For solvated structures, harmonic vibrational frequencies were calculated by first optimizing the geometries using B3LYP and the def2-TZVPP basis set. In the case of non-solvated structures, only the Pd atom and the bound nitrosyl ligand were allowed to relax before performing frequency calculations.

NBO analyses were performed on B3LYP-optimized geometries employing NBO 3.1[152] as implemented in Gaussian 16. The visualization of the analyses was done in GaussView 6.[153]

3.2.4 Zeolite Synthesis and Characterization

We synthesized Pd/SSZ-13, Pd/ZSM-5, Pd/BEA catalysts via incipient wetness impregnation using the SSZ-13 zeolites purchased from ACS materials: Type HC (Si/Al = 15, H^+ form) and Type B (Si/Al = 10, NH_4^+ form), ZSM-5 and BEA zeolites purchased from Zeolyst Inc: CP814E* (Si/Al = 12.5, NH_4^+ form) and CBV 3024E (Si/Al = 15, NH_4^+ form). We followed a three-step calcination process (80°C for 2 hours, 105°C for 10 hours and 600°C for 4 hours with a 1°C/min ramp rate in between) to transform the zeolites into the proton form and dehydrate the zeolites before introducing Pd. We used palladium (II) nitrate di-hydrate as the precursor and dissolved the Pd into 28% ammonia hydroxide solution, both of which were purchased from Sigma Aldrich. The mass of Pd and parent zeolites were measured to achieve 1 wt.% or 0.5 wt.% Pd weight loading. The volume of Pd containing solution was the same as the pore volume of the zeolite. Immediately following the calcination to gain the proton form, the Pd precursor solution was added drop-wise with rigorous stirring and mixing to form a slurry. We then repeated the same calcination process on the slurry after Pd was introduced. Si/Al ratios and Pd/Al ratios of the resulting samples were confirmed by inductively coupled plasma optical emission spectroscopy

(ICP-OES) analysis at Galbraith Laboratories, Knoxville TN. We also used X-ray diffraction (XRD) to confirm the zeolite morphology and crystallinity of the Pd/SSZ-13 (Si/Al = 8.9, Pd/Al = 0.056). XRD patterns were collected using a PANalytical X'Pert Pro multi-purpose diffractometer with Cu Kα X-ray source and a vertical circle theta:theta goniometer at an incident radius of 240 mm. We performed H_2 temperature programmed reduction (H_2-TPR) on a Micromeritics AutoChem 2920 system with 5% H_2 (Ultra-high purity, Paxair) and a temperature range from 313 K to 873 K to identify Pd speciation and confirm Pd ion-exchange level in Pd/SSZ-13 (Si/Al = 8.9, Pd/Al = 0.056). We first pre-treated the sample at 873 K in 10% O_2 and cooled down to 313 K in 10% O_2 before turning off O_2 and flowing H_2. The sample was purged by H_2 for 1 hour before the temperature ramp. A repetition of the exact same procedure including O_2 pretreatment was also performed right after the first H_2-TPR experiment. XRD and H_2-TPR results are reported in supporting information.

3.2.5 Details of Spectroscopic Methods (DRIFTS, XAS, EXAFS)

We collected DRIFTS spectra at 4 cm^{-1} resolution on a Thermo Scientific Nicolet iS50 FTIR spectrometer with a Harrick Praying Mantis DRIFTS cell and accessories in-stalled. We averaged 64 spectra for background collection and 32 spectra for each sample spectrum, of which the acquisition time is 48 seconds and 24 seconds, respectively. We used Praxair research purity gas cylinders as the source of NO, CO, O_2 and He, and applied moisture and O_2 traps purchased from Matheson on the He carrier gas line. We used a homemade bubbler and deionized H_2O to introduce H_2O vapor into the manifold and confirmed the H_2O concentration using an MKS MG2030 IR analyzer. We measured the temperatures of the cell and the bubbler using K-type thermocouples. When conducting ex-situ characterization, a cold trap was also applied to further eliminate any trace amount of H_2O and we collected spectra with KBr in the cell under the exact same conditions for background subtraction. We also performed in-situ NO adsorption, NO+CO co-adsorption, and CO addition experiments in the presence and absence of H_2O. A moisture trap and a cold trap were used to collect NO adsorption spectra in the absence of H_2O, and we collected back-ground from a sample at 473 K in 10% O_2 that had been pretreated at 873 K in 10% O_2 to be consistent with the NO adsorption experiments. We also collected back-ground spectra from 873 K O_2 pretreated and H_2O hydrated samples to be consistent with NO adsorption and CO addition experiments in the presence of H_2O.

We collected Pd K edge (23450 eV) X-ray absorption spectra for Pd/SSZ-13 (Si/Al = 8.9, Pd/Al = 0.056) at beam 8-ID of the National Synchrotron Light Source II, Upton NY. All measurements were performed with an electron storage ring operated at 3 GeV and a beam current of 400 mA. We pelletized the catalysts to 225-425 μm and loaded them into 0.25-inch stainless steel tube placed inside an aluminum heating jacket. We collected spectra of the ambient exposed sample with no additional treatment. More details of the in-situ reactor cell can be found elsewhere.[154] Pd K edge in-situ XAS dehydration experiments were performed at beam 10-ID of the Advanced Photon Source, Lemont IL. Measurements were taken in transmission mode with a stainless-steel sample holder, a quartz tube reactor and X-ray transparent windows.

3.2.6 NO Temperature Programmed Desorption and Steady-State CO Oxidation

We conducted the NO temperature programmed desorption and CO oxidation experiments in a 0.25-inch quartz tube reactor placed in a horizontal tubular Thermo Fisher furnace. 40 mg of catalyst were pelletized into 225-425 μm particles and loaded into the quartz tube reactor, kept in place by quartz wool on both sides of the bed. All gas components except H_2O and N_2 were metered from Praxair-supplied ultra-high purity gas cylinders. N_2, the carrier gas in all cases, was purified from compressed air by a Parker N_2 generator. Deionized H_2O was injected using a

Bronkhorst controlled evaporator mixer (CEM). We kept the total flow rate at 546 standard cubic centimeters per minute, to achieve a monolith equivalent gas hour space velocity of 30,000 hr^{-1}. We measured and recorded catalyst bed temperature and outlet gas compositions using a K-type thermocouple at the outlet of the catalyst bed and an MKS MG2030 IR analyzer, respectively. Between each NOx-TPD and CO oxidation experiment, we changed and pretreated samples at 873 K in 10% O_2 balanced by N_2 for 45 min. Inlet concentrations were 200 ppm NO, 10% O_2 and 0 or 4.5% H_2O for the NOx-TPD experiments, and 0 or 200 ppm NO, 200 ppm CO, 10% O_2 and 0 or 4.5% H_2O for the CO oxidation experiments. The temperature ramp was performed from 350 K to 900 K at a ramp rate of 30 K/min. We performed the same 873 K in 10% O_2 pre-treatment followed by N_2 purge at 873 K and cooling in N_2 before measuring the steady state water gas shift activity with the inlet concentrations as 200 ppm CO and 4.5% H_2O.

3.3 Results and discussion

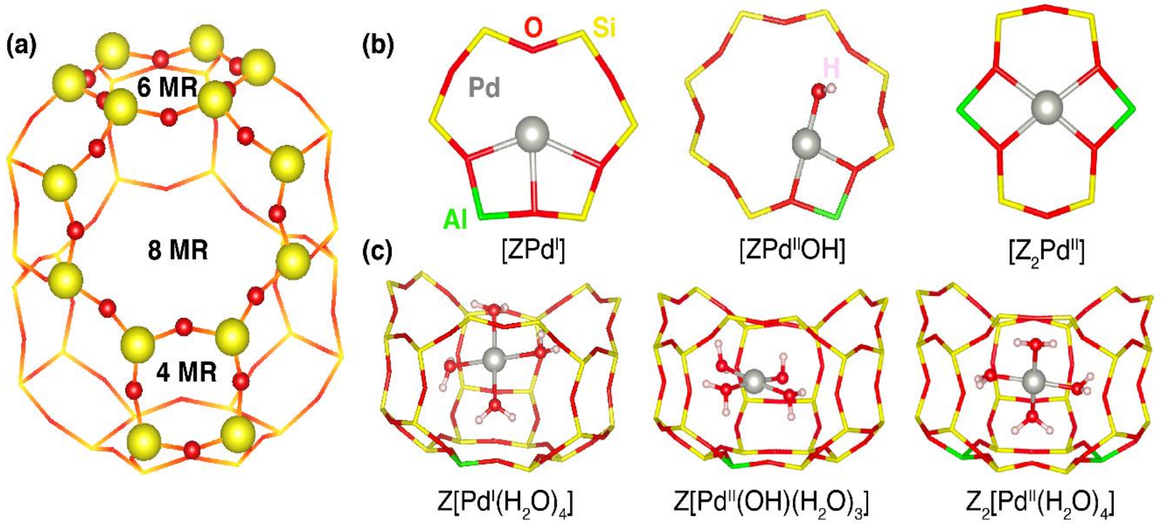

Figure 3.2. (a) Framework of the SSZ-13 cage made up of four-, six- and eight-membered rings (MR), and HSE06-optimized structures of **(b)** 1Al and 2Al Pd-exchanged sites and **(c)** hydrated sites.

3.3.1 Pd Cation Speciation in the Absence of H_2O, 1Al vs 2Al.

Motivated by NO- and CO-probe molecule spectroscopy-based evidence (FTIR, EXAFS and XRD)[34,35,50,59,60] and DFT calculations[34,36,61] we constructed molecular models for Pd charge-compensated by one or two Al T-sites in SSZ-13 zeolites. SSZ-13, classified as a chabazite (CHA) framework type,[62] is made up of four-, six-, and eight-membered rings (MR) arranged into an ~8 Å diameter cage with 3.8 × 3.8 × 3.8 Å pore dimensions, illustrated in Figure 3.1a. We denote (Figure 3.1b) Pd^{I} cations exchanged at one Al T-site in SSZ-13 as $[ZPd^{I}]$, and Pd^{II} cations exchanged at one and two Al T-sites as $[ZPd^{II}OH]$ and $[Z_2Pd^{II}]$, respectively. 'Z' symbolizes the Si T-site substituted by Al, and when enclosed in square brackets, represents bonding of the Pd cation and its associated ligands with the zeolite framework. CHA has one symmetry distinct T-site; therefore, substitution of a single Si^{IV} with Al^{III} encompasses all Z-structures. Pd^{I} and $[PdOH]^{+}$ can reside either in the 6MR or 8MR of the 1Al site, hence we compared the energies of both of these configurations using DFT with the GGA-PBE and HSE06 functionals. We observed that Pd^{I} prefers to locate in the 6MR, bound to two zeolitic framework oxygen (O_f) proximal to Al (Al-O_f) and one Si-O_f, with Pd-O_f bond lengths ranging from 2.18 to 2.38 Å. Pd-OH favors the 8MR, attached to two Al-O_f, with similar Pd-O_fAl bond distances of ~2.09 Å, for both PBE and HSE06. Both species have a three-fold coordinated geometry as shown in Figure 3.1b.

Incorporation of two Al results in multiple configurations, which can be codified by Al-Al distance and the number of T-sites separating the Al pair, denoted as nearest neighbors (NN).[63] Figure 3.2 reports the lowest energy structure computed using the PBE functional for each of the 25 possible Al-Al configurations in a 36 T-site supercell adhering to Löwenstein's rule[64,65] (structures are included in the supporting information CONTCARS attachment); full results are detailed in supporting information. We also optimized a subset of structures using HSE06; relative energies were analogous for both functionals (supporting information). Pd^{II} displays a proclivity for Al pairs in the same 6MR; the lowest energy corresponds to that of the 6MR 3NN configuration where Pd^{II} is present in the center of the ring and connected to four Al-O$_f$. This is followed by the 2NN (+65 kJ mol^{-1}) configuration, with the Pd bonded to three Al-O$_f$ and one Si-O$_f$. Similar to common configurations observed for Pd^{II} homogeneous complexes, Pd has a four-fold coordinated, planar geometry with Pd-O bond distances of ~2Å in these configurations.[14,34,66,67] The other Al pair configurations are +110-210 kJ mol^{-1} higher in relative energy. Cu^{II} (1.4 Å ionic radii) and Co^{II} (2.0 Å) have been observed to preferentially locate to 2Al 6MR in SSZ-13 and our computed results for PdII (1.6 Å) are consistent with this observation.[63,68–75]

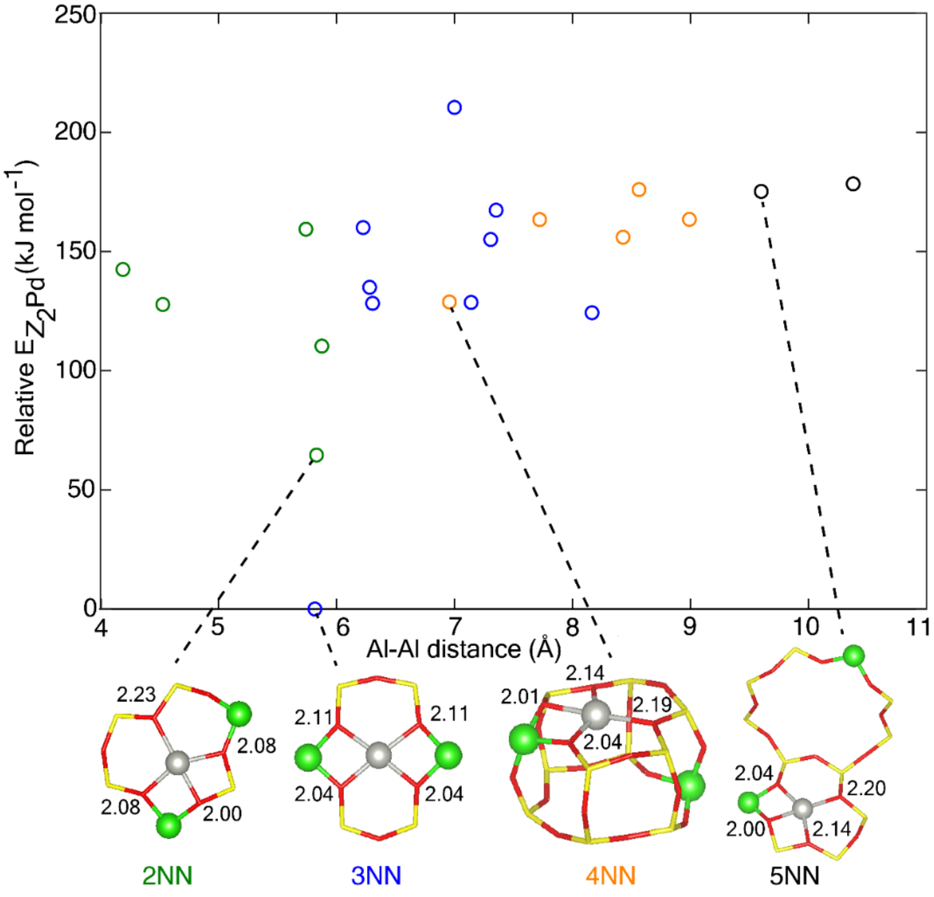

Figure 3.2. Z_2Pd energy vs Al-Al distance, relative to the lowest energy 3NN 6MR structure, based on PBE calculations. Only the lowest energy structure in each of the 25 Al-Al arrangements complying with Löwenstein's rule have been plotted. The Pd-O$_f$ bond lengths (in Å) in each nearest-neighbor (NN) configuration are shown.

To compare the energetics of 1Al and 2Al Pd-exchanged sites, we evaluated the energy required to transfer the Pd cation from the 2Al site to 1Al. Since this mechanism is not unique, we considered different probable routes by constructing Z2 and Z sites in the same, as well as separate, supercells; details of all the reactions considered are provided in supporting information.

$$[\mathrm{Z_2Pd^{II}(H_2O)}] \rightarrow [\mathrm{ZPd^{II}OH}]/[\mathrm{ZH}],\ \Delta E = +85\ \mathrm{kJ\ mol^{-1}}$$

$$[\mathrm{Z_2Pd^{II}}] + \tfrac{1}{2}\mathrm{H_2O} - \tfrac{1}{4}\mathrm{O_2} \rightarrow [\mathrm{ZH}]/[\mathrm{ZPd^{I}}],\ \Delta E = +82\ \mathrm{kJ\ mol^{-1}}$$

Computed reaction energies are endothermic and indicate a Pd cation will preferentially exchange at 6MR Z2 sites instead of forming [ZPd^{I}] or [$ZPd^{II}OH$].

Since Pd preferentially locates at 6MR 2Al sites, identical to Cu and Co, we utilized previously reported and validated models for Al distribution in CHA for common syntheses to estimate the Pd/Al ratio, expressed as a function of Si/Al, at which all 6MR 2Al sites would be saturated.[68,75,76] Cation-exchanged Pd/SSZ-13 materials used in the experiments described below (Si/Al = 9, 15, and 17, and Pd/Al = 0.016, 0.032 and 0.056, 0.046), and reported elsewhere, fall well below the threshold of Pd/Al necessary to saturate all 6MR 2Al sites (Si/Al = 9, Pd/Al = 0.146, and Si/Al = 15, Pd/Al = 0.092, Si/Al = 17, Pd/Al = 0.081). [68] We next confirmed the absence of [$ZPd^{II}OH$] by comparing IR spectra of H/SSZ-13 and Pd/SSZ-13 under dry conditions. Similar FTIR characterization for Cu/SSZ-13 showed the appearance of [$CuOH]^+$ at 3660 cm^{-1} in materials with Cu:Al > 0.21.[68] Our DFT computed harmonic frequency for the O-H stretch in [$ZPd^{II}OH$] is an analogous 3661 cm^{-1}. Thus, a feature for [$PdOH]^+$ at a similar frequency would appear in the FTIR spectra of Pd/SSZ-13 sample, should it contain a population of [$ZPd^{II}OH$] sites. To validate this hypothesis, we synthesized and characterized ion-exchanged Pd/SSZ-13 zeolites (Si/Al = 9 and 15, and Pd/Al = 0.016, 0.032 and 0.056) using a modified ion-exchange method.[34] Full details of the synthesis and characterization are reported in section 4.4. We pretreated all H/SSZ-13 and Pd/SSZ-13 samples at 873 K in 10% O_2 for 1 hour, and then collected diffuse reflectance infrared Fourier-transform spectra (DRIFTS) at 473 K in 10% O_2. As illustrated in Figure 3.3a, we observed features attributed to Brønsted sites at 3600 cm-1 and 3580 cm^{-1}, and silanol at 3730 cm^{-1}.[77–79] We do not observe a difference in the peak intensity around 3660 cm^{-1} between the H/SSZ-13 and Pd/SSZ13 materials. The absence of a new feature at 3660 cm^{-1}, where other M-OH stretches have been observed,[68] along with our DFT-computed $[PdOH]^+$ frequency, implies an absence of $[ZPd^{II}OH]$. Taken together, our results indicate that, in the absence of other adsorbates, exchanged Pd ions are solely $[Z_2Pd^{II}]$ at the 6MR 2Al sites. This observation is consistent across all synthesized samples with varying Si/Al and Pd/Al ratios (supporting information).

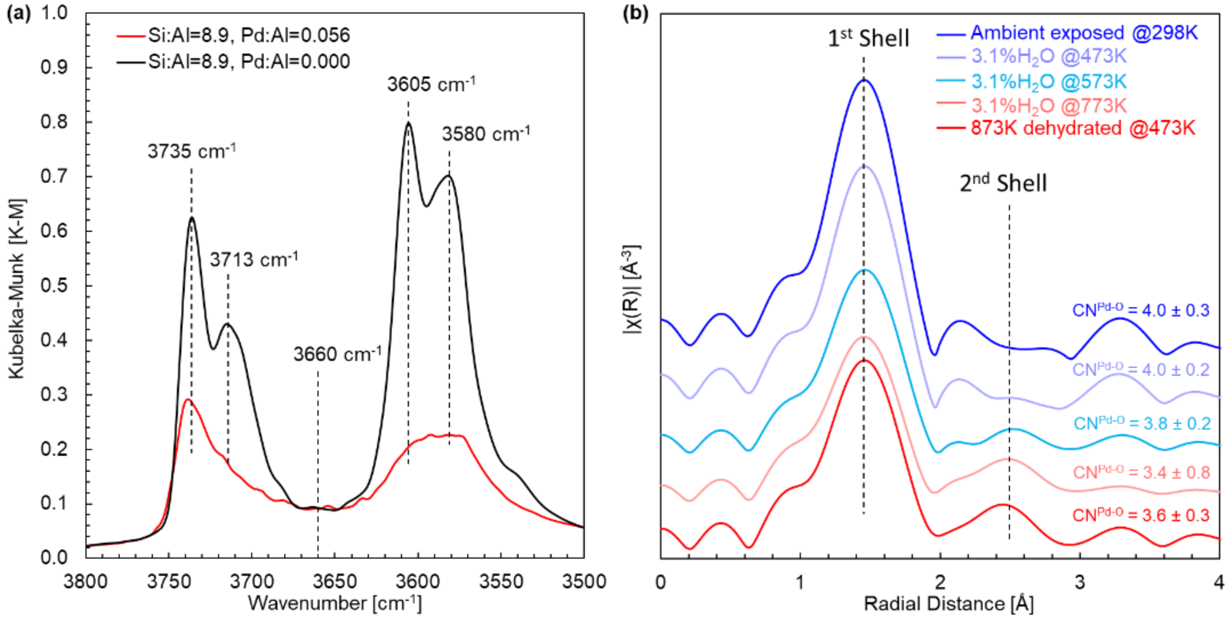

Figure 3.3. **(a)** Ex-situ DRIFTS spectra of Pd/SSZ-13 (red solid line) and H/SSZ-13 (black solid line) collected at 473 K in 10% O_2 after 873 K 10% O_2 pretreatment. **(b)** EXAFS spectra of Pd/SSZ-13 collected at: 298 K after exposed to ambient (blue); 473 K with 10% O_2 and 3.1% H_2O (light purple); 573 K with 10% O_2 and 3.1% H_2O (light blue); 773 K with 10% O_2 and 4.5% H_2O (pink); 473 K after dehydration in 10% O_2 at 873 K (red).

3.3.2 Pd Speciation in the Presence of H_2O

To follow the coordination of H_2O with exchanged Pd at 1Al and 2Al sites, we computed the structures and ad-sorption energies of xH_2O molecules (x = 1 - 6) on three commonly proposed Pd cation motifs: [Z_2Pd^{II}], [$ZPd^{II}OH$], and [ZPd^{I}].[36,37,61,80,81]

$$1\text{Al}: \mathrm{ZPd^{I}(H_2O)}_{x-1} + \mathrm{H_2O} \xrightarrow{\Delta E_{\text{ads}}} \mathrm{ZPd^{I}(H_2O)}_x$$

$$\mathrm{ZPd^{II}(OH)(H_2O)}_{x-1} + \mathrm{H_2O} \xrightarrow{\Delta E_{\text{ads}}} \mathrm{ZPd^{II}(OH)(H_2O)}_x$$

$$2\text{Al}: \mathrm{Z_2Pd^{II}(H_2O)}_{x-1} + \mathrm{H_2O} \xrightarrow{\Delta E_{\text{ads}}} \mathrm{Z_2Pd^{II}(H_2O)}_x$$

The lowest energy structures for each of the xH_2O adsorbed geometries obtained after AIMD simulations, (full details in section 4.1) were computed using both PBE and HSE06 functionals with the Becke-Johnson damping method (D3(BJ)vdw) included for dispersion corrections. HSE06 calculation results are summarized in Table 3.1. Calculated energies are similar for PBE and HSE06 (supporting information 2.2.1-1, and optimized structures are in the supporting information CONTCARS attachment) and show good agreement with reported PBE adsorption energies of xH2O (x = 1 - 4) ligands on [$ZPd^{II}OH$] and [ZPd^{I}] sites in H/BEA zeolite, and x = 1 on the [Z_2Pd^{II}] site in SSZ-13.[34,36,61] Normalized Pd oxidation states evaluated using Bader charge analysis are detailed in supporting information.

Table 3.1 H_2O Adsorption Energies (ΔE_{ads}), and Mobilities and Coordination Numbers of Pd sites with xH_2O (x = 1 - 4), Calculated Using HSE06-D3(BJ)vdw[a].

Adsorption Site	$+xH_2O$	1	2	3	4
[ZPd^I]	ΔE_{ads} (kJ mol^{-1})	-105	-76	-77	-63
	O_f / CN	2/3	0/2	0/3	0/4
	Mobility	0.8	2.2	1.4	1.8
[$ZPd^{II}OH$]	ΔE_{ads} (kJ mol^{-1})	-147	-53	-126	-71
	O_f / CN	2/4	1/4	0/4	0/4
	Mobility	0.4	1.0	1.4	2.6
[Z_2Pd^{II}]	ΔE_{ads} (kJ mol^{-1})	-52	-127	-88	-87
	O_f / CN	3/4	2/4	1/4	0/4
	Mobility	0.2	0.4	0.4	1.0

[a] CN and O_f denote the coordination number of Pd and the number of zeolitic framework oxygen bonded to it.

Hydration of [Z_2Pd^{II}] facilitates the movement of the Pd ion from 6MR (Figure 3.1b) to 8MR and finally, to the center of the zeolite cage (Figure 3.1c). Each H_2O molecule adsorbed replaces the zeolitic framework oxygen (O_f), until at x = 4, the Pd^{II} cation detaches from the framework, attaining a four-fold, square planar geometry, which is commonly observed in Pd-organometallic complexes.[14,34,66,67] Additional H_2O molecules (x = 5, 6) are physisorbed on the completely hydrated Pd complex, without altering the coordination chemistry and are ignored in the subsequent calculations. [$ZPd^{II}OH$] displays identical behavior and coordination chemistry with H_2O, forming a four-fold, square planar hydrated Pd complex at x = 3 as shown in Figure 3.1c. In contrast to the Pd^{II} species, [ZPd^I] evidences a different coordination behavior with H2O. Adsorption of a single H_2O molecule on Pd^I forms a two-fold coordinated linear complex, still attached to the zeolite framework. Subsequently adsorbed H_2O molecules change the Pd^I-hydrated complex to a linear, two-fold coordinated geometry, followed by three-fold and four-fold coordinated structures, separated from the zeolite framework. These H_2O-solvated Pd complexes, detached from the zeolite framework and mobile, have not been considered in the previous Pd/zeolite literature.

To further quantify the observed H_2O-promoted Pd mobility in the zeolite cage, we resolved the supercell into a 0.2 × 0.2 × 0.2 Å grid, and accounted for the number of cubes the Pd ion moved to during the course of an AIMD simulation at 298 K. The count was scaled by the grid volume and normalized by the scaled volume of $Z_2[Pd^{II}(H_2O)_4]$ (Pd mobility = 1.0). Table 3.1 reports the results of the mobility analysis; we generally observe that Pd mobility is enhanced as the degree of hydration is increased. There is however, a notable exception; the Pd mobility of $Z[Pd^{I}(H_2O)_2]$ is higher than $Z[Pd^{I}(H_2O)_3]$ owing to the former's H_2O-solvated linear two-fold coordinated structure, which can traverse the zeolite cage more easily due to its smaller size.

We also considered hydration of Pd bonded to O or H ligands that have been proposed in the literature, such as PdO and PdO_2.[34,48,59,61,82] Details of all 21 Pd species evaluated at 1Al and 2Al sites and their H_2O adsorption energies are provided in supporting information. We then compared their relative stabilities expressed as a function of temperature and chemical potentials of hydrogen and oxygen, referenced to H_2O and O_2, respectively. Z_* represents Z and Z_2 sites.

$$\mathrm{Z_*Pd} + \frac{x}{2}\left(\mathrm{H_2O} - \frac{1}{2}\,\mathrm{O_2}\right) + \frac{y}{2}\,\mathrm{O_2} \xrightarrow{\Delta \mathrm{G_{form}}} \mathrm{Z_*PdH}_x\mathrm{O}_y$$

The formation free energies (ΔG_{form}) of the $Z_*PdH_xO_y$ species are estimated using HSE06-D3(BJ)vdw and thermodynamic correlations described in section 3.4.2. We used the HSE06-computed energy of the exchange reaction eq 1 reported in section 3.2.1 for the formation of

[ZPd^{II}OH] from [Z$_2$Pd^{II}(H$_2$O)], to offset their 0 K energies, and collate the 1Al and 2Al structures on a common energy scale, with [Z$_2$Pd^{II}] defined as the zero of energy. Figure 3.4a illustrates the formation free energies at low temperature (condition 1, 298 K, 4.5% H$_2$O, and 10% O$_2$) and elevated temperature (condition 2, 773 K, 3.1% H$_2$O, and 10% O$_2$). These temperatures are characteristic of NO storage and release in PNAs, catalytic CO and hydrocarbon oxidation, and Wacker oxidation [37,38,45,47,48,51,59,60,80,81,83,84] and allow comparison of our computations with DRIFTS and X-ray absorption spectroscopy (XAS) data. The lowest free energy species at 298 K (condition 1) from Figure 3.4a is Z$_2$[Pd^{II}(H$_2$O)$_4$], followed by [Z$_2$Pd^{II}(H$_2$O)$_3$] which is +32 kJ mol^{-1} higher in energy. Formation of other Pd species at the 2Al site, such as [Z$_2$Pd^{II}], [Z$_2$Pd^{III}O] and [Z$_2$Pd^{II}O$_2$] are all endergonic, with [Z$_2$Pd^{III}O] being the least favorable species at this temperature. The lowest free energy structure at the 1Al site is Z[Pd^{II}(OH)(H$_2$O)$_3$], while the hydrated form of a Pd^{I} ion at the same site, Z[Pd^{I}(H$_2$O)$_4$], is endergonic by +51 kJ mol^{-1}. This is followed by species of varying degrees of hydration of [ZPd^{I}] and [ZPd^{II}O$_2$] at the 1Al site. As the temperature is increased to 773 K (condition 2), the free energies of all the hydrated species increase significantly, leaving [Z$_2$Pd^{II}] as the most stable species at the 2Al site, and [ZPd^{I}] at the 1Al site.

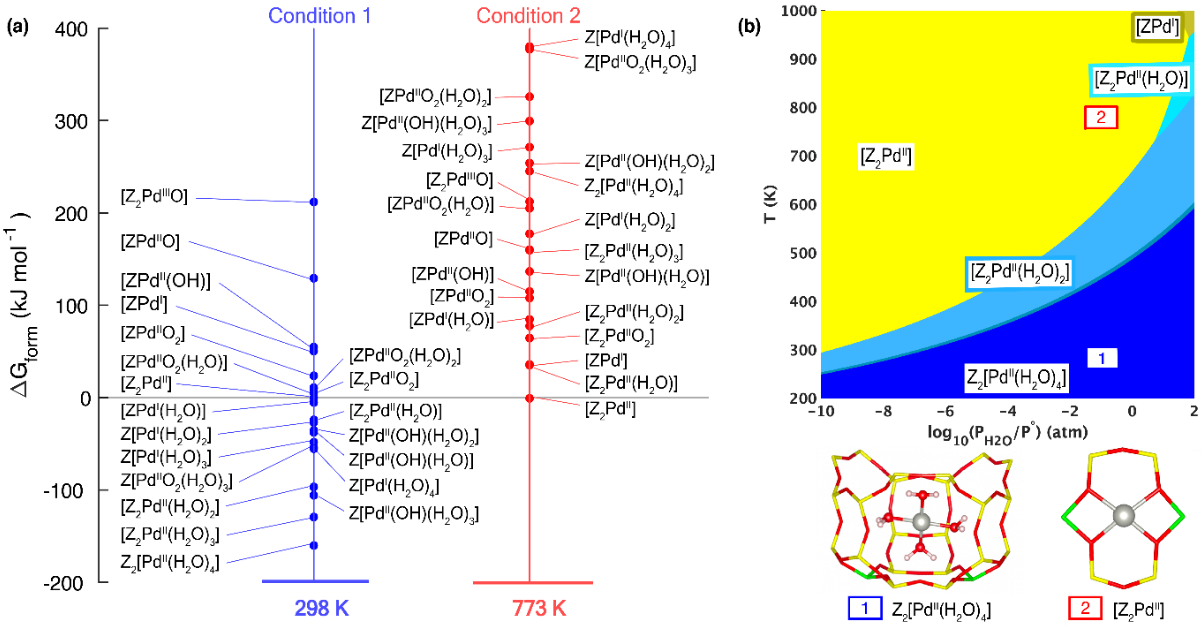

Figure 3.4. (a) Formation free energies (ΔG_{form}) of $Z_*PdH_xO_y$ species at 1Al and 2Al sites represented on a common energy scale at condition 1 (298 K, 4.5% H_2O, 10% O_2), and condition 2 (773 K, 3.1% H_2O, 10% O_2), and **(b)** Thermodynamic phase diagrams for 1Al and 2Al Pd-exchanged sites on a common energy scale based on HSE06-D3(BJ)vdw calculated energies. (The low and high temperature conditions are labeled accordingly on the phase diagrams with the structures shown for the corresponding minimum free energy species)

We extended the results of Figure 4a to formulate a combined phase diagram for $Z_*PdH_xO_y$ shown in Figure 3.4b, plotted over a range of temperatures and H_2O pressures at 10% O_2. HSE06-computed phase diagrams of individual 1Al and 2Al sites are shown in supporting information. Conditions 1 and 2 considered in Figure 3.4a are labeled on the phase diagram. The lowest energy species at low temperature and high H_2O pressure are the completely hydrated $Z_2[Pd^{II}(H_2O)_4]$ complexes; as the temperature is increased, waters of hydration desorb, giving the adsorbate-free $[Z_2Pd^{II}]$.

To validate the predicted characteristics of Pd cations we performed in-situ XAS experiments on a Pd/SSZ-13 sample (Si/Al = 17, Pd/Al = 0.046) at 298 K after ambience exposure, 473 K and 773 K in the presence of 10% O_2 and 3.1% H_2O, and at 473 K following dehydration at 873 K in 10% O_2. The extended X-ray absorption fine structure (EXAFS) spectra are shown in Figure 3.3b and additional details of the XAS experiments and fitting are reported in supporting information. We do not observe EXAFS features associated with higher shell Pd-O-Pd scattering in any of the collected spectra, confirming the absence of PdO nanoparticles in our materials, and X-ray absorption near edge structure (XANES) results show a similar edge energy to a $Pd^{II}O$ standard, confirming all cations have an oxidation state of 2+.

We observe a first shell Pd-O bond distance of 2.01±0.1 Å with a coordination number of 4.0±0.3, and absence of second shell scatter after exposure to either ambience at 298 K or to 10% O_2 and 3.1% H_2O at 473 K (blue lines). These spectra are equivalent to those of homogeneous aqueous PdII and Cu^{II} ions.[85,86] Our results are in agreement with the phase diagram prediction shown in Figure 3.4b, and support the formation of H_2O-solvated $Z_2[Pd^{II}(H_2O)_4]$ complexes detached from the zeolite framework.

EXAFS spectra collected at 773 K in 3.1% H_2O and 10% O_2 (pink line), or at 473 K following treatment at 873 K in 10% O_2 and 0% H_2O (red line), exhibit second shell scattering (attributed to framework Si/Al)[68] and a slightly lower Pd-O coordination number, similar to dehydrated Cu/SSZ-13.[68] We interpret these results as the dehydration of $Z_2[Pd_{II}(H_2O)_4]$ to $[Z_2Pd^{II}]$ at 773 K in the presence of 3.1% H_2O, in agreement with the phase diagram prediction shown in Figure 3.4b. In-situ DRIFTS dehydration experiments reported in supporting information Figure S3b, show similar trends in dehydration temperature.

3.3.3 NO Adsorption Energies

We computed NO adsorption energies, in the presence and absence of xH_2O ($x = 0 - 3$), at the 1Al and 2Al Pd sites employing the AIMD and geometry optimization proto-cols described in section 3.4.1 using both PBE-D3(BJ)vdw and HSE06-D3(BJ)vdw per the following reactions:

$$1\text{Al: } \mathrm{ZPd^{I}(H_2O)}_x + \mathrm{NO} \xrightarrow{\Delta E_{\mathrm{ads}}} \mathrm{ZPd(H_2O)}_x\mathrm{(NO)}$$

$$\mathrm{ZPd^{II}(OH)(H_2O)}_x + \mathrm{NO} \xrightarrow{\Delta E_{\mathrm{ads}}} \mathrm{ZPd^{II}(OH)(H_2O)}_x\mathrm{(NO)}$$

$$2\text{Al: } \mathrm{Z_2Pd^{II}(H_2O)}_x + \mathrm{NO} \xrightarrow{\Delta E_{\mathrm{ads}}} \mathrm{Z_2Pd^{II}(H_2O)}_x\mathrm{(NO)}$$

Full details and structure files along with the Pd oxidation states assessed by HSE06-computed Bader charges can be found in supporting information, and the CONTCARS attachment. Table 3.2 reports the computed NO binding energies; depending on the choice of functional, we observe differences as large as +99 kJ mol^{-1} for the same structure, in contrast with H_2O binding energies (supporting information). The significant disparity in NO adsorption energies is consistent with observations in the literature, which concur that GGA methods tend to overestimate the exothermicity of NO binding energies on Cu/SSZ-13 zeolites by > 90 kJ mol^{-1}.[87,88,89]

Regardless of the functional used, NO binding energies display similar qualitative trends, with [Z_2Pd^{II}] being the least, and [ZPd^{I}] the most exothermic. Geometries of NO-adsorbed species at 1Al and 2Al Pd sites, optimized using both PBE and HSE06 functionals, yield similar structures; HSE06-optimized structures are shown in Figure 3.5a. Khivantsev et al. reported a similar PBE NO binding geometry and energy on [Z_2Pd^{II}] in the 6MR.34,36 However, for [$ZPd^{II}OH$] and [ZPd^{I}], we found that NO causes relocation of the Pd cation to a lower energy minima for both PBE and HSE06. [$ZPd^{II}OH$], initially present in the plane of the 8MR, moved to the periphery of the 6MR upon adsorbing NO. Likewise, [ZPd^{I}(NO)] migrates to a lower energy geometry in the 8MR, as opposed to the reported 6MR; [34,36] the former being +50 kJ mol^{-1} more exothermic.

Table 3.2 NO Adsorption Energies (ΔE_{ads}), and Mobilities and Coordination Numbers of Pd sites in the Absence and Presence of xH$_2$O Molecules (x = 0 - 3), Calculated Using PBE-D3(BJ)vdw and HSE06-D3(BJ)vdw[a].

Adsorption Site	+xH$_2$O		0	1	2	3
[ZPd^{I}(NO)]	ΔE_{ads}	PBE	-272	-239	-240	-224
	(kJ mol^{-1})	HSE06	-175	-142	-141	-146
	O$_f$ / CN		3/4	2/4	0/3	0/4
	Mobility		0.4	1.6	1.6	0.8
[ZPd^{II}OH (NO)]	ΔE_{ads}	PBE	-195	-126	-157	-99
	(kJ mol^{-1})	HSE06	-140	-58	-103	-37
	O$_f$ / CN		2/4	1/4	0/4	0/4
	Mobility		0.4	0.6	0.4	0.8
[Z$_2$Pd^{II}(NO)]	ΔE_{ads}	PBE	-123	-150	-120	-123
	(kJ mol^{-1})	HSE06	-70	-106	-60	-68
	O$_f$ / CN		4/4	2/4	1/4	0/4
	Mobility		0.2	0.4	0.4	0.2

[a] CN and O$_f$ denote the coordination number of Pd and the number of zeolitic framework oxygen bonded to it.

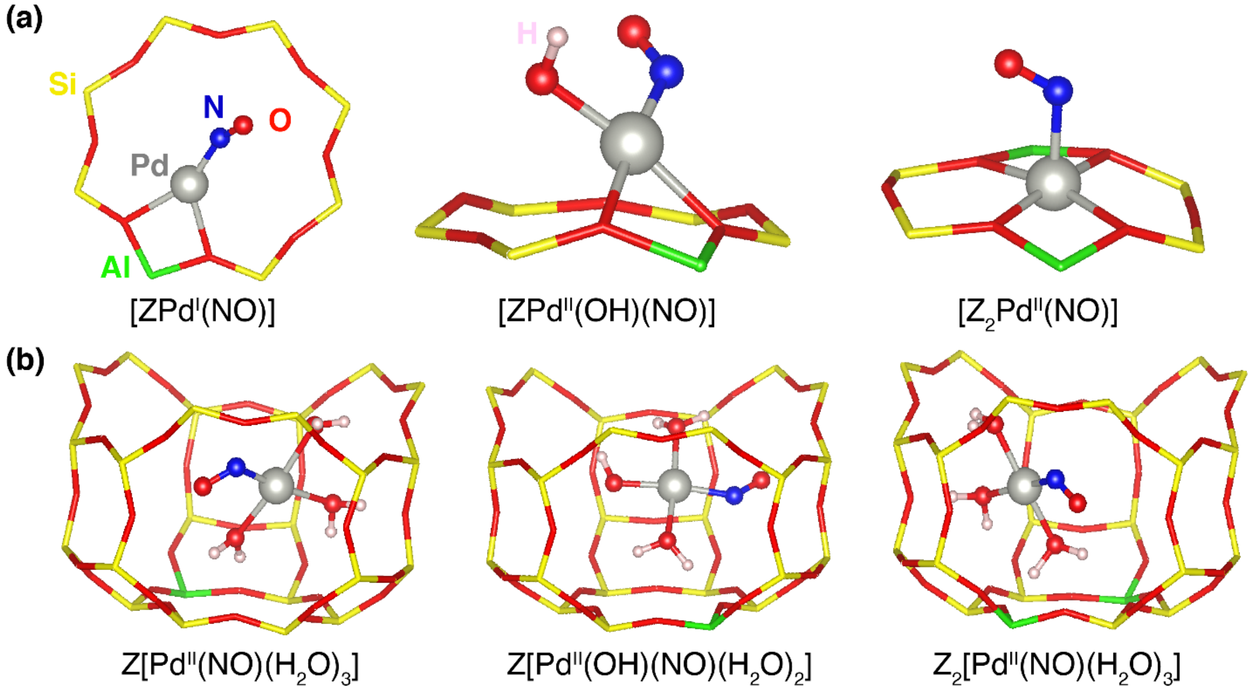

Figure 3.5. HSE06-optimized structures of **(a)** NO adsorbed on 1Al and 2Al Pd-exchanged sites, and **(b)** NO adsorbed in the presence of H_2O.

Adsorption of subsequent H_2O break the Pd-O_f bonds, eventually forming the favored four-fold coordinated, square planar hydrated Pd-nitrosyl complex at the center of the zeolite cage, at x = 2 in $[ZPd^{II}(OH)]$, and x= 3 in $[ZPd^{I}]$ and $[Z2Pd^{II}]$, shown in Figure 3.5b. Similar to Cu-mixed ligand mobile complexes,[90] the hydrated Pd-nitrosyl complexes exhibited Pd mobility (normalized to $Z_2[Pd^{II}(H_2O)_4] = 1.0$) as well, although slightly reduced in comparison to their fully H_2O-solvated analogues. The NO adsorption energy and optimized structure evaluated by Khivantsev et al. for $[Z_2Pd^{II}(NO)(H_2O)]$ using the PBE functional is consistent with our PBE results.[34,36] Formation of the mobile hydrated Pd-nitrosyl complexes detached from the zeolite framework requires adsorption of at least 2 H_2O for all three models. However, calculations with NO in the presence of > 1 H_2O on either $[Z_2Pd^{II}]$ or $[ZPd^{I}]$ and $[ZPd^{II}(OH)]$ have not been reported elsewhere.

To explore the adsorption of multiple NO, we determined the energy to adsorb a second NO molecule on [ZPd^{I}(NO)], [ZPd^{II}(OH)(NO)], and [Z_2Pd^{II}(NO)], using both PBE and HSE06; results are tabulated in supporting information and structures files are provided in the CONTCARS attachment. PBE-computed values parallel those reported in the literature.[34,36,61] HSE06 calculations demonstrate more endothermic energies for adsorption of the second NO on all structures. Moreover, HSE06 calculations showed that the adsorption of a second NO on [ZPd^{I}(NO)(H_2O)$_2$], [ZPd^{II}(OH)(NO)(H_2O)] and [Z_2Pd^{II}(NO)(H_2O)$_2$] was comparatively weaker than that of adsorbing a third H_2O molecule on these sites, implying the preferential adsorption of multiple H_2O molecules over multiple NO molecules for H_2O-solvated structures.

We considered NO adsorption on all 21 Pd-bound ligands at the 1Al and 2Al sites considered under hydrothermal conditions and employed thermodynamic analysis to evaluate their relative free energies with O_2, H_2O and NO as the references for oxygen, hydrogen and nitrogen, respectively. The formation free energies (ΔG_{form}) of the $Z_*PdH_xO_y(NO)_z$ species are computed as per section 3.4.2 using both PBE-D3(BJ)vdw and HSE06-D3(BJ)vdw energies, and both exchange reaction energies with both functionals (eqs. 1 and 2).

$$\mathrm{Z_*Pd} + \frac{x}{2}\left(\mathrm{H_2O} - \frac{1}{2}\,\mathrm{O_2}\right) + \frac{y}{2}\,\mathrm{O_2} + \mathrm{zNO} \xrightarrow{\Delta \mathrm{G_{form}}} \mathrm{Z_*PdH}_x\mathrm{O}_y\mathrm{(NO)_z}$$

The four resulting thermodynamic phase diagrams are provided in supporting information. While both PBE and HSE06 predict the same minimum free energy species, the P_{H2O} and T range over which the NO-bound species exist differ significantly between the two functionals. To determine which of these two DFT models are accurate, we next turn to coupled cluster theory-computed NO adsorption energies on candidate structures from our thermodynamic analysis.

3.3.4 Electronic Structures and Vibrational Frequencies of Pd-NO Structures

We first constructed two sets of molecular models for the minimum free energy species resulting from our thermo-dynamic analysis: H_2O-solvated Pd, and zeolite cluster models. For the H_2O-solvated Pd model, we extracted the four-fold coordinated hydrated-Pd complexes, as shown in Figure 3.1b, from the PBE-optimized periodic geometries of $Z[Pd^{I}(H_2O)_4]$, $Z[Pd^{II}(OH)(H_2O)_3]$, and $Z_2[Pd^{II}(H_2O)_4]$. Since this model is devoid of the zeolite framework, we compensated the charge by applying an appropriate uniform background charge. Next, we computed the energy required to exchange a single H_2O with NO, forming the hydrated-Pd nitrosyl complexes depicted in Figure 3.5b:

$$1\mathrm{Al}\colon \mathrm{Z[Pd^{I}(H_2O)_4] + NO} \overset{\Delta E}{\rightarrow} \mathrm{Z[Pd^{II}(H_2O)_3(NO)] + H_2O}$$

$$\mathrm{Z[Pd^{II}(OH)(H_2O)_4] + NO} \overset{\Delta E}{\rightarrow} \mathrm{Z[Pd^{II}(OH)(H_2O)_3(NO)] + \ H_2O}$$

$$2\mathrm{Al}\colon \mathrm{Z_2[Pd^{II}(H_2O)_4] + NO} \overset{\Delta E}{\rightarrow} \mathrm{Z_2[Pd^{II}(H_2O)_3(NO)] + H_2O}$$

The calculated energies required to replace H_2O with NO were then approximated per the method proposed by Sauer and co-workers[91–96], and reported in Table 3.3:

$$\mathrm{E_{supercell}^{HSE06}} \approx \mathrm{E_{supercell}^{GGA}} + \mathrm{E_{cluster}^{HSE06}} - \mathrm{E_{cluster}^{GGA}}$$

To validate our methodology, we computed cluster model single-point energies using the HSE06 functional and def-2TZVPP basis set for comparison to our supercell HSE06 calculations.

Comparison of the HSE06-computed energies for the periodic model with the H_2O-solvated Pd cluster model are within ±9 kJ mol^{-1}, demonstrating that the zeolite-excluded model is reasonably accurate. We also considered another hybrid DFT functional, B3LYP, and found the results agreed with HSE06 within ±15 kJ mol^{-1}. To benchmark our DFT results we performed WFT CCSD(T) calculations, which have been shown to be accurate for transition metal cations such as Cu, Fe, Cr, Ni, etc. [97–103] Computed CCSD(T) energies are reported in Table 3.3. We observe that HSE06 and B3LYP hybrid DFT functionals are within ±18 kJ mol^{-1} of the CCSD(T)-computed energies. These results substantiate the reliability of hybrid functionals over GGA for computation of NO binding energies.

Table 3.3 Comparison of Adsorption Energies for the Periodic Model with Zeolite Cluster Models for 1Al and 2Al Pd-exchanged Sites. All Reported Energies are in kJ mol^{-1} and Frequencies are in cm^{-1}.

	PBE/PW	HSE06/PW	HSE06/def2-TZVPP	B3LYP/def2-TZVPP	CCSD(T)/def2-TZVPP	B3LYP/def2-TZVPP NO
$Z_*[Pd(H_2O)_x] + NO \xrightarrow{\Delta E} Z_*[Pd(H_2O)_{x-1}(NO)] + H_2O$						
$Z[Pd^{II}(NO)(H_2O)_3]$	-169	-80	-78	-84	-74	1798
$Z[Pd^{II}OH(NO)(H_2O)_2]$	-49	+14	+23	+17	+5	1878
$Z_2[Pd^{II}(NO)(H_2O)_3]$	-52	+12	+6	+6	+8	1986
$[Z_*PdH_xO_y] + NO \xrightarrow{\Delta E_{ads}} [Z_*PdH_xO_y(NO)]$						
$[ZPd^{I}(NO)]$	-257	-159	-160	-171	NC	1853
$[ZPd^{II}OH(NO)]$	-185	-124	-127	-112	NC	1848
$[Z_2Pd^{II}(NO)]$	-108	-52	-50	-41	NC	1866

NC - not calculated, PW – plane wave

Subsequently, we calculated NO adsorption energies on the 1Al and 2Al Pd-exchanged sites in the zeolite cluster model using HSE06 and B3LYP functionals with the def2-TZVPP basis set:

$$\text{1Al: } [\mathrm{ZPd^{I}}] + \mathrm{NO} \xrightarrow{\Delta E_{\mathrm{ads}}} [\mathrm{ZPd^{I}(NO)}]$$

$$[\mathrm{ZPd^{II}(OH)}] + \mathrm{NO} \xrightarrow{\Delta E_{\mathrm{ads}}} [\mathrm{ZPd^{II}(OH)(NO)}]$$

$$\text{2Al: } [\mathrm{Z_2Pd^{II}}] + \mathrm{NO} \xrightarrow{\Delta E_{\mathrm{ads}}} [\mathrm{Z_2Pd^{II}(NO)}]$$

The CCSD(T) method was not implemented for this model due to the computational expense. Table 3.3 reports the NO adsorption energies on these cluster models. Analogous to the H_2O-solvated Pd model, energies of the HSE06-computed periodic model are similar to the cluster HSE06 and B3LYP calculations within ±3 kJ mol^{-1}. PBE-computed values vary by 100 kJ mol^{-1} from their hybrid functional counterparts. Our H_2O-solvated and zeolite cluster models showcase good accuracy for the NO energy landscape in Pd/SSZ-13. The structures for both models can be found in the supporting information CONTCARS attachment.

We next evaluated the vibrational frequencies for the species considered in the H_2O-solvated Pd and zeolite cluster models, using B3LYP/def2-TZVPP optimization and frequency calculations. We chose this combination of method and basis set since the scaled[104] gas-phase NO vibrational frequency (1904.0 cm^{-1}) is in close agreement with experiment (1904.1 cm^{-1}).[105] Table 3.3 reports the computed frequencies for each structure, additional details of the calculations can be found in section 3.4.3 and supporting information. Nitrosyl frequencies range from 1798 to

1986 cm^{-1}. We demonstrate below that these deviations are closely tied to the electronic structure of the Pd-NO complexes.

To gain insight into the nature of the Pd-NO moieties for H2O-solvated structures, we performed Natural Bond Order (NBO) analysis[106–112] on the B3LYP optimized structures using CCSD(T)-computed electronic structures. Electron occupancies along with geometries of the Pd-NO moieties are depicted in Figure 3.6, and further detailed in supporting information. NBO analyses assign neutral nitrosyl ligands for $Z_2[Pd(NO)(H_2O)_3]$ and $Z[Pd(OH)(NO)(H_2O)_2]$, confirming the Bader charge assignment of Pd^{II} for both species. However, localization of the electron densities of N and Pd-N bond is different among the two structures. NBO analyses yield electron populations of 1.89 and 0.98 for the N lone pairs, and populations of 0.99 and 1.95 for the Pd-N bonding orbitals, for $Z_2[Pd^{II}(NO)(H_2O)_3]$ and $Z[Pd^{II}(OH)(NO)(H_2O)_2]$, respectively. This discrepancy elongates the Pd-N distance and shortens the nitrosyl bond length for $Z_2[Pd^{II}(NO)(H_2O)_3]$, resulting in a 100 cm^{-1} increase in its frequency in comparison to $Z[Pd^{II}(OH)(NO)(H_2O)_2]$. NBO analysis of $Z[Pd(NO)(H_2O)_3]$ yields a full lone pair of electrons to the N atom, and a full pair of electrons to the Pd-N bond. NBO results are consistent with an oxidation state of -1 to the nitrosyl ligand (NO^-) and 2+ to Pd, which we assign as $Z[Pd^{II}(NO^-)(H_2O)_3]$.

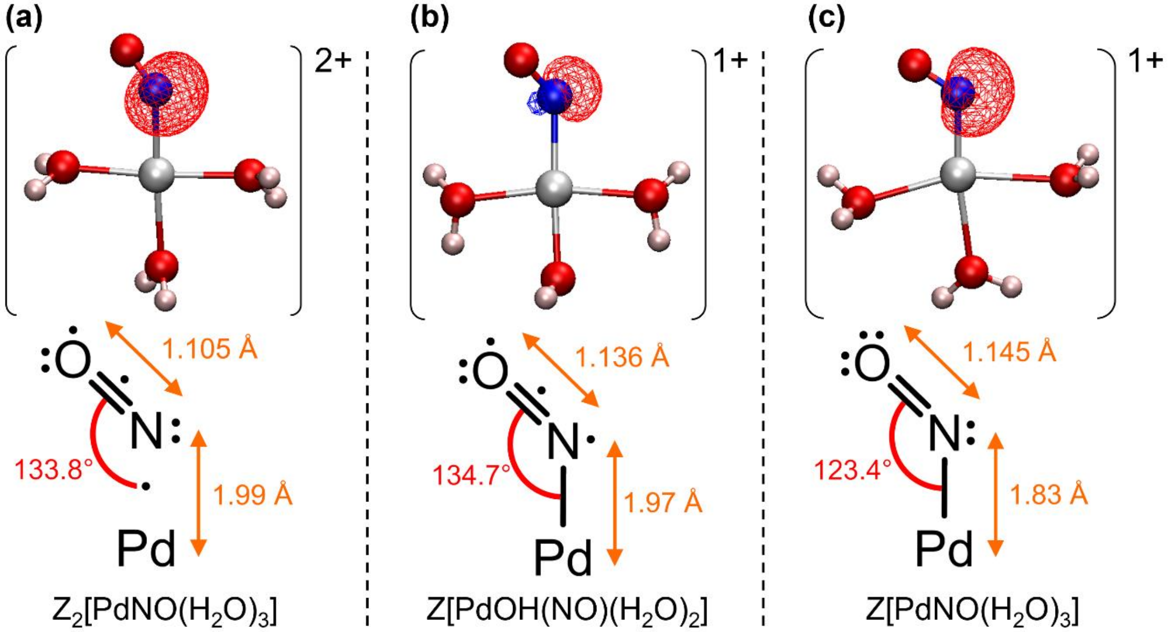

Figure 3.6. CCSD(T) calculated NBOs for B3LYP optimized geometries of **(a)** $Z_2[PdNO(H_2O)_3]$, **(b)** $Z[PdOH(NO)(H_2O)_2]$, and **(c)** $Z[PdNO(H_2O)_3]$. Red and blue isosurfaces indicate the different phases of the NBOs. NBO assigned Lewis dot structures for each species' Pd-NO moiety are beneath their NBO representations, with emphasis on the occupancy of the unbound N valence electrons. Pd-NO bond angles and distances are also displayed. The isovalues used for NBO plots are ±0.15.

We next incorporated zero-point, and vibrational free energies (detailed in supporting information), and HSE06-D3(BJ)vdw-computed energies to formulate a thermodynamic phase diagram of $Z_*PdH_xO_y(NO)_z$ species. Figure 3.7a reports the lowest free energy species as a function of temperature and H2O partial pressure, with O_2 and NO concentrations of 10% and 200 ppm, respectively. The lowest free energy species in the absence of H_2O and at 298 K is $[Z_2Pd^{II}(NO)]$. Reduction of Pd^{II} to $[ZPd^{I}(NO)]$ is predicted for low P_{H2O} ($-15 < \log(P_{H2O}/P°) < -6$), amounting to ppm levels of H_2O, at ambient temperatures. $[ZPd^{I}(NO)]$ and $[Z_2Pd^{II}(NO)]$ are close in free energy across this range of P_{H2O}, and possess similar NO vibrational frequencies, making it difficult to discern which species might be observed during experiments performed in the absence of H_2O. For 1 - 4.5% H_2O, conditions more representative of application and experiment, the lowest energy species from 298 - 660 K is $Z[Pd^{II}(NO^{-})(H_2O)_3]$. As temperature increases to 403 K at 4.5% H_2O, the lowest energy species at the 1Al site, $Z[Pd^{II}(NO^{-})(H_2O)_3]$, and the 2Al site, $Z_2[Pd^{II}(H_2O)_4]$ are 8 kJ mol^{-1} apart. The Boltzmann distribution of species at these conditions predicts that 10% of the Pd sites will be H_2O-solvated as $Z_2[Pd^{II}(H_2O)_4]$. The subtle difference in free energy between these two species at 403 K, and between $Z[Pd^{II}(NO^{-})(H_2O)_3]$ and $[ZPd^{I}(NO)]$ near 600 K, are sensitive to the inclusion of vibrational free energies. With further increase in temperature, $Z[Pd^{II}(NO^{-})(H_2O)_3]$ loses water of hydration along with NO to revert to the original adsorbate-free $[Z_2Pd^{II}]$ site at 700 K. At 4.5% H_2O, 10% O_2 and 200 ppm NO results suggest a nominal NO adsorption stoichiometry of:

$$\mathrm{Z_2[Pd^{II}(H_2O)_4] + NO} \xrightarrow[-8\ \mathrm{kJ\ mol^{-1}}]{\Delta G(403\ \mathrm{K})} \mathrm{Z[Pd^{II}(NO^{-})(H_2O)_3]/[ZH]} + \frac{1}{2}\ \mathrm{H_2O} + \frac{1}{4}\mathrm{O_2}$$

Similarly, the NO desorption stoichiometry is:

$$\mathrm{Z[Pd^{II}(NO^{-})(H_2O)_3]/[ZH]} + \tfrac{1}{4}\mathrm{O_2} \xrightarrow[-16\ \mathrm{kJ\ mol^{-1}}]{\Delta G(773\ \mathrm{K})} \mathrm{[Z_2Pd^{II}]} + \frac{7}{2}\mathrm{H_2O} + \mathrm{NO}$$

Our thermodynamic model thus, predicts a reaction environment-induced change in the number of Al sites charge compensating the Pd cation in the zeolite upon exposure to NO and during subsequent dehydration. The underlying kinetics of this non-elementary process are still unclear.

We next performed isothermal NO adsorption at 353 K followed by temperature programmed desorption (TPD) experiments (30 K/min ramp rate) under 4.5% H_2O, and dry conditions (< 5 ppm H_2O), to qualitatively compare the relative NO binding energies of the most abundant surface intermediates, namely, $[Z_2Pd^{II}(NO)]$ or $[ZPd^{I}(NO)]$ under dry conditions, and $Z[Pd^{II}(NO^-)(H_2O)_3]$ in the presence of 4.5% H_2O. The NOx-TPD profile from Pd/SSZ-13 under dry conditions before peak deconvolution is shown in supporting information, as is the one from H/SSZ-13. Peak deconvolution, also shown in supporting information, was performed using these two profiles to separate NO adsorption on Pd-related species from NO interacting with zeolitic AlO_4^- sites. As shown in Figure 3.8, the majority of NOx desorbs from Pd at temperatures near 500 K under dry conditions, whereas the NOx desorption profile peaks at around 750 K in the presence of 4.5% H_2O. This difference in NO de-sorption temperatures agrees with the phase diagram prediction in Figure 3.7b featuring lower free energy of $Z[Pd^{II}(NO^-)(H_2O)_3]$ compared to $[Z_2Pd^{II}(NO)]$ or $[ZPd^{I}(NO)]$, and thus a higher NOx desorption temperature in the presence of H_2O (Figure 3.7a). In the presence of 4.5% H_2O, we also observed additional NOx adsorption at around 440 K, likely due to the small difference (8 kJ mol^{-1}) in free energies between $Z_2[Pd^{II}(H_2O)_4]$ and $Z[Pd^{II}(NO^-)(H_2O)_3]$ in this temperature range, or the kinetics of H_2O desorption and NO adsorption. Integrating the desorption peak gives a 1.05±0.1 NO:Pd ratio in the presence of H_2O, in agreement with the HSE06-computed pre-diction for endothermic adsorption of a second NO on $Z[Pd^{II}(NO^-)(H_2O)_3]$. The free energy calculations discussed above are based on thermodynamics, without considering differences between H_2O and NO adsorption and desorption kinetics. Nevertheless, the difference be-tween NOx-TPD profiles is captured by the computed phase diagram.

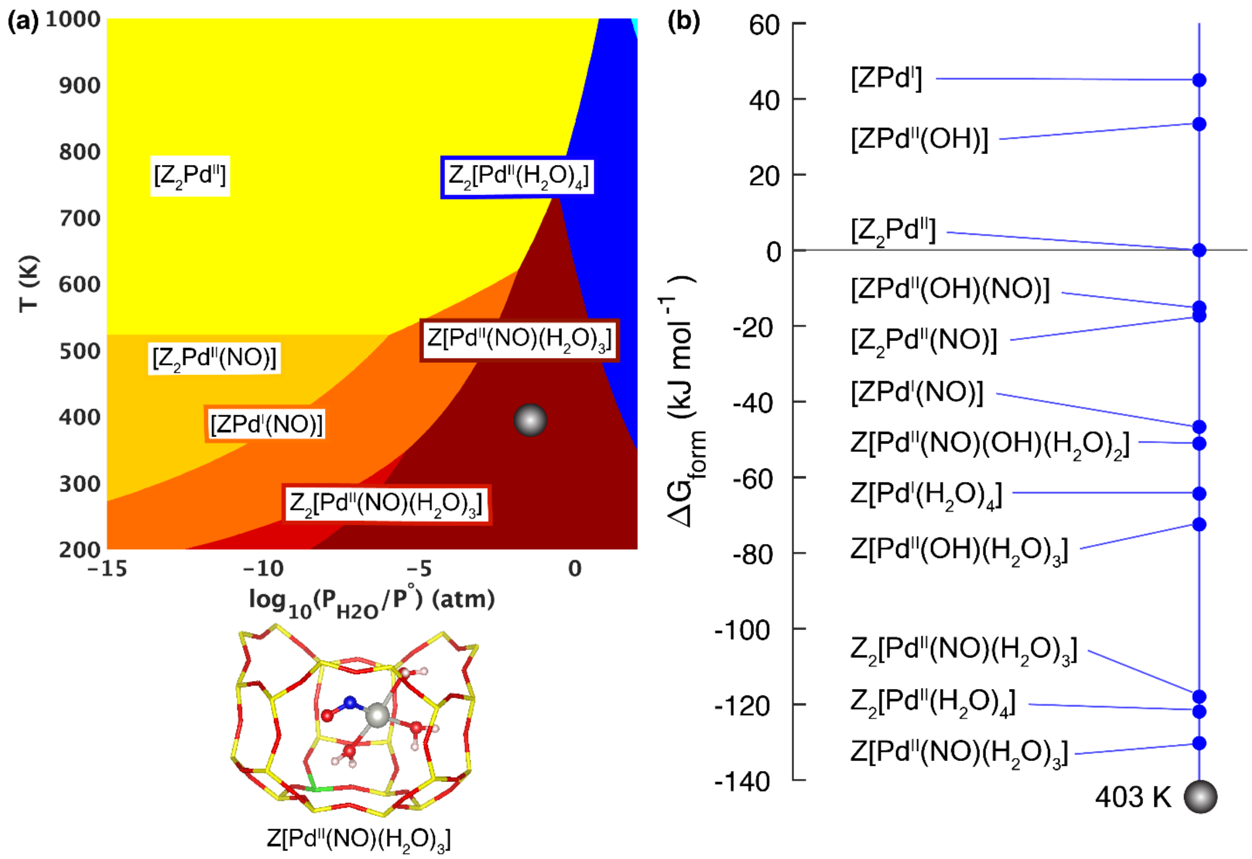

Figure 3.7. (a) Thermodynamic phase diagram for $Z_*PdH_xO_y(NO)_z$ species at 1Al and 2Al Pd-exchanged sites on a common energy scale incorporating the zero-point, and vibrational free energies, and HSE06-computed energies, and **(b)** Formation free energies (ΔGform) of $Z_*PdH_xO_y(NO)_z$ species at 1Al and 2Al sites represented on a common energy scale at 403 K, 4.5% H2O, 10% O2, 200 ppm NO.

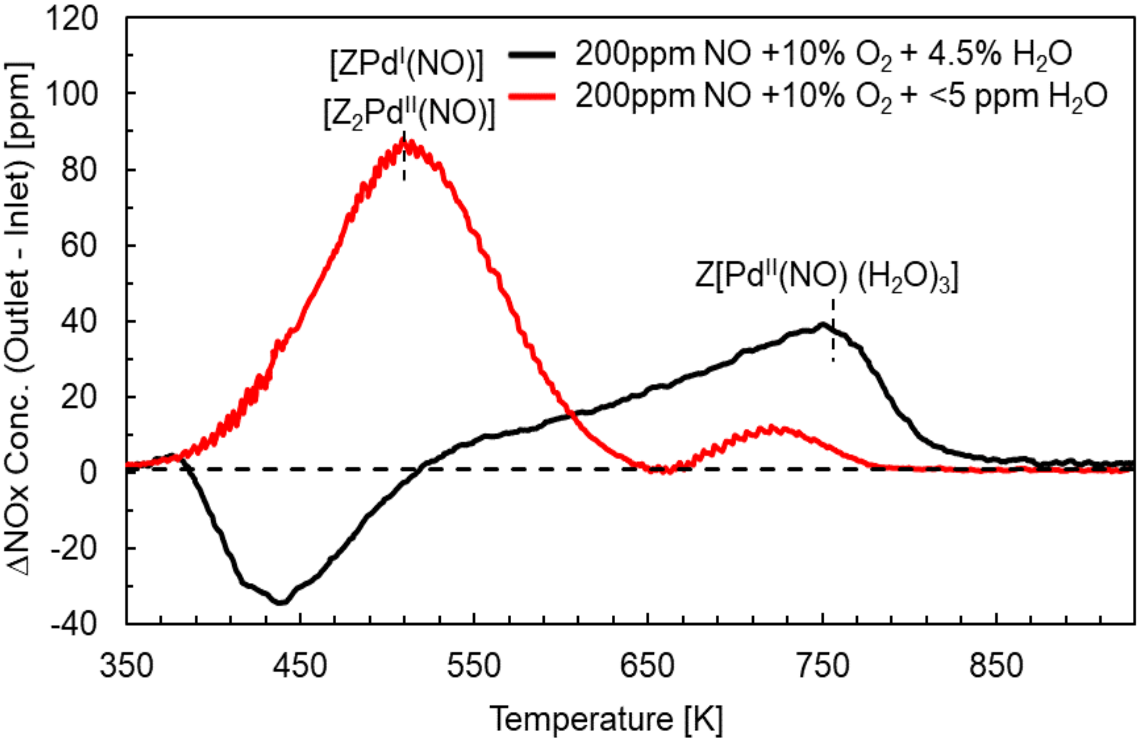

Figure 3.8. NO_x temperature programmed desorption (NO_x-TPD) profiles of Pd/SSZ-13 (Si/Al = 9, Pd/Al = 0.056) in the presence of 200 ppm NO, 10% O_2, 4.5% H_2O (red) and < 5ppm H_2O (black) at a ramp rate of 30 K/min.

3.3.5 Experimental IR Frequencies

To further validate the structures predicted by our molecular models, we collected in-situ NO adsorption DRIFTS spectra at 473 K and 403 K in 10% O_2, 200 ppm NO and a wide range of P_{H2O}. As is shown in Figure 3.9a, a spectrum collected at 473 K under dry conditions in the presence of 200 ppm NO and 10% O_2 has an IR absorption peak at 1858 cm^{-1}, and another at 2200 cm^{-1}, the latter is shown in supporting information. Peak assignments for the > 2100 cm^{-1} IR features have been widely discussed in the literature, appearing on H-zeolites, and are assigned to stretching of NO^+ interacting with zeolitic AlO_4^- sites.[33,52,113,114] The identity of the Pd-related NO stretching feature at 1858 cm^{-1} can be assigned to either [Z_2Pd^{II}(NO)] or [ZPd^{I}(NO)], substantiated by the DFT-calculated vibrational frequencies of 1866 cm^{-1} and 1853 cm^{-1} in Table 3.3. Although we cannot differentiate between [$Z_2Pd^{II}(NO)$] and [$ZPd^{I}(NO)$] based on IR frequencies, we posit that only one of these two species should exist un-der dry conditions due to the single symmetric peak observed.

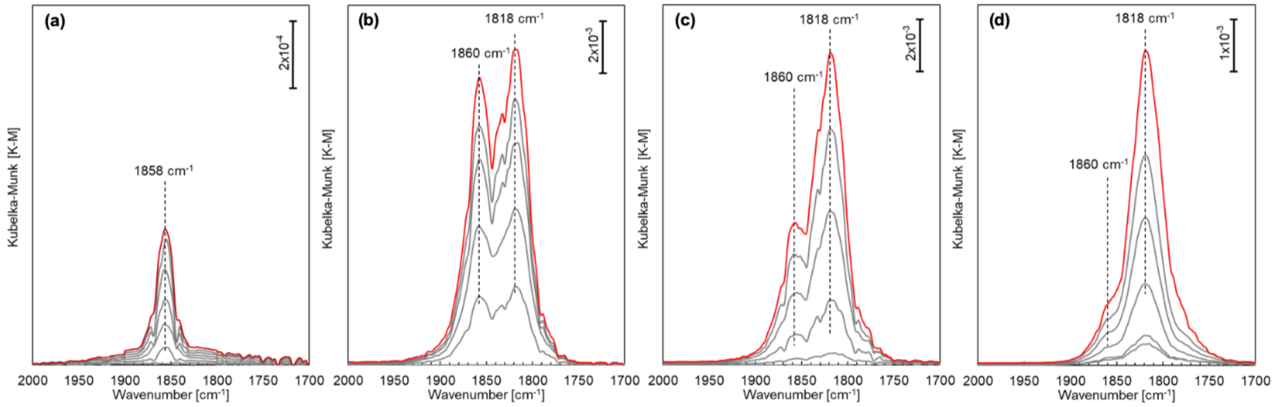

Figure 3.9. In-situ NO adsorption DRIFTS spectra of Pd/SSZ-13 (Si/Al = 9, Pd/Al = 0.056) collected at: **(a)** 473 K with 200 ppm NO, 10% O_2; **(b)** 473 K with 200 ppm NO, 10% O_2 and 1.3% H_2O; **(c)** 403 K with 200 ppm NO, 10% O_2 and 1.3% H_2O; **(d)** 403 K with 200 ppm NO, 10% O_2 and 4.5% H_2O. Red spectra are the final spectra collected after saturation and grey traces are time resolved spectra collected before saturation with 10 min time intervals. Background spectra were collected at **(a)** 473 K with 10% O_2; **(b)** 473 K with 10% O_2 and 1.3% H_2O; **(c)** 403 K with 10% O_2 and 1.3% H_2O; **(d)** 403 K with 10% O_2 and 4.5% H_2O.

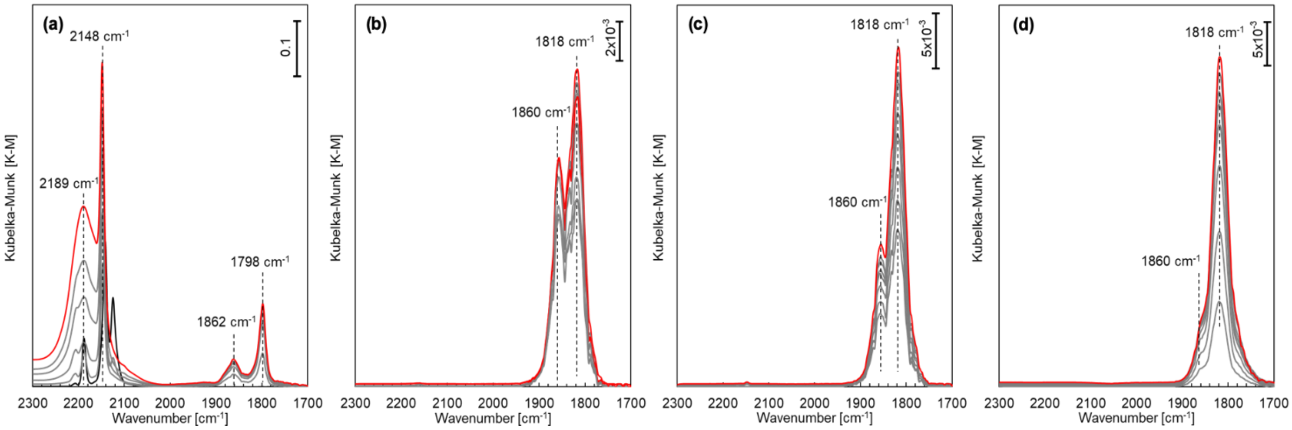

Figure 3.10. In-situ DRIFTS spectra of Pd/SSZ-13 (Si/Al = 9, Pd/Al = 0.056) collected at: **(a)** 353 K during 200 ppm NO addition after exposure to 10% O_2, 20 ppm H_2O and 200 ppm CO; **(b)** 403 K during 200 ppm CO addition after exposure to 10% O_2, 1.3% H_2O and 200 ppm NO; **(c)** 473 K during 200 ppm CO addition after exposure to 10% O_2, 1.3% H_2O and 200 ppm NO; **(d)** 403 K during 200 ppm CO addition after exposure to 10% O_2, 4.5% H_2O and 200 ppm NO. Background spectra were collected at **(a)** 353 K with 10% O_2 and 20 ppm H_2O; **(b)** 403 K with 10% O_2 and 1.3% H_2O; **(c)** 473 K with 10% O_2 and 1.3% H_2O; **(d)** 403 K with 10% O_2 and 4.5% H_2O.

To determine the effect of H_2O on Pd-NO speciation we collected DRIFTS spectra in the presence of 200 ppm NO, 10% O_2 and 1.3% H_2O at 473 K and 403 K shown in Figure 3.9b and Figure 3.9c. We observed the appearance of a new IR feature at 1810 cm^{-1} in the presence of 1.3% H_2O and the disappearance of the >2100 cm^{-1} features, the latter is shown in supporting information Figures S10-S12. The intensity of the 1810 cm^{-1} peak was larger at the lower temperature. Figure 3.9d shows the spectrum collected at 403 K with 200 ppm NO, 10% O_2 and 4.5% H_2O, where the peak intensity at 1810 cm^{-1} increases significantly relative to the peak at 1860 cm^{-1}. A similar peak shift upon addition of H_2O was observed by Chen et. al.[47] We attribute this behavior to the formation of $Z[Pd^{II}(NO^-)(H_2O)_3]$, the lowest free energy species in the presence of H_2O according to the phase diagram in Figure 3.7, and the DFT-computed NO vibrational frequency of 1798 cm^{-1} for $Z[Pd^{II}(NO^-)(H_2O)_3]$ in Table 3.3. The NO stretching frequency at around 1810 cm^{-1} has been previously reported as $[ZPd^{I}(NO)]$ in the absence of H_2O.[34,36,37] However, our DRIFTS experiments clearly demonstrate that this feature has P_{H2O} and T dependencies indicating a H_2O-solvated structure. We observed no nitrate or nitrite formation in the presence of percentage-level H_2O and have reported spectra with these regions included in the supporting information Figures S10-S12. Spectra taken (supporting information) in the presence of 200 ppm NO, 10% O_2 and 20 ppm H_2O are representative of those reported as being in the absence of H_2O elsewhere.[34]

3.3.6 CO Adsorption and Oxidation

The effect of H_2O noted above could also impact other reactions since Pd cations formed in the presence and absence of H_2O are two intrinsically different species. CO has been reported to adsorb on Pd cations in Pd/SSZ-13 and may also contribute to irreversible degradation of

PNAs.[81] Therefore, we chose CO adsorption and oxidation as probe reactions to further investigate the H_2O-solvation effect.

We collected DRIFTS spectra in the presence of 200 ppm CO, 200 ppm NO, 10% O_2 and 20 ppm – 4.5% H_2O. At 20 ppm H_2O, CO stretching frequencies appear at 2148 and 2189 cm^{-1} (Figure 3.10a), consistent with spectra reported by Khivantsev et al. under similar conditions.[37] However, exposure to 1.3 - 4.5% H_2O (Figure 3.10b-d) causes the disappearance of all CO stretching frequencies (~2100-2300 cm^{-1}), resulting in the recovery of the spectra collected in the absence of CO reported in Figure 3.9b-d.

We attribute the vanishing of CO frequencies to the more exothermic binding of NO on Pd as compared to CO, in the presence of H_2O, forming predominantly $Z[Pd^{II}(NO^-)(H_2O)_3]$ under these conditions. The HSE06 computed binding energy of CO is -59 kJ mol^{-1} on $Z[Pd^{I}(H_2O)_4]$, and -80 kJ mol^{-1} for NO (supporting information), which supports this hypothesis. Further, replacement of H_2O with CO on $Z[Pd^{II}(NO^-)(H_2O)_3]$ is computed to be endothermic (+44 kJ mol^{-1}), indicating co-adsorption of CO is prohibitive.

We performed steady-state CO oxidation experiments between 373 K to 473 K in the presence and absence of 4.5% H_2O, where 200 ppm CO was present at all times (Figure 3.11, additional details in supporting information). We also measured water gas shift (WGS) activity on the same catalyst to eliminate a possible change in activation energy due to the onset of the WGS reaction (blue circles). CO oxidation rates measured in the presence of 4.5% H_2O are significantly higher than those measured in the absence of H_2O. Formation of Pd nano-particles is not detected under these conditions (Figure S14, additional details in supporting information), suggesting H_2O-solvated Pd complexes are the active site for catalytic CO oxidation. The different CO oxidation activation energies further highlight the distinction between H_2O-solvated and dehydrated Pd. This may be due H_2O assisted O_2 activation, or mobilization of Pd cations to form transient multinuclear complexes.[7,10,11,115] Table 3.1 suggests a possible correlation between Pd cation mobility and CO oxidation activity. We also performed steady-state CO oxidation experiments in the presence of NO, with and without 4.5% H_2O, with 200 ppm CO, 200 ppm NO and 10% O_2. The near-zero CO oxidation activity in the presence of 200 ppm NO and 4.5% H_2O reported in supporting information provides further evidence that CO adsorption is prohibitive on $Z[Pd^{II}(NO^{-})(H_2O)_3]$.

Figure 3.11. CO oxidation rates measured on Pd/SSZ-13 (Si/Al = 9, Pd/Al = 0.056) in the presence of: 200 ppm CO, 10% O_2 and 4.5% H_2O (red square); 200 ppm NO, 200 ppm CO, 10% O_2 and 4.5% H_2O (purple diamond); 200 ppm CO and 10% O_2 (black triangle); 200 ppm NO, 200 ppm CO and 10% O_2 (green circle). Water gas shift rates measured on Pd/SSZ-13 (Si/Al = 9, Pd/Al = 0.056) in the presence of 200 ppm CO and 4.5% H_2O (blue circle).

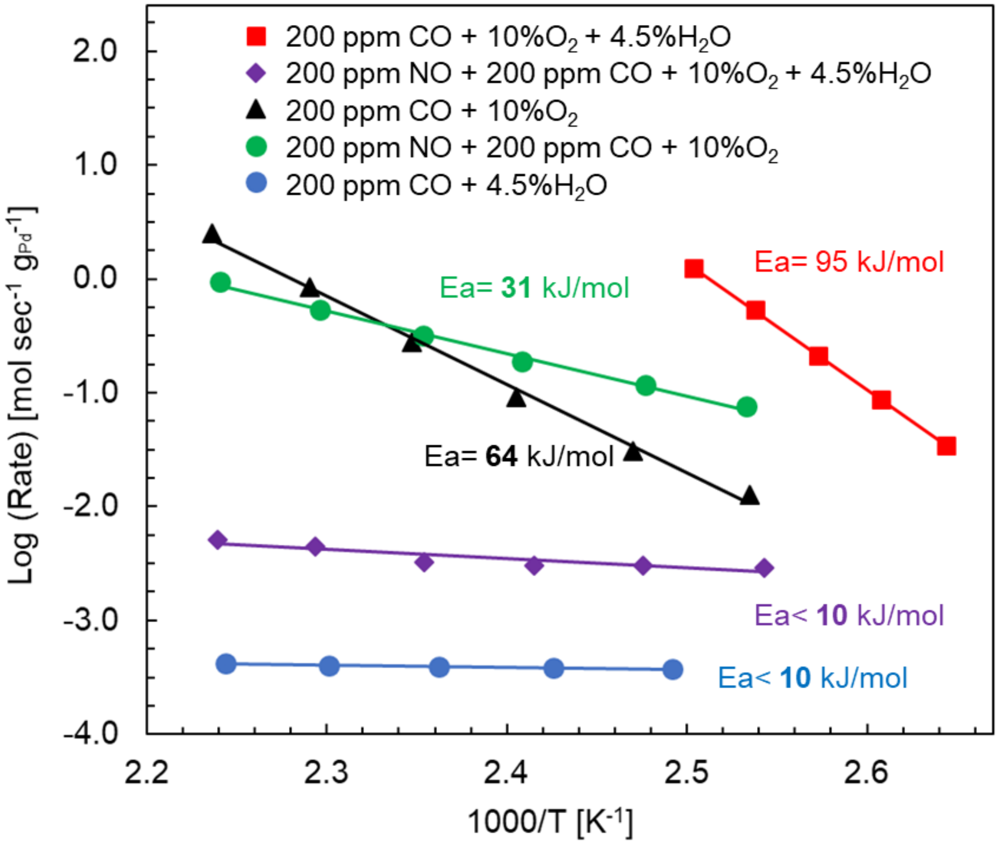

Taken together, our results show that CO oxidation is promoted by formation of H_2O-solvated Pd complexes in the absence of NO. However, in the presence of NO and practically relevant H_2O pressures at $\leqslant$ 473 K CO adsorption is inhibited. We find no evidence to support the formation of $Pd^{II}(NO)(CO)$ complexes under these conditions.

3.3.7 Comparison with ZSM-5 and BEA Zeolites

We have demonstrated that the presence of H_2O leads to the solvation of Pd and Pd-NO complexes. The EXAFS spectrum of H_2O exposed Pd/SSZ-13 reported in Figure 3.3 lacks second shell scattering at T $\leqslant$ 473 K, which suggests that these hydrated complexes are detached from the zeolite framework. A similar solvation effect induced by NH3 has also been observed in Cu/SSZ-13. At temperatures lower than 523 K NH_3-solvated Cu complexes form and interact with the zeolite framework through electrostatic tethering.[7,9] Motivated by these observations, we hypothesized that the nature of hydrated Pd-NO complexes with-in different zeolite frameworks should be similar, although the Pd-NO complexes formed in the absence of H_2O can differ due to differences in initial Pd speciation.

To test this hypothesis, we extended our in-situ NO adsorption DRIFTS experiments on Pd/SSZ-13 (Si/Al = 9, Pd/Al = 0.056) to Pd/ZSM-5 (Si/Al = 15, Pd/Al = 0.094) and Pd/BEA (Si/Al = 12.5, Pd/Al = 0.079), and first performed NO adsorption in the absence of H_2O at 423 K, followed by NO adsorption in the presence of 4.5% H_2O at 353 K. Figure 3.12 shows that the DRIFTS spectra collected in the absence of water (solid lines) for Pd/BEA and Pd/ZSM-5 are significantly different from Pd/SSZ-13 in terms of both the number of features and their frequencies. NO stretching features at 1881 cm^{-1} and 1836 cm^{-1} on Pd/ZSM-5, and 1849 cm^{-1} on Pd/BEA are consistent with the reported NO stretching features in the Pd/zeolite literature.[33,48,83,116] The primary NO adsorption sites in the absence of H_2O for BEA and ZSM-5 are unknown, and appear to give rise to different NO stretching frequencies and potentially different Pd/zeolite binding energies.[47] Additionally, more than one NO stretching feature is observed with Pd/ZSM-5 and Pd/BEA, indicating more heterogeneous Pd cation speciation resulting from different framework topology and Al distributions compared to SSZ-13.[53,117–120] However, DRIFTS spectra collected after NO adsorption in the presence of 4.5% H_2O (dashed lines) show similar IR features regardless of zeolite topology. Dominating features at 1818 cm^{-1} for Pd/SSZ-13, 1814 cm^{-1} for Pd/ZSM-5, and 1808 cm^{-1} for Pd/BEA demonstrate a more homogenized distribution of Pd cations, even though the peak positions of these features are slightly different, likely due to the effect of zeolite cage geometry.[47] This result supports the hypothesis that the hydration of Pd cations causes them to detach from the zeolite and give way to homogenized and H_2O-solvated $Z[Pd^{II}(NO^-)(H_2O)_3]$ complexes within different zeolite frameworks.

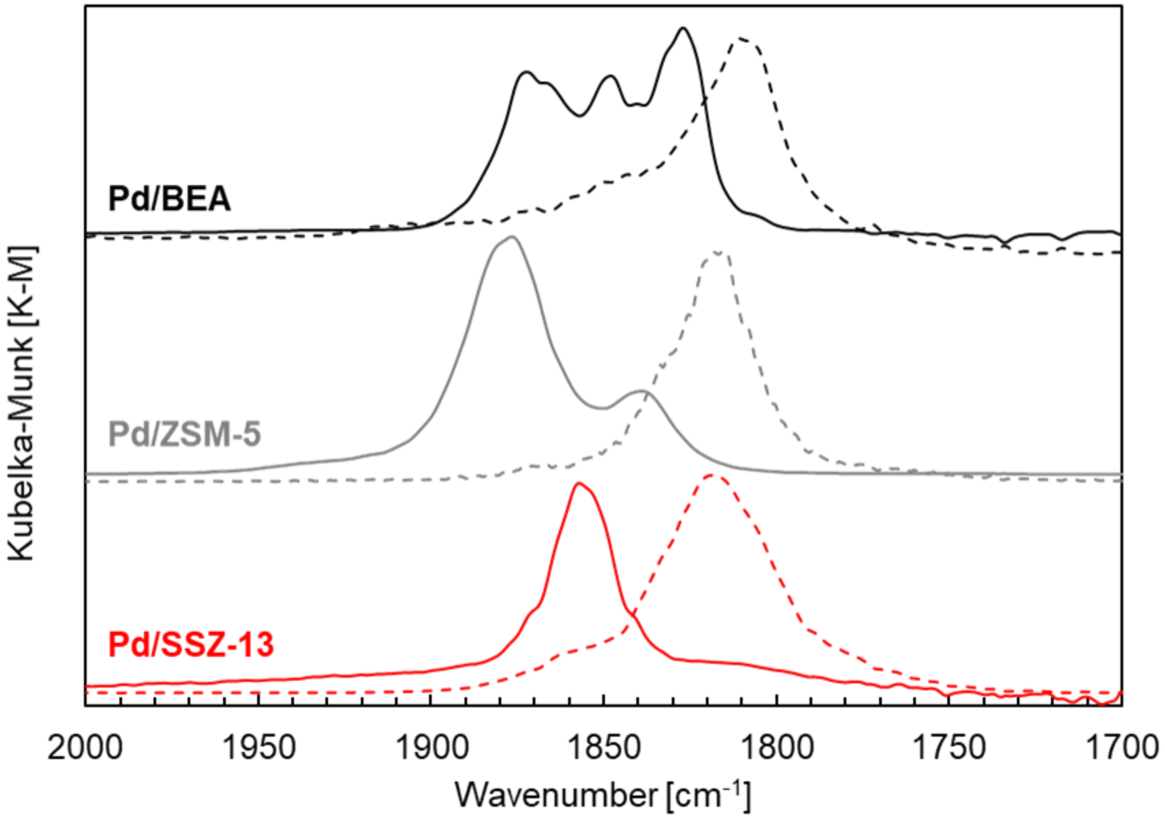

Figure 3.12. In-situ NO adsorption DRIFTS spectra of Pd/SSZ-13 (red), Pd/ZSM-5 (gray) and Pd/BEA (black). Spectra are collected at: 473 K with 200 ppm NO, 10% O_2 (solid line) and 403 K with 200 ppm NO, 10% O_2 and 4.5% H_2O (dashed line) for Pd/SSZ-13; 373 K with 200 ppm NO, 10% O_2 (solid line) and 373 K with 200 ppm NO, 10% O_2 and 4.5% H_2O (dashed line) for Pd/ZSM-5; 353 K with 200 ppm NO, 10% O_2 (solid line) and 353 K with 200 ppm NO, 10% O_2 and 4.5% H_2O (dashed line) for Pd/BEA. Background spectra were collected at: 473 K with 10% O_2 (solid line) and 403 K with 10% O_2 and 4.5% H_2O (dashed line) for Pd/SSZ-13; 373 K with 10% O_2 (solid line) and 373 K with 10% O_2 and 4.5% H_2O (dashed line) for Pd/ZSM-5; 353 K with 10% O_2 (solid line) and 353 K with 10% O_2 and 4.5% H_2O (dashed line) for Pd/BEA. Peak heights are normalized to the intensity of the dominating feature of each spectrum to highlight the difference in peak numbers and positions.

3.4 Conclusions

We show here that Pd ions and Pd-NO complexes are sensitive to environmental conditions and interrogation of their speciation is possible through a combined approach of experiment and computational modeling. Exposure of Pd-zeolites to H_2O and NO causes profound changes that are captured through condition-dependent spectroscopic and kinetic experiments, and by previously unexplored computational models that incorporate H_2O-solvation, AIMD simulations, hybrid-exchange DFT functionals, and WFT calculations. As shown here, GGA functionals, such as PBE, do not accurately describe Pd-NO complexes.

We show that exchanged Pd cations in SSZ-13 zeolites with Si/Al = 9 and Si/Al = 15 preferentially locate to 2Al 6MR sites as $[Z_2Pd^{II}]$, similar to their Cu and Co analogues. In contrast to Cu, and consistent with Co, the computed energies of forming $[ZPd^{II}OH]$ moieties are prohibitive, and we do not detect their presence in any of our materials. Our findings may shed light on experimental difficulties with exchanging Pd-cations in SSZ-13, especially at higher Si/Al ratios where the density of 2Al 6MR sites may be small. Neither our computational or experimental results suggest the presence of Pd^{I}, or the higher oxidation states Pd^{III} and Pd^{IV} in as-synthesized Pd-zeolites, consistent with prior assertions.[36] Exposure to H_2O at < 573 K solvates and mobilizes Pd ions, similar to observations for Cu/zeolites.[68] Catalytic CO oxidation and IR experiments further emphasize the chemical differences between $[Z_2Pd^{II}]$ and $Z_2[Pd^{II}(H_2O)_4]$. These conditions are similar to those used for catalytic Wacker oxidation (378 K, ~0.3-3% H_2O) on Cu-Pd/zeolite Y:

$$2C_2H_4 + O_2 \rightarrow 2C_2H_4O$$

where a H_2O apparent order of 0.73 was measured.[46] Under these conditions we expect both Pd and Cu cations[68] to be H_2O-solvated, and the mobility of both ions could play an important role in the mechanism.

Exposure to NO facilitates transformation from 2Al to 1Al Pd-exchange sites. At < 5 ppm of H_2O, both $[Z_2Pd^{II}NO]$ and $[ZPd^{I}NO]$ are close in free energy. Under conditions of more practical relevance, $Z[Pd^{II}(NO^-)(H_2O)_3]$ becomes the dominant and lowest free energy species, desorbing NO at a higher temperature than its dehydrated counterparts, and prohibits the adsorption of CO. The recognition of H_2O-solvated Pd-nitrosyl complexes unifies disparate and contradictory assignments in the Pd/zeolite literature, draws strong connections to homogeneous Pd inorganic chemistry, and provides a molecularly detailed description of the Pd-complexes relevant to PNA and catalytic oxidation. These solvated Pd-nitrosyl complexes are less mobile than their fully H_2O-solvated counterparts, which may have mechanistic consequences for CO oxidation, and could be beneficial for preventing Pd deactivation processes in these materials.

Zeolites of varying topology evidence a heterogeneous distribution of Pd-NO complexes that coalesce into one spectral feature upon exposure to H_2O. Although reported NO adsorption and desorption concentration vs time profiles, and NO desorption temperatures, vary with zeolite topology, the formation of homogeneous-like nitrosyl complexes among multiple zeolites potentially removes one of the constraints for optimizing PNA materials.

Our results suggest the following nominal stoichiometry for NO adsorption/desorption processes:

$$\xrightarrow{\hspace{8em}\text{Temperature}\hspace{8em}}$$

$$Z_2[Pd^{II}(H_2O)_4] \underset{-OH}{\overset{+NO}{\leftrightharpoons}} Z[Pd^{II}NO^-(H_2O)_3]/[ZH] \underset{\substack{-3H_2O,\\ -H,-NO}}{\leftrightharpoons} [Z_2Pd^{II}]$$

This cascade is obviously non-elementary and involves activated processes for NO adsorption and desorption. The transport and kinetics of these adsorption and desorption processes are likely influenced by zeolite topology, but their mechanistic details remain unclear. Nevertheless, our results provide the thermodynamic roadmap for future mechanistic studies. Our findings underscore the importance of environmental conditions in the formation of metal complexes in zeolites, and the need for experimental and computational approaches that interrogate their chemical nature under practical conditions.

3.5 References

(1) Kosinov, N.; Liu, C.; Hensen, E. J. M.; Pidko, E. A. Engineering of Transition Metal Catalysts Confined in Zeolites. *Chem. Mater.* **2018**, *30* (10), 3177–3198.

(2) Li, Y.; Li, L.; Yu, J. Applications of Zeolites in Sustainable Chemistry. Chem 2017, 3 (6), 928–949.

(3) Harris, J. W.; Bates, J. S.; Bukowski, B. C.; Greeley, J.; Gounder, R. Opportunities in Catalysis over Metal-Zeotypes Enabled by Descriptions of Active Centers Beyond Their Binding Site. ACS Catal. 2020, 9476–9495.

(4) Dusselier, M.; Davis, M. E. Small-Pore Zeolites: Synthesis and Catalysis. Chem. Rev. 2018, 118 (11), 5265–5329.

(5) Thomas, J. M.; Raja, R.; Lewis, D. W. Single-Site Heterogeneous Catalysts. Angew. Chem. Int. Ed. 2005, 44 (40), 6456–6482.

(6) Paolucci, C.; Di Iorio, J. R.; Schneider, W. F.; Gounder, R. Solvation and Mobilization of Copper Active Sites in Zeolites by Ammonia: Consequences for the Catalytic Reduction of Nitrogen Oxides. Acc. Chem. Res. 2020, 53 (9), 1881–1892.

(7) Paolucci, C.; Khurana, I.; Parekh, A. A.; Li, S.; Shih, A. J.; Li, H.; Di Iorio, J. R.; Albarracin-Caballero, J. D.; Yezerets, A.; Miller, J. T.; Delgass, W. N.; Ribeiro, F. H.; Schneider, W. F.; Gounder, R. Dynamic Multinuclear Sites Formed by Mobilized Copper Ions in NOx Selective Catalytic Reduction. Science 2017, 357 (6354), 898–903.

(8) Chen, L.; Falsig, H.; Janssens, T. V. W.; Grönbeck, H. Activation of Oxygen on (NH3CuNH3)+ in NH3-SCR over Cu-CHA. J. Catal. 2018, 358, 179–186.

(9) Brogaard, R. Y.; Kømurcu, M.; Dyballa, M. M.; Botan, A.; Van Speybroeck, V.; Olsbye, U.; De Wispelaere, K. Ethene Dimerization on Zeolite-Hosted Ni Ions: Reversible Mobilization of the Active Site. ACS Catal. 2019, 9 (6), 5645–5650.

(10) Gao, F.; Mei, D.; Wang, Y.; Szanyi, J.; Peden, C. H. F. Selective Catalytic Reduction over Cu/SSZ-13: Linking Homo- and Heterogeneous Catalysis. J. Am. Chem. Soc. 2017, 139 (13), 4935–4942.

(11) Negri, C.; Selleri, T.; Borfecchia, E.; Martini, A.; Lomachenko, K. A.; Janssens, T. V. W.; Cutini, M.; Bordiga, S.; Berlier, G. Structure and Reactivity of Oxygen-Bridged Diamino Dicopper(II) Complexes in Cu-Ion-Exchanged Chabazite Catalyst for NH3-Mediated Selective Catalytic Reduction. J. Am. Chem. Soc. 2020, 142 (37), 15884–15896.

(12) Mingos, D. M. P.; Crabtree, R. H. Comprehensive Organometallic Chemistry III; Elsevier: Amsterdam; Boston, 2007.

(13) Canty, A. J. Higher Oxidation State Organopalladium and Platinum Chemistry; Springer, 2011.

(14) Henry, P. Palladium Catalyzed Oxidation of Hydrocarbons; Springer Science & Business Media, 2012.

(15) Balch, A. L. Odd Oxidation States of Palladium and Platinum. Comments Inorg. Chem. 1984, 3 (2–3), 51–67.

(16) Powers, D. C.; Ritter, T. Bimetallic Pd(III) Complexes in Palladium-Catalysed Carbon–Heteroatom Bond Formation. Nature Chemistry, 2009, 1, 302–309.

(17) Mirica, L. M.; Khusnutdinova, J. R. Structure and Electronic Properties of Pd(III) Complexes. Coord. Chem. Rev. 2013, 257 (2), 299–314.

(18) Goggin, P. L.; Mink, J. Palladium(I) Carbonyl Halide Complexes. J. Chem. Soc. Dalton Trans. 1974, No. 5, 534.

(19) Jaworski, J. N.; Kozack, C. V.; Tereniak, S. J.; Knapp, S. M. M.; Landis, C. R.; Miller, J. T.; Stahl, S. S. Operando Spectroscopic and Kinetic Characterization of Aerobic Allylic C–H Acetoxylation Catalyzed by Pd(OAc)2/4,5-Diazafluoren-9-One. J. Am. Chem. Soc. 2019, 141 (26), 10462–10474.

(20) Canty, A. J. The+ IV Oxidation State in Organopalladium Chemistry. Platin. Met. Rev. 1993, 37 (1), 2–7.

(21) Canty, A. J. Development of Organopalladium(IV) Chemistry: Fundamental Aspects and Systems for Studies of Mechanism in Organometallic Chemistry and Catalysis. Acc. Chem. Res. 1992, 25 (2), 83–90.

(22) Canty, A. J. Organopalladium and Platinum Chemistry in Oxidising Milieu as Models for Organic Synthesis Involving the Higher Oxidation States of Palladium. Dalton Trans. 2009, No. 47, 10409.

(23) Muñiz, K. High-Oxidation-State Palladium Catalysis: New Reactivity for Organic Synthesis. Angew. Chem. Int. Ed. 2009, 48 (50), 9412–9423.

(24) Sehnal, P.; Taylor, R. J. K.; Fairlamb, I. J. S. Emergence of Palladium(IV) Chemistry in Synthesis and Catalysis. Chem. Rev. 2010, 110 (2), 824–889.

(25) Xu, L.-M.; Li, B.-J.; Yang, Z.; Shi, Z.-J. Organopalladium(Iv) Chemistry. Chem. Soc. Rev. 2010, 39 (2), 712–733.

(26) Shimada, S.; Li, Y.-H.; Choe, Y.-K.; Tanaka, M.; Bao, M.; Uchimaru, T. Multinuclear Palladium Compounds Containing Palladium Centers Ligated by Five Silicon Atoms. Proc. Natl. Acad. Sci. U. S. A. 2007, 104 (19), 7758–7763.

(27) Chen, W.; Shimada, S.; Tanaka, M. Synthesis and Structure of Formally Hexavalent Palladium Complexes. Science 2002, 295 (5553), 308–310.

(28) Knott, B. C.; Nimlos, C. T.; Robichaud, D. J.; Nimlos, M. R.; Kim, S.; Gounder, R. Consideration of the Aluminum Distribution in Zeolites in Theoretical and Experimental Catalysis Research. ACS Catal. 2018, 8 (2), 770–784.

(29) Dědeček, J.; Sobalík, Z.; Wichterlová, B. Siting and Distribution of Framework Aluminium Atoms in Silicon-Rich Zeolites and Impact on Catalysis. Catal. Rev. 2012, 54 (2), 135–223.

(30) Sklenak, S.; Dědeček, J.; Li, C.; Wichterlová, B.; Gábová, V.; Sierka, M.; Sauer, J. Aluminum Siting in Silicon-Rich Zeolite Frameworks: A Combined High-Resolution 27Al NMR Spectroscopy and Quantum Mechanics / Molecular Mechanics Study of ZSM-5. Angew. Chem. Int. Ed. 2007, 46 (38), 7286–7289.

(31) Yokoi, T.; Mochizuki, H.; Namba, S.; Kondo, J. N.; Tatsumi, T. Control of the Al Distribution in the Framework of ZSM-5 Zeolite and Its Evaluation by Solid-State NMR Technique and Catalytic Properties. J. Phys. Chem. C 2015, 119 (27), 15303–15315.

(32) Pinar, A. B.; Gómez-Hortigüela, L.; McCusker, L. B.; Pérez-Pariente, J. Controlling the Aluminum Distribution in the Zeolite Ferrierite via the Organic Structure Directing Agent. Chem. Mater. 2013, 25 (18), 3654–3661.

(33) Descorme, C.; Gélin, P.; Primet, M.; Lécuyer, C. Infrared Study of Nitrogen Monoxide Adsorption on Palladium Ion-Exchanged ZSM-5 Catalysts. Catal. Lett. 1996, 41 (3), 133–138.

(34) Khivantsev, K.; Jaegers, N. R.; Kovarik, L.; Hanson, J. C.; Tao, F. (Feng); Tang, Y.; Zhang, X.; Koleva, I. Z.; Aleksandrov, H. A.; Vayssilov, G. N.; Wang, Y.; Gao, F.; Szanyi, J. Achieving Atomic Dispersion of Highly Loaded Transition Metals in Small-Pore Zeolite SSZ-13: High-Capacity and High-Efficiency Low-Temperature CO and Passive NO x Adsorbers. Angew. Chem. 2018, 130 (51), 16914–16919.

(35) Khivantsev, K.; Jaegers, N. R.; Kovarik, L.; Prodinger, S.; Derewinski, M. A.; Wang, Y.; Gao, F.; Szanyi, J. Palladium/Beta Zeolite Passive NOx Adsorbers (PNA): Clarification of PNA Chemistry and the Effects of CO and Zeolite Crystallite Size on PNA Performance. Appl. Catal. Gen. 2019, 569 (August 2018), 141–148.

(36) Khivantsev, K.; Jaegers, N. R.; Koleva, I. Z.; Aleksandrov, H. A.; Kovarik, L.; Engelhard, M.; Gao, F.; Wang, Y.; Vayssilov, G. N.; Szanyi, J. Stabilization of Super Electrophilic Pd+2 Cations in Small-Pore SSZ-13 Zeolite. J. Phys. Chem. C 2020, 124 (1), 309–321.

(37) Khivantsev, K.; Gao, F.; Kovarik, L.; Wang, Y.; Szanyi, J. Molecular Level Understanding of How Oxygen and Carbon Monoxide Improve NOx Storage in Palladium/SSZ-13 Passive NOx Adsorbers: The Role of NO+ and Pd(II)(CO)(NO) Species. J. Phys. Chem. C 2018, 122 (20), 10820–10827.

(38) Khivantsev, K.; Jaegers, N. R.; Kovarik, L.; Hu, J. Z.; Gao, F.; Wang, Y.; Szanyi, J. Palladium/Zeolite Low Temperature Passive NOx Adsorbers (PNA): Structure-Adsorption Property Relationships for Hydrothermally Aged PNA Materials. Emiss. Control Sci. Technol. 2020, 6, 126–138.

(39) Kowalak, S.; Weiss, R. C.; Balkus, K. J. Zeolite Encapsulated Pd(Salen), a Selective Hydrogenation Catalyst. J. Chem. Soc. Chem. Commun. 1991, No. 1, 57–58.

(40) Zhang, J.; Wang, L.; Shao, Y.; Wang, Y.; Gates, B. C.; Xiao, F.-S. A Pd@Zeolite Catalyst for Nitroarene Hydrogenation with High Product Selectivity by Sterically Controlled Adsorption in the Zeolite Micropores. Angew. Chem. Int. Ed. 2017, 56 (33), 9747–9751.

(41) Armor, J. Catalytic Reduction of Nitrogen Oxides with Methane in the Presence of Excess Oxygen: A Review. Catal. Today 1995, 26 (2), 147–158.

(42) Cargnello, M.; Jaen, J. J. D.; Garrido, J. C. H.; Bakhmutsky, K.; Montini, T.; Gamez, J. J. C.; Gorte, R. J.; Fornasiero, P. Exceptional Activity for Methane Combustion over Modular Pd@CeO2 Subunits on Functionalized Al2O3. Science 2012, 337 (6095), 713–717.

(43) Petrov, A. W.; Ferri, D.; Tarik, M.; Kröcher, O.; van Bokhoven, J. A. Deactivation Aspects of Methane Oxidation Catalysts Based on Palladium and ZSM-5. Top. Catal. 2017, 60 (1–2), 123–130.

(44) Losch, P.; Huang, W.; Vozniuk, O.; Goodman, E. D.; Schmidt, W.; Cargnello, M. Modular Pd/Zeolite Composites Demonstrating the Key Role of Support Hydrophobic/Hydrophilic Character in Methane Catalytic Combustion. ACS Catal. 2019, 9 (6), 4742–4753.

(45) Petrov, A. W.; Ferri, D.; Krumeich, F.; Nachtegaal, M.; van Bokhoven, J. A.; Kröcher, O. Stable Complete Methane Oxidation over Palladium Based Zeolite Catalysts. Nat. Commun. 2018, 9 (1), 2545.

(46) Imbao, J.; Bokhoven, J. A. van; Clark, A.; Nachtegaal, M. Elucidating the Mechanism of Heterogeneous Wacker Oxidation over Pd-Cu/Zeolite Y by Transient XAS. Nat. Commun. 2020, 11 (1), 1–9.

(47) Chen, H.-Y.; Collier, J. E.; Liu, D.; Mantarosie, L.; Durán-Martín, D.; Novák, V.; Rajaram, R. R.; Thompsett, D. Low Temperature NO Storage of Zeolite Supported Pd for Low Temperature Diesel Engine Emission Control. Catal. Lett. 2016, 146 (9), 1706–1711.

(48) Zheng, Y.; Kovarik, L.; Engelhard, M. H.; Wang, Y.; Wang, Y.; Gao, F.; Szanyi, J. Low-Temperature Pd/Zeolite Passive NOx Adsorbers: Structure, Performance, and Adsorption Chemistry. J. Phys. Chem. C 2017, 121 (29), 15793–15803.

(49) Mihai, O.; Trandafilović, L.; Wentworth, T.; Torres, F. F.; Olsson, L. The Effect of Si/Al Ratio for Pd/BEA and Pd/SSZ-13 Used as Passive NOx Adsorbers. Top. Catal. 2018, 61 (18–19), 2007–2020.

(50) Ryou, Y. S.; Lee, J.; Cho, S. J.; Lee, H.; Kim, C. H.; Kim, D. H. Activation of Pd/SSZ-13 Catalyst by Hydrothermal Aging Treatment in Passive NO Adsorption Performance at Low Temperature for Cold Start Application. Appl. Catal. B Environ. 2017, 212, 140–149.

(51) Gu, Y.; Epling, W. S. Passive NOx Adsorber: An Overview of Catalyst Performance and Reaction Chemistry. Appl. Catal. Gen. 2019, 570 (September 2018), 1–14.

(52) Gupta, A.; Kang, S. B.; Harold, M. P. NOx Uptake and Release on Pd/SSZ-13: Impact Of Feed Composition and Temperature. Catal. Today 2020, in press.

(53) Ambast, M.; Karinshak, K.; Rahman, B. Md. M.; Grabow, L. C.; Harold, M. P. Passive NOx Adsorption on Pd/H-ZSM-5: Experiments and Modeling. Appl. Catal. B Environ. 2020, 269, 118802.

(54) Malamis, S. A.; Harold, M. P.; Epling, W. S. Coupled NO and C3H6 Trapping, Release and Conversion on Pd/BEA: Evaluation of the Lean Hydrocarbon NOx Trap. Ind. Eng. Chem. Res. 2019, 58 (51), 22912–22923.

(55) Malamis, S. A.; Harold, M. P. Optimizing the Lean Hydrocarbon NO Trap: Sequential and Dual-Layer Configurations. Catal. Today 2020, in press.

(56) Theis, J. R.; Ura, J. A. Assessment of Zeolite-Based Low Temperature NOx Adsorbers: Effect of Reductants during Multiple Sequential Cold Starts. Catal. Today 2020, in press.

(57) Primet, M.; Ben Taarit, Y. Infrared Study of Oxidized and Reduced Palladium Loaded Zeolites. J. Phys. Chem. 1977, 81 (13), 1317–1324.

(58) Che, M.; Dutel, J. F.; Gallezot, P.; Primet, M. A Study of the Chemisorption of Nitric Oxide on PdY Zeolite. Evidence for a Room Temperature Oxidative Dissolution of Palladium Crystallites. J. Phys. Chem. 1976, 80 (21), 2371–2381.

(59) Ryou, Y. S.; Lee, J.; Lee, H.; Kim, C. H.; Kim, D. H. Effect of Various Activation Conditions on the Low Temperature NO Adsorption Performance of Pd/SSZ-13 Passive NOx Adsorber. Catal. Today 2019, 320 (x), 175–180.

(60) Kim, Y.; Hwang, S.; Lee, J.; Ryou, Y. S.; Lee, H.; Kim, C. H.; Kim, D. H. Comparison of NO x Adsorption/Desorption Behaviors over Pd/CeO 2 and Pd/SSZ-13 as Passive NO x Adsorbers for Cold Start Application. Emiss. Control Sci. Technol. 2019, 5 (2), 172–182.

(61) Mei, D.; Gao, F.; Szanyi, J.; Wang, Y. Mechanistic Insight into the Passive NOx Adsorption in the Highly Dispersed Pd/HBEA Zeolite. Appl. Catal. Gen. 2019, 569 (x), 181–189.

(62) Baerlocher, C.; McCusker, L. B. Database of Zeolite Structures http://www.iza-structure.org/databases/.

(63) Li, S.; Li, H.; Gounder, R.; Debellis, A.; Müller, I. B.; Prasad, S.; Moini, A.; Schneider, W. F. First-Principles Comparison of Proton and Divalent Copper Cation Exchange Energy Landscapes in SSZ-13 Zeolite. J. Phys. Chem. C 2018, 122 (41), 23564–23573.

(64) Loewenstein, W. The Distribution of Aluminum in the Tetrahedra of Silicates and Aluminates. Am. Mineral. 1954, 39 (1–2), 92–96.

(65) Bell, R. G.; Jackson, R. A.; Catlow, C. R. A. Löwenstein’s Rule in Zeolite A: A Computational Study. Zeolites 1992, 12 (7), 870–871.

(66) Hayton, T. W.; Legzdins, P.; Sharp, W. B. Coordination and Organometallic Chemistry of Metal-NO Complexes. Chem. Rev. 2002, 102 (4), 935–991.

(67) Crabtree, R. H. Making Sense of Organometallic Complexes. In The Organometallic Chemistry of the Transition Metals; John Wiley & Sons, Ltd, 2014; pp 40–68.

(68) Paolucci, C.; Parekh, A. A.; Khurana, I.; Di Iorio, J. R.; Li, H.; Albarracin Caballero, J. D.; Shih, A. J.; Anggara, T.; Delgass, W. N.; Miller, J. T.; Ribeiro, F. H.; Gounder, R.; Schneider, W. F. Catalysis in a Cage: Condition-Dependent Speciation and Dynamics of Exchanged Cu Cations in Ssz-13 Zeolites. J. Am. Chem. Soc. 2016, 138 (18), 6028–6048.

(69) Wang, L.; Chen, H.; Wang, W. N–H Bond Activation in Ammonia by TM-SSZ-13 (Fe, Co, Ni and Cu) Zeolites: A First-Principles Calculation. Phys. Chem. Chem. Phys. 2019, 21 (3), 1506–1513.

(70) Fickel, D. W.; Lobo, R. F. Copper Coordination in Cu-SSZ-13 and Cu-SSZ-16 Investigated by Variable-Temperature XRD. J. Phys. Chem. C 2010, 114 (3), 1633–1640.

(71) Szanyi, J.; Kwak, J. H.; Zhu, H.; Peden, C. H. F. Characterization of Cu-SSZ-13 NH3 SCR Catalysts: An in Situ FTIR Study. Phys. Chem. Chem. Phys. 2013, 15 (7), 2368–2380.

(72) Korhonen, S. T.; Fickel, D. W.; Lobo, R. F.; Weckhuysen, B. M.; Beale, A. M. Isolated Cu2+ Ions: Active Sites for Selective Catalytic Reduction of NO. Chem. Commun. 2010, 47 (2), 800–802.

(73) Fickel, D. W.; D'Addio, E.; Lauterbach, J. A.; Lobo, R. F. The Ammonia Selective Catalytic Reduction Activity of Copper-Exchanged Small-Pore Zeolites. Appl. Catal. B Environ. 2011, 102 (3), 441–448.

(74) Di Iorio, J. R.; Nimlos, C. T.; Gounder, R. Introducing Catalytic Diversity into Single-Site Chabazite Zeolites of Fixed Composition via Synthetic Control of Active Site Proximity. ACS Catal. 2017, 7 (10), 6663–6674.

(75) Di Iorio, J. R.; Gounder, R. Controlling the Isolation and Pairing of Aluminum in Chabazite Zeolites Using Mixtures of Organic and Inorganic Structure-Directing Agents. Chem. Mater. 2016, 28 (7), 2236–2247.

(76) Bates, S. A.; Verma, A. A.; Paolucci, C.; Parekh, A. A.; Anggara, T.; Yezerets, A.; Schneider, W. F.; Miller, J. T.; Delgass, W. N.; Ribeiro, F. H. Identification of the Active Cu Site in Standard Selective Catalytic Reduction with Ammonia on Cu-SSZ-13. J. Catal. 2014, 312, 87–97.

(77) Bordiga, S.; Vitillo, J. G.; Ricchiardi, G.; Regli, L.; Cocina, D.; Zecchina, A.; Arstad, B.; Bjørgen, M.; Hafizovic, J.; Lillerud, K. P. Interaction of Hydrogen with MOF-5. J. Phys. Chem. B 2005, 109 (39), 18237–18242.

(78) Smith, L. J.; Davidson, A.; Cheetham, A. K. A Neutron Diffraction and Infrared Spectroscopy Study of the Acid Form of the Aluminosilicate Zeolite, Chabazite (H- SSZ-13). Catal. Lett. 1997, 49 (3), 143–146.

(79) Sierka, M.; Sauer, J. Proton Mobility in Chabazite, Faujasite, and ZSM-5 Zeolite Catalysts. Comparison Based on Ab Initio Calculations. J. Phys. Chem. B 2001, 105 (8), 1603–1613.

(80) Lee, J.; Ryou, Y.; Hwang, S.; Kim, Y.; Cho, S. J.; Lee, H.; Kim, C. H.; Kim, D. H. Comparative Study of the Mobility of Pd Species in SSZ-13 and ZSM-5, and Its Implication for Their Activity as Passive NO x Adsorbers (PNAs) after Hydro-Thermal Aging. Catal. Sci. Technol. 2019, 9 (1), 163–173.

(81) Gu, Y.; Zelinsky, R. P.; Chen, Y.-R.; Epling, W. S. Investigation of an Irreversible NOx Storage Degradation Mode on a Pd/BEA Passive NOx Adsorber. Appl. Catal. B Environ. 2019, 258, 118032.

(82) Aylor, A. W.; Lobree, L. J.; Reimer, J. A.; Bell, A. T. Investigations of the Dispersion of Pd in H-ZSM-5. J. Catal. 1997, 172 (2), 453–462.

(83) Vu, A.; Luo, J.; Li, J.; Epling, W. S. Effects of CO on Pd/BEA Passive NOx Adsorbers. Catal. Lett. 2017, 147 (3), 745–750.

(84) Moliner, M.; Corma, A. From Metal-Supported Oxides to Well-Defined Metal Site Zeolites: The next Generation of Passive NO x Adsorbers for Low-Temperature Control of Emissions from Diesel Engines. React. Chem. Eng. 2019, 4 (2), 223–234.

(85) Ruhela, R.; S. Tomar, B.; K. Singh, A.; C. Hubli, R.; K. Suri, A. Investigation of the Extraction Complexes of Palladium(Ii) with Novel Thiodiglycolamide and Dithiodiglycolamide Ligands by EXAFS and Computational Methods. Dalton Trans. 2013, 42 (19), 7085–7091.

(86) Vanelderen, P.; Vancauwenbergh, J.; Sels, B. F.; Schoonheydt, R. A. Coordination Chemistry and Reactivity of Copper in Zeolites. Coord. Chem. Rev. 2013, 257 (2), 483–494.

(87) Göltl, F.; Hafner, J. Structure and Properties of Metal-Exchanged Zeolites Studied Using Gradient-Corrected and Hybrid Functionals. III. Energetics and Vibrational Spectroscopy of Adsorbates. J. Chem. Phys. 2012, 136 (6), 064503.

(88) Anggara, T.; Paolucci, C.; Schneider, W. F. Periodic DFT Characterization of NO x Adsorption in Cu-Exchanged SSZ-13 Zeolite Catalysts. J. Phys. Chem. C 2016, 120 (49), 27934–27943.

(89) Paolucci, C.; Di Iorio, J. R.; Ribeiro, F. H.; Gounder, R.; Schneider, W. F. Chapter One - Catalysis Science of NOx Selective Catalytic Reduction With Ammonia Over Cu-SSZ-13 and Cu-SAPO-34. In Advances in Catalysis; Song, C., Ed.; Academic Press, 2016; Vol. 59, pp 1–107.

(90) Negri, C.; Borfecchia, E.; Cutini, M.; Lomachenko, K. A.; Janssens, T. V. W.; Berlier, G.; Bordiga, S. Evidence of Mixed-Ligand Complexes in Cu−CHA by Reaction of Cu Nitrates with NO/NH3 at Low Temperature. ChemCatChem 2019, 11 (16), 3828–3838.

(91) Bulánek, R.; Drobná, H.; Nachtigall, P.; Rubeš, M.; Bludský, O. On the Site-Specificity of Polycarbonyl Complexes in Cu/ Zeolites : Combined Experimental and DFT Study. Phys. Chem. Chem. Phys. 2006, 8 (47), 5535–5542.

(92) Tuma, C.; Sauer, J. A Hybrid MP2/Planewave-DFT Scheme for Large Chemical Systems: Proton Jumps in Zeolites. Chem. Phys. Lett. 2004, 387 (4), 388–394.

(93) Tuma, C.; Sauer, J. Treating Dispersion Effects in Extended Systems by Hybrid MP2:DFT Calculations—Protonation of Isobutene in Zeolite Ferrierite. Phys. Chem. Chem. Phys. 2006, 8 (34), 3955–3965.

(94) Hansen, N.; Kerber, T.; Sauer, J.; Bell, A. T.; Keil, F. J. Quantum Chemical Modeling of Benzene Ethylation over H-ZSM-5 Approaching Chemical Accuracy: A Hybrid MP2:DFT Study. J. Am. Chem. Soc. 2010, 132 (33), 11525–11538.

(95) Svelle, S.; Tuma, C.; Rozanska, X.; Kerber, T.; Sauer, J. Quantum Chemical Modeling of Zeolite-Catalyzed Methylation Reactions: Toward Chemical Accuracy for Barriers. J. Am. Chem. Soc. 2009, 131 (2), 816–825.

(96) Bludský, O.; Rubeš, M.; Soldán, P.; Nachtigall, P. Investigation of the Benzene-Dimer Potential Energy Surface: DFT/CCSD(T) Correction Scheme. J. Chem. Phys. 2008, 128 (11), 114102.

(97) Goncalves, T. J.; Plessow, P. N.; Studt, F. On the Accuracy of Density Functional Theory in Zeolite Catalysis. ChemCatChem 2019, 11 (17), 4368–4376.

(98) Chen, J.; Chan, B.; Shao, Y.; Ho, J. How Accurate Are Approximate Quantum Chemical Methods at Modelling Solute–Solvent Interactions in Solvated Clusters? Phys. Chem. Chem. Phys. 2020, 22 (7), 3855–3866.

(99) Grein, F. Ground and Low-Lying Excited C2v States of FeO2—A Challenge to Computational Methods. Int. J. Quantum Chem. 2009, 109 (3), 549–558.

(100) Hait, D.; Tubman, N. M.; Levine, D. S.; Whaley, K. B.; Head-Gordon, M. What Levels of Coupled Cluster Theory Are Appropriate for Transition Metal Systems? A Study Using Near-Exact Quantum Chemical Values for 3d Transition Metal Binary Compounds. J. Chem. Theory Comput. 2019, 15 (10), 5370–5385.

(101) Weaver, M. N.; Merz, K. M. Assessment of the CCSD and CCSD(T) Coupled-Cluster Methods in Calculating Heats of Formation for Cu Complexes. Mol. Phys. 2009, 107 (8–12), 1251–1259.

(102) Nielsen, I. M. B.; Allendorf, M. D. High-Level Ab Initio Thermochemical Data for Halides of Chromium, Manganese, and Iron. J. Phys. Chem. A 2005, 109 (5), 928–933.

(103) Liu, F.; Kulik, H. J. Impact of Approximate DFT Density Delocalization Error on Potential Energy Surfaces in Transition Metal Chemistry. J. Chem. Theory Comput. 2020, 16 (1), 264–277.

(104) Johnson, R. Computational Chemistry Comparison and Benchmark Database, NIST Standard Reference Database 101. National Institute of Standards and Technology 2002.

(105) Irikura, K. K. Experimental Vibrational Zero-Point Energies: Diatomic Molecules. J. Phys. Chem. Ref. Data 2007, 36 (2), 389–397.

(106) Carpenter, J. E.; Weinhold, F. Analysis of the Geometry of the Hydroxymethyl Radical by the "Different Hybrids for Different Spins" Natural Bond Orbital Procedure. J. Mol. Struct. THEOCHEM 1988, 169, 41–62.

(107) Foster, J. P.; Weinhold, F. Natural Hybrid Orbitals. J. Am. Chem. Soc. 1980, 102 (24), 7211–7218.

(108) Reed, A. E.; Weinhold, F. Natural Bond Orbital Analysis of Near-Hartree–Fock Water Dimer. J. Chem. Phys. 1983, 78 (6), 4066–4073.

(109) Reed, A. E.; Weinstock, R. B.; Weinhold, F. Natural Population Analysis. J. Chem. Phys. 1985, 83 (2), 735–746.

(110) Reed, A. E.; Weinhold, F. Natural Localized Molecular Orbitals. J. Chem. Phys. 1985, 83 (4), 1736–1740.

(111) Reed, A. E.; Curtiss, L. A.; Weinhold, F. Intermolecular Interactions from a Natural Bond Orbital, Donor-Acceptor Viewpoint. Chem. Rev. 1988, 88 (6), 899–926.

(112) Weinhold, F.; Carpenter, J. E. The Natural Bond Orbital Lewis Structure Concept for Molecules, Radicals, and Radical Ions. In The Structure of Small Molecules and Ions; Naaman, R., Vager, Z., Eds.; Springer US: Boston, MA, 1988; pp 227–236.

(113) Pommier, B.; Gelin, P. Infrared and Volumetric Study of NO Adsorption on Pd-H-ZSM-5. Phys. Chem. Chem. Phys. 2001, 3 (6), 1138–1143.

(114) Hadjiivanov, K.; Saussey, J.; Freysz, J. L.; Lavalley, J. C. FT-IR Study of NO + O2 Co-Adsorption on H-ZSM-5: Re-Assignment of the 2133 Cm−1 Band to NO+ Species. Catal. Lett 1998, 52, 103–108.

(115) Villamaina, R.; Iacobone, U.; Nova, I.; Ruggeri, M. P.; Collier, J.; Thompsett, D.; Tronconi, E. Low-T CO Oxidation over Cu−CHA Catalysts in Presence of NH3: Probing the

Mobility of CuII Ions and the Role of Multinuclear CuII Species. ChemCatChem 2020, 12 (15), 3795–3795.

(116) Chakarova, K.; Ivanova, E.; Hadjiivanov, K.; Klissurski, D.; Knözinger, H. Co-Ordination Chemistry of Palladium Cations in Pd-H-ZSM-5 as Revealed by FTIR Spectra of Adsorbed and Co-Adsorbed Probe Molecules (CO and NO). Phys Chem Chem Phys 2004, 006 (13), 3702–3709.

(117) Jacobs, P. A.; Von Ballmoos, R. Framework Hydroxyl Groups of H-ZSM-5 Zeolites. J. Phys. Chem. 1982, 86 (15), 3050–3052.

(118) Yokoi, T.; Mochizuki, H.; Biligetu, T.; Wang, Y.; Tatsumi, T. Unique Al Distribution in the MFI Framework and Its Impact on Catalytic Properties. Chem. Lett. 2017, 46 (6), 798–800.

(119) Bortnovsky, O.; Sobal, Z. Exchange of Co(II) Ions in H-BEA Zeolites: Identification of Aluminum Pairs in the Zeolite Framework. Microporous Mesoporous Mater. 2001, 46 (2–3), 265–275.

(120) Dědeček, J.; Kaucký, D.; Wichterlová, B.; Gonsiorová, O. Co2+ Ions as Probes of Al Distribution in the Framework of Zeolites. ZSM-5 Study. Phys Chem Chem Phys 2002, 4 (21), 5406–5413.

(121) Kresse, G.; Furthmüller, J. Efficient Iterative Schemes for Ab Initio Total-Energy Calculations Using a Plane-Wave Basis Set. Phys. Rev. B 1996, 54 (16), 11169–11186.

(122) Perdew, J. P.; Wang, Y. Accurate and Simple Analytic Representation of the Electron-Gas Correlation Energy. Phys. Rev. B 1992, 45 (23), 13244–13249.

(123) Grimme, S.; Antony, J.; Ehrlich, S.; Krieg, H. A Consistent and Accurate Ab Initio Parametrization of Density Functional Dispersion Correction (DFT-D) for the 94 Elements H-Pu. J. Chem. Phys. 2010, 132 (15), 154104.

(124) Grimme, S.; Ehrlich, S.; Goerigk, L. Effect of the Damping Function in Dispersion Corrected Density Functional Theory. J. Comput. Chem. 2011, 32 (7), 1456–1465.

(125) Heyd, J.; Scuseria, G. E.; Ernzerhof, M. Hybrid Functionals Based on a Screened Coulomb Potential. J. Chem. Phys. 2003, 118 (18), 8207–8215.

(126) Heyd, J.; Scuseria, G. E. Efficient Hybrid Density Functional Calculations in Solids: Assessment of the Heyd-Scuseria-Ernzerhof Screened Coulomb Hybrid Functional. J. Chem. Phys. 2004, 121 (3), 1187–1192.

(127) Heyd, J.; Scuseria, G. E.; Ernzerhof, M. Erratum: "Hybrid Functionals Based on a Screened Coulomb Potential" [J. Chem. Phys. 118, 8207 (2003)]. J. Chem. Phys. 2006, 124 (21), 219906.

(128) Krukau, A. V.; Vydrov, O. A.; Izmaylov, A. F.; Scuseria, G. E. Influence of the Exchange Screening Parameter on the Performance of Screened Hybrid Functionals. J. Chem. Phys. 2006, 125 (22), 224106.

(129) Blöchl, P. E. Projector Augmented-Wave Method. Phys. Rev. B 1994, 50 (24), 17953–17979.

(130) Kresse, G.; Joubert, D. From Ultrasoft Pseudopotentials to the Projector Augmented-Wave Method. Phys. Rev. B 1999, 59 (3), 1758–1775.

(131) Bader, R. F. W. Atoms in Molecules : A Quantum Theory; Oxford : Clarendon press, 1990.

(132) Tang, W.; Sanville, E.; Henkelman, G. A Grid-Based Bader Analysis Algorithm without Lattice Bias. J. Phys. Condens. Matter Inst. Phys. J. 2009, 21 (8), 084204.

(133) Sanville, E.; Kenny, S. D.; Smith, R.; Henkelman, G. Improved Grid-Based Algorithm for Bader Charge Allocation. J. Comput. Chem. 2007, 28 (5), 899–908.

(134) Henkelman, G.; Arnaldsson, A.; Jónsson, H. A Fast and Robust Algorithm for Bader Decomposition of Charge Density. Comput. Mater. Sci. 2006, 36 (3), 354–360.

(135) Yu, M.; Trinkle, D. R. Accurate and Efficient Algorithm for Bader Charge Integration. J. Chem. Phys. 2011, 134 (6), 064111.

(136) Bray, J. M.; Schneider, W. F. CHAPTER 2:First-Principles Thermodynamic Models in Heterogeneous Catalysis. In Computational Catalysis; 2013; pp 59–115.

(137) Penninger, M. W.; Kim, C. H.; Thompson, L. T.; Schneider, W. F. DFT Analysis of NO Oxidation Intermediates on Undoped and Doped LaCoO3 Perovskite. J. Phys. Chem. C 2015, 119 (35), 20488–20494.

(138) McQuarrie, D. A.; Simon, J. D. Molecular Thermodynamics; University Science Books: Sausalito, California, 1999.

(139) Göltl, F.; Sautet, P.; Hermans, I. Can Dynamics Be Responsible for the Complex Multipeak Infrared Spectra of NO Adsorbed to Copper(II) Sites in Zeolites? Angew. Chem. Int. Ed. 2015, 54 (27), 7799–7804.

(140) Göltl, F.; Sautet, P.; Hermans, I. The Impact of Finite Temperature on the Coordination of Cu Cations in the Zeolite SSZ-13. Catal. Today 2016, 267, 41–46.

(141) Paolucci, C.; Verma, A. A.; Bates, S. A.; Kispersky, V. F.; Miller, J. T.; Gounder, R.; Delgass, W. N.; Ribeiro, F. H.; Schneider, W. F. Isolation of the Copper Redox Steps in the Standard Selective Catalytic Reduction on Cu-SSZ-13. Angew. Chem. Int. Ed Engl. 2014, 53 (44), 11828–11833.

(142) Piccini, G.; Sauer, J. Quantum Chemical Free Energies: Structure Optimization and Vibrational Frequencies in Normal Modes. J. Chem. Theory Comput. 2013, 9 (11), 5038–5045.

(143) Dauenhauer, P. J.; Abdelrahman, O. A. A Universal Descriptor for the Entropy of Adsorbed Molecules in Confined Spaces. ACS Cent. Sci. 2018, 4 (9), 1235–1243.

(144) Jørgensen, M.; Chen, L.; Grönbeck, H. Monte Carlo Potential Energy Sampling for Molecular Entropy in Zeolites. J. Phys. Chem. C 2018, 122 (35), 20351–20357.

(145) Campbell, C. T.; Sellers, J. R. V. The Entropies of Adsorbed Molecules. J. Am. Chem. Soc. 2012, 134 (43), 18109–18115.

(146) Li, H.; Paolucci, C.; Schneider, W. F. Zeolite Adsorption Free Energies from Ab Initio Potentials of Mean Force. J. Chem. Theory Comput. 2018, 14 (2), 929–938.

(147) Frisch, M. J.; Trucks, G. W.; Schlegel, H. B.; Scuseria, G. E.; Robb, M. A.; Cheeseman, J. R.; Scalmani, G.; Barone, V.; Petersson, G. A.; Nakatsuji, H.; Li, X.; Caricato, M.; Marenich, A. V.; Bloino, J.; Janesko, B. G.; Gomperts, R.; Mennucci, B.; Hratchian, H. P.; Ortiz, J. V.; Izmaylov, A. F.; Sonnenberg, J. L.; Williams; Ding, F.; Lipparini, F.; Egidi, F.; Goings, J.; Peng, B.; Petrone, A.; Henderson, T.; Ranasinghe, D.; Zakrzewski, V. G.; Gao, J.; Rega, N.; Zheng, G.; Liang, W.; Hada, M.; Ehara, M.; Toyota, K.; Fukuda, R.; Hasegawa, J.; Ishida, M.; Nakajima, T.; Honda, Y.; Kitao, O.; Nakai, H.; Vreven, T.; Throssell, K.; Montgomery Jr., J. A.; Peralta, J. E.; Ogliaro, F.; Bearpark, M. J.; Heyd, J. J.; Brothers, E. N.; Kudin, K. N.; Staroverov, V. N.; Keith, T. A.; Kobayashi, R.; Normand, J.; Raghavachari, K.; Rendell, A. P.; Burant, J. C.; Iyengar, S. S.; Tomasi, J.; Cossi, M.; Millam, J. M.; Klene, M.; Adamo, C.; Cammi, R.; Ochterski, J. W.; Martin, R. L.; Morokuma, K.; Farkas, O.; Foresman, J. B.; Fox, D. J. Gaussian 16 Rev. C.01; Wallingford, CT, 2016.

(148) Lee, C.; Yang, W.; Parr, R. G. Development of the Colle-Salvetti Correlation-Energy Formula into a Functional of the Electron Density. Phys. Rev. B 1988, 37 (2), 785–789.

(149) Becke, A. D. Density-functional Thermochemistry. III. The Role of Exact Exchange. J. Chem. Phys. 1993, 98 (7), 5648–5652.

(150) Kendall, R. A.; Dunning, T. H.; Harrison, R. J. Electron Affinities of the First-row Atoms Revisited. Systematic Basis Sets and Wave Functions. J. Chem. Phys. 1992, 96 (9), 6796–6806.

(151) Woon, D. E.; Dunning, T. H. Gaussian Basis Sets for Use in Correlated Molecular Calculations. III. The Atoms Aluminum through Argon. J. Chem. Phys. 1993, 98 (2), 1358–1371.

(152) Glendenning, E.; Reed, A.; Carpenter, J.; Weinhold, F. NBO Version 3.1. 2001.

(153) Dennington, R.; Keith, T. A.; Millam, J. M. GaussView Version 6; 2019.

(154) Kammert, J. D.; Brezicki, G.; Acevedo-Esteves, R.; Stavitski, E.; Davis, R. J. High-Throughput Operando-Ready X-Ray Absorption Spectroscopy Flow Reactor Cell for Powder Samples. Rev. Sci. Instrum. 2020, 91 (1), 013107.

Chapter 4. Investigation of NO Adsorption and Desorption on a Pd/ZSM-5 Passive NOx Adsorber

This chapter consists of a manuscript that is currently under review at Oak Ridge National Lab for publication.

4.1 Introduction

NOx abatement technologies for diesel-engine exhaust aftertreatment include state-of-the-art ammonia/urea selective catalytic reduction (SCR) systems which are effective above 200 °C.[155–157] Control of cold-start NOx emissions, those below 200 °C, is critical for meeting the increasingly stringent emissions regulations on oxides of nitrogen (NOx) for lean-burn diesel-fueled vehicles,[158–161] making the need for efficient low temperature catalysis and trap materials even more urgent.[159,162]

Multiple authors have reported passive NOx adsorbers (PNA) being able to trap NOx at low temperatures and release NOx at temperatures above which the urea SCR system can efficiently eliminate NOx emissions. [159,160,162-169] Chen and coworkers were the first to report that Pd ion-exchanged zeolites show superior NOx storage capacity and sulfur tolerance when compared to metal-oxide supported NOx adsorbers under complex exhaust compositions.[170] Pd ion-exchanged zeolites have garnered significant attention and studies are converging on Pd^{2+} cations within the zeolite framework being able to trap NOx at low temperatures in the presence of excess oxygen typical of diesel-engine exhausts, thus providing a possible pathway to mitigating cold-start NOx emissions.[171–173] The NOx storage capacity, temperature of NOx release from the PNA, rate of NOx adsorption and durability of the PNA have been found to be influenced by several parameters such as the type of zeolite, synthesis method, activation strategy, and exhaust composition.[170,163,168,174–176]

As synthesized Pd/BEA, Pd/SSZ-13 and Pd/ZSM-5 have reasonable NOx trapping capacities, but their desorption profiles, specifically the temperature window of NOx release, vary.[166,170] For example, the NOx desorption temperature window of Pd/BEA is relatively low (180-250 °C), meaning some portion of the trapped NOx will desorb before the SCR catalysts can achieve high NOx conversion.[170,177] The NOx desorption temperature window for Pd/SSZ-13 is higher (280-450 °C), but too high to fully regenerate under realistic exhaust conditions.[166,168] The NOx desorption temperature window for Pd/ZSM-5 seems to be more ideal (200-400 °C) for diesel engine after-treatment systems.[170] Furthermore, Pd/ZSM-5 has also been reported to simultaneously trap hydrocarbons and NO at low temperatures and act as a bifunctional trapping material making it an attractive PNA candidate for cold start applications.[178]

Although Pd ion-exchanged into ZSM-5 zeolites are interesting PNA candidates as they exhibit significant NOx storage capacity and reasonable NOx desorption temperatures,[165,166,170] the nature of Pd within a ZSM-5 zeolite and its speciation under realistic exhaust conditions, are not well understood. The Pd speciation and NO adsorption mechanism on Pd/zeolites has been extensively investigated under more ideal conditions.[179–182] While experimental studies on PNAs have proposed several possible NOx storage sites in a zeolite and NOx adsorption mechanisms,[166,176,183,184] the literature has not converged on the mechanism of a system that involves H_2O, NO and CO. Hence, investigating Pd speciation and NO adsorption sites under realistic conditions is critical to fully understanding the NO adsorption mechanism within Pd/ZSM-5.

The current contribution focuses on gaining a better understanding of the underlying chemistry involved in the NO adsorption and desorption phenomena on Pd/ZSM-5 PNAs through flow reactor experiments combined with in-situ DRIFTS investigations. The flow reactor experiments include a systematic study on the effects of gas composition (including changes in NO, CO, O_2, H_2O and CO_2 concentration) and temperature on PNA NO uptake and release. DRIFTS studies identified the effect of hydration on Pd speciation and the key surface intermediates during NO adsorption. Based on key observations from the flow reactor and DRIFTS experiments a simplified mechanism that captures the key observations is proposed which provides the foundation for future modelling efforts.

4.2 Experimental methods

4.2.1 Passive NOx adsorber (PNA)

The PNA core sample (2.0 cm by 5.0 cm) used in this study is a model Diesel Cold Start Concept (dCSC) Catalyst component obtained from Johnson Matthey. The PNA was a Pd-exchanged ZSM-5 with a Pd loading of 1.8g/L. The PNA was washcoated onto 400 counts per square inch (cpsi) cordierite monolith core. The PNA was degreened at 600 °C for 4 h under 10% O_2 and 7% H_2O prior to running any experiments.

4.2.2 Flow reactor

A LabVIEW (National Instruments)-controlled synthetic exhaust flow reactor system was used to conduct NO uptake/release experiments on the PNA. The reactor schematic is shown elsewhere.[31] A bank of mass-flow controllers (MKS Instruments) was used to vary the composition of the feed to understand the impact of the various constituents on NO adsorption on the PNA. Water vapor was added into the reaction mixture using an HPLC pump (Eldex Optos 1LMP) and a custom-built water-preheater assembly.[175] Pneumatically controlled 4-way valves (Valco A24UWE) were used to introduce CO and NO to achieve step changes in composition during the bypass and adsorption steps.

The Pd/ ZSM-5 core sample was wrapped in non-woven alumina (Cotronics) tape and loaded in a 25 mm OD quartz tube. The quartz reactor tube was packed with quartz tubes (3 mm OD, 1mm ID) upstream of the PNA core sample to increase heat transfer to the feed gas. To ensure isothermal conditions across the PNA, five K-type thermocouples were placed into the reactor at the following points: (i) 5mm upstream of the catalyst inlet, (ii) in a central catalyst channel at the axial mid-point, (iii) in a radial catalyst channel at the axial mid-point, (iv) in a central catalyst channel at the catalyst outlet, and (v) in a radial catalyst channel at the catalyst outlet. The quartz tube reactor assembly was then placed into two furnaces (Lindberg Blue/M) placed side-by-side, one to facilitate isothermal conditions and one to preheat the gases. The exit steam composition from the reactor was analyzed using a Multigas 2030HS FTIR spectrometer (MKS Instruments).

4.2.3 Experiment Protocol: NO adsorption and Temperature Programmed Desorption (TPD)

A systematic study was conducted by varying the NO exposure conditions (as summarized in Table 4.1) to understand the impact of each of the parameters on NO uptake and release. The experimental protocol used to measure NO uptake and release is shown in Table 4.2; the temperatures and concentrations listed are for the “baseline” conditions, but they varied in other experiments. Each experiment began with a pretreatment at 600 °C to ensure that all the NO stored in the prior experiment had been released and the Pd was in a fully oxidized state. After the pretreatment, the PNA sample was cooled to the desired operating temperature under the O_2, H_2O, and CO_2 concentrations used in the exposure step. After the PNA temperature was stable, CO was introduced. Five minutes later, NO was introduced. The NO exposure step continued until the measured NO outlet concentration achieved a steady state. The time to reach steady state varied with the NO concentration and temperature, but generally was 10-20 min. After the NO concentration achieved a steady state, the NO was switched off and the catalyst temperature was ramped to 600 °C at 20 °C/min after the NO concentration decreased below 1 ppm. The catalyst was held at 600 °C for 10 min before proceeding to the next experiment.

Table 4.1: NO exposure conditions

Parameter	**Range**	**Baseline Conditions**
NO	25 ppm -1600 ppm	200 ppm
CO	50 ppm - 800 ppm	200 ppm
O_2	1 % - 13 %	10 %
H_2O	5 % - 13 %	7 %
CO_2	0 % - 13 %	0 %
N_2	--	Balance
Adsorption Temperature	75 °C - 225 °C	100 °C
Gas Hourly Space Velocity (GHSV)	--	30000 hr^{-1}

Table 4.2. Experiment protocol with sample conditions

Step	**Description**	**Time (min)**	**T (°C)**	**NO (ppm)**	**CO (ppm)**	**O_2 (%)**	**H_2O (%)**
1	Pretreat	30	600	0	0	10	7
2	Cool	varies	600-100	0	0	10	7
3	CO exposure	5	100	0	200	10	7
4	NO exposure	varies	100	200	200	10	7
5	Stop NO exposure	varies	100	0	200	10	7
6	TPD	25	100-600	0	200	10	7
7	Hold	10	600	0	200	10	7

4.2.4 In-situ Diffuse Reflectance Infrared Fourier Transform Spectroscopy (DRIFTS)

In order to gain insights into the surface intermediates and reactions on the PNA during NO adsorption, controlled experiments were conducted using DRIFTS on an Agilent Cary 670 FTIR spectrometer. A Harrick Praying Mantis DRIFTS accessory coupled with a liquid nitrogen-cooled mercury-cadmium-telluride (MCT) detector was used to collect the FTIR adsorption spectra. The DRIFTS accessory consisted of a Harrick high temperature reaction chamber with ZnSe windows for precise control of the catalyst temperature along with gas flow capabilities specially designed for in-situ analysis of the surface of the sample. A thin layer of the washcoated sample (~0.3 cm^2) from the Pd/ZSM-5 core was placed on a bed of stainless-steel beads in the sample holder and degreened at 600 °C prior to the experiments. A bank of mass flow controllers (MKS Instruments) was used to control the composition of the gas flowing over the sample, the NO, CO and O_2 concentrations are the same as listed in Table 4.2. Water, at 1.0 and 4.5 % levels, was introduced to the feed using a saturator immersed in a recirculating constant temperature bath. Prior to NO adsorption, the sample was pretreated at 550 °C in the presence of 10% O_2 for 30 min. The sample was cooled to the NO adsorption temperature in 10% O_2 and depending on the NO adsorption experiment condition, background spectra were collected in the presence or absence of H_2O. 64 spectra were averaged for background collection and 32 spectra were averaged for sample spectra. Spectra were collected during NO adsorption under various feed conditions until saturation, and during a temperature programmed desorption from the adsorption temperature to 500 °C. Additionally, to investigate the interaction between NO and CO, spectra were collected during CO adsorption and with NO addition after the saturation of CO adsorption.

4.3 Results

Preliminary experiments revealed that the NO storage capacity of the Pd/ZSM-5 material decreased with each experiment.[177,186] Since this degradation confounded attempts to investigate the impacts of operating conditions on NO storage and release, dozens of NO storage-release cycles were conducted under the baseline conditions until consecutive NO storage capacities were stable. The initial NO storage capacity corresponded to a NO:Pd ratio of 0.4 based on total Pd loading. After dozens of cycles, the stabilized NO:Pd ratio dropped to 0.2. While this Pd utilization is lower than what has been reported in the literature for other Pd-zeolite PNAs prior to any degradation, and is non-optimal from a device size and cost standpoint, experiments conducted on this material can still provide useful insights into the mechanisms for NO storage and release.

4.3.1 Impact of synthetic exhaust parameters on NO storage and release

Once the stability of the PNA was established, a systematic investigation was carried out by independently varying the NO exposure conditions to gain an understanding of the impact of key parameters, with their ranges listed in Table 4.1, on the NO storage and release. Every set of experiments included the baseline conditions to ensure consistency in the behavior of the PNA over time.

Figure 4.1 shows the measured catalyst temperatures and outlet concentrations of CO, NO, and CO_2 during an experiment conducted under the baseline NO exposure conditions detailed in Table 4.1. Aside from providing a visual summary of the protocol that was used for most of the experiments, this data set illustrates a few other key points about the behavior of the Pd/ZSM-5 PNA under the protocol used. Figure 4.1(a) shows all five thermocouple temperatures and demonstrates that the PNA was under isothermal conditions (±2 °C) during the adsorption step.

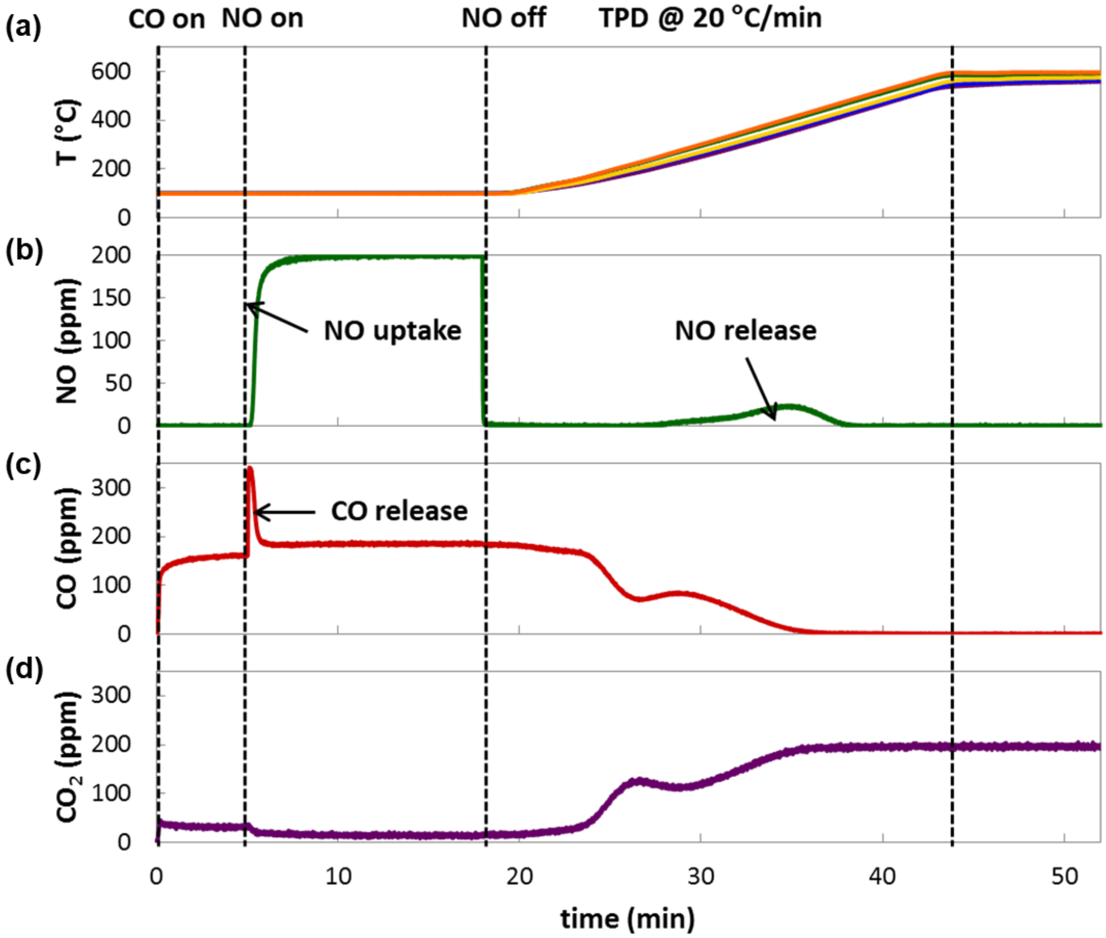

Figure 4.1 Baseline experimental dataset showing (a) temperatures measured by the 5 thermocouples in the reactor, (b) NO concentration profiles, (c) CO concentration profiles, and (d) CO_2 concentration profiles at 100 °C before NO introduction, during isothermal NO adsorption, and during TPD from 100-500 °C. Feed conditions: 200 ppm NO, 200 ppm CO, 10% O_2, 7% H_2O, 0% CO_2, GHSV 30,000 hr^{-1}

The NO concentration profile in Figure 4.1(b) shows a delay between when the NO is first turned on and when NO starts to break through. This time period of complete uptake demonstrates that the Pd/ZSM-5 material is effective as a passive NOx adsorber.

The TPD portion of the experiment protocol also allows measurement of the temperatures at which NO is released from the Pd/ZSM-5 PNA. For the baseline experiment shown in Figure 4.1 and all subsequent experiments below, the NO adsorbed on the PNA was released between 200 °C to 400 °C. Also, the TPD profiles show multiple NOx desorption peaks indicating multiple types of storage sites. Note, formation of other oxides of nitrogen such as NO_2 or N_2O was not observed.

The CO concentration profile in Figure 4.1(c) shows two interesting features. At the very beginning of the experiment, when CO is first turned on, there is a period of time before the CO concentration reaches a steady state. Since the CO_2 concentration in Figure 4.1(d) is fairly steady during the same time period, CO is being stored on the PNA indicated by the slow approach to steady state. This explanation is further supported by the release of CO when NO is introduced – the NO appears to displace the CO from the storage sites. Integrating the transient CO profiles reveals that all the CO stored at the beginning of the experiment is released upon introduction of NO. This implies that there is no evidence for co-adsorption of NO and CO and NO binds stronger to the storage sites than CO on this Pd/ZSM-5 under these operating conditions.

The CO_2 concentration profile in Figure 4.1(d) also yields some insights into the PNA behavior. CO_2 formation upon introduction of CO indicates activity for CO oxidation even at 100 °C. This CO_2 formation almost completely disappears upon introduction of NO, indicating the inhibition effect of NO on CO oxidation. Additionally, a non-typical CO oxidation light-off behavior was observed during the temperature ramp at around 150 °C. As we will discuss later, this non-typical change in CO oxidation activity is due to the dehydration of Pd cations.

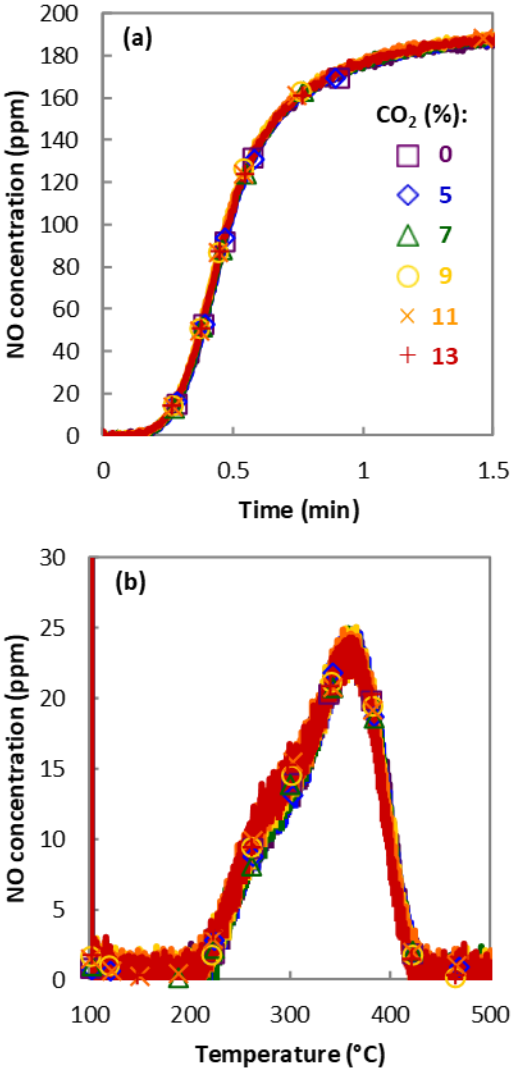

Figure 4.2 NO concentration profiles during (a) NO adsorption at 100 °C and (b) TPD from 100-500 °C as the CO_2 concentration is varied. Feed conditions: 200 ppm NO, 200 ppm CO, 10% O_2, 7% H_2O, 0-13% CO_2, GHSV 30,000 hr^{-1}

4.3.1.1 Effect of CO_2

In order to understand the effect of CO_2 concentration on the NO storage and release, the concentration of CO_2 was varied from 0% to 13% while keeping the concentrations of the other constituents in the feed constant. In Figure 4.2 (a), the NO concentration profiles during NO adsorption on the PNA at 100 °C show that the NO uptake rate on the PNA does not change as the CO_2 concentration is varied in the feed. Total NO uptake for each experiment is calculated by integrating the difference between the NO inlet concentration and the NO breakthrough profile and these data are shown in Figure 4.3. Furthermore, as shown in Figure 4.2 (b), the NO concentration profiles observed during the temperature programmed desorption (TPD) from 100 °C to 500 °C, which are indicative of both the NO storage capacity and the binding energy of the stored NO, also remain unchanged as the CO_2 concentration is increased from 0% to 13%. Total NO release is calculated by integrating the area under the NO concentration profile during the TPD, and these data are also shown in Figure 4.3. The calculated uptake and release were within experimental error for all the experiments conducted, indicating that all the NO stored during the adsorption step is released during the TPD as NO. As CO_2 did not have a significant impact on either the NO uptake rate, the NO storage capacity of the PNA or the NO desorption profile, it plays no role in the mechanisms for NO storage and release. For the sake of simplicity, CO_2 has been excluded from the feed in the experiments discussed in the following sections.

The agreement between the NO adsorbed and desorbed is consistent for all the experiments presented in this paper. The desorbed quantity being slightly higher than the adsorbed quantity may be due to nonlinearities in the FTIR calibration – the measured NO concentrations during the TPD are quite low (< 25 ppm), and small offsets in the measured concentration integrated over long time periods could add up to more significant errors.

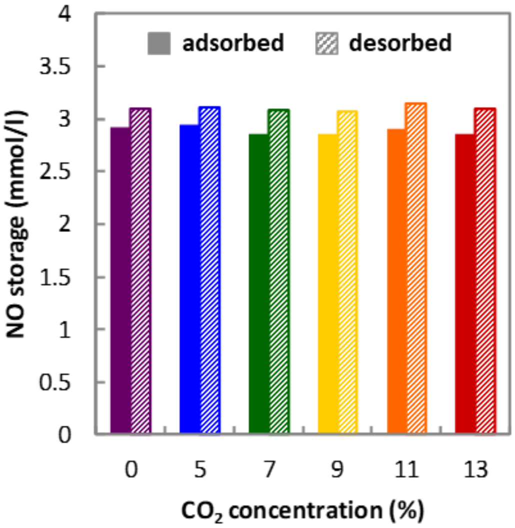

Figure 4.3 Total NO storage as measured from NO adsorbed at 100 °C (solid fill) and NO desorbed during TPD from 100-500 °C (diagonal line fill) as the CO_2 concentration is varied in experiments conducted with Pd/ZSM-5. Feed conditions: 200 ppm NO, 200 ppm CO, 10% O_2, 7% H_2O, 0-13% CO_2, GHSV 30000 hr^{-1}

4.3.1.2 Effect of O_2

The O_2 concentration was varied from 1% to 13% in the feed to understand the impact of O_2 on the NO storage and release. Since the Pd/ZSM-5 was provided as a model component of a low temperature trap for diesel applications,[163] the exhaust composition contained sufficient O_2 for all experiments to maintain net lean operating conditions. The NO concentration profiles during NO exposure to the PNA at 100 °C in Figure 4.4 (a) show that increasing the O_2 concentration from 1% to 13% did not have a significant effect on the NO uptake rate of the PNA. Additionally, NO storage capacity was essentially unchanged as is shown in Figure 4.4 (b). the NO concentration profiles during the TPD from 100 °C to 500 °C (data not shown for brevity) showed minimal variation with the O_2 concentration in the feed, so variations with O_2 concentration were not considered in the development of an NO storage and release mechanism.

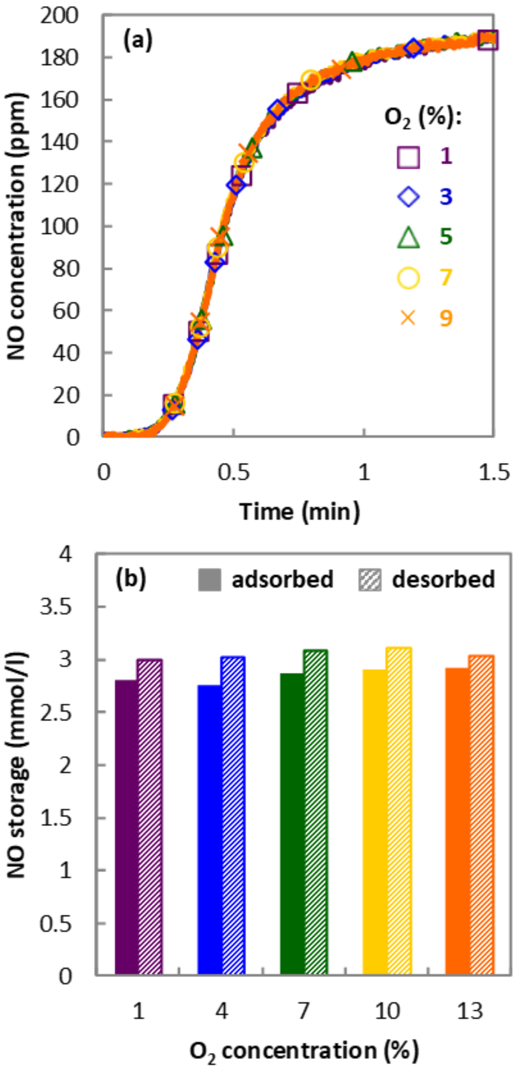

Figure 4.4 (a) NO concentration profiles during NO adsorption at 100 °C and (b) total NO storage as measured from NO adsorbed at 100 °C (solid fill) and NO desorbed during TPD from 100-500 °C (diagonal line fill) as the O_2 concentration is varied in experiments conducted with Pd/ZSM-5. Feed conditions: 200 ppm NO, 200 ppm CO, **1-13% O_2**, 7% H_2O, 0% CO_2, GHSV 30000 hr^{-1}

4.3.1.3 Effect of NO concentration

In order to understand the impact of NO concentration on the NO storage and release, the NO concentration was varied from 25 ppm to 1600 ppm during NO exposure under isothermal conditions at 100 °C. Figure 4.5 shows that increasing the NO concentration during NO adsorption reduces the time to NO breakthrough. The available NO storage sites fill faster with higher NO flux. Interestingly, even at the highest NO concentration, there is still a time period at the beginning of NO exposure during which all the NO is being stored – the rate of NO adsorption is still sufficient to overcome mass transfer limitations and the increase in NO flux.

Figure 4.5 shows the integrated NO storage during isothermal adsorption and release during the TPD as the inlet NO concentration was varied. The NO storage capacity of the Pd/ZSM-5 is essentially unchanged even as the NO concentration is varied over two orders of magnitude. Thus, for the adsorption conditions investigated here, the thermodynamic equilibrium between NO adsorption and NO desorption strongly favors the former.

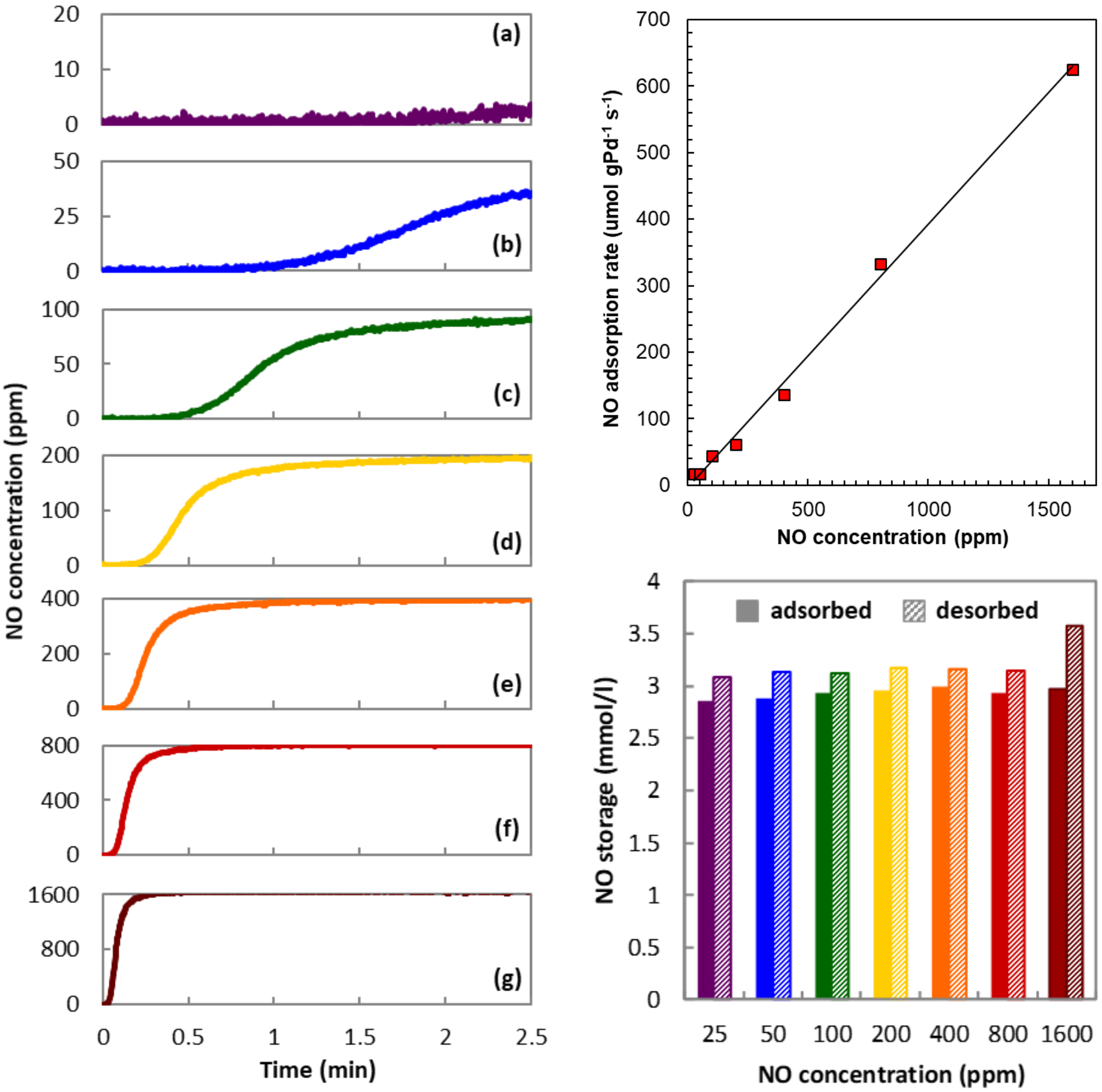

Figure 4.5 NO concentration profiles during NO adsorption on Pd/ZSM-5 at 100 °C at different NO concentrations (in ppm): (a) 25, (b) 50, (c) 100, (d) 200, (e) 400, (f) 800, (g) 1600. Feed conditions: **25-1600 ppm NO**, 200 ppm CO, 10% O_2, 7% H_2O, 0% CO_2, GHSV 30000 hr^{-1}

4.3.1.4 Effect of H_2O concentration

The impact of the H_2O on the NO storage and release was investigated by varying the H_2O concentration in the feed from 5% to 13% during isothermal NO adsorption on the PNA at 100 °C as well as at 150 °C. From the NO concentration profiles during NO exposure at 100 °C displayed in Figure 4.6 (a), it is observed that, as the concentration of H_2O in the reaction feed is increased from 5% to 9%, the time needed for saturation increases indicating an overall slower rate of NO adsorption. Upon increasing the H_2O concentration in the feed beyond 9%, no changes were observed. Interestingly, the total NO storage (Figure 4.6 (b)) is essentially unchanged by the H_2O concentration. H_2O appears to slow the kinetics of NO uptake but does not prevent NO from storing at the Pd sites.

On the other hand, as observed in Figure 4.6 (c), when NO is adsorbed on the PNA at 150 °C, varying the H_2O concentration in the feed has minimal impact on the NO adsorption. Furthermore, consistent with findings reported in the earlier section 4.3.1.4, the NO uptake rate during isothermal NO exposure is higher at 150 °C for all the H_2O concentrations considered in this study.

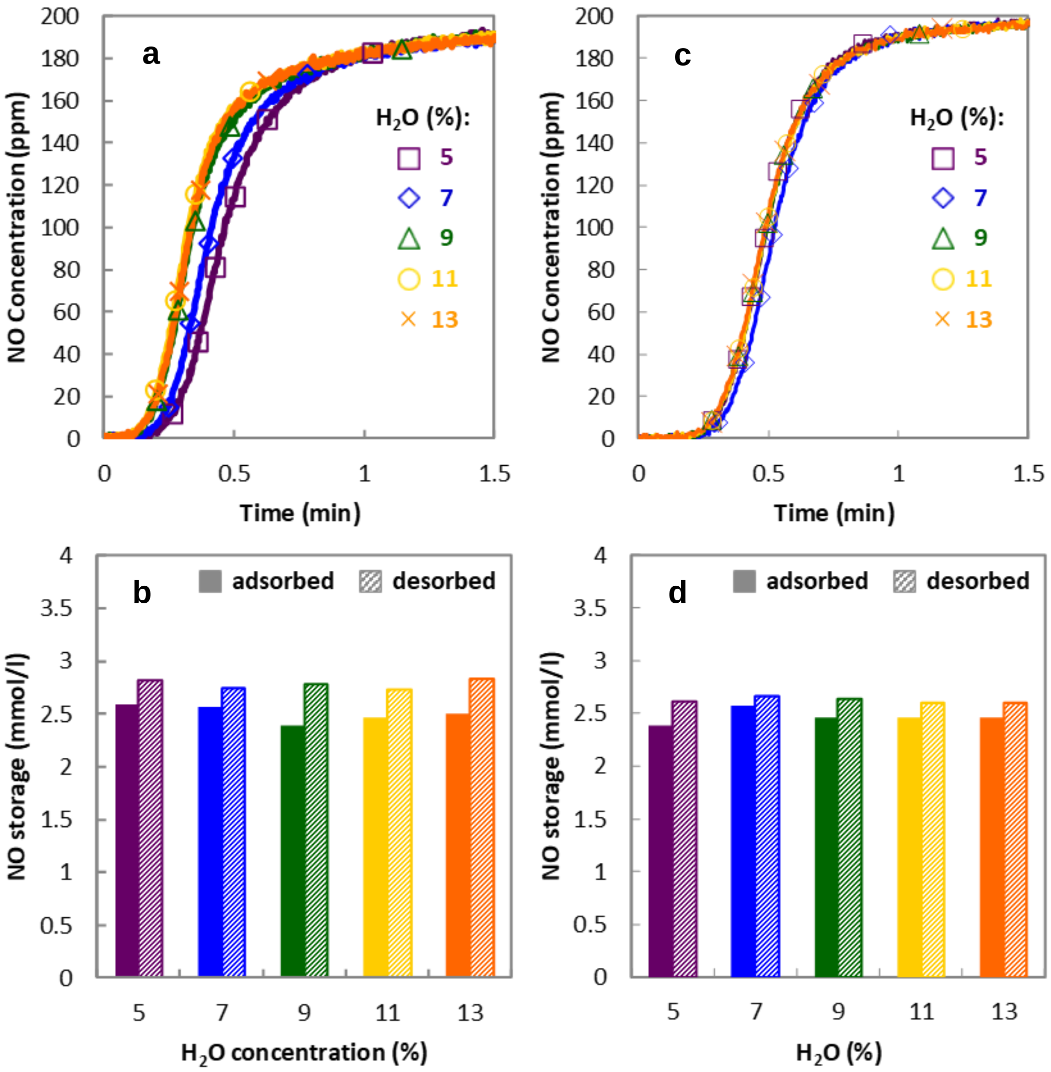

Figure 4.6 (a) NO concentration profiles during NO adsorption at 100 °C and (b) total NO storage as measured from NO adsorbed at 100 °C (solid fill) and NO desorbed during TPD from 100-500 °C (diagonal line fill) as the H_2O concentration is varied in experiments conducted with Pd/ZSM-5. (c) NO concentration profiles during NO adsorption at 150 °C and (d) total NO storage as measured from NO adsorbed at 150 °C (solid fill) and NO desorbed during TPD from 100-500 °C (diagonal line fill) as the H_2O concentration is varied in experiments conducted with Pd/ZSM-5. Feed conditions: 200 ppm NO, 200 ppm CO, 10% O_2, **5-13% H_2O**, 0% CO_2, GHSV 30000 hr^{-1}

4.3.1.5 Effect of CO

The effect of CO concentration on NO storage and release is of significant interest as CO is an integral component of diesel exhaust and has been found to impact the oxidation state of the ion-exchanged Pd within the zeolite.[169,177] Furthermore, other researchers have found that CO promotes NO adsorption on Pd-exchanged zeolites.[187] As noted above in Figure 4.1, all the CO that adsorbs on the Pd/ZSM-5 PNA sample is subsequently released upon introduction of NO, indicating that NO and CO are not co-adsorbed under these operating conditions.

The NO concentration profiles in Figure 4.7 show that CO has a significant impact on the rate of NO adsorption. In the absence of CO, the initial rate of NO adsorption is slow, and NO breaks through almost immediately after its introduction. After this rapid breakthrough, the NO concentration slowly increases until it finally reaches the inlet value. In the presence of CO, the initial rate of NO adsorption is much faster, and NO breakthrough is delayed. After breakthrough, the NO concentration increases to the inlet level faster than in the absence of CO. The total NO storage is very similar with and without CO , but the rate of NO adsorption is quite different.

The effect of CO on NO storage and release was further investigated by varying the CO concentration in the feed from 50 ppm CO to 800 ppm CO during isothermal NO adsorption at 100 °C. The NO concentration profiles during NO adsorption in Figure 4.9 (a) show that as the CO concentration is increased from 50 ppm to 800 ppm in the feed, the initial NO uptake rate increases up to ~ 400 ppm CO. Further increasing the CO concentration to 800 ppm has minimal impact on the initial NO uptake rate. The rate differences can be seen in the crossover of the NO concentration profiles in Figure 4.9 (a): at 800 ppm CO, the NO breakthrough occurs much later than at the lower CO concentrations, but the NO concentration more rapidly approaches the inlet value; at 50 ppm CO, the NO breakthrough occurs earlier, but the approach to the inlet NO concentration occurs more slowly, indicating that the Pd/ZSM-5 is storing more NO at later adsorption times. The total NO stored during both adsorption and release in Figure 4.9 (b) shows only a small effect of changing CO concentration. Thus, as with H_2O at 100 °C, the primary impact of changing CO concentration appears to be on the rate of NO adsorption on the Pd sites rather than the total amount of NO that can be stored at those sites.

The next logical step was to evaluate the effects of CO concentration on NO adsorption at 150 °C, which is shown in Figure 4.9. Interestingly, varying CO concentration from 50-400 ppm had minimal effect on either the rate of NO adsorption in Figure 4.9 (c) or the total NO stored in Figure 4.9 (d). Further increasing CO concentration to 800 ppm caused a small decrease in total NO stored, which is also apparent in earlier NO breakthrough.

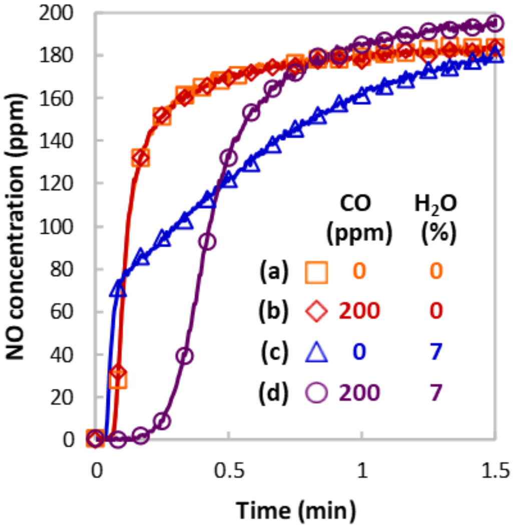

Figure 4.7 NO concentration profiles during NO adsorption at 100 °C under (a) 0ppm CO, 0% H_2O, (b) 200ppm CO, 0% H_2O, (c) 0 ppm CO, 7% H_2O, and (d) 200 ppm CO, 7% H_2O. Feed conditions: 200 ppm NO, 0 or 200 ppm CO, 10% O_2, 0 or 7% H_2O, 0% CO_2, GHSV 30000 hr^{-1}

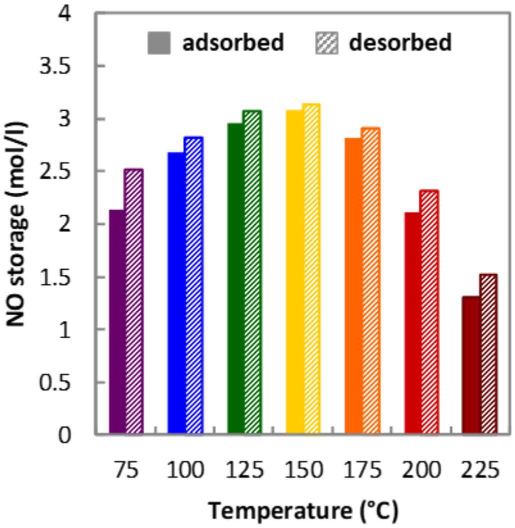

Figure 4.8 (a) Total NO storage on the PNA as measured form NO adsorbed and (b) NO desorbed during TPD as the NO adsorption temperature is varied from **75 °C to 225 °C** in experiments conducted with Pd/ZSM-5. Feed conditions: 200 ppm NO, 200 ppm CO, 10% O_2, 7% H_2O, 0 % CO_2, GHSV 30000 hr^{-1}

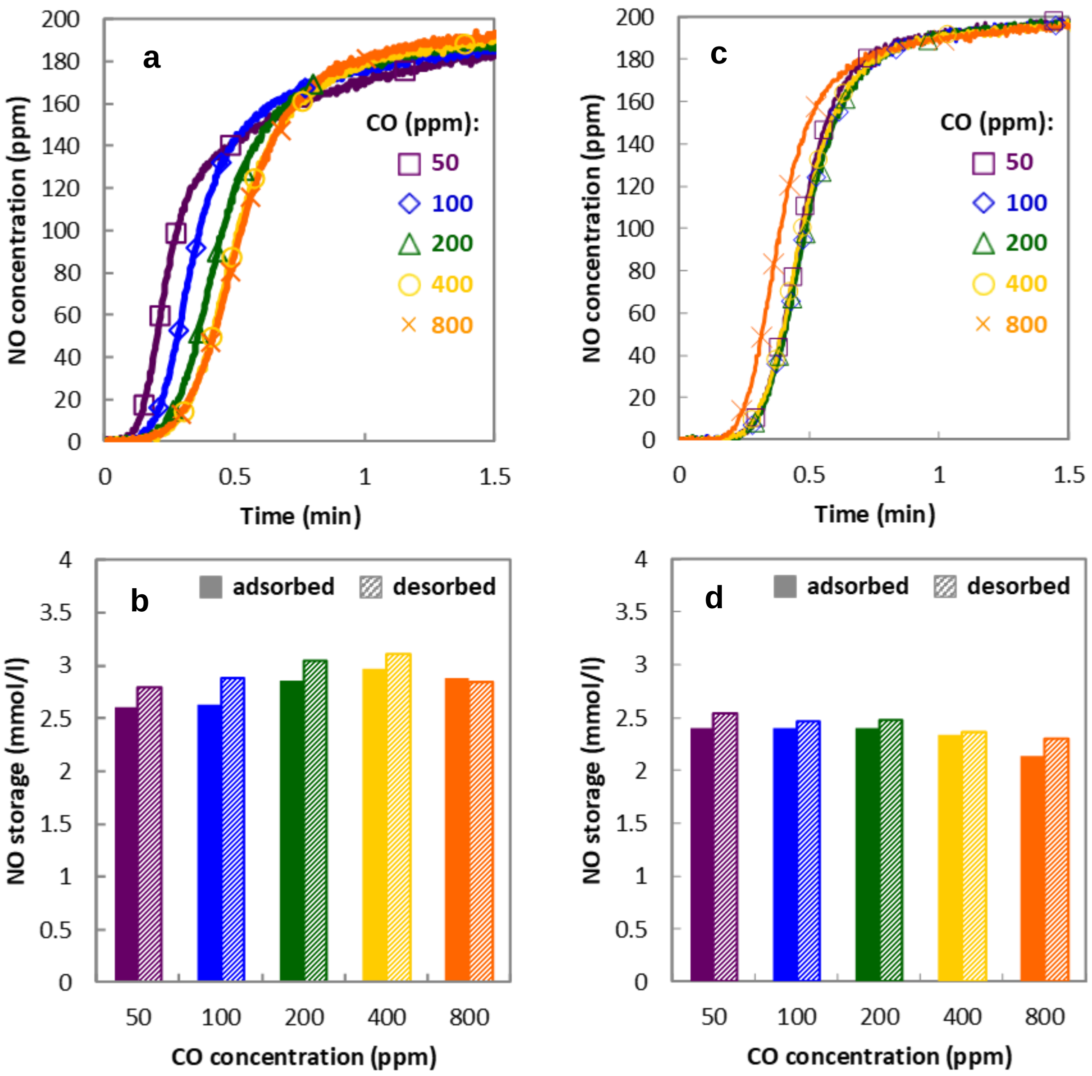

Figure 4.9: (a) NO concentration profiles during NO adsorption at 100 °C and (b) total NO storage as measured from NO adsorbed at 100 °C (solid fill) and NO desorbed during TPD from 100-500 °C (diagonal line fill) as the CO concentration is varied in experiments conducted with Pd/ZSM-5. Feed conditions: 200 ppm NO, **50-800 ppm CO**, 10% O_2, 7% H_2O, 0% CO_2, GHSV 30000 hr^{-1}

4.3.2 Identification of surface intermediates with in situ DRIFTS

H_2O is a major constituent in engine exhaust, and the flow reactor experiments showed significant impact of operating conditions including H_2O concentration and adsorption temperature on NO storage and release characteristics. In an attempt to establish the connection between the observed H_2O and temperature effects on the NO storage and release and the nature of Pd storage sites, DRIFTS spectra under similar conditions were collected and used to provide mechanistic insights.

As is shown in Figure 4.10, we first collected spectra after 200 ppm NO and 10% O2 exposure at 100 °C and a subsequent Ar purge in the absence of H_2O to understand the initial speciation of Pd/ZSM-5 as a NOx storage material. We observe IR peaks at 2128 cm^{-1}, 1873 cm^{-1} and 1839 cm^{-1}, and broad IR bands ranging from 1500 cm^{-1} to 1700 cm^{-1}. Additionally, we collected spectra at 100 °C and 175 °C in the presence of 1% and 4.5% of H_2O to gain insights into the surface intermediates formed under more realistic conditions. As is shown in Figure 4.10, the spectra collected at 100 °C show clear H_2O concentration dependence. As the H_2O concentration is increased from 0% to 1%, a new IR feature at 1818 cm^{-1} appears, while the relative intensity of the peak at 1873 cm^{-1} diminishes. At 4.5% H_2O, a single peak in the N-O stretching region at 1818 cm^{-1} dominates the IR spectrum. DRIFTS spectra collected at 175 °C demonstrate that this change can be reversed by increasing temperature. Specifically, Figure 4.11 shows that when the sample was exposed to 200 ppm NO, 10% O_2 and 4.5% H_2O at 175 °C, the peak at 1818 cm^{-1} disappears and the two features (1873 cm^{-1} and 1838 cm^{-1}) previously observed in the absence of H_2O restore.

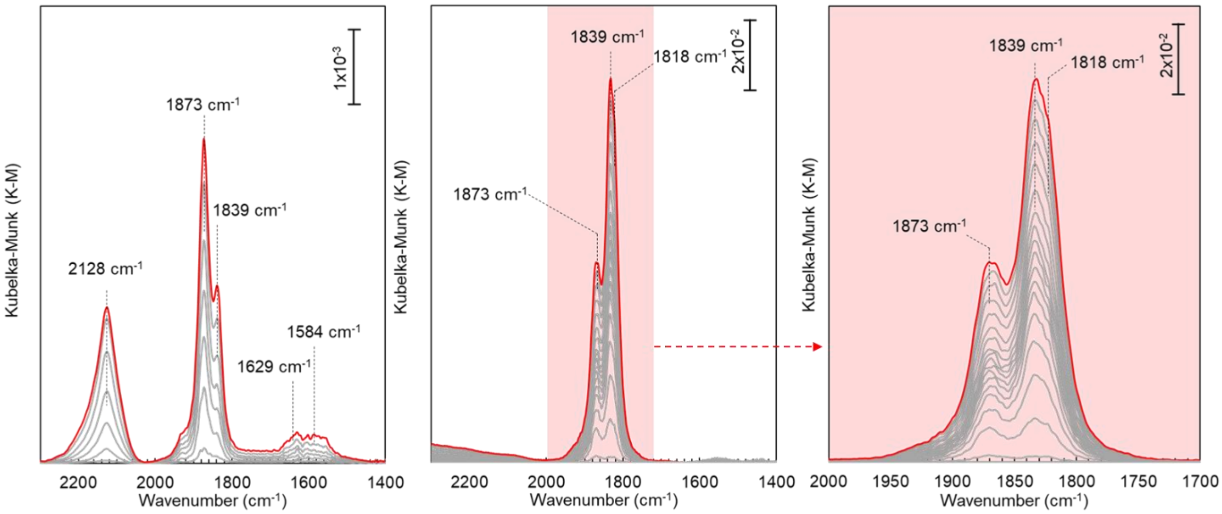

Figure 4.10 In-situ DRIFTS spectra during NO adsorption at 100 °C under dry conditions on the Pd/ZSM-5 PNA sample.

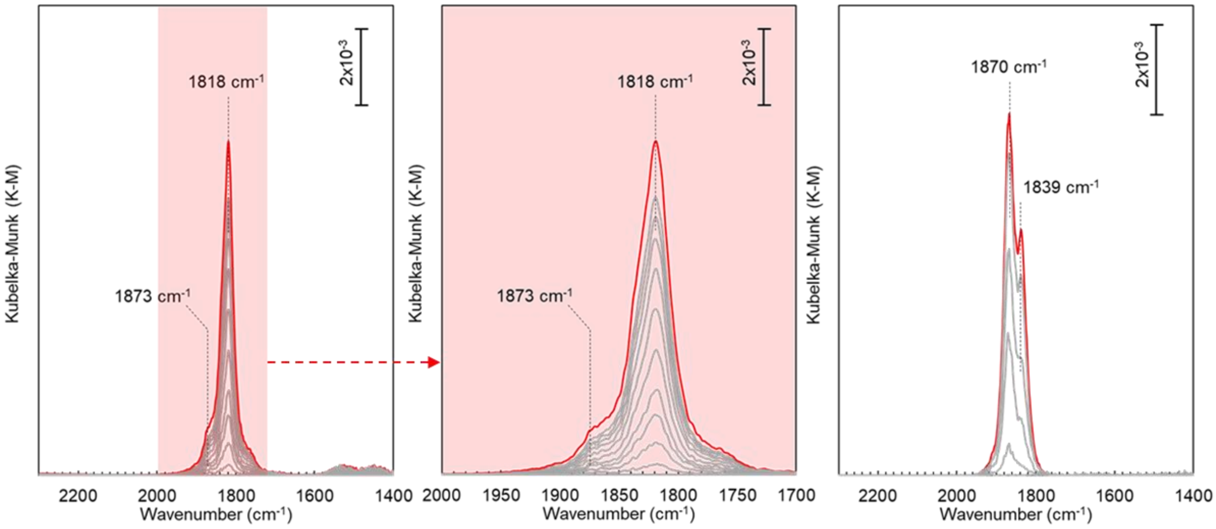

Figure 4.11 In situ DRIFTS spectra during NO adsorption at 100 °C and 175 °C under wet conditions on the Pd/ZSM-5 PNA sample.

To gain insights into the interactions between adsorbed NO and CO, in-situ DRIFTS experiments have been conducted during CO adsorption under dry and wet conditions at 100 °C. A separate experiment was performed where after CO saturation in the presence of 4.5% H_2O NO was added. When CO is adsorbed onto the Pd/ZSM-5 sample under dry conditions at 100 °C, we observed multiple CO stretching spectral features at 2175 cm^{-1}, 2140 cm^{-1}, 2122 cm^{-1}, 2108 cm^{-1} and 1966 cm^{-1}. However, once H_2O is introduced into the system, we observe the disappearance of peaks at 2175 cm^{-1}, 2108 cm^{-1} and shifts in peak position of the others due to hydration.[175] Meanwhile, a relatively weak CO stretching is also observed at 1966 cm^{-1} under dry conditions and shifts to 1960 cm^{-1} after the introduction of H_2O, which has also been attributed to hydration.[175] The following Ar purge led to the decrease in peak intensity at 1960 cm^{-1} and the disappearance of features at 2133 cm^{-1} and 2107 cm^{-1}

Lastly, the DRIFTS spectra for NO adsorption at 100 °C after CO saturation in the presence of 4.5% of H_2O was collected and displayed in Figure 4.12, note the background of these spectra were collected after saturation of CO and H_2O adsorption. The peak at 1818 cm^{-1} develops immediately after the introduction of NO. Simultaneously, the appearance of the negative peak intensities at 1970 cm^{-1}, 2123 cm^{-1} and 2142 cm^{-1} indicates the consumption of adsorbed CO species.

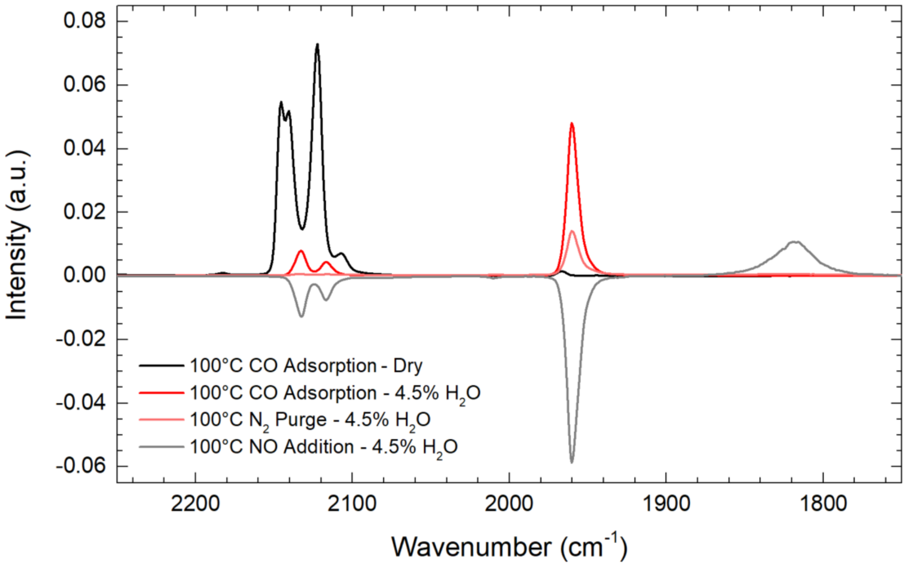

Figure 4.12: In-situ DRIFTS spectra during CO adsorption at 100 °C under dry and wet conditions followed by NO adsorption at 100 °C under wet conditions on the Pd/ZSM-5 PNA sample.

4.4 Discussion

4.4.1 NO adsorption in the absence of H_2O

The IR features observed in Figure 16 have been reported and mostly well identified based on surface chemistry studies of the interaction between NO and Pd/ZSM-5 under ultra-high vacuum conditions.[179,181,182,188,189] The wide IR band centered at 2130 cm^{-1} has been assigned to the linear N-O stretching frequency of NO^+ interacting with AlO_4^- from the zeolite framework.[182,188,190] Consistent with literature reported observation, the peak intensity at 2130 cm^{-1} deceased significantly during Ar purge at 100°C, indicating this interaction is relatively weak.[179] Nitrate and nitrite formation can be facilitated via formation of NO_2 by PdO and Bronsted acid sites,[191] which leads to the presence of IR bands in the 1600 cm^{-1} region.[188] These species are generally not coordinated with Pd and are absent in the presence of H_2O or at higher temperatures as is shown in Figure 16, and thus provide no information about initial Pd speciation nor the mechanism under realistic conditions. When it comes to the adsorbed NO on Pd cationic species, IR peak assignments and the molecular structure of these surface intermediates are still debatable. According to previously reported results, the two IR features at 1873 cm^{-1} and 1838 cm^{-1} were assigned to the stretching frequencies of NO directly coordinated with Pd^{2+} and Pd^+ cations, respectively.[179] The existence of Pd^{2+} and Pd^+ was, however, not well justified. Although Descorme et al. proposed the reduction of Pd^{2+} to Pd^+ upon NO exposure supported by the simultaneous NO_2 formation in the absence of O_2, direct characterization of Pd^+ has only been reported in Pd/Y after H_2 exposure.[192,193] Pd^{2+} cationic species, however, have been more widely observed within different zeolitic systems, likely due to the four-coordinated structure stabilized by aluminum pairs. Furthermore, the NO stretching frequencies of these Pd^{II}-NO complexes depend on the zeolite topology and aluminum distribution.[172,180] Although molecular structures of

Pd-NO species are not the main focus of this work, Figure 16 indicates that there are at least two different Pd-NO complexes in the absence of H_2O.[165,170,174] We, therefore, attribute IR features at 1873 cm^{-1} and 1838 cm^{-1} to NO adsorbed on two different Pd^{2+} entities that locate in different zeolite cages, or experience different ligand environments but share the same oxidation state. Thus, NO adsorption on cationic Pd in the absence of H_2O can be represented by the reaction in equation (E1):

$$Z_2[Pd^{II}] + NO \rightleftharpoons Z_2[Pd^{II}NO] \qquad \textbf{(E1)}$$

The spectral features in Figure 16 originate from the adsorption of NO on Pd, and we attribute the $Z_2[Pd^{II}NO]$ species in equation (E1) to the features at 1873 cm^{-1} and 1838 cm^{-1}.

4.4.2 NO adsorption in the presence of H_2O

The hydration of Pd cations has been previously reported and appears to significantly influence the nature of Pd and NO adsorption mechanism.[171,194] In fact, as is shown in Figure 16, we observe significant differences in the IR spectra when H_2O is introduced. The evolution of the peak at 1818 cm^{-1} clearly demonstrates the formation of a new Pd-NO complex, and the single peak spectra at 4.5% H_2O also suggests a more homogenous Pd speciation in the presence of H_2O. CO oxidation light-off curves shown in the supporting information also indicate that Pd species formed in the presence and absence of H_2O are intrinsically different since the CO oxidation activity in the presence of H_2O is significantly higher. These results are consistent with our previous observations using Pd/SSZ-13 and strongly support the hydration of Pd cations in the presence of H_2O, which can be represented by the reaction in equation (E2):

$$Z_2[Pd^{II}] + 4H_2O \rightleftharpoons [Z_2Pd^{II}(H_2O)_4] \qquad \textbf{(E2)}$$

Our previous study on Pd/SSZ-13 showed that the Pd cations are solvated by four water molecules under these conditions to maintain a four-fold coordinated structure. Moreover, H_2O solvated Pd is no longer attached to the zeolite, and thus exhibits homogeneous speciation.[196] Although the H_2O solvation effect was fully investigated using Pd/SSZ-13, IR characterization of other Pd/zeolites suggest that the detachment of Pd cations from the zeolite is a universal behavior for almost all Pd zeolite systems under similar conditions.[42] Hence the NO adsorption on Pd/ZSM-5 in the presence of H_2O, which represents more realistic exhaust conditions, can be represented by the reaction in equation (E3):

$$[Z_2Pd^{II}(H_2O)_4] + NO \rightleftharpoons [Z_2Pd^{II}(H_2O)_3NO] + H_2O \qquad \textbf{(E3)}$$

In our previous work we showed that the formation of $Z[Pd^{II}(NO^-)(H_2O)_3]$ involves the oxidation of NO or CO and the migration of Pd from 2Al site to 1Al site after solvation.[196] However, here we did not observe significant transient CO_2 or NO_2 formation during CO or NO adsorption on Pd/ZSM-5, and thus propose $[Z_2Pd^{II}(H_2O)_3NO]$ is the dominating species and corresponds to the IR feature at 1818 cm^{-1} in Figure 16. Notably, NO adsorption in the absence of H_2O has been reported to exhibit higher NO storage capacity due to the contribution of zeolite Bronsted acid sites,[166] however, reaction (E3) also indicates that severe hydration will lead to lower NO storage capacity due to the equilibrium shift following the reverse reaction. This phenomenon has indeed been reported in the literature.[187] In contrast, the H_2O desorption induced by increasing temperature can, however, enhance NO storage capability, which is captured in section 4.3.1.4 Figure 8 by the increase in NOx storage capacities up to 150 °C. Additionally DRIFTS spectra collected at 175 °C in the presence of H_2O provide more mechanistic insights of this process, and show that the Pd^{II}-NO species formed under this condition are the same species formed under dry conditions. This process can be represented by the reaction in equation (E4)

$$[Z_2Pd^{II}(H_2O)_3NO] \rightleftharpoons 3H_2O + Z_2[Pd^{II}NO] \qquad \textbf{(E4)}$$

The transition from hydrated Pd^{II}-NO species (1818 cm^{-1}) to dehydrated Pd^{II}-NO species (1873 cm^{-1} and 1839 cm^{-1}) in Figure 17 suggest that H_2O desorbs from Pd at a lower temperature than NO and the complete dehydration can be facilitated by simply increasing temperature. Both DRIFTS spectra collected at 175 °C in Figure 17 and the maximized NO storage capacity at 150 °C in Figure 9 indicate complete dehydration at around 150 °C. As was mentioned and shown in the supporting information, the CO oxidation activity of Pd cations in the hydrated form is significantly better than the dehydrated form. Hence, a consequence of dehydration is that CO oxidation activity should decrease during the temperature ramp, which is shown in Figure 1 and explains the non-typical CO_2 light-off behavior.

Further increasing temperature leads to NO desorption via the reverse reaction of (E1). The decrease in NO storage capacity at temperatures above 150 °C observed in Figure 8 is, therefore, expected due to the increasingly thermodynamically favored NO desorption. This behavior is also necessary for the Pd/ZSM-5 to operate as a PNA – the NO stored at low temperatures must be released at higher temperatures for a PNA to be useful. More importantly, the NO temperature programmed desorption profiles in Figure 2**,** which is in the presence of H_2O, exhibit two NO release peaks. If Pd is still hydrated, we would only see one NO desorption peak. Since we see two, this agrees well with our hypothesis that the complete dehydration occurred before NO desorption. Additionally, this is also consistent with there being at least two different kinds of Pd species under dry conditions and when Pd is dehydrated during TPD.

The results in sections 4.3.1.3 and 4.3.1.5 demonstrated that the equilibrium NO storage capacity is not influenced by H_2O and NO concentrations. This suggests that NO adsorption following reaction (E3) is exothermic and favored under the conditions a PNA typically operates. However, the rate of adsorption is influenced by both NO and H_2O concentrations. Consistent with the proposed reaction (E3), we found a first order dependence of NO adsorption rate on NO concentration as well as the inhibition by H_2O. Although expected the inhibition of H_2O on NO adsorption rate is not fully understood suggesting that reaction (E3) is not an elementary reaction.

4.4.3 Effect of CO in the presence of H_2O

DRIFTS spectra collected during CO adsorption in the absence of H_2O shown in Figure 18 provides similar information about the initial Pd speciation as NO DRIFTS experiments. We observed the formation of di-carbonyl species coordinated with Pd^{2+} cations at 2175, 2144, 2140, and 2122 cm^{-1}.[166] CO adsorption on reduced Pd particles is observed at 2107,1965 and 1945 cm^{-1}.[195] As is previously mentioned, there are at least two Pd^{2+} species in the zeolite, and thus multiple vibrational frequencies associated with carbonyl species are expected and observed in the 2100-2200 cm^{-1} region. However, once H_2O is introduced into the system, we observe the disappearance of peaks at 2175, 2108 cm^{-1} and shifts in peak position of the others in the carbonyl region. We attribute this phenomenon, again, to the hydration of Pd cations, and thus a more homogeneous Pd speciation. The doublet at 2132 cm^{-1} and 2117 cm^{-1} can now be assigned to hydrated Pd^{II}-dicarbonyl species$[Z_2Pd^{II}(H_2O)_2(CO)_2]$. Meanwhile, a new feature at 1960 cm^{-1} appears after the introduction of H_2O and becomes the dominating feature. Although this peak locates in the C-O stretching region that is typically associated with Pd^0 particles, H_2O influencing C-O stretching frequency of mono-carbonyl species has been reported in Pd/BEA,[175] and our previous work has shown hydration led to a 60 cm^{-1} peak shift in N-O stretching frequency in Pd/SSZ-13.[196]

Moreover, the peak at 1960 cm^{-1} is significantly more intense than would be expected for a peak associated with C-O stretching on Pd^0 particles, as suggested by the intensity of C-O stretching on Pd^0 particles peak (1966 cm^{-1}) under dry conditions shown in Figure 18. Hence, we assign this peak at 1960 cm^{-1} to $[Z_2Pd^{II}(H_2O)_3CO]$ since the hydration of mono-carbonyl species can also lead to the significant peak shift to a lower wave number.[175] The following Ar purge led to the disappearance of features at 2133 cm^{-1} and 2107 cm^{-1} indicating the instability of Pd^{II}-dicarbonyl species and $[Z_2Pd^{II}(H_2O)_3CO]$ as the only remaining Pd-CO species. Therefore, CO adsorption in the presence of 4.5% H_2O can be represented by the reaction in equations (E5) and (E6):

$$[Z_2Pd^{II}(H_2O)_4] + CO \rightleftharpoons [Z_2Pd^{II}(H_2O)_3CO] + H_2O \qquad \textbf{(E5)}$$

$$[Z_2Pd^{II}(H_2O)_4] + 2CO \rightleftharpoons [Z_2Pd^{II}(H_2O)_2(CO)_2] + 2H_2O \qquad \textbf{(E6)}$$

Figure 18 also shows the influence of NO adsorption on CO IR features after CO saturation in the presence of H_2O. More specifically, after a background taken upon the saturation of CO adsorption in the presence of H_2O, the subsequent NO adsorption led to the evolution of the mono-nitrosyl Pd species at 1818 cm^{-1} observed before and negative peaks at wavenumbers associated with hydrated mono- and di- carbonyl Pd complexes at 2133 cm^{-1}, 2107 cm^{-1} and 1960 cm^{-1}. These results suggest that CO was replaced by NO during NO adsorption because NO binds with Pd more strongly than CO in the presence of H_2O. This process can be represented by the reaction in equation (E6):

$$[Z_2Pd^{II}(H_2O)_3CO] + NO \rightleftharpoons [Z_2Pd^{II}(H_2O)_3NO] + CO \qquad \textbf{(E6)}$$

NO replacing CO provides an explanation for the transient CO release during NO adsorption at 100 °C, as is described in section 4.3.1 Figure 1. $[Z_2Pd^{II}(H_2O)_3NO]$ is considered to be the most stable surface intermediate formed in the presence of NO, CO, and H_2O. Khivantsev et al. provided strong IR evidence for the formation of a CO and NO co-adsorbed carbonyl-nitrosyl Pd complex on a Pd/SSZ-13 PNA catalyst under dry conditions.[187] However, we did not observe the related IR feature and therefore, have no evidence to support the existence of CO and NO co-adsorbed carbonyl-nitrosyl Pd complex in the presence of H_2O. Therefore, formation of hydrated Pd^{II}-NO is proposed to be the dominating species regardless of the presence of CO. However, we do notice the change in the rate of NO adsorption in section 4.3.1.6 with and without CO pre-saturation and it appears that (E6) is kinetically faster than (E3). The effect of CO concentration on the rate of NO replacing CO is due likely due to the different amounts of $[Z_2Pd^{II}(H_2O)_3CO]$ formed driven by different CO concentrations via (E5), and with (E6) faster than (E3) the increase in NO adsorption rate continues until the complete consumption of $[Z_2Pd^{II}(H_2O)_3CO]$. Notably, this is not the only process that occurs during NO adsorption in the presence of H_2O and CO, since $[Z_2Pd^{II}(H_2O)_4]$ exists. NO adsorption via E3 can also take place simultaneously and explains the slow approach to saturation in Figure 12(a). Note that when the NO exposure temperature is above 150 °C, neither H_2O nor CO has a significant impact on NO storage and release, and thus after dehydration equation (E1) is sufficient to describe the NO desorption process even in the presence of CO.

Finally, we combine the 6 proposed key reactions to form a PNA mechanism that captures the PNA performance and DRIFTS results under all investigated conditions and is consistent with the existing literature.

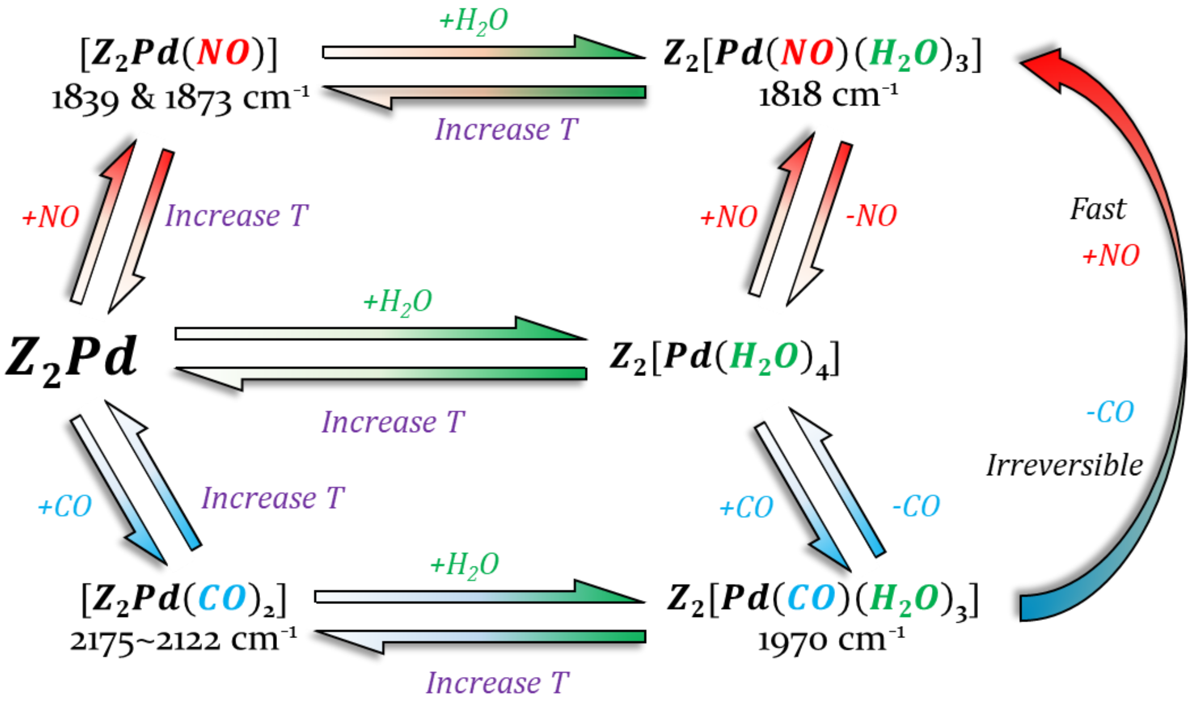

Figure 4.13: In-situ DRIFTS spectra during CO adsorption at 100 °C under dry and wet conditions followed by NO adsorption at 100 °C under wet conditions on the Pd/ZSM-5 PNA sample.

4.5 Conclusions

A systematic flow reactor and IR characterization study was conducted to understand the impact of NO adsorption temperature, and the concentrations of NO, CO, and H_2O on Pd/ZSM-5 NO storage and release. CO_2 and O_2 concentration have minimal effect on NO adsorption and release. The NO adsorption rate has a first order dependence on NO concentration, but the NO concentration does not impact total NO storage capacity. NO storage capacity increased from 75 to 150 °C due to the dehydration of Pd, and decreased from 150 to 225 °C due to the increasingly thermodynamically favored NO desorption. The NO uptake rate on the fully hydrated Pd species is slower compared to the hydrated Pd-CO complex, therefore, pre-saturation of CO accelerates NO adsorption in the presence of H_2O at low temperatures. CO has no effect on the NO adsorption rate at temperatures $\geqslant$150 °C, again due to the dehydration of Pd. IR characterization shows Pd species formed in the absence and presence of H_2O are intrinsically different, which leads to the difference in their CO oxidation activities. The dehydration of Pd that occurs during the TPD experiments leads to the decrease in CO oxidation activity and the non-typical CO oxidation light-off behavior. Using 6 proposed key reaction based on the IR characterization, reactor results and literature a mechanism for NO adsorption and desorption on Pd/ZSM-5 is proposed.

4.6 References

(155) F. Gramigni, T. Selleri, I. Nova, E. Tronconi, Catalyst systems for selective catalytic reduction + NO: X trapping: From fundamental understanding of the standard SCR reaction to practical applications for lean exhaust after-treatment, React. Chem. Eng. 4 (2019) 1165–1178.

(156) C.K. Lambert, Perspective on SCR NOx control for diesel vehicles, React. Chem. Eng. 4 (2019) 969–974.

(157) A.M. Beale, F. Gao, I. Lezcano-Gonzalez, C.H.F. Peden, J. Szanyi, Recent advances in automotive catalysis for NOx emission control by small-pore microporous materials, Chem. Soc. Rev. 44 (2015) 7371–7405.

(158) M.P. Harold, NOx storage and reduction in lean burn vehicle emission control: A catalytic engineer's playground, Curr. Opin. Chem. Eng. 1 (2012) 303–311.

(159) H.Y. Chen, S. Mulla, E. Weigert, K. Camm, T. Ballinger, J. Cox, P. Blakeman, Cold start concept (CSC^{TM}): A novel catalyst for cold start emission control, SAE Tech. Pap. 2 (2013) 372–381.

(160) Y. Gu, W.S. Epling, Passive NOx adsorber: An overview of catalyst performance and reaction chemistry, Appl. Catal. A Gen. 570 (2019) 1–14.

(161) M. Moliner, A. Corma, From metal-supported oxides to well-defined metal site zeolites: The next generation of passive NO x adsorbers for low-temperature control of emissions from diesel engines, React. Chem. Eng. 4 (2019) 223–234.

(162) J. Lee, J.R. Theis, E.A. Kyriakidou, Vehicle emissions trapping materials: Successes, challenges, and the path forward, Appl. Catal. B Environ. 243 (2019) 397–414.

(163) H.-Y. Chen, D. Liu, E. Weigert, L. Cumaranatunge, K. Camm, P. Bannon, J. Cox, L. Arnold, Durability Assessment of Diesel Cold Start Concept (dCSC^{TM}) Technologies, SAE Int. J.

Engines. 10 (2017) 2017-01–0955.

(164) J.R. Theis, C.K. Lambert, An assessment of low temperature NOx adsorbers for cold-start NOx control on diesel engines, Catal. Today. 258 (2015) 367–377.

(165) J. Lee, Y. Ryou, S.J. Cho, H. Lee, C.H. Kim, D.H. Kim, Investigation of the active sites and optimum Pd/Al of Pd/ZSM–5 passive NO adsorbers for the cold-start application: Evidence of isolated-Pd species obtained after a high-temperature thermal treatment, Appl. Catal. B Environ. 226 (2018) 71–82.

(166) Y. Zheng, L. Kovarik, M.H. Engelhard, Y. Wang, Y. Wang, F. Gao, J. Szanyi, Low-Temperature Pd/Zeolite Passive NOx Adsorbers: Structure, Performance and Adsorption Chemistry, J. Phys. Chem. C. (2017) acs.jpcc.7b04312.

(167) A. Wang, K. Xie, A. Kumar, K. Kamasamudram, L. Olsson, Layered Pd/SSZ-13 with Cu/SSZ-13 as PNA − SCR dual-layer monolith catalyst for NOx abatement, Catal. Today. (2020) 0–1.

(168) Y. Ryou, J. Lee, S.J. Cho, H. Lee, C.H. Kim, D.H. Kim, Activation of Pd/SSZ-13 catalyst by hydrothermal aging treatment in passive NO adsorption performance at low temperature for cold start application, Appl. Catal. B Environ. 212 (2017) 140–149.

(169) Y. Ryou, J. Lee, Y. Kim, S. Hwang, H. Lee, C.H. Kim, D.H. Kim, Effect of reduction treatments (H2 vs. CO) on the NO adsorption ability and the physicochemical properties of Pd/SSZ-13 passive NOx adsorber for cold start application, Appl. Catal. A Gen. 569 (2019) 28–34.

(170) H.-Y. Chen, J.E. Collier, D. Liu, L. Mantarosie, D. Durán-Martín, V. Novák, R.R. Rajaram, D. Thompsett, Low Temperature NO Storage of Zeolite Supported Pd for Low Temperature Diesel Engine Emission Control, Catal. Letters. 146 (2016) 1706–1711.

(171) A. Gupta, S.B. Kang, M.P. Harold, NOx uptake and release on Pd/SSZ-13: Impact Of Feed composition and temperature, Catal. Today. (2020) 0–1.

(172) O. Mihai, L. Trandafilović, T. Wentworth, F.F. Torres, L. Olsson, The Effect of Si/Al Ratio for Pd/BEA and Pd/SSZ-13 Used as Passive NOx Adsorbers, Top. Catal. 0 (2018) 0.

(173) A. Porta, T. Pellegrinelli, L. Castoldi, R. Matarrese, S. Morandi, S. Dzwigaj, L. Lietti, Low Temperature NOx Adsorption Study on Pd-Promoted Zeolites, Top. Catal. 0 (2018) 0.

(174) J. Lee, Y. Ryou, S. Hwang, Y. Kim, S.J. Cho, H. Lee, C.H. Kim, D.H. Kim, Comparative study of the mobility of Pd species in SSZ-13 and ZSM-5, and its implication for their activity as passive NOx adsorbers (PNAs) after hydro-thermal aging, Catal. Sci. Technol. 9 (2019) 163–173.

(175) D. Mei, F. Gao, J. Szanyi, Y. Wang, Mechanistic insight into the passive NOx adsorption in the highly dispersed Pd/HBEA zeolite, Appl. Catal. A Gen. 569 (2019) 181–189.

(176) M. Ambast, K. Karinshak, B.M.M. Rahman, L.C. Grabow, M.P. Harold, Passive NOx adsorption on Pd/H-ZSM-5: Experiments and modeling, Appl. Catal. B Environ. 269 (2020) 118802.

(177) Y. Gu, R.P. Zelinsky, Y.-R. Chen, W.S. Epling, Investigation of an irreversible NOx storage degradation Mode on a Pd/BEA passive NOx adsorber, Appl. Catal. B Environ. 258 (2019) 118032.

(178) Y. Murata, T. Morita, K. Wada, H. Ohno, NOx Trap Three-Way Catalyst (N-TWC) Concept: TWC with NOx Adsorption Properties at Low Temperatures for Cold-Start Emission Control, SAE Int. J. Fuels Lubr. 8 (2015) 454–459.

(179) C. Descorme, P. Gelin, M. Primet, C. Lecuyer, Infrared study of nitrogen monoxide adsorption on palladium ion-exchanged ZSM-5 catalysts, Catal. Letters. 41 (1996) 133–138.

(180) B. Pommier, P. Ge´lin, On the nature of Pd species formed upon exchange of H-ZSM-5 with Pd(NH3)42+ and calcination in O2, Phys. Chem. Chem. Phys. 1 (1999) 1665–1672.

(181) K. Okumura, J. Amano, N. Yasunobu, M. Niwa, X-ray Absorption Fine Structure Study of the Formation of the Highly Dispersed PdO over ZSM-5 and the Structural Change of Pd Induced by Adsorption of NO, J. Phys. Chem. B. 104 (2000) 1050–1057.

(182) B. Pommier, P. Gelin, Infrared and volumetric study of NO adsorption on Pd-H-ZSM-5, Phys. Chem. Chem. Phys. 3 (2001) 1138–1143.

(183) K. Khivantsev, N.R. Jaegers, L. Kovarik, J.C. Hanson, F. (Feng) Tao, Y. Tang, X. Zhang, I.Z. Koleva, H.A. Aleksandrov, G.N. Vayssilov, Y. Wang, F. Gao, J. Szanyi, Achieving Atomic Dispersion of Highly Loaded Transition Metals in Small-Pore Zeolite SSZ-13: High-Capacity and High-Efficiency Low-Temperature CO and Passive NO x Adsorbers, Angew. Chemie Int. Ed. 57 (2018) 16672–16677.

(184) A. Vu, J. Luo, J. Li, W.S. Epling, Effects of CO on Pd/BEA Passive NOx Adsorbers, Catal. Letters. 147 (2017) 745–750.

(185) S. Sinha Majumdar, J.A. Pihl, T.J. Toops, Reactivity of novel high-performance fuels on commercial three-way catalysts for control of emissions from spark-ignition engines, Appl. Energy. 255 (2019) 113640.

(186) J.R. Theis, J.A. Ura, Assessment of zeolite-based Low temperature NOx adsorbers: Effect of reductants during multiple sequential cold starts, Catal. Today. (2020).

(187) K. Khivantsev, F. Gao, L. Kovarik, Y. Wang, J. Szanyi, Molecular Level Understanding of How Oxygen and Carbon Monoxide Improve NO x Storage in Palladium/SSZ-13 Passive NO x Adsorbers: The Role of NO + and Pd(II)(CO)(NO) Species, J. Phys. Chem. C. 122 (2018) 10820–10827.

(188) L.J. Lobree, A.W. Aylor, J.A. Reimer, A.T. Bell, NO Reduction by CH 4 in the Presence of O 2 over Pd-H-ZSM-5, 204 (1999) 189–204.

(189) K. Chakarova, E. Ivanova, K. Hadjiivanov, D. Klissurski, H. Knözinger, Co-ordination chemistry of palladium cations in Pd-H-ZSM-5 as revealed by FTIR spectra of adsorbed and co-adsorbed probe molecules (CO and NO), Phys. Chem. Chem. Phys. 006 (2004) 3702–3709.

(190) K. Hadjiivanov, J. Saussey, J.L. Freysz, FT-IR study of NO+O2 co-adsorption on H-ZSM-5: re-assignment of the 2133 cm−1 band to NO+ specie, Catal. Letters. 52 (1998) 103–108.

(191) T. Salavati-fard, R.F. Lobo, L.C. Grabow, Linking low and high temperature NO oxidation mechanisms over Brønsted acidic chabazite to dynamic changes of the active site, J. Catal. 389 (2020) 195–206.

(192) M. Primet, Y. Ben Taarit, Infrared study of oxidized and reduced palladium loaded zeolites, J. Phys. Chem. 81 (1977) 1317–1324.

(193) M. Che, J.F. Dutel, P. Gallezot, M. Primet, A study of the chemisorption of nitric oxide on PdY zeolite. Evidence for a room temperature oxidative dissolution of Pd crystallites, J. Phys. Chem. 80 (1976) 2371–2381.

(194) J. Lee, J. Kim, Y. Kim, S. Hwang, H. Lee, C.H. Kim, D.H. Kim, Improving NOx storage and CO oxidation abilities of Pd/SSZ-13 by increasing its hydrophobicity, Appl. Catal. B Environ. 277 (2020) 119190.

(195) I. V. Yudanov, R. Sahnoun, K.M. Neyman, N. Rösch, J. Hoffmann, S. Schauermann, V. Johánek, H. Unterhalt, G. Rupprechter, J. Libuda, H.J. Freund, CO adsorption on Pd nanoparticles: Density functional and vibrational spectroscopy studies, J. Phys. Chem. B. 107 (2003) 255–264.

(196) K. Mendal, Y.Gu, K. S. Westendorff, S. Li, J. A.Pihl, L. C. Grabow, W. S. Epling, and C. Paolucci, Condition-Dependent Pd Speciation and NO adsorption in Pd/Zeolites, ACS Catal. 2020

Chapter 5. Investigation of An Irreversible NOx Storage Degradation Mode on Pd/BEA as A Model Catalyst for Passive NOx Adsorption

This chapter is published in Applied Catalysis B: Environmental and can be found as: Y. Gu, R.P. Zelinsky, Y.-R. Chen, W.S. Epling, Investigation of an irreversible NOx storage degradation Mode on a Pd/BEA passive NOx adsorber, Appl. Catal. B Environ. 258 (2019) 118032.

5.1 Introduction

There has been significant progress in automobile NOx abatement technologies[1–6]. Current state-of-the-art selective catalytic reduction (SCR) catalysts designed for diesel NOx abatement can meet currently required regulation limits, and have proven hydrothermally stable[7–11]. However, progressively more stringent emission regulations as well as fuel economy requirements drive the need for further advancement in exhaust after-treatment technologies[12]. Notably, the development of advanced compression ignition technologies usually results in a lower exhaust temperature[13]. To meet these even more stringent regulations, and the challenges associated with lower exhaust temperatures, low-temperature catalysis remains a research focus[13–15]. The remediation of “cold start” NOx, namely NOx emitted before the after-treatment system is warmed up enough to achieve high pollutant conversions, remains challenging. Arguably, the SCR catalytic activity at low temperatures can be improved with new catalyst designs and formulations. However, urea decomposition, as the current in application ammonia source, occurs at temperatures above 180 °C[16].

Passive NOx adsorbers (PNAs) are proposed as one of the solutions to help address cold start NOx emissions[17–20]. PNAs can trap NOx at low temperatures, thereby removing NOx during cold start. An appropriate NOx desorption temperature window is also key to ultimately reducing NOx, since desorption at too low of a temperature will allow it to slip through the SCR catalyst unconverted[18]. PNA candidate materials have been evaluated. Crocker's group investigated a series of Pd- and Pt-promoted alumina and ceria/zirconia PNAs. They studied formulation performance dependency and provided insight into the NOx trapping and release characteristics of these model systems[21–24]. Theis et al. looked into the exhaust composition effects on the NOx adsorption and desorption behavior of Pd promoted ceria/zirconia[25–28]. Chen et. al. have shown that Pd/zeolite systems performed significantly better than ceria-based PNAs in terms of NOx storage capacity per unit mass of precious metal, NOx desorption temperature and their real exhaust compatibilities[29]. Since then, Pd/BEA, Pd/ZSM-5 and Pd/SSZ-13 have attracted significant attention[30–36]. In terms of the NOx trapping mechanism, it is believed that ion-exchanged cationic Pd species are the key adsorption sites. For example, Zheng et al. and Ryou et al. have tested and characterized a series of Pd/zeolite systems and concluded that Pd cations are the dominant trapping sites and a thermal or hydrothermal treatment during catalyst synthesis plays an important role in forming those sites via Pd dispersion into the zeolite system[37–39]. In addition, using a modified ion-exchange method, Khivantsev et al. were able to achieve a 1:1 NOx-to-Pd ratio, thus maximizing the atomic utilization[40].

Because the PNA is the most upstream after-treatment system component, or integrated with the most upstream component, these trapping sites will be exposed to a variety of exhaust gas compositions. Therefore, to better characterize NOx trapping and release, as well as understand potential degradation modes, this catalyst needs to be evaluated during and after exposure to exhaust gas components. Effects of O_2, H_2O and CO_2 have been studied for example. It was found that O_2 is key to high NOx storage capacity under dry conditions due to the formation of nitrate and nitrite species[41], however, CO_2 does not have a significant impact on the NOx storage capacity of Pd/BEA neither does it affect NOx desorption[42]. For Pd-SSZ-13, H_2O inhibits NOx adsorption by strongly interacting with Bronsted sites at low temperatures, thus resulting in a significant decrease in NOx storage capacity[29].The effect of CO has also been studied. Vu et al. found that CO can shift NOx desorption temperatures to a more ideal range[42], and in a recently published work, Ryou et al. also found that CO can reduce Pd cations and accelerate particle sintering under rich conditions[43].

In this paper, Pd/BEA was chosen as a model PNA, and its NOx trapping and desorption characteristics were evaluated under simulated exhaust conditions, with the emphasis on the impact of CO. An irreversible NOx storage degradation mode was observed and a mechanistic explanation provided.

5.2 Experimental methods

5.2.1 Catalyst Synthesis

A series of Pd impregnated catalysts as well as the proton form catalysts/adsorbers were synthesized and evaluated in this study. All Pd-containing catalysts were prepared via incipient wetness impregnation, and some of the resulting powder was used to wash-coat cordierite monolith substrates. The ammonium form of BEA zeolite with a 12.5 Si/Al ratio was purchased from Zeolyst Inc. A three-step calcination process (80 °C for 2 hours, 105 °C for 10 hours and 500 °C for 4 hours with a ramp rate of 1 °C/min) was used to transform the BEA zeolite into proton form before introducing Pd. $Pd(NO_3)_2$ dissolved in nitric acid was selected as the precursor, which was purchased from Sigma Aldrich. Deionized water was used to dilute the Pd solution, such that the volume of Pd containing solution was the same as the pore volume of the zeolite, and to achieve 1 wt.% or 0.5 wt.% of Pd. Immediately following the calcination to make the proton form, the $Pd(NO_3)_2$ solution was drop wise added with rigorous stirring and mixing. After Pd was introduced, the same calcination process was repeated.

A slurry was prepared to washcoat 300 cpsi cordierite monolith, which contained a large portion of freshly calcined catalyst powder, deionized water and an alumina colloidal binder solution purchased from Nyacol Nano Technologies, Inc. The zeolite-to-alumina mass ratio was 8:1. Before washcoating, the slurry was agitated and ball-milled with ceramic beads overnight. Monolithic cordierite substrates were trimmed to fit a 0.5-inch ID quartz tube, then dipped into the prepared slurry and dried with flowing air at 120 °C. After drying, the mass of the wash-coated monolith cores was measured to calculate the washcoat loading, and this process was repeated several times until a 1g/in^3 washcoat loading was achieved. Finally, the three-step calcination process was repeated.

The freshly calcined catalysts were hydrothermally aged by exposing the catalysts in either powder form or monolith form to a gas mixture of 10% O_2 and 10% H_2O balanced by N_2 for 16 hours at a space velocity of 30,000 hr^{-1}. The monolith equivalent space velocity of powder form reactor was maintained at 30,000 hr^{-1} assuming uniform powder distribution on the same monolith substrate with a 1g/in^3 washcoat loading. The hydrothermal aging temperature for the samples evaluated ranged from 600 to 800 °C with a 50 °C increment. Samples are labeled as Pd/BEA-600HTA, Pd/BEA-650HTA and so on.

5.2.2 Catalyst Characterization

Crystallinity of the catalysts after calcination and hydrothermal aging were investigated via X-ray diffraction (XRD) using a PANalytical X’Pert Pro multi-purpose diffractometer. Cu Kα X-ray source and a vertical circle theta:theta goniometer with an incident radius of 240 mm were used. Scanning transmission electron micrographs (STEM) were collected on a FEI Titan transmission electron microscope in HAADF mode. H_2 temperature programmed reduction (H_2-TPR) data were collected using a Micromeritics AutoChem 2920 system.

5.2.3 Catalyst Evaluation

The low-temperature NOx storage experiments were conducted in a 0.5-inch quartz tube reactor horizontally placed in a tubular furnace purchased from Thermo Fisher. To simulate diesel exhaust conditions, a gas mixture of 10% O_2, 5% H_2O and 200 ppm of NO was chosen as a basic gas composition, and 200 ppm of CO were added in some cases to evaluate NO and CO co-adsorption. All the gases were balanced by N_2. All gas components were purchased from Praxair except N_2 which was purified from compressed air by a Parker N_2 generator. H_2O was injected using a Bronkhorst controlled evaporator mixer (CEM). The total flowrate was controlled to maintain a 30,000 hr^{-1} space velocity under standard conditions. 80 °C was chosen as the adsorption temperature, consistent with previous work[42]. Before exposing the catalysts to the simulated exhaust described above, the samples were exposed to 10% O_2 and balance N_2. Low-temperature NOx adsorption experiments were initiated by a simultaneous switch of two four-way valves located upstream and downstream of the reactor. The reactor temperature was measured by a K-type thermocouple inserted into the reactor along the axial direction at the downstream end of the monolith. Reactor outlet gas composition was measured and recorded by an MKS IR analyzer, MG2030. After the PNA was saturated, a subsequent temperature programmed desorption (TPD) experiment was initiated by linearly ramping the reactor temperature from 80 to 600 °C with a ramp rate of 100 °C/min and the same gas composition as the adsorption phase. When the reactor temperature reached 600 °C, the gas composition was switched to 10% O_2 balanced by N_2.

Between each low-temperature NOx storage experiment, a high-temperature oxidative pretreatment was conducted by flowing 10% O_2 balanced by N_2 at 600 °C for 45 min if not otherwise specified. H_2 pretreatment and NO_2 pretreatment were also conducted in some cases by flowing 5% H_2 balanced by N_2 or 1000 ppm of NO_2, 500 ppm of NO and 10% of O_2 at 600 °C. Samples that have gone through H_2 and NO_2 pretreatments are labeled as H_2 reduced and NO_2

pretreated, respectively. The sequence of the basic set of experiments is described in Table 5.1. More details of specific experiments are listed in Table 5.2.

Table 5.1 Experiment protocols used to quantify NOx storage capacity for each hydrothermally treated sample after hydrothermal treatment

Experiment	Exhaust composition	Temperature Profile
O_2 treatment	10% O_2 and N_2 balance	600 °C
Test cycle 1	10% O_2, 5% H_2O, 200 ppm NO and N_2 balance	10 C/min ramp to 600 °C
O_2 treatment	10% O_2 and N_2 balance	600 °C
Test cycle 2	10% O_2, 5% H_2O, 200 ppm NO, 200 ppm CO and N_2 balance	10 C/min ramp to 600 °C
O_2 treatment	10% O_2 and N_2 balance	600 °C
Test cycle 3	10% O_2, 5% H_2O, 200 ppm NO, 200 ppm CO and N_2 balance	10 C/min ramp to 600 °C
O_2 treatment	10% O_2 and N_2 balance	600 °C
Test cycle 4	10% O_2, 5% H_2O, 200 ppm NO, 200 ppm CO and N_2 balance	10 C/min ramp to 600 °C
O_2 treatment	10% O_2 and N_2 balance	600 °C
Test cycle 5	10% O_2, 5% H_2O, 200 ppm NO and N_2 balance	10 C/min ramp to 600 °C
H_2 treatment	5% H_2 and N_2 balance	600 °C
Test cycle 6	10% O_2, 5% H_2O, 200 ppm NO and N_2 balance	10 C/min ramp to 600 °C
O_2 treatment	10% O_2 and N_2 balance	600 °C
Test cycle 7	10% O_2, 5% H_2O, 200 ppm NO and N_2 balance	10 C/min ramp to 600 °C

Table 5.2 NO adsorption and desorption experiment protocol used to test the CO-exposed and NO_2-regenerated sample after hydrothermal treatment

Experiment	Exhaust composition	Temperature profile
O_2 treatment	10% O_2 and N_2 balance	600 °C
Test cycle 1	10% O2, 5% H2O, 200 ppm NO and N_2 balance	10 C/min ramp to 600 °C
O_2 treatment	10% O_2 and N_2 balance	600 °C
Test cycle 2	10% O_2, 5% H_2O, 200 ppm NO, 200 ppm CO and N_2 balance	10 C/min ramp to 200 °C
O_2 treatment	10% O_2 and N_2 balance	600 °C
NO_2 treatment	800 ppm NO_2, 800 ppm NO, 10% O_2 and N_2 balance	600 °C
Test cycle 3	10% O_2, 5% H_2O, 200 ppm NO and N_2 balance	10 C/min ramp to 600 °C
H_2 treatment	5% H_2 and N_2 balance	600 °C
Test cycle 4	10% O_2, 5% H_2O, 200 ppm NO and N_2 balance	10 C/min ramp to 600 °C
O_2 treatment	10% O_2 and N_2 balance	600 °C
Test cycle 5	10% O_2, 5% H_2O, 200 ppm NO and N_2 balance	10 C/min ramp to 600 °C

5.3 Results and discussion

5.3.1 X-Ray diffraction

XRD powder diffraction patterns of freshly calcined Pd/BEA samples as well as an H/BEA sample are shown in **Figure 5.1 A**. Apart from the BEA morphology being observed in all three samples, PdO and Pd particles coexist[44] in Pd impregnated samples even at 0.5 wt.% Pd loading, which indicates that a significant portion of Pd introduced during catalyst synthesis has not been ion-exchanged. Researchers from PNNL looked into the pH effect on the ion-exchange level when impregnating Pd into small pore zeolites, and concluded that higher pH and ammonium form zeolites are key to atomic dispersion of Pd[40]. An acidic environment was maintained when preparing the catalysts for this NOx storage study, which may explain the low ion-exchange level and existence of Pd/PdO particles.

Pd/BEA PNAs were exposed to high temperatures to evaluate hydrothermal stability. Previous research has shown that exposing BEA zeolites to high water content at high enough temperature can severely damage zeolite crystallinity via dealumination[45]. As is shown in **Figure 5.1 B**, the main BEA feature at around $2\theta = 22.5°$ remains even with the hydrothermal aging temperature as high as 800 °C, demonstrating hydrothermal stability to that temperature. Since during the NOx adsorption and TPD experiments the temperature never exceeded 650 °C, it is assumed that the BEA morphology remained throughout. With the increase in hydrothermal aging temperature, the Pd(111) and Pd(200) features grew and the PdO(101) feature shrunk. This could be due to the sintering of the extra-framework Pd and Pd ion exchanging during the hydrothermal aging process, which consumes PdO to facilitate protonalysis[46].

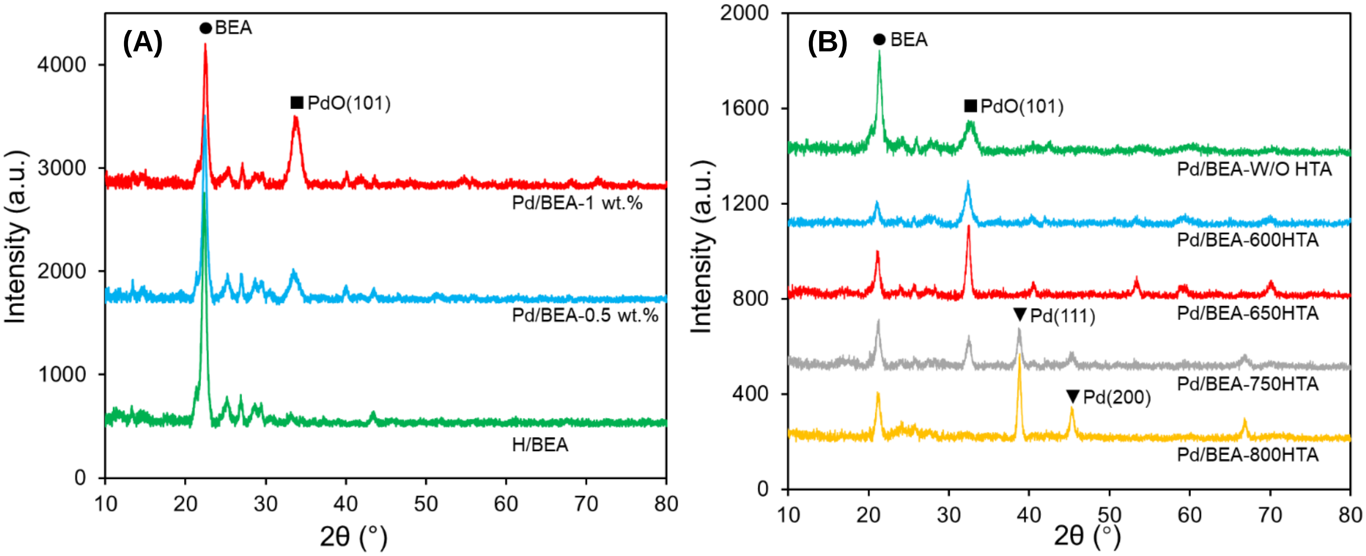

Figure 5.1 Powder form XRD patterns of H-BEA(A.Green), 0.5 wt.% Pd/BEA (A.Cyan), and 1 wt.% Pd/BEA (A.Red), and hydrothermally treated 1 wt.% Pd/BEA samples with different hydrothermal aging temperatures: 500C freshly calcined (B.Green), 600C hydrothermally aged (B.Cyan), 650C hydrothermally aged (B.Red), 750C hydrothermally aged (B.Grey), 800C hydrothermally aged (B.Yellow) at different temperatures

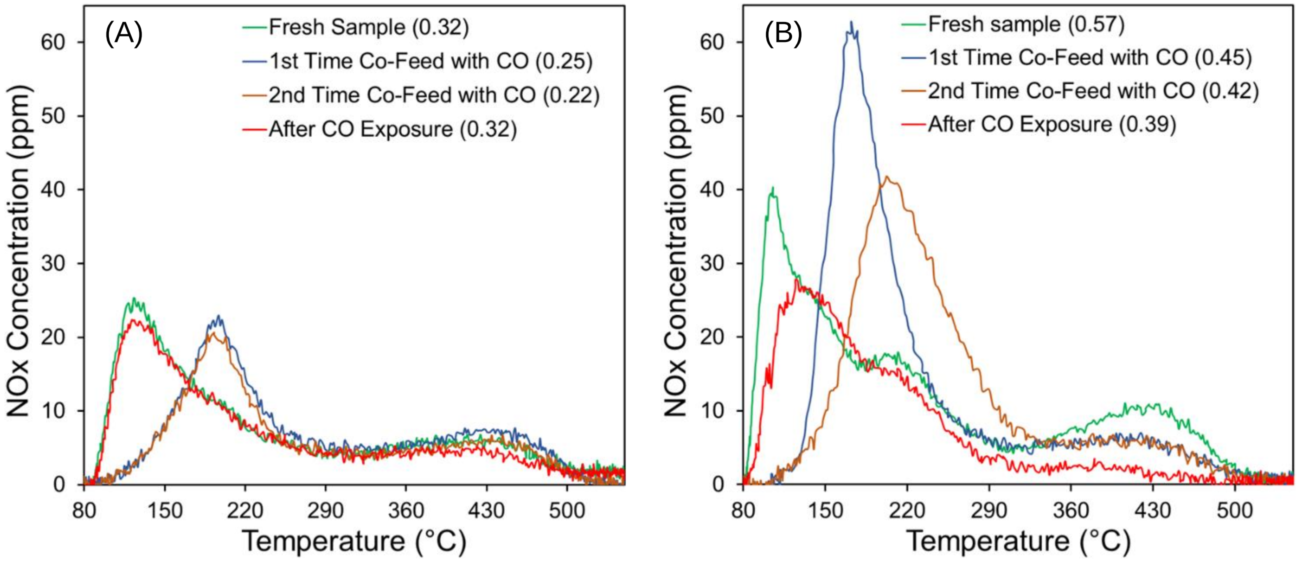

Figure 5.2 NOx TPD profiles of consecutive NOx storage test cycles. Fresh sample (Green) and After CO Exposure (Red) storage tests are performed with 200 ppm NO, 5% H_2O and 10% O_2. 1st Time Co-Feed with CO (Blue) and 2nd Time Co-Feed with CO (Brown) tests are performed with 200 ppm CO, 200 ppm NO, 5% H_2O and 10% O_2. Samples used are **(A)** Pd-BEA-600HTA, **(B)** Pd-BEA-750HTA

5.3.2 NO adsorption and H_2-TPR

Selected NOx TPD profiles from a series of experiments following the testing protocol described in the experimental section are shown in **Figure 5.2**. TPD data sets for a 600 °C hydrothermally aged sample (Pd/BEA-600HTA) and a 750 °C hydrothermally aged sample (Pd/BEA-750HTA) are plotted in **Figure 5.2 A** and **Figure 5.2 B**, respectively. The desorption profile of fresh Pd/BEA-600HTA when CO is absent in the gas stream consists of a major peak at around 120 °C, a shoulder at around 200 °C and a minor feature at around 430 °C. The NOx-to-Pd ratio was calculated based on the amount adsorbed during the NOx adsorption phase. The 0.32 ratio obtained is low compared to other reported values[29,47]. Furthermore, the NOx desorption temperature is not satisfactory with most of the NOx desorbing below 200 °C. However, when CO was introduced into the gas stream, the desorption feature at 120 °C shifted to 200 °C and the minor feature at around 430 °C remained unaffected. This behavior has been previously reported in multiple Pd-zeolite systems, but the actual mechanism has yet to be determined[34,42,48]. Two of the most convincing mechanisms are the reduction of Pd strengthening the NO-Pd bond and the formation of a NO-Pd(II)-CO like surface intermediate[41,47,49]. Apart from the desorption temperature shift, the addition of CO into the gas stream also led to a slight decrease in NOx uptake. The first repetition of the NO and CO co-adsorption experiment did not show a significant difference other than a further decreased NOx-to-Pd ratio. Further repetition of the NO and CO co-adsorption experiments were conducted, of which the TPD profiles are not shown here because no changes were observed, and there were no more changes in the NOx-to-Pd ratio. Lastly, a NO adsorption was performed in the absence of CO, after the consecutive NO and CO co-adsorption experiments, which is labeled in **Figure 5.2 A** as “After CO Exposure”. The TPD profile has the same desorption characteristics as those prior to CO exposure, indicating no changes of storage site distribution before and after CO exposure, i.e. the changes observed with CO exposure were reversible in this case.

For the sample that was hydrothermally aged at a higher temperature, Pd/BEA-750HTA sample, prior to CO exposure, “Fresh Sample”, there is a significant increase in NOx adsorption capacity relative to Pd/BEA-600HTA. The NOx-to-Pd ratio based on the amount adsorbed, listed in the figure, is 0.57 whereas after 600°C hydrothermally aging it was 0.32. Furthermore, peak areas at 100-120 °C and 430 °C in the TPD profile increased. A similar hydrothermal aging effect has been reported in the literature for Pd/SSZ-13, where Ryou et al. showed that after hydrothermal aging a new NOx desorption feature appeared with a significant increase in NOx storage capacity[39]. It was concluded that the hydrothermal treatment helped disperse the Pd within the system and thus boosted the ion-exchange level[50]. Although Pd/BEA is a different system, the natures of the Pd species are believed to be similar, which will be supported in the discussion of H_2-TPR results later. Following the same testing protocol as that for Pd/BEA-600HTA, two consecutive NO and CO co-adsorption experiments were conducted. As shown in **Figure 5.2 B**, when CO was present, the desorption temperature of the more weakly bonded species, again, shifted to higher temperature. However, the desorption feature originally located at 180 °C appeared to broaden and its peak temperature shifted to 220 °C. Subsequent repetitions exhibited no variation. After NO and CO co-adsorption a NO adsorption probe experiment was used to see if CO changed the distribution of storage sites. Interestingly, even after only two adsorption experiments with CO, there was a loss of NOx storage capacity as evidenced by the elimination of peak at 430 °C and the decreased peak area at 100-120 °C. Therefore, unlike the Pd/BEA-600HTA sample, there was an irreversible change after CO exposure.

Atomically dispersed Pd cationic species are believed to be the most efficient NOx storage sites[29,40,41,49]. From the comparison of the 600 and 750 °C hydrothermally treated samples, the 750 °C treatment provided an initially higher ion-exchange level, however, the increase in NOx storage capacity was vulnerable to CO exposure, as the NOx storage capacity decreased after 2 cycles of NO and CO co-adsorption and TPD. The NO probe experiment after the CO exposure TPD profiles of both Pd/BEA-600HTA and Pd/BEA-750HTA appear similar to the fresh profiles, although the amount of NOx adsorbed on the Pd/BEA-750HTA decreased. One of the possible reasons to explain the decreased ion-exchange level is the CO reduction of Pd^{2+} species leading to Pd particle formation and growth, which has been reported by Ryou et al[43]. Although all the experiments here were conducted under lean conditions, complete CO oxidation is not achieved >200 °C, as is shown in **Fig. S3**. Therefore, during the adsorption phase and TPD to at least 200 °C, CO is available to reduce Pd^{2+} species.

H_2-TPR was used to understand the nature of the Pd. Two consecutive H_2-TPR runs were performed on the 600 and 750 °C hydrothermally aged samples and the data are plotted in **Figure 5.3 A**. TPR profiles of both Pd/BEA-600HTA and Pd/BEA-750HTA fresh samples (solid lines) consist of two main features in the low temperature region: a negative peak at around 60 °C due to the decomposition of PdH (H_2 is generated) and a positive peak at around 100 °C associated with the reduction of Pd^{2+} to metallic Pd (H_2 is consumed). The Pd^{2+} reduction feature of Pd/BEA-600HTA is not as significant as the Pd^{2+} reduction feature of Pd/BEA-750HTA. This result supports the conclusion drawn from the NOx adsorption and TPD comparison, where the initial ion-exchange level of Pd/BEA-750HTA is higher. In the high temperature region shown in **Figure 5.3 B**, another reduction feature at 400 °C and a shoulder at 550 °C are observed for both Pd/BEA-750HTA and Pd/BEA-600HTA samples. Since these are at a higher temperature, we speculate that these features are attributed to the reduction of Pd^+. Notably, the peak area of the Pd^+ reduction features for both Pd/BEA-750HTA and Pd/BEA-600HTA samples are similar, which suggests the same amount of Pd^+ exists in both samples.

After H_2-TPR, Pd cationic species are reduced to metallic Pd and it has been reported that a high temperature oxidative pretreatment is able to regenerate Pd cations in Pd/NaY after reduction[51,52]. To assess similarity with the Pd/BEA system, H_2-TPR was repeated after an oxidative pretreatment at 600 °C, and these results are shown as dashed lines in **Figure 5.3**. The Pd^{2+} reduction feature of both samples disappeared and there was a more significant PdH decomposition peak in both cases. This suggests that after H_2 reduction at 600 °C, the reduced Pd^{2+} was not regenerated by the oxidative pretreatment and based on the larger PdH peak, bigger Pd particles formed. However, the Pd^+ reduction features for both samples after the oxidative pretreatment are identical to the ones of the fresh samples, indicating regeneration of Pd^+. Although H_2 reduction is different from CO reduction in terms of their corresponding reaction mechanisms, CO has been reported to be a better reductant in reducing Pd in Pd/SSZ13, i.e. it reduces Pd and causes particle agglomeration more easily, due to the enhanced mobility of Pd-carbonyl species[43].

To further investigate the characteristics of this irreversible degradation mode, Pd/BEA samples hydrothermally aged at other temperatures were also evaluated. NOx-to-Pd ratios before and after CO exposure are quantified and shown in **Figure 5.4** as “Fresh sample” and “CO exposed”**.** All samples except Pd/BEA-600C suffer from the irreversible degradation caused by CO exposure and their post-CO exposure NOx-to-Pd ratios are all around 0.3. It is also worth mentioning that the NOx-to-Pd ratios of the fresh samples followed the same trend reported in the

Pd/SSZ-13 system, thus it is believed that the hydrothermal aging effect on Pd distribution is consistent within these two different Pd-zeolite systems.

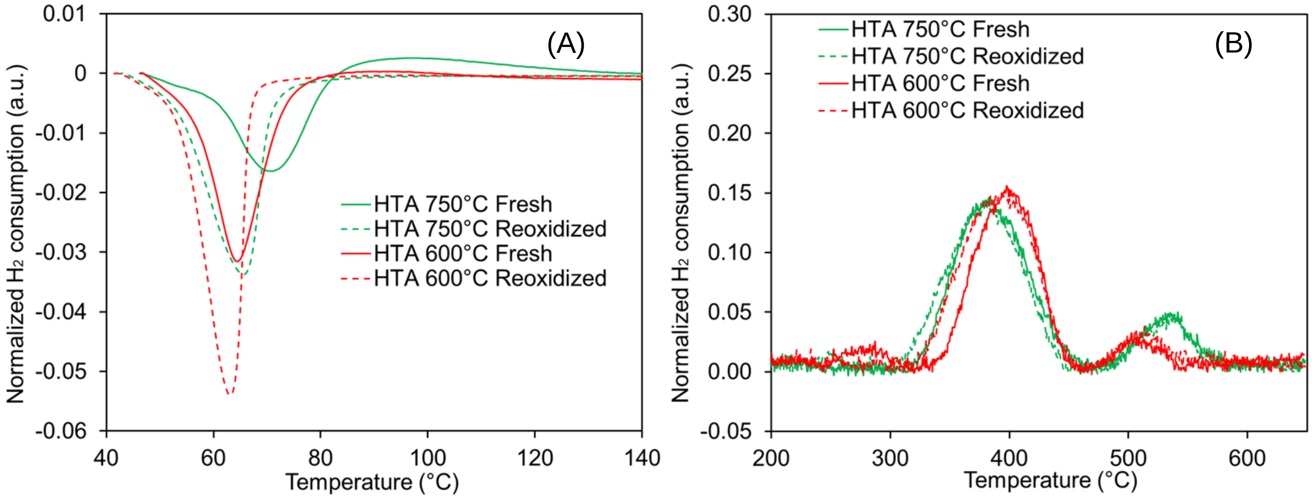

Figure 5.3 H_2-TPR profile of samples hydrothermally aged at 600 and 750 °C and immediate repetition after a reoxidation pretreatment.

Apart from fresh and CO-exposed samples, the NOx storage capacity of H_2-reduced and O_2-reoxidized samples were also measured and shown in **Figure 5.4**. Interestingly, H_2 reduced samples store the least NOx and an oxidative pretreatment regenerated the NOx storage capacity to post-CO exposure levels. This quantification result is consistent with the H_2-TPR result where loss of Pd^{2+} and regeneration of Pd^{+} are observed when comparing the fresh and reoxidized TPR profiles. In other words, H_2 pretreatment at 600 °C reduced Pd^{+} leading to a further decrease of the NOx storage capacity, which can be regenerated by an O_2 pretreatment at 600 °C, shown as H_2-reduced and Re-oxidized in Fig. 4. Interestingly, though the total loss of cationic Pd species was observed in H_2O free H_2-TPR, a total loss in NOx storage capacity was not observed. This indicates that as soon as the catalyst is exposed to the O_2 and H_2O containing gas stream after H_2 reduction at 600 °C, part of the NOx storage capacity can be regenerated. Pd^{2+} was reduced by CO during NOx adsorption and TPD experiments at temperatures lower than 200 °C. The regeneration of Pd^{+} is facilitated with the presence of H_2O and O_2.

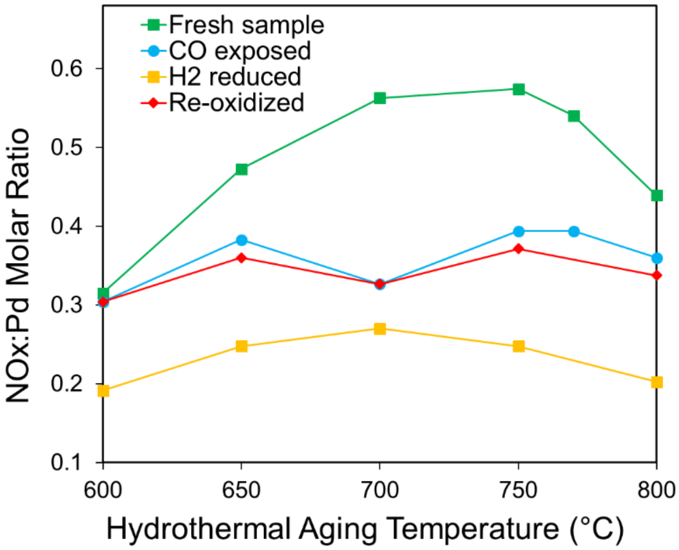

Figure 5.4 NOx: Pd ratio calculated from low temperature NOx uptake over samples aged at different temperatures.

Although it has been reported that CO is able to readily reduce Pd cations[53] and it has been proven that high temperature H_2 reduction leads to loss of cations[54], the link between the reduced NOx storage capacity and the loss of Pd^{2+} as the CO vulnerable storage sites has not been established. Moreover, whether the loss of Pd^{2+} happens at elevated temperature where CO oxidation has achieved 100% conversion or at low temperatures where CO oxidation has not lit off remains unresolved. This can be an important factor in determining the after-treatment design, as the first case, CO completely converted, can be avoided by integrating a diesel oxidation catalyst (DOC). However, the latter case, CO available, cannot because of the limited CO oxidation activity of DOCs at low temperatures. To further look into the mechanism of this irreversible loss of NOx storage degradation, a 750 °C hydrothermally treated sample was exposed to CO at 80 °C for 20 minutes followed by a temperature programmed desorption (TPD) to 200 °C, where the adsorbed CO is all released, after which an NO adsorption followed by TPD experiment was performed. The TPD profile is shown in **Figure 5.5** labeled as “CO TPD to 200 C”. Also, a CO-exposed Pd/BEA-750HTA sample was exposed to a regeneration gas mixture consisting of 1500 ppm NO_2, 800 ppm NO and 15% of O_2 balanced by N_2, which has been reported to selectively regenerate Pd^{2+} from PdOx particles via accelerated protonalysis[46]. After a 24-hour NO_2 regeneration, the same NO adsorption/TPD probe experiment was again performed, and the TPD profile is shown as “NO2 regenerated” in **Figure 5.5** together with TPD profiles of fresh and CO-exposed Pd/BEA-750HTA samples. Details of the experiment procedure are listed in **Table 5.2**. H_2-TPR profiles from all four different states are also shown in **Figure 5.6** for comparison. CO exposure and NO_2 regeneration only affected the desorption features at 100 and 430 °C whereas the peak at 200 °C remained unaffected. Their corresponding Pd^{2+} reduction features in H_2-TPR profiles are proportional to the NOx uptake measured from NO adsorption experiments. This supports the hypothesis that the loss of NOx storage capacity is explicitly attributed to the irreversible loss of Pd^{2+} caused by CO exposure, more importantly, CO exposure at temperatures no higher than 200 °C already led to Pd^{2+} reduction. However, CO nears 100% conversion at ~200 °C and therefore the reduction of Pd^{2+} only occurs during the adsorption phase and the initial part of the TPD. Hence, for one adsorption and desorption cycle, a limited time is available to facilitate the degradation, which is why changes in the NOx storage capacity as well as the NOx TPD profile were observed during the first repeats of the NO and CO co-adsorption experiments, and eventually reached a stable state.

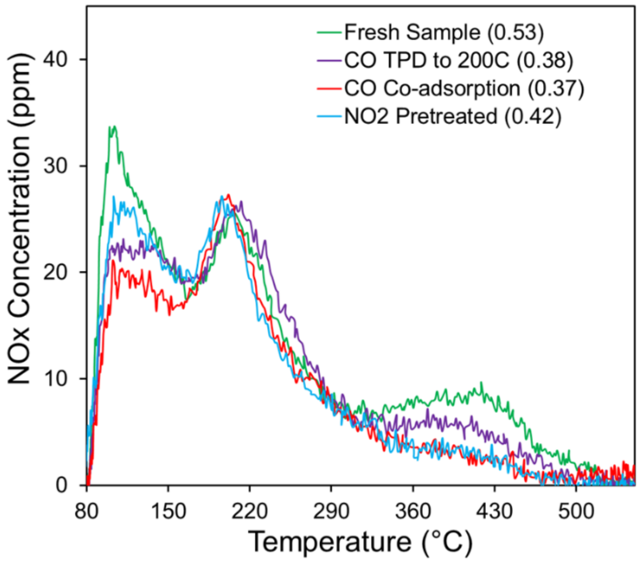

Figure 5.5 NOx TPD profile of the fresh, degraded, and regenerated Pd-BEA-750HTA sample

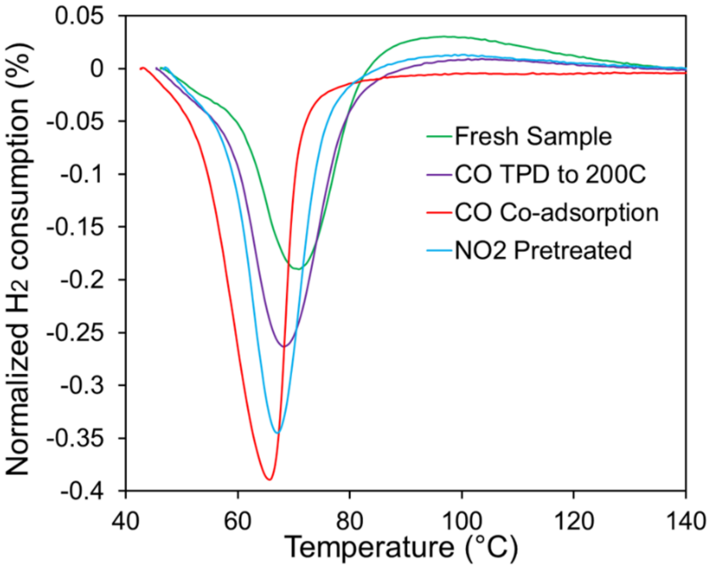

Figure 5.6 H_2-TPR profile of fresh, degraded, and regenerated Pd-BEA-750HTA sample

As discussed previously, NOx TPD profiles of almost all fresh samples consist of three NOx desorption features indicating at least three different type of surface intermediates or 3 different storage sites. NO interacting with/adsorbing onto Bronsted acid sites can be eliminated due to the presence of H_2O[29]. Moreover, Pd and PdOx particles are believed to be unable to uptake NOx[55]. Therefore, Pd cationic species are assumed to be responsible for low temperature NOx storage in our Pd/BEA system, of which, a certain type of Pd^{2+} is vulnerable to CO exposure even under lean conditions, and Pd^{+} can be easily regenerated with the presence of H_2O and O_2 even at 80 °C. To assess the identity and the structure of the CO vulnerable Pd^{2+} species, the amount of H_2 associated with the Pd^{2+} reduction feature was quantified from H_2-TPR results as is the amount of stored NOx associated with the vulnerable Pd^{2+} species from NOx-TPD results. **Figure 5.7** suggests that they follow a linear relationship with a NOx-to-Pd ratio of 0.5.

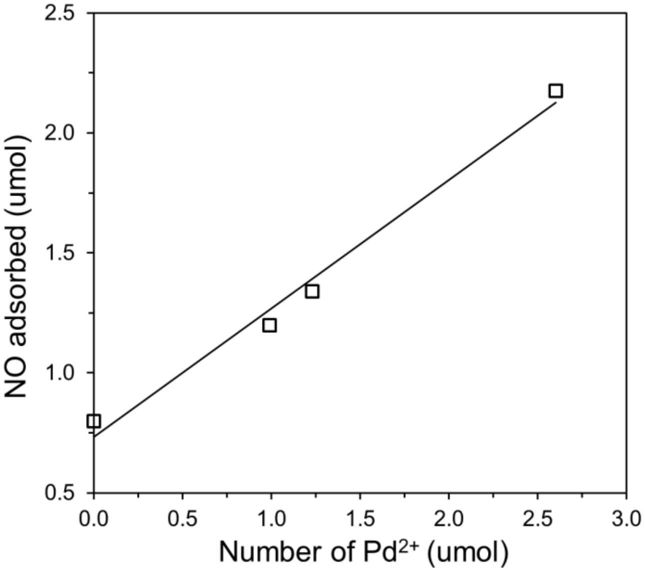

Figure 5.7 NO adsorbed as a function of the number of Pd^{2+}

5.3.3 HAADF-STEM

In addition to the characterization of Pd/BEA samples by H_2-TPR, TEM was used to image the unexchanged Pd nanoparticles that reside on the external surface and outside the zeolite cages. As shown in **Figure 5.8**, STEM images of Pd/BEA calcined at 500 °C **(A)**, hydrothermally aged at 750 °C **(B)**, H_2 reduced at 600 °C **(C)**, and CO-exposed Pd/BEA **(D)** all show the existence of Pd particles. Due to the incomplete ion-exchange of the freshly calcined sample, Pd particles are present throughout the selected area in **Figure 5.8 A**. After the calcination process, the average particle size was around 5 nm, and based on the NOx adsorption and H_2 TPR results, most of the Pd particles locate on the zeolite external surface due to the limited pore opening of BEA structure. The average Pd particle size increased after hydrothermal aging at 750 °C, as shown in **Figure 5.8 B**. This may appear to contradict the increase in the NOx storage capacity, but in fact, some Pd can diffuse into the zeolite and reach a Bronsted acid site to facilitate protonalysis, which results in a higher ion-exchange level[38,39,46]. Therefore, Pd particle agglomeration and ion-exchange via protonalysis happened simultaneously during hydrothermal aging. A NOx storage capacity increase has also been observed for Pd/SSZ-13[39,50] and protonalysis was mechanistically proven for a Pd/NaY model catalyst[46]. Notably, protonalysis is an activated and particle size dependent process, that is, if the Pd particle size is too large the activation energy of the protonalysis process will be too high to compete with particle agglomeration[46]. However, particle agglomeration was not observed for Pd/SSZ-13 and Pd/ZSM-5 and a possible explanation could be the larger pore opening of Pd/BEA allowing bigger particles to form. The STEM image of a H_2-reduced Pd/BEA sample is shown in **Figure 5.8 C**, and interestingly, a significant amount of Pd particles ranging from 2-3 nm are evident. This could be due to the reduction of atomically dispersed Pd cationic species and insufficient time for particles to agglomerate. Finally, a STEM image of a CO-exposed Pd/BEA sample is shown in **Figure 5.8 D**, and significantly larger Pd particles are evident with an average particle size around 12 nm. CO, as a key component of diesel exhaust, has been proven to accelerate Pd particle agglomeration by itself under rich conditions[54]. Notably, for all the NO and CO co-adsorption and TPD experiments, near 100% CO conversion was achieved at temperatures ~200 °C, in other words the highest CO exposure temperature is around 200 °C. Therefore, the comparison of **Figure 5.8 D** and **Figure 5.8 B** suggests that during the NO and CO co-adsorption experiment, Pd particles becomes significantly larger. Meanwhile, H_2-TPR results from the same samples showed a decreased amount of Pd^{2+} after CO exposure. This suggests a two-step process, the reduction of Pd^{2+} by CO generating small Pd particles and then these small particles agglomerate preventing Pd from being ion-exchanged back into the zeolite framework. Herein, we attribute the irreversible loss of the NOx storage capacity to this Pd redistribution process.

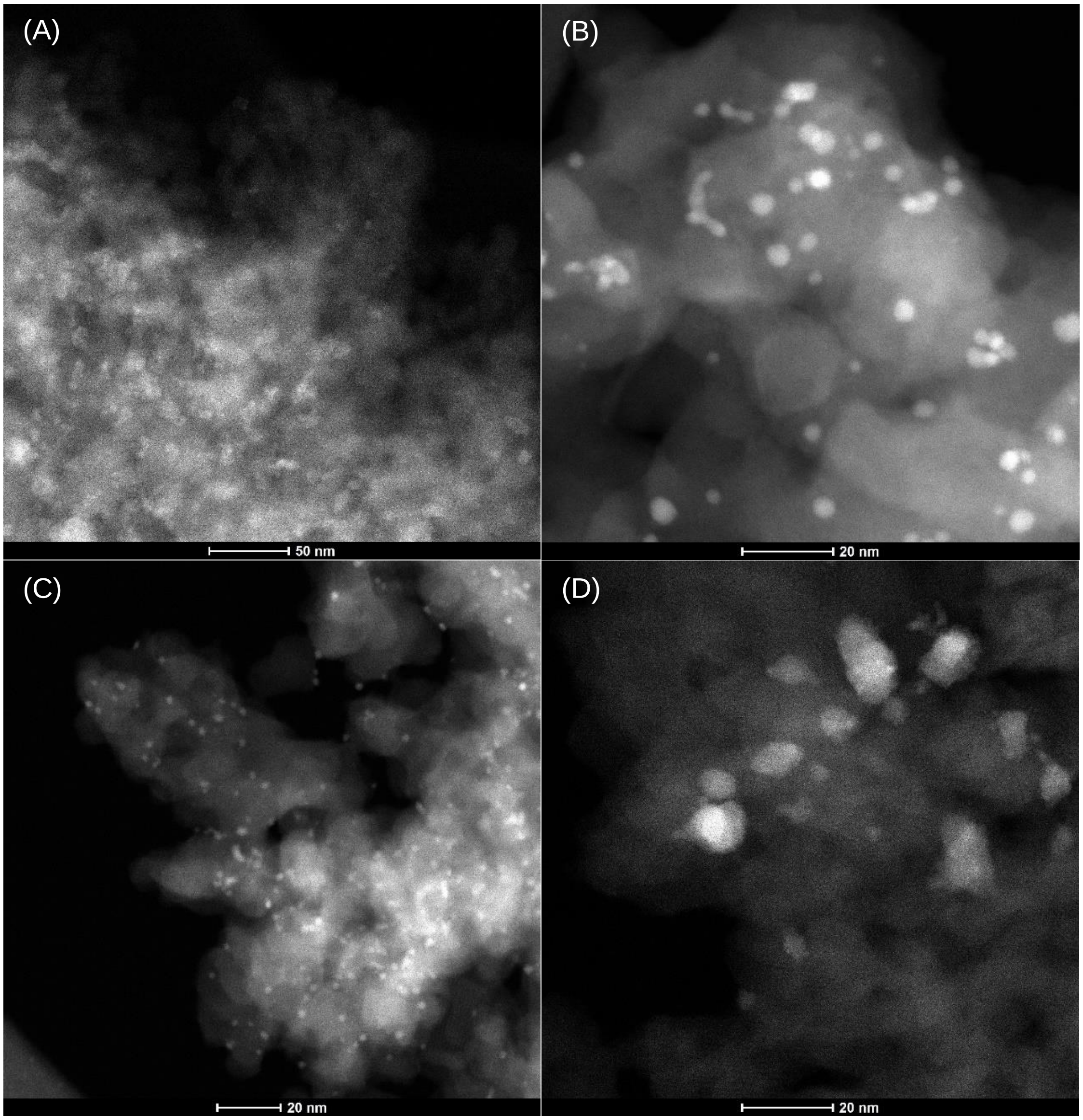

Figure 5.8 STEM images of **A.** a freshly calcined Pd/BEA; **B.** Pd/BEA-750HTA after O_2 pretreatment at 600 °C; **C.** Pd/BEA-750HTA after H_2 pretreatment at 600 °C; **D.** Pd/BEA-750HTA after CO exposure.

5.4 Conclusions

Pd/BEA passive NOx adsorbers were evaluated for low-temperature NOx adsorption and NOx release, using adsorption and TPD experiments. The results revealed the mechanism of an irreversible degradation mode caused by CO exposure. H_2-TPR and the TPD experiments show that different Pd cationic species exist within the Pd/BEA system and are NOx storage sites, part of which are also vulnerable to degradation via CO exposure. H_2-TPR and STEM imaging showed that CO exposure at temperatures lower than 200 °C leads to an irreversible loss of Pd^{2+} due to a two-step Pd^{2+} reduction and particle agglomerating process. And CO plays an important role in accelerating the particle agglomeration. We speculate that Pd^{+} also contributes to NOx storage and is less vulnerable to CO or reductant as the reduction of Pd^{+} to Pd^{0} can be reversed. The irreversible NOx storage degradation can be partially regenerated by a long duration NO_2 exposure. Overall, to slow PNA degradation via CO exposure, a highly active DOC is necessary, additionally, NO_2 generated from DOC can also lead to regeneration of NOx storage via accelerated protonalysis.

5.5 References

[1] S. Matsumoto, Recent advances in automobile exhaust catalysts, Catal. Today. 90 (2004) 183–190.

[2] A.M. Beale, F. Gao, I. Lezcano-Gonzalez, C.H.F. Peden, J. Szanyi, Recent advances in automotive catalysis for NO x emission control by small-pore microporous materials, Chem. Soc. Rev. 44 (2015) 7371–7405.

[3] H.C. Frey, Trends in onroad transportation energy and emissions, J. Air Waste Manage. Assoc. 68 (2018) 514–563.

[4] T. Johnson, Vehicular Emissions in Review, SAE Int. J. Engines. 9 (2016) 2016-01–0919.

[5] B.T. Johnson, Diesel Engine Emissions and Their Control, Platin. Met. Rev. 52 (2008) 23–37.

[6] M. V. Twigg, Progress and future challenges in controlling automotive exhaust gas emissions, Appl. Catal. B Environ. 70 (2007) 2–15.

[7] F. Gao, Y. Wang, M. Kollár, N.M. Washton, J. Szanyi, C.H.F. Peden, A comparative kinetics study between Cu/SSZ-13 and Fe/SSZ-13 SCR catalysts, Catal. Today. 258 (2015) 347–358.

[8] P. Forzatti, I. Nova, E. Tronconi, New “Enhanced NH 3 -SCR” Reaction for NOx Emission Control, Ind. Eng. Chem. Res. 49 (2010) 10386–10391.

[9] D. Wang, Y. Jangjou, Y. Liu, M.K. Sharma, J. Luo, J. Li, K. Kamasamudram, W.S. Epling, A comparison of hydrothermal aging effects on NH 3 -SCR of NO x over Cu-SSZ-13 and Cu-SAPO-34 catalysts, Appl. Catal. B Environ. 165 (2015) 438–445.

[10] Y. Jangjou, Q. Do, Y. Gu, L.-G. Lim, H. Sun, D. Wang, A. Kumar, J. Li, L.C. Grabow, W.S. Epling, Nature of Cu Active Centers in Cu-SSZ-13 and Their Responses to SO 2 Exposure, ACS Catal. 8 (2018) 1325–1337.

[11] J.A. Loiland, R.F. Lobo, Oxidation of zeolite acid sites in NO/O 2 mixtures and the catalytic properties of the new site in NO oxidation, J. Catal. 325 (2015) 68–78.

[12] H.C. Frey, Trends in onroad transportation energy and emissions, J. Air Waste Manage. Assoc. 68 (2018) 514–563.

[13] C. Sharp, C.C. Webb, S. Yoon, M. Carter, C. Henry, Achieving Ultra Low NOX Emissions Levels with a 2017 Heavy-Duty On-Highway TC Diesel Engine - Comparison of Advanced Technology Approaches, SAE Int. J. Engines. 10 (2017) 2017-01–0956.

[14] M. Moliner, A. Corma, From metal-supported oxides to well-defined metal site zeolites: the next generation of passive NO x adsorbers for low-temperature control of emissions from diesel engines, React. Chem. Eng. (2019).

[15] J. Lee, J.R. Theis, E.A. Kyriakidou, Vehicle emissions trapping materials: Successes, challenges, and the path forward, Appl. Catal. B Environ. 243 (2019) 397–414.

[16] V. Schmeisser, M. Weibel, L. Sebastian Hernando, I. Nova, E. Tronconi, M.P. Ruggeri, Cold Start Effect Phenomena over Zeolite SCR Catalysts for Exhaust Gas Aftertreatment, SAE Int. J. Commer. Veh. 6 (2013) 190–199.

[17] V. Schmeisser, M. Weibel, L. Sebastian Hernando, I. Nova, E. Tronconi, M.P. Ruggeri, Cold Start Effect Phenomena over Zeolite SCR Catalysts for Exhaust Gas Aftertreatment, SAE Int. J. Commer. Veh. 6 (2013) 2013-01-1064.

[18] Y. Gu, W.S. Epling, Passive NOx adsorber: An overview of catalyst performance and reaction chemistry, Appl. Catal. A Gen. 570 (2019) 1–14.

[19] H.-Y. Chen, D. Liu, E. Weigert, L. Cumaranatunge, K. Camm, P. Bannon, J. Cox, L. Arnold, Durability Assessment of Diesel Cold Start Concept (dCSC^{TM}) Technologies, SAE Int. J. Engines. 10 (2017) 2017-01–0955.

[20] H.-Y. Chen, S. Mulla, E. Weigert, K. Camm, T. Ballinger, J. Cox, P. Blakeman, Cold Start Concept (CSC^{TM}): A Novel Catalyst for Cold Start Emission Control, SAE Int. J. Fuels Lubr. 6 (2013) 2013-01–0535.

[21] S. Jones, Y. Ji, A. Bueno-Lopez, Y. Song, M. Crocker, CeO2-M2O3 Passive NO x Adsorbers for Cold Start Applications, Emiss. Control Sci. Technol. 3 (2017) 59–72.

[22] Y. Ji, D. Xu, S. Bai, U. Graham, M. Crocker, B. Chen, C. Shi, D. Harris, D. Scapens, J. Darab, Pt- and Pd-Promoted CeO 2 –ZrO 2 for Passive NOx Adsorber Applications, Ind. Eng. Chem. Res. 56 (2017) 111–125.

[23] S. Jones, Y. Ji, M. Crocker, Ceria-Based Catalysts for Low Temperature NO x Storage and Release, Catal. Letters. 146 (2016) 909–917.

[24] Y. Ji, S. Bai, M. Crocker, Al2O3-based passive NOx adsorbers for low temperature applications, Appl. Catal. B Environ. 170–171 (2015) 283–292.

[25] J.R. Theis, C.K. Lambert, An assessment of low temperature NOx adsorbers for cold-start NOx control on diesel engines, Catal. Today. 258 (2015) 367–377.

[26] J.R. Theis, C.K. Lambert, Mechanistic assessment of low temperature NO x adsorbers for cold start NO x control on diesel engines, Catal. Today. 258 (2017) 367–377.

[27] J.R. Theis, C. Lambert, The Effects of CO, C_2H_4, and H_2O on the NO_x Storage Performance of Low Temperature NO_x Adsorbers for Diesel Applications, SAE Int. J. Engines. 10 (2017) 2017-01–0942.

[28] Y. Ji, D. Xu, M. Crocker, J.R. Theis, C. Lambert, A. Bueno-Lopez, D. Harris, D. Scapens, Mn-based mixed oxides for low temperature NOx adsorber applications, Appl. Catal. A Gen. 567 (2018) 90–101.

[29] H.-Y. Chen, J.E. Collier, D. Liu, L. Mantarosie, D. Durán-Martín, V. Novák, R.R.

Rajaram, D. Thompsett, Low Temperature NO Storage of Zeolite Supported Pd for Low Temperature Diesel Engine Emission Control, Catal. Letters. 146 (2016) 1706–1711.

[30] O. Mihai, L. Trandafilović, T. Wentworth, F.F. Torres, L. Olsson, The Effect of Si/Al Ratio for Pd/BEA and Pd/SSZ-13 Used as Passive NOx Adsorbers, Top. Catal. 0 (2018) 0.

[31] S. Ren, S.J. Schmieg, C.K. Koch, G. Qi, W. Li, Investigation of Ag-based low temperature NOx adsorbers, Catal. Today. 258 (2015) 378–385.

[32] J. Lee, Y. Ryou, S.J. Cho, H. Lee, C.H. Kim, D.H. Kim, Investigation of the active sites and optimum Pd/Al of Pd/ZSM–5 passive NO adsorbers for the cold-start application: Evidence of isolated-Pd species obtained after a high-temperature thermal treatment, Appl. Catal. B Environ. 226 (2018) 71–82.

[33] A. Porta, T. Pellegrinelli, L. Castoldi, R. Matarrese, S. Morandi, S. Dzwigaj, L. Lietti, Low Temperature NOx Adsorption Study on Pd-Promoted Zeolites, Top. Catal. 0 (2018) 0.

[34] Y. Zheng, L. Kovarik, M.H. Engelhard, Y. Wang, Y. Wang, F. Gao, J. Szanyi, Low-Temperature Pd / Zeolite Passive NOx Adsorbers : Structure , Performance and Adsorption Chemistry Low-Temperature Pd / Zeolite Passive NOx Adsorbers : Structure , Performance and Adsorption Chemistry Abstract :, (2017) 1–10.

[35] J. Lee, Y. Ryou, S. Hwang, Y. Kim, S.J. Cho, H. Lee, C.H. Kim, D.H. Kim, Comparative study of the mobility of Pd species in SSZ-13 and ZSM-5, and its implication for their activity as passive NO x adsorbers (PNAs) after hydro-thermal aging, Catal. Sci. Technol. 9 (2019) 163–173.

[36] D. Mei, F. Gao, J. Szanyi, Y. Wang, Mechanistic insight into the passive NOx adsorption in the highly dispersed Pd/HBEA zeolite, Appl. Catal. A Gen. 569 (2019) 181–189.

[37] Y. Zheng, L. Kovarik, M.H. Engelhard, Y. Wang, Y. Wang, F. Gao, J. Szanyi, Low-Temperature Pd/Zeolite Passive NO x Adsorbers: Structure, Performance, and Adsorption Chemistry, J. Phys. Chem. C. 121 (2017) 15793–15803.

[38] Y. Ryou, J. Lee, H. Lee, C.H. Kim, D.H. Kim, Effect of various activation conditions on the low temperature NO adsorption performance of Pd/SSZ-13 passive NOx adsorber, Catal. Today. 320 (2019) 175–180.

[39] Y. Ryou, J. Lee, S.J. Cho, H. Lee, C.H. Kim, D.H. Kim, Activation of Pd/SSZ-13 catalyst by hydrothermal aging treatment in passive NO adsorption performance at low temperature for cold start application, Appl. Catal. B Environ. 212 (2017) 140–149.

[40] K. Khivantsev, N.R. Jaegers, L. Kovarik, J.C. Hanson, F.F. Tao, Y. Tang, X. Zhang, I.Z. Koleva, H.A. Aleksandrov, G.N. Vayssilov, Y. Wang, F. Gao, J. Szanyi, Achieving Atomic Dispersion of Highly Loaded Transition Metals in Small-pore Zeolite SSZ-13: A New Class of High-capacity and High-efficiency Low Temperature CO and NOx Adsorbers, Angew. Chemie. (2018).

[41] K. Khivantsev, F. Gao, L. Kovarik, Y. Wang, J. Szanyi, Molecular Level Understanding of How Oxygen and Carbon Monoxide Improve NO x Storage in Palladium/SSZ-13 Passive NO x Adsorbers: The Role of NO + and Pd(II)(CO)(NO) Species, J. Phys. Chem. C. 122 (2018) 10820–10827.

[42] A. Vu, J. Luo, J. Li, W.S. Epling, Effects of CO on Pd/BEA Passive NOx Adsorbers, Catal. Letters. 147 (2017) 745–750.

[43] Y. Ryou, J. Lee, Y. Kim, S. Hwang, H. Lee, C.H. Kim, H.K. Do, Effect of reduction treatments (H2 vs. CO) on the NO adsorption ability and the physicochemical properties of Pd/SSZ-13 passive NOx adsorber for cold start application, Appl. Catal. A Gen. (2018).

[44] A.K. Datye, J. Bravo, T.R. Nelson, P. Atanasova, M. Lyubovsky, L. Pfefferle, Catalyst microstructure and methane oxidation reactivity during the Pd↔PdO transformation on alumina supports, Appl. Catal. A Gen. 198 (2000) 179–196.

[45] M. Iwasaki, H. Shinjoh, ChemComm Hydrothermal stability enhancement by sequential ion-exchange of rare earth metals on Fe / BEA zeolites used as NO reduction catalysts w, (2011) 3966–3968.

[46] B.J. Adelmana, W.M.H. Sachtler, The effect of zeolitic protons on NO , reduction over Pd / ZSM-5 catalysts, Science (80-.). 14 (1997).

[47] Y. Gu, W.S. Epling, Passive NOx adsorber: An overview of catalyst performance and reaction chemistry, Appl. Catal. A Gen. 570 (2019) 1–14.

[48] J.R. Theis, C. Lambert, The Effects of CO, C 2 H 4 , and H 2 O on the NO x Storage Performance of Low Temperature NO x Adsorbers for Diesel Applications, SAE Int. J. Engines. 10 (2017) 2017-01–0942.

[49] K. Khivantsev, N.R. Jaegers, L. Kovarik, S. Prodinger, M.A. Derewinski, Y. Wang, F. Gao, J. Szanyi, Palladium/Beta zeolite passive NOx adsorbers (PNA): Clarification of PNA chemistry and the effects of CO and zeolite crystallite size on PNA performance, Appl. Catal. A Gen. 569 (2019) 141–148.

[50] Y. Ryou, J. Lee, H. Lee, C.H. Kim, D.H. Kim, Effect of various activation conditions on the low temperature NO adsorption performance of Pd/SSZ-13 passive NOx adsorber, Catal. Today. (2017).

[51] S.T. Homeyer, W.M.H. Sachtler, Oxidative redispersion of palladium and formation of PdO particles in NaY, Appl. Catal. 54 (1989) 189–202.

[52] S. HOMEYER, Elementary steps in the formation of highly dispersed palladium in NaY I.

Pd ion coordination and migration, J. Catal. 117 (1989) 91–101.

[53] A.W. Aylor, L.J. Lobree, J.A. Reimer, A.T. Bell, Investigations of the Dispersion of Pd in H-ZSM-5, J. Catal. 172 (1997) 453–462.

[54] Y. Ryou, J. Lee, Y. Kim, S. Hwang, H. Lee, C.H. Kim, D.H. Kim, Effect of reduction treatments (H2 vs. CO) on the NO adsorption ability and the physicochemical properties of Pd/SSZ-13 passive NOx adsorber for cold start application, Appl. Catal. A Gen. 569 (2019) 28–34.

[55] M. Ogura, M. Hayashi, S. Kage, M. Matsukata, E. Kikuchi, Determination of active palladium species in ZSM-5 zeolite for selective reduction of nitric oxide with methane, Appl. Catal. B Environ. 23 (1999) 247–257.

Chapter 6. Investigation of the Degradation Mechanism of Pd/Zeolite Based Passive NOx Adsorbers: Interconversion between Ions and Particles

6.1 Introduction

Fully ion-exchanged Pd/SSZ-13 model passive NOx adsorbers (PNA) have been reported to exhibit NOx storage capability that can achieve 1:1 Pd:NO ratios.[1,2] A modified ion-exchange method can be used to achieve atomic dispersion of Pd within the zeolite framework thus maximizing the Pd atomic utilization for NOx storage, indicating the unimolecular nature of NO adsorption on cationic Pd species.[1] Low Si:Al ratio and NH_3 solvated Pd cations are key to atomically dispersing Pd. A NO storage capacity-to-Pd ratio of 1:1 can be attained on a fully ion-exchanged Pd/SSZ-13 PNA. However, despite the high initial NOx storage capacity, Pd/zeolite-based PNAs experience degradation upon exposure to CO and irreversibly lose NOx storage capacity over adsorption-desorption cycles.[3] Literature reported cyclic PNA behavior indicates that the CO induced degradation mode described in the previous chapter is not specific to Pd/BEA and appears to be a general phenomenon to Pd/zeolite based PNA materials.[4]

Oxidation of CO during the cold start is challenging due to limited activity of the diesel oxidation catalyst, and CO is an exhaust component during the cold start.[5] Hence, the inevitable CO exposure imposes a major concern that prevents this technology from commercialization. The preliminary research reported in the literature and our results presented in the previous chapter propose, as a simplified mechanism, CO exposure causes the detachment of Pd cations from the zeolite and formation of PdO particles. However, there appears to be insufficient understanding of the temperature dependence of the cation/particle interconversion and this degradation reversibility. More specifically, the temperature required for Pd detachment to occur and the temperature required for the formation of PdO particles to be irreversible are not clear.

In this chapter, we synthesized a fully ion-exchanged and a 50% ion-exchanged Pd/SSZ-13 model PNA to compare their cyclic degradation behavior and performed in situ X-ray spectroscopy to understand the degradation mechanism. We demonstrate that with a higher ion-exchange level Pd/SSZ-13 exhibits significantly better CO oxidation activity and more resistant against CO induced degradation. In situ extended X-ray absorption results show that Pd cations can be readily reduced in a CO and H_2O mixture at temperatures above 573K and form Pd particles. The temperature at which the particles are formed influence the particle size, and small particles formed at low temperatures can be fully regenerated back into cations with an oxidative treatment. High temperature accelerates particle agglomeration and causes the formation of larger PdO particles thus the irreversible loss of Pd cations.

6.2 Materials and methods

Experiment methods and samples used in this study are identical to that described in Chapter 2 and Chapter 3.2, thus are not introduced in this chapter to avoid redundancy.

6.3 Results and discussion

6.3.1 Catalyst Characterization

The two samples used in this study were characterized with transmission electron microscopy and X-ray absorption spectroscopy, of which the results are shown in Figure 6.1 and Figure 6.2. We demonstrate, on the fully ion-exchanged sample (Pd/SSZ-13 - IE 100), that there was no significant PdO or Pd particle formation indicated by the absence of higher shell Pd-O-Pd or Pd-Pd scattering features at radial distances above 2.5Å, which can be clearly observed from Pd foil at 2.7 Å and bulk PdO at 3.3 Å, respectively. The spectrum collected from $Pd(NO_3)_2 \cdot 2H_2O$ shares the same first shell Pd-O scattering feature with Pd/SSZ-13 - IE 100, further confirming the atomic dispersion of Pd. We observe a Pd-O-Pd scattering feature at 3.3 Å from the spectrum collected from the 50% ion-exchanged sample and attribute this feature to the formation of PdO particles. Notably, there is no difference in Pd loading or synthesis procedure between the two samples characterized but the different Si:Al ratios (Si:Al=9 for Pd/SSZ-13 - IE 100 and Si:Al=16 Pd/SSZ-13 - IE 50) were confirmed with ICP-OES analysis and appears to be a factor leading to different ion-exchange levels. Additionally, the X-ray near edge absorption spectra shown in Figure 6.1(b) indicate that both samples share the same edge energy with a PdO standard and exhibit 2+ oxidation state of Pd under ambient conditions. TEM images taken on Pd/SSZ-13 - IE 100 and Pd/SSZ-13 - IE 50 are shown in Figure 6.2. In agreement with the X-ray absorption characterization results, we observe almost no Pd/PdO particles on Pd/SSZ-13 - IE 100 due to the high ion-exchange level and a significant amount Pd/PdO particles formed on Pd/SSZ-13 – IE 50.

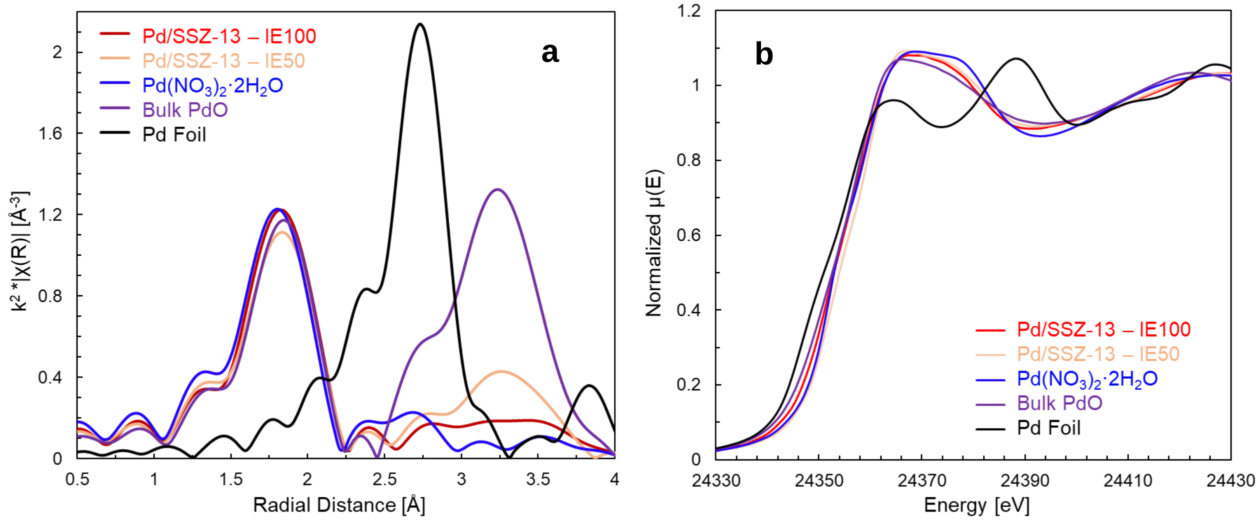

Figure 6.1 Extended X-ray absorption fine structure (b) and near edge X-ray absorption spectra of the Pd/SSZ-13 samples, Pd(NO$_3$)$_2$·2H$_2$O, Pd foil, and bulk PdO taken under ambient conditions with no pretreatment.

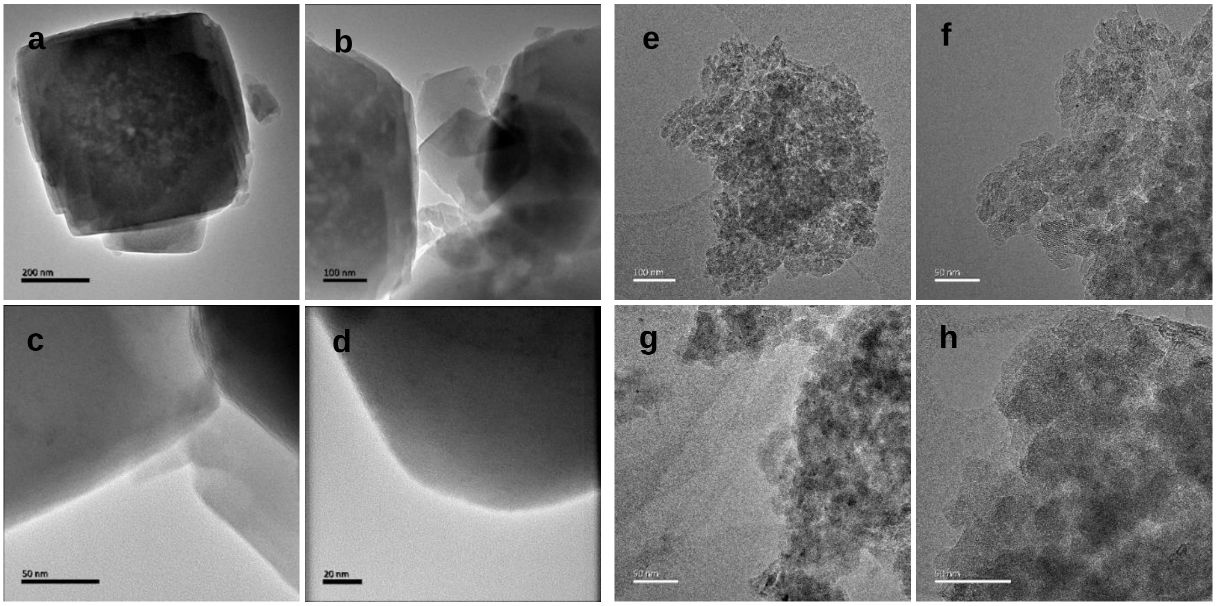

Figure 6.2 TEM images of (a) - (d) the fully ion-exchanged Pd/SSZ-13 and (e) - (f) the 50% ion-exchanged after ambient exposure.

6.3.2 Cyclic NOx-TPD and CO-TPR

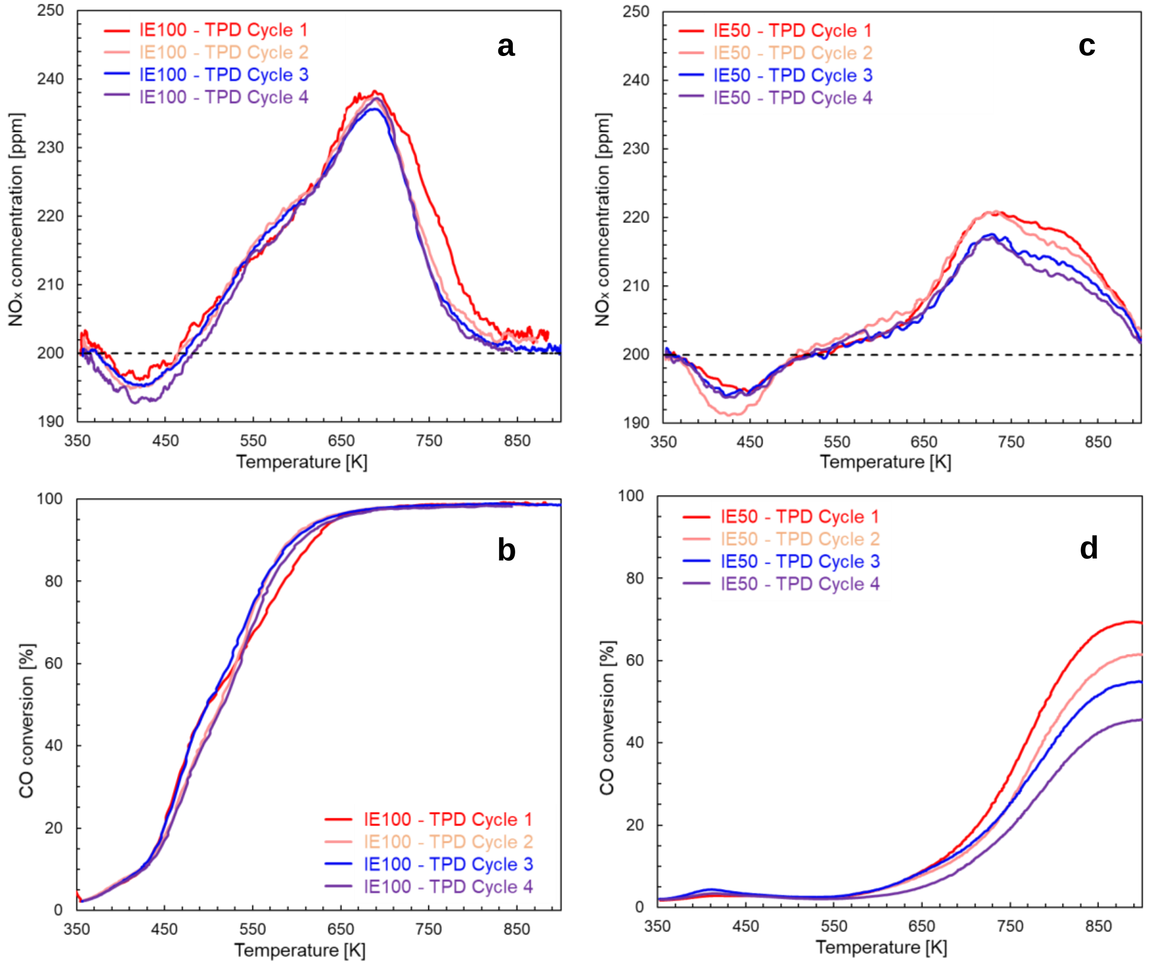

Figure 6.3 Consecutive NOx-TPD profiles (upper panel) and the simultaneous CO oxidation light-off curves (lower panel) of Pd/SSZ-13 - IE100 (a) and (b) and Pd/SSZ-13 – IE50 (c) and (d) over the first four cycles. Feed composition: 200 ppm NO, 200 ppm CO, 4.5% H_2O, 10% O_2 and N_2 balance. Space velocity: 60,000 hr^{-1}

Table 6.1 Comparison of NOx storage capacity between Pd/SSZ-13 – IE50 and Pd/SSZ-13 - IE100

Sample	Support	1st NOx:Pd	4th NOx:Pd	Si/Al		Pd Loading	
				Nominal	ICP-OES	Target	ICP
IE100	H-SSZ-13	1.05 ± 0.1	0.91 ± 0.1	10	**9**	1 wt.%	**0.84 wt.%**
IE50	H-SSZ-13	0.55 ± 0.1	0.38 ± 0.1	15	**16**	1 wt.%	**0.79 wt.%**

The NOx-TPD profiles of both samples and their simultaneous CO oxidation light-off curves are shown in Figure 6.3. We also calculated and report the corresponding NOx storage capacities in Table 6.1. As is indicated by the 1st NOx:Pd ratio listed in Table 6.1, the IE100 sample exhibits a NOx:Pd ratio of 1.05, which is almost twice the capacity of the IE50 sample, these results provide further evidence that the Pd distribution between the two samples differ and that their ion-exchange levels correlate to the NOx:Pd ratio as Pd cations are the most effective NOx storage sites. However, NOx-TPD profiles for both samples show a decrease in overall NOx storage capacity over the first four cycles, and IE50 seems to be more vulnerable under the same experiment conditions, which is captured by the relatively more rapid loss in NOx storage capacity. We report the NOx:Pd ratios of both samples after the 4th TPD cycle in Table 6.1, with a 10% loss of total storage capacity over the first four cycles on IE100 and a 20% loss on IE50. These results suggest that, apart from the difference in initial NOx storage capacities, Pd distribution also affects the resistance of the PNA materials against CO induced degradation.

Additionally, CO oxidation light-off curves for both samples measured during NOx-TPD clearly show that IE100 is more active for CO oxidation than IE50 under the test conditions and can achieve 100% conversion at temperatures above 700K. Although the mechanistic reason behind the different CO oxidation activities needs further investigation, we know from the previous chapter that this directly leads to the PNAs being exposed to CO at different temperatures which may have a consequence on the degradation behavior. In other words, the enhanced resistance against CO induced degradation maybe a result of better CO oxidation activity thus less high temperature CO exposure.

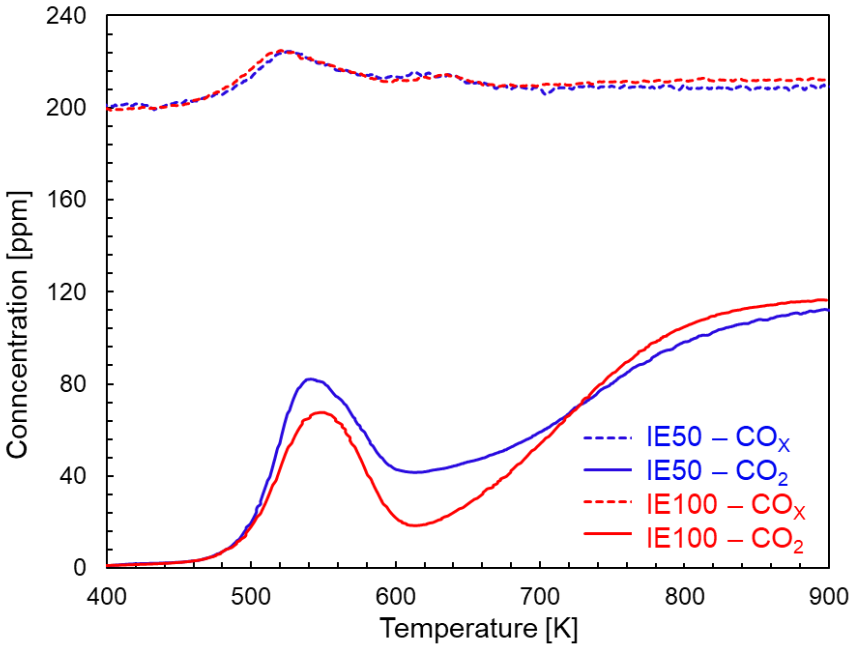

Figure 6.4 CO_2 and CO + CO_2 profiles of Pd/SSZ-13 - IE100 (red) and Pd/SSZ-13 – IE50 (blue) during CO temperature programmed reduction. Feed composition: 200 ppm CO, 4.5% H_2O, 10% O_2 and N_2 balance. Space velocity: 60,000 hr^{-1}

To understand whether or not different CO exposure temperatures will impact the PNA degradation behavior, we performed CO temperature programmed reduction (TPR) experiments in the presence of H_2O, of which the results are shown in Figure 6.4. Because of the absence of O_2 during the temperature ramp, Pd is expected to be reduced from Pd^{II} to Pd^0, and as a product of the reduction reaction, CO_2 will form once the temperature needed to reduce Pd is reached. We observe transient CO_2 formation on both samples at 550K suggesting the reduction of Pd at this temperature and the formation of metallic Pd, which is active for the water gas shift (WGS) reaction thus the increase in CO_2 formation as the temperature is increased further. These results provide direct evidence that CO exposure at temperatures higher than 550K will lead to the reduction of Pd. CO light-off curves for IE50 and IE100 shown in Figure 6.3 (c) and (d) suggest that during the temperature ramp both samples were exposed to CO at 550K due to limited oxidation activity thus the occurrence of the reduction of Pd. However, during NOx-TPD or under realistic conditions, the presence of O_2 will lead to the immediate reoxidation of reduced Pd. Thus, although CO-TPR can be used as a direct probe of Pd reducibility, it does not provide insights into the irreversible changes that may happen during this process under realistic conditions.

6.3.3 In situ EXAFS

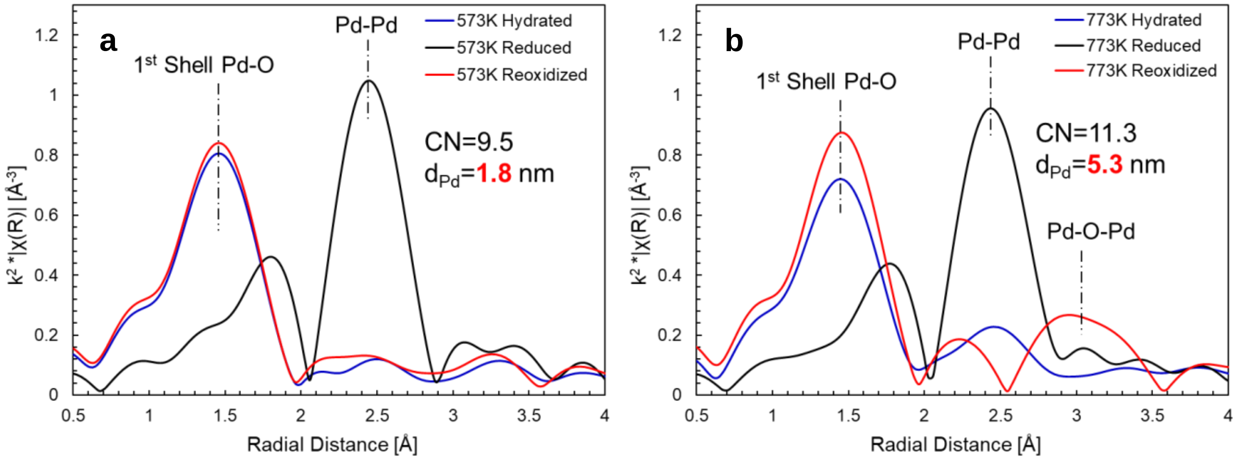

Figure 6.5 In situ extended X-ray absorption fine structures of Pd/SSZ-13 - IE100 during CO reduction and O_2 reoxidation at (a) 573K and (b) 773K. Feed composition: Hydrated – 10% O_2, 3.1% H_2O and N_2 balance; Reduced – 1000 ppm CO, 3.1% H_2O and N_2 balance; Reoxidized – 10% O_2 and N_2 balance;

Having shown that Pd can be readily reduced at 550K in the presence of CO and H_2O, we next performed in situ X-ray absorption spectroscopy experiments to further investigate the reversibility of the reduction and re-oxidation process at two different temperatures and report the corresponding EXAFS spectra in Figure 6.5. A spectrum collected from a hydrated IE100 sample at 573K is shown in Figure 6.5(a), where we observe a single Pd-O scattering feature at 1.5Å and no higher shell scattering features. This result is consistent with the spectrum collected from an ambient exposed IE100 sample shown in Figure 6.1(a) and indicates the presence of homogeneous water solvated Pd cations. As O_2 was removed and CO was introduced into the feed, we observed the appearance of a Pd-Pd scattering feature at 2.5Å indicating the reduction of Pd cations and the formation of metallic Pd particles, which is in agreement with CO-TPR results shown in Figure 6.4. After fitting the Pd-Pd single shell scattering path using Pd foil as a reference, we found the coordination number of this scattering feature to be 9.5, which indicates the average particle size of Pd is around 1.8 nm.[6-8] Once CO was shut off and O_2 was introduced back into the feed at 573K to re-oxidize Pd, the Pd-O scattering feature restores to the initial level and the Pd-Pd scattering feature completely disappears. These results demonstrate that the reduction and the oxidative regeneration of Pd cations are reversible at 573K and indicate that the exposure of CO, H_2O and O_2 should not lead to irreversible changes of the Pd distribution within the zeolite. When the same set of experiments was performed at 773K, as is shown in Figure 6.5(b) we observe again the reduction of Pd captured by the appearance of the Pd-Pd scattering feature at 2.5Å upon CO exposure but a significantly higher Pd-Pd coordination number of 11.3, which corresponds to an average particle size of 5.3 nm.[6-8] Additionally, the following O_2 treatment did not recover all the Pd cations and led to the formation of PdO particles captured by a higher shell scattering feature at 3Å. These results provide evidence that as the temperature of the reduction and reoxidation is increased, reduced Pd particles agglomerate and grow into bigger Pd particles, which cannot be regenerated at these temperatures. Furthermore, the irreversible migration of Pd from cations to PdO particles leads to a decrease in the overall Pd ion-exchange level, which can be used to explain the aforementioned loss of NOx storage capacity. Notably, both sets of experiments were performed stepwise fashion and samples were given sufficient time to be reduced during CO exposure. Hence, the particle sizes measured do not represent the case where these catalysts exposed to CO, H_2O and O_2 simultaneously during NOx-TPD. However, these results along with the CO light-off curves and NOx-TPD profiles shown in Figure 6.3 indicate that even with limited high temperature CO exposure in the presence of O_2, the occurrence of irreversible Pd migration is evident due to the loss of NOx storage capacity and the shift in CO light-off temperature over the first four cycles.

6.4 CO oxidation kinetics

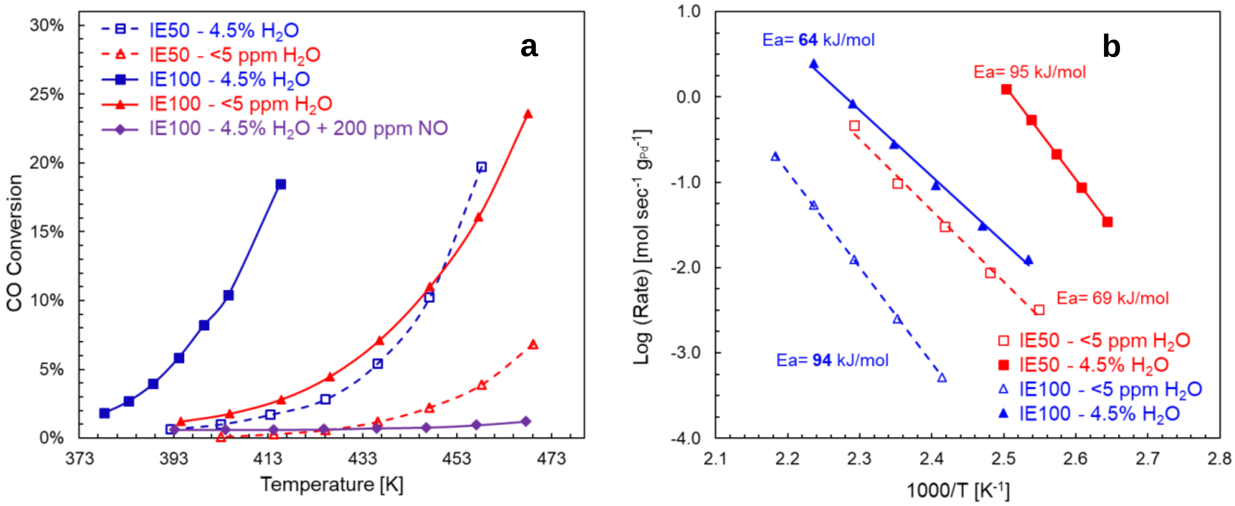

Figure 6.6 CO oxidation conversions (a) and the corresponding Arrhenius plot (b) measured from IE50 and IE100 samples under dry (200 ppm CO, <5 ppm H_2O and 10%O_2) and wet (200 ppm CO, 4.5% H_2O and 10% O_2) conditions in the abscence of NO, and wet condition in the presence of NO (200 ppm NO, 200 ppm CO, 4.5% H_2O and 10% O_2); Space velocity: 60,000 hr^{-1}

Having established the connection between high temperature CO exposure and the irreversible degradation of Pd/zeolite based PNAs, it is apparent that the CO oxidation activity of the PNAs themselves can be critical to their resistance against degradation. As is discussed with Figure 6.3, the difference in CO light-off behavior will have a direct impact on the CO exposure conditions, which additionally affects their degradation behavior under cyclic NOx adsorption and desorption conditions. Furthermore, as an indirect probe, CO oxidation activity changes as a function of Pd speciation and Pd distribution and thus can be used as an indicator of Pd migration. Hence, understanding CO oxidation activity of different Pd species and how it changes as a function of gas composition can provide mechanistic insight. Here we report CO conversions and apparent CO oxidation activation energies for IE100 and IE50. The IE100 sample provides characteristics of CO oxidation on Pd cations, and as is shown in Figure 6.6 (a) the presence of 4.5% H_2O leads to a significant increase in CO conversion. This phenomenon is discussed in chapter 3 with the observed H_2O solvation of Pd cations, and we speculate that the increase in CO oxidation activity is due to the enhancement in Pd mobility and the formation of multinuclear Pd cationic species. However, we also speculate that CO oxidation within zeolite voids and channels are influenced by heat and mass transfer, thus the apparent activation energies measured cannot be used to directly support the change in CO oxidation mechanism. When it comes to the comparison between IE100 and IE50 under dry conditions, we observed a significantly lower CO conversion on IE50. As is mentioned in section 6.2.1, Pd loadings for both samples were almost identical and IE50 consists of a significant amount of Pd particles. A lower CO conversion compared to IE100 under dry conditions could be due to the intrinsically different oxidation activities of PdO particles and Pd cations or less Pd sites for CO oxidation due to the presence of PdO particles. The promotion of CO oxidation by H_2O can also be observed on IE50, although the conversion is lower than IE100 in the presence of H_2O. In addition, we observe very different activation energies as the concentration of H_2O changes. For the IE100 sample, CO oxidation in the presence of 4.5% H_2O exhibits an activation energy of 94 $kJ\cdot mol^{-1}$ which is 30 $kJ\cdot mol^{-1}$ higher than that measured in the absence of H_2O. All of these results indicate that CO oxidation in the presence and absence of H_2O is mechanistically different due to different Pd speciation, and that the formation of PdO particles introduces a different CO oxidation pathway and leads to the decrease in overall CO oxidation activity. These results are consistent with the cyclic TPD experiments shown in Figure 6.3 where a shift of CO oxidation light-off curves to higher temperature was observed as a result of Pd migrating from cation form to the particle domain. Furthermore, as is reported in Figure 6.6

(a), we observed close to zero CO conversion in the presence of both H_2O and NO. This result indicates that NO adsorption on Pd cations inhibits CO oxidation in the presence of H_2O, due to the formation of stable Pd-nitrosyl species and the prohibitive CO adsorption discussed in Chapter 3. Notably, during the low temperature NO adsorption and TPD experiments, Pd/zeolite based PNAs experience significant changes in CO oxidation activity due to the several process discussed in this work including: NO desorption, Pd dehydration, Pd reduction by CO, reoxidation of Pd and the regeneration of Pd cations.

6.5 Conclusions

We show with cyclic NOx-TPD that both atomically dispersed and 50% ion-exchanged Pd/SSZ-13 PNAs irreversibly lose NOx storage capacity after being exposed to CO. Pd cations ion-exchanged into the zeolite framework can be reduced by CO at temperatures above 550K in the presence of H_2O. In situ EXAFS experiments demonstrate that the reduction and regeneration of Pd cations are reversible at 573K but are partially irreversible at 773K due to the formation of larger Pd particles. CO reduction of Pd cations and subsequent particle agglomeration occurring at elevated temperatures leads to irreversible Pd migration thus the irreversible loss of NOx storage capacity, which is responsible for the degradation observed over the first four cycles. CO oxidation over Pd/SSZ-13 PNAs are influenced by several transient processes that take place during NOx release, and to summarize we list them as non-elementary reactions using the representation defined in chapter 3 as follows:

NO desorption: $ZH + Z[Pd^{II}(NO^{-})(H_2O)_4] \rightleftharpoons Z_2[Pd^{II}(H_2O)_4] + H + NO$

Pd dehydration: $Z_2[Pd^{II}(H_2O)_4] \rightleftharpoons Z_2[Pd^{II}] + 4H_2O$

Pd reduction by CO: $Z_2[Pd^{II}] + CO + H_2O \rightleftharpoons Pd^0 + +2ZH + CO_2$

Pd reoxidation: $Pd^0 + O \rightleftharpoons PdO$

Pd cation regeneration(protonolysis): $PdO + 2ZH \rightleftharpoons Z_2Pd + 3H_2O$

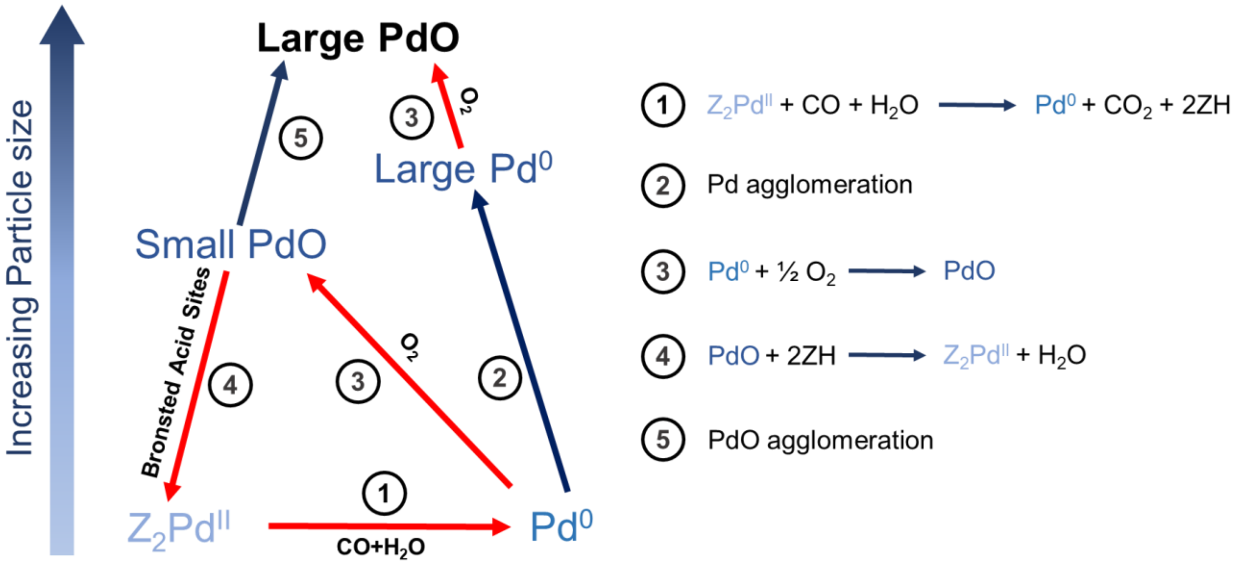

Figure 6.7 Schematic representation of Pd/zeolite based PNA degradation mechanism

Particle agglomeration in the form of either reduced Pd particles or PdO particles, although not represented as a chemical reaction, represents another process that leads to the degradation of Pd/zeolite based PNAs. Combining all the key processes we present a schematic representation of the mechanism behind the degradation mechanism discussed.

6.6 References

[1] K. Khivantsev, N.R. Jaegers, L. Kovarik, J.C. Hanson, F. (Feng) Tao, Y. Tang, X. Zhang, I.Z. Koleva, H.A. Aleksandrov, G.N. Vayssilov, Y. Wang, F. Gao, J. Szanyi, Achieving Atomic Dispersion of Highly Loaded Transition Metals in Small-Pore Zeolite SSZ-13: High-Capacity and High-Efficiency Low-Temperature CO and Passive NO x Adsorbers, Angew. Chemie Int. Ed. 57 (2018) 16672–16677.

[2] K. Mandal, Y. Gu, K.S. Westendorff, S. Li, J.A. Pihl, L.C. Grabow, W.S. Epling, C. Paolucci, Condition-Dependent Pd Speciation and NO adsorption in Pd/Zeolites, ACS Catal. (2020).

[3] Y. Gu, R.P. Zelinsky, Y.-R. Chen, W.S. Epling, Investigation of an irreversible NOx storage degradation Mode on a Pd/BEA passive NOx adsorber, Appl. Catal. B Environ. 258 (2019) 118032.

[4] J.R. Theis, J.A. Ura, Assessment of zeolite-based Low temperature NOx adsorbers: Effect of reductants during multiple sequential cold starts, Catal. Today. (2020).

[5] M.J. Hazlett, M. Moses-Debusk, J.E. Parks, L.F. Allard, W.S. Epling, Kinetic and mechanistic study of bimetallic Pt-Pd/Al_2O_3 catalysts for CO and C_3H_6 oxidation, Appl. Catal. B Environ. 202 (2017) 404–417.

[6] K. Sasaki, Nanoparticle size evaluation of catalysts by EXAFS : Advantages and limitations, 128 (2016) 101–109.

[7] J.T. Miller, A.J. Kropf, Y. Zha, J.R. Regalbuto, L. Delannoy, C. Louis, E. Bus, The effect of gold particle size on Au – Au bond length and reactivity toward oxygen in supported catalysts, 240 (2006) 222–23

[8] A.I. Frenkel, C.W. Hills, R.G. Nuzzo, Feature article, 105 (2001).4.

Chapter 7. Integration of an Oxidation Catalyst with Pd/Zeolite-Based Passive NOx Adsorbers: Impacts on Degradation Resistance and Desorption Characteristics

This chapter consists of a manuscript submitted to Industrial & Engineering Chemistry Research that is currently under review.

7.1 Introduction

Catalytic NOx abatement from mobile sources has been successfully commercialized using three-way catalytic converters (TWC), lean NOx traps (LNT), and ammonia selective catalytic reduction (NH_3-SCR) systems.[1–8] However, automobile NOx emissions continue to be a major concern for urban air quality mainly due to the inefficiency of these NOx reduction systems at low temperatures.[9–14] Low temperatures limit their ability to reduce NOx during engine cold start and low load operating cycles.[15–17] Furthermore, combustion improvements are expected to lead to lower exhaust temperature and potentially longer cold start duration.[13,15] Hence, the control of NOx emissions at low temperature is critical for compliance with the increasingly stringent emissions regulations and generally better performance under real driving conditions.[18,19]

Passive NOx adsorbers (PNA), being able to trap NOx at low temperatures and subsequently release them at temperatures above which the downstream catalysts can efficiently convert NOx, are proposed as a solution to address the cold start NOx emission problem.[20–23] Pd ion-exchanged zeolites are promising PNA materials as they exhibit significant low temperature NOx storage capacity and reasonable NOx release temperature windows.[24–26] Recent studies on Pd/zeolite PNAs reveal that Pd^{2+} cations located at the ion-exchange position of the zeolite support can directly bind with molecular NO, and form Pd-nitrosyl species that are responsible for low temperature NOx adsorption.[27–35] Our recent study demonstrated the H_2O solvated nature of these Pd cations within the zeolite framework under cold start conditions and provided a thorough understanding of mechanistic aspects of NO adsorption and desorption energetics.[36] However, the gas composition under realistic exhaust conditions is far more complicated than simulated exhaust conditions often reported in the literature.[37] For example, exposure to CO has been shown to influence the NOx desorption temperature, indicating a chemical interaction with the Pd-nitrosyl species.[30,32,37] Furthermore, our early work reported an irreversible loss of NOx storage capacity after several NO and CO co-adsorption cycles within a Pd/BEA model PNA system.[38] Characterization results indicate that Pd cations are detached from the zeolite and form large PdO particles on the external surface of the zeolite crystal, which are thus hard to regenerate.[38] Similar behavior was also reported on a Pd/SSZ-13 PNA system by Theis et al.[39] Although there is still a mechanistic understanding of this degradation mode, CO exposure under cold start conditions is inevitable thus this observed loss of NOx storage is a major concern for practical application. Based on reported PNA studies, the aforementioned irreversible degradation induced by CO appears to be the main limitation preventing this technology from commercialization.[38]

PNAs are often studied as an independent component, which has provided unique insight into their behavior, [20,24,26,28,33–35,37,39–45] but may not reasonably represent the architecture of a practical exhaust after-treatment system.[21,22,46–48] For example, a cold start concept catalyst proposed by Johnson Matthey includes a NOx adsorber and oxidation catalyst integrated together, and the system performance differs from any one of its components.[21] More importantly, as is widely discussed in the literature and as mentioned above, PNA performance is very sensitive to exhaust compositions thus the integration with an oxidation catalyst could lead to very different system performance and potentially a solution to CO induced degradation.

In this paper, we present a cyclic NOx adsorption and temperature programmed desorption (TPD) study on a Pd/SSZ-13 model PNA, and an integrated system that contains the PNA component and a Pt/Al_2O_3 model diesel oxidation catalyst (DOC). We report their NOx storage capacities over 15 TPD cycles and compare NOx release temperature windows and the resistance against CO induced degradation. Additionally, we performed experiments with controlled CO and NO_2 exposure to decouple the effect of DOC integration on the system adsorption and desorption characteristics to reconcile observed differences. Most importantly, we demonstrate that the integration of a PNA with an oxidation catalyst can lead to improved resistance against CO induced degradation and could be a solution to maximize the durability of Pd/zeolite based PNA systems.

7.2 Methods

7.2.1 Catalyst Synthesis

A Pd/SSZ-13 passive NOx adsorber as well as a Pt/Al_2O_3 oxidation catalyst were synthesized and evaluated in this study. Pd/SSZ-13 was prepared via incipient wetness impregnation. The proton form of SSZ-13 zeolite with a nominal Si/Al ratio of 10 was purchased from ACS Material Inc. We followed a three-step calcination process (80 °C for 2 hours, 105 °C for 10 hours and 600 °C for 4 hours with a ramp rate of 1 °C/min) in flowing air to dehydrate the parent zeolite and desorb any residual contaminants before introducing Pd. $Pd(NO_3)_2 \cdot 2H_2O$, as the Pd precursor, purchased from Sigma Aldrich was dissolved in a 28% ammonium hydroxide solution also purchased from Sigma Aldrich. The volume of the solution was controlled to be the same as the zeolite micropore volume, and the amount of precursor added was calculated such that the mass of Pd would be 1 wt.%. Immediately after the three-step calcination, the Pd solution was added into the zeolite powder at room temperature with rigorous stirring. After the Pd solution was well mixed with the zeolite powder forming a brown slurry, the same calcination process was repeated to facilitate Pd ion-exchange. A 1.8 wt.% Pt/Al_2O_3 was also prepared via wetness impregnation. Pt, in the form of a $Pt(NH_3)_4(NO_3)_2$ solution, was deposited into γ-Al_2O_3, both purchased from Sigma Aldrich. After the wetness impregnation, the catalyst was dried at 50 °C for 12 hours, followed by a calcination at 550 °C for 4 hours with a ramp rate of 1 °C/min.

The freshly calcined catalysts were pelletized into 225-425 μm particles and loaded into a quartz tube reactor for testing. Prior to these tests, samples were hydrothermally aged by exposing the catalysts to a gas mixture of 10% O_2 and 5% H_2O balanced by N_2 at 600°C for 4 hours at a space velocity of 30,000 hr^{-1}.

7.2.2 Catalyst Characterization

Si/Al ratio (Si:Al=8.9) and Pd loading (0.84 wt.%, Pd:Al=0.05) of the as synthesized PNA sample were confirmed by inductively coupled plasma optical emission spectroscopy (ICP-OES) analysis at Galbraith Laboratories, Knoxville TN. We next characterized Pd/SSZ-13 with Pd K edge (23450 eV) X-ray absorption spectroscopy (XAS) using beam 8-ID of the National Synchrotron Light Source II, Upton NY. All measurements were performed with an electron storage ring operated at 3 GeV and a beam current of 400 mA. The pelletized sample was loaded into a 0.25-inch stainless steel tube placed inside an aluminum heating jacket. We collected spectra of the ambient exposed sample with no additional treatment to characterize the Pd speciation and distribution. Additionally, transmission electron micrographs were collected on a FEI Titan transmission electron microscope (TEM) to further confirm the absence of significant Pd particle formation.

We report the extended X-ray absorption fine structures (EXAFS) of the Pd/SSZ-13 sample in Figure 6.1(a) along with $Pd(NO_3)_2 \cdot 2H_2O$ and bulk PdO as two Pd^{2+} standards that represent atomically dispersed Pd cations and PdO particles, respectively. EXAFS of a Pd foil is also shown in the figure as a reference for Pd^0. The first shell scattering feature at around 1.8 Å is similar to that of $Pd(NO_3)_2 \cdot 2H_2O$ suggesting the interaction between zeolite framework O atoms and the predominant formation of highly dispersed Pd cations. The lack of a higher shell scattering feature at R>2.5 Å in the EXAFS spectrum of Pd/SSZ-13, which is present in the EXAFS of bulk PdO, indicates almost 100% ion-exchange of Pd into the SSZ-13 zeolite.[33] TEM images of selected areas further confirm the absence of significant Pd or PdO particle formation, which is in agreement with the EXAFS characterization results.

Pt particle size measurements of Pt/Al_2O_3 were performed on an ASAP 2020 Plus Micromeritics system using CO chemisorption. The catalyst was pretreated in ultra-high purity hydrogen for 2 hours at 400 °C for complete reduction, after which the system was evacuated for 2 hours and cooled to 35°C. Adsorption isotherms were taken at 35 °C and the stoichiometric ratio of CO to Pt was assumed to be 1:1. The particle size was estimated based on the CO uptake measured from the total isotherm, of which the result is 1.03 nm.

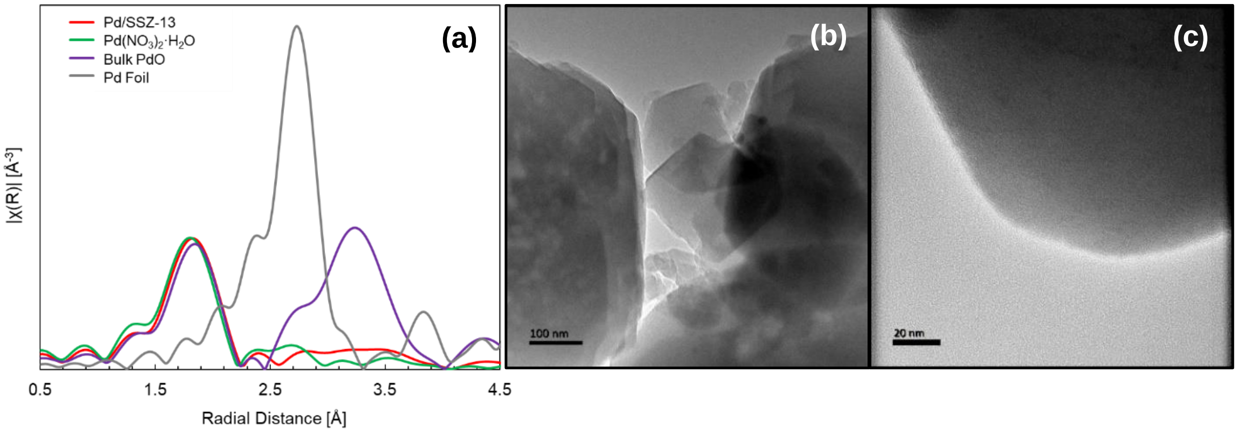

Figure 7.1 X-ray absorption fine structure (a) of the Pd/SSZ-13 sample, $Pd(NO_3)_2 \cdot 2H_2O$, Pd foil, and bulk PdO taken under ambient conditions with no pretreatment. TEM images (b) - (d) of the fresh Pd/SSZ-13 PNA after ambient exposure.

7.2.3 Catalyst Evaluation

We performed low-temperature NOx storage experiments with a 0.25-inch quartz tube reactor horizontally placed in a Mini-mite tubular furnace purchased from Thermo Fisher. A gas mixture of 10% O_2, 5% H_2O, 200 ppm of CO and 200 ppm of NO balanced by N_2 was chosen as the basic gas composition to simulate diesel exhaust conditions and evaluate NO and CO co-adsorption. All gas components are from ultra-high purity (UHP) gas cylinders purchased from Praxair. H_2O was injected into the manifold using a Bronkhorst controlled evaporator mixer (CEM). The total flowrate was controlled to maintain a 60,000 hr^{-1} monolith equivalent space velocity under standard conditions assuming $2g \cdot in^{-3}$ washcoat loading. We choose 80 °C as the adsorption temperature to represent cold start conditions and to be consistent with our previous work. [36,38] Before exposing the catalysts to the simulated exhaust described above, we exposed the samples to 10% O_2 and balance N_2 at 600 °C for 45 min, which is later referred to as the O_2 pretreatment. Following the pretreatment, the samples were cooled to 80 °C in 10% O_2 and the low-temperature NOx adsorption experiments were initiated by introducing the exhaust mixture into the reactor. The catalyst bed temperature was measured by two K-type thermocouples inserted into the reactor along the axial direction, where the tips are right next to the catalyst bed at both the downstream and upstream of the catalyst. Gas compositions of the reactor outlet as well as the bypass line were measured using an MKS IR analyzer, MG2030. After the PNA was considered saturated, a subsequent TPD experiment was initiated by linearly ramping the reactor temperature from 80 to 600 °C with a ramp rate of 90 °C/min. Feed gas composition remained the same during the temperature ramp, and immediately after the NOx desorption, an O_2 pretreatment was performed by switching the feed gas to 10% O_2 and balance N_2. The low temperature NO and CO co-adsorption and TPD in the presence of CO were repeated on the same sample for a number of cycles to mimic the repetitive cold start of an engine and evaluate the durability of the system under cyclic conditions.

As an attempt to understand the effect of PNA integration with an oxidation catalyst, three catalytic systems were employed in this work. Namely, a Pd/SSZ-13 PNA, a Pt/Al_2O_3 DOC and an integrated system that contains 1/3 DOC and 2/3 PNA by mass. For the PNA+DOC integrated system investigated in this work, we considered only one configuration, where the DOC is upstream of the PNA and the two catalyst beds were separated by quartz wool to avoid physical contact.

We also performed TPD experiments with controlled CO and NO_2 exposure to understand the impact of CO on PNA and PNA+DOC desorption characteristics. One experiment excluded CO during the TPD. A low temperature NOx storage experiment was first performed as described in this section, but we turned off CO after the saturation of NO adsorption. A linear temperature ramp from 80 to 600 °C with a ramp rate of 90 °C/min was then performed in the absence of CO after purging CO with the exhaust mixture for 5 min. Lastly, a low temperature NOx storage experiment in the presence of NO_2 was performed by adding 30 ppm of NO_2 into the feed and decreasing the NO concentration to 170 ppm, thus maintaining a 200 ppm NOx concentration to be comparable. CO was absent throughout this experiment including the TPD.

7.3 Results and discussion

7.3.1 PNA Degradation Characteristics

NOx-TPD profiles and CO oxidation light-off curves from the first three cycles of the cyclic test are reported in Figure 6.2. We observe significant NOx release within a temperature window of 350 - 550 °C in Figure 6.2 (a). We also observed a NOx adsorption feature, indicated by the negative peak centered around 180 °C, even after the saturation of NO adsorption at 80 °C.

This NOx adsorption feature we denote a secondary uptake, which contributes to 15 - 20% of the total NOx storage capacity. We integrated the NOx desorption peaks to calculate the total NOx storage capacity and confirmed the closure of mass balance (± 5%) by comparing the storage capacities measured from both adsorption and desorption. Finally, we calculated the NOx-to-Pd ratios ($R_{NOx:Pd}$) by normalizing the total NOx storage capacities based on the moles of Pd in the PNAs. The $R_{NOx:Pd}$ of the first TPD cycle is 0.98 ± 0.05 which suggests that approximately every Pd atom adsorbs one NOx molecule. This result is consistent with the literature reported $R_{NOx:Pd}$ of an atomically dispersed Pd/SSZ-13 PNA material and indicates almost 100% ion-exchange of Pd into the SSZ-13 framework.[33] Although the NOx storage capacity of the first cycle is consistent with the maximum use of Pd reported in the literature, we observe a slight loss of total NOx storage capacity over the 2nd and 3rd TPD desorption cycles in Figure 6.2 (a). $R_{NOx:Pd}$ of the 2nd and 3rd TPD desorption cycles are 0.96 and 0.94, respectively, showing a decrease in total NOx storage capacity. As is detailed in the experimental methods section, a high temperature O_2 pretreatment was always performed prior to the low temperature NO adsorption and TPD experiments, thus the loss of NOx storage capacity indicates an irreversible change of PNA NO storing capability. This phenomenon was indeed observed within a similar system under the exact same conditions, more specifically, our earlier work reported a CO induced irreversible degradation mode observed on a Pd/BEA model PNA, and we have attributed the loss of NOx storage capacity to the detachment of Pd cations from the zeolite and the subsequent formation of PdO particles. [38] Although the observed change in Pd/SSZ-13 NOx storage capacity is not as significant as Pd/BEA over the first three cycles, the shift in CO oxidation light-off curves observed from Figure 6.2 (b) demonstrates a change in CO oxidation activity suggesting Pd migration from cations to particles. [36,49] Additionally, we observe a continuous decrease in the amount of released NOx as shown in the NOx-TPD profiles of the last 10 cycles in the supporting information **Figure S1.** Over the course of 15 cycles, $R_{NOx:Pd}$ dropped from 0.98 to 0.76. The observed PNA degradation occurring on Pd/SSZ-13 is essentially the same as Pd/BEA, although it takes more cycles to see a significant change in $R_{NOx:Pd}$. A decrease in CO oxidation activity is also observed with a continuous shift in light off curves to higher temperature as is shown in supporting information **Figure S1**. These degradation characteristics are consistent with literature reported results under similar conditions, and highlight the detrimental effect of co-feeding CO.[37–39] For instance, Theis et al. reported the NOx storage capacities of Pd/BEA and Pd/SSZ-13 PNAs over consecutive cold start tests with a variety of gas compositions. The results show that regardless of the zeolite topology, as long as CO is present during the experiments, whether cofed with H_2 or C_2H_4, the NOx storage capacity drops as the number of cycles increases.[39] Combining literature reported results with the degradation characteristics reported here, we can reasonably relate the degradation mode to CO exposure and generalize it to Pd/zeolite based PNAs.

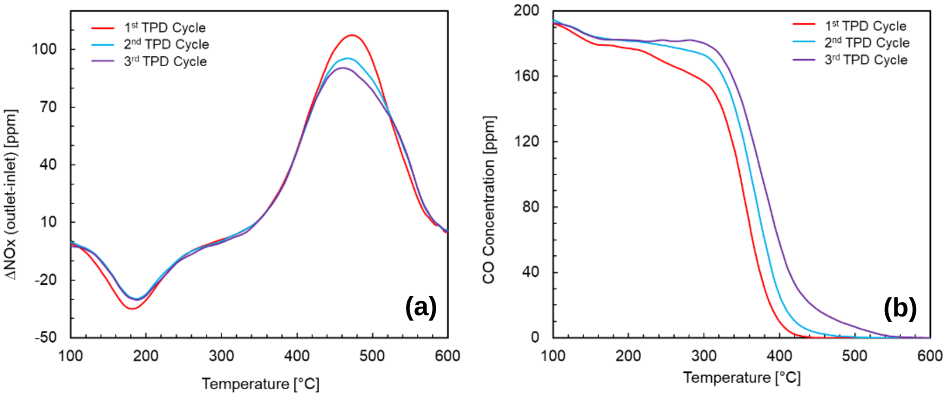

Figure 7.2 Consecutive NOx-TPD profiles (a) and the simultaneous CO oxidation light-off curves (b) of Pd/SSZ-13 PNA over the first three cycles. Feed composition: 200 ppm NO, 200 ppm CO, 4.5% H_2O, 10% O_2 and N_2 balance.

7.3.2 Integration of PNA with an Oxidation Catalyst

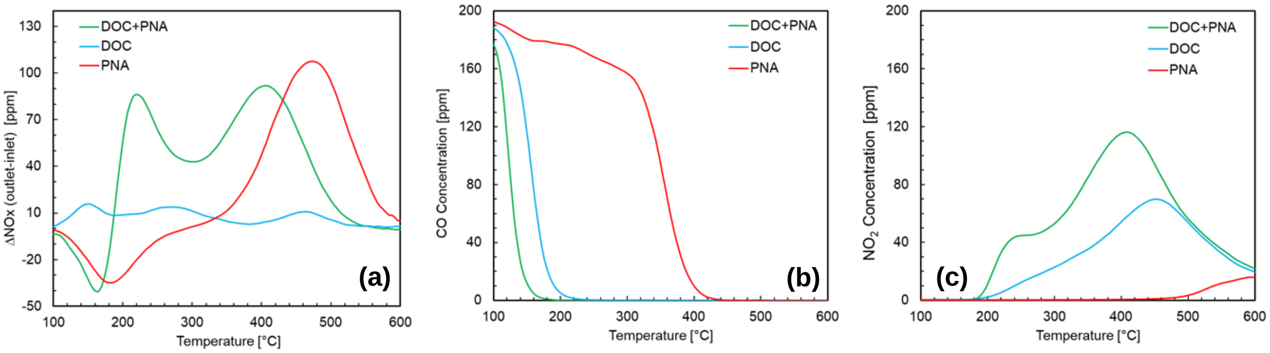

Figure 7.3 NOx-TPD profiles (a), and the simultaneous CO oxidation light-off curves (b) and NO_2 concentration profiles (c) of Pd/SSZ-13 PNA (red), Pt/Al_2O_3 (light blue) and PNA+DOC integrated with Pt/Al_2O_3 (green) during the temperature ramp. Feed composition: 200 ppm NO, 200 ppm CO, 4.5% H_2O, 10% O_2 and N_2 balance.

Having established the correlation between CO exposure and the observed PNA degradation mode, we next performed a similar series of TPD cycles on an PNA+DOC integrated system that contains the Pd/SSZ-13 PNA discussed in the previous section and a Pt/Al_2O_3 DOC. Control experiments were also performed on the Pt/Al_2O_3 DOC catalyst. **Figure 7.3** reports the NOx TPD profiles, CO oxidation light off curves, and profiles of NO_2 released during the first cycle over the three different systems. As is shown in **Figure 7.3 (a)**, we observed different NOx release features from the PNA+DOC integrated system compared to the experiment using only the PNA. The integration with the DOC leads to formation of two different NOx release features instead of one, as was observed with the PNA, featuring the appearance of a low temperature (220 °C) NOx desorption peak and overall, less NOx desorbed above 400°C. This shift in NOx desorption temperature is potentially beneficial when applying this system to lean burn diesel engine exhaust, where the exhaust temperature is typically lower than 400 °C.[11,12] Despite the significant change in NOx desorption characteristics, the initial $R_{NOx:Pd}$ of the PNA+DOC integrated system is 1.05±0.05, which is slightly higher than the initial $R_{NOx:Pd}$ of the PNA by itself. This indicates that the PNA is still the main NOx storage material within the PNA+DOC integrated system. The slight increase in total NOx storage capacity is likely due to a small amount of nitrate formed on the DOC component [50] indicated by the not negligible amount of NOx released during TPD shown in **Figure 7.3 (a)**.

The CO oxidation light-off curves shown in Figure 6.3 (b) demonstrate a significant difference in CO oxidation activities between the PNA and DOC, and that the highest CO oxidation activity is achieved by integrating the two components. Note that Pd/SSZ-13 is a comparatively inactive CO oxidation catalyst before NOx release starts.[51] More specifically, CO oxidation is inhibited by adsorbed NOx[36,52] thus the observation of the simultaneous NOx release and the onset of CO oxidation captured by the desorption profile and light off curve in Figure 6.3 (a)&(b). It is apparent in comparing CO oxidation on Pt/Al_2O_3 with the PNA+DOC integrated system that the majority of the CO oxidation activity comes from the DOC. Additionally, the observed difference in CO oxidation activities of the three studied systems will lead to the PNA being exposed to different amounts of CO at different temperatures. As is shown in Figure 6.3 (c), the difference in CO exposure additionally influences NO_2 formation, which could affect the NOx release characteristics. Unlike the CO oxidation light-off curves of the three reported systems, where the effect of DOC integration appears to be additive, the NO_2 formation of the PNA+DOC integrated system is significantly higher than that observed over the individual components. The difference between the NO_2 release profiles from the PNA and the PNA+DOC integrated system suggests that NO_2 was released from the PNA component at temperatures from 200 to 450 °C. Furthermore, NO_2 formation was not observed until CO oxidation reached 100% conversion in all three systems. This can be explained by (1) the reaction between CO and NO_2 forming CO_2 and NO or (2) the competition between CO and NO oxidation for dissociated oxygen on Pt.[53–58] Based on these observations, we conclude that the effect of DOC integration includes the enhancement in overall oxidation activity of the system, as expected. Another consequence we observe is the appearance of a lower NOx release feature, which could be potentially explained by the absence of CO, or the early onset of NO oxidation, or both during TPD. Therefore, we examined the effect of CO and NO2 individually.

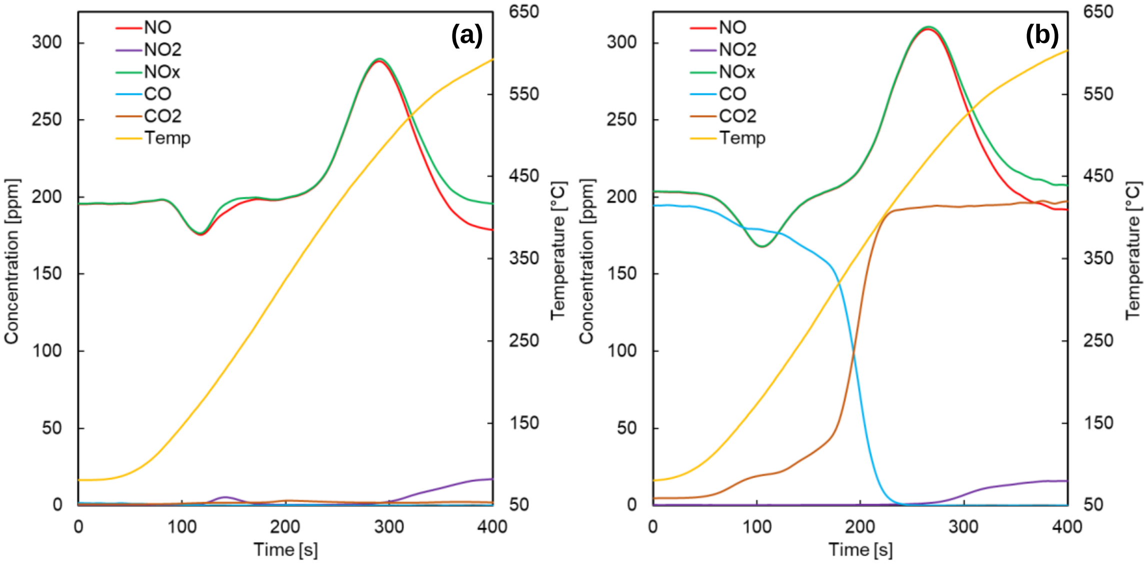

Figure 7.4 Concentration profiles of NOx (green), NO (red), NO_2 (purple), CO (light blue) and CO_2 (orange), and temperature profiles (yellow) during the temperature ramp in the absence of 200 ppm of CO (a) and presence of CO (b). Data collected on Pd/SSZ-13 PNA. Feed composition during adsorption: 200 ppm NO, 200 ppm CO, 4.5% H_2O, 10% O_2 and N_2 balance.

7.3.3 Effect of CO and NO_2

To decouple the effects of DOC integration on NOx desorption characteristics, and understand the evolution of the low temperature NOx release feature we next performed a series of experiments on the PNA and PNA+DOC integrated system investigating the role of CO and NO_2 as they are the key gas components that we observed impacting the NOx desorption characteristics.

We first compared the TPD results of the PNA in the presence and absence of CO after low temperature NO adsorption in the presence of CO. More specifically, we performed NO adsorption in the presence of CO until saturation in both cases, and in one case shut off the CO 10 minutes before the TPD starts. This can also be visualized by the absence of CO or CO_2 in **Figure 7.4 (a)**. The NOx storage capacity is consistent with $R_{NOx:Pd}$ equaling 0.98 for both cases. However, there is no difference in the NOx desorption temperature windows indicating that CO exposure up to about 400 °C does not influence NOx desorption temperature, thus the effect of DOC integration and the evolution of a low temperature NOx release feature cannot be simply explained by the difference in CO exposure shown in **Figure 7.3 (b)**.

As mentioned in the previous section and shown in **Figure 7.3 (c)**, NO_2 formation over the DOC observed at a lower temperature compared to the PNA might contribute to the change in the overall NOx release temperature window for the PNA+DOC integrated system. To validate this hypothesis, we performed a similar experiment with the PNA but in the presence of 30 ppm NO_2 and absence of CO, to eliminate the consumption of NO_2 by CO, during both the adsorption and desorption. The TPD concentration profiles are shown in **Figure 7.5**. The results suggest that co-feeding NO_2 before the temperature ramp leads to NOx release at even lower temperatures (150 °C). Based on these results, we propose that there are two NOx desorption events on the PNA whether integrated with the DOC or not, and one of them is sensitive to NO_2 formation. The other one, centered around 400 °C, is not influenced by CO or NO_2 exposure during the temperature ramp. However, the NOx release profile shown in **Figure 7.5** differs from those shown in **Figure 7.3 (a)**, more specifically, although we did see the evolution of the lower temperature NOx release feature, it is not identical to that shown in Figure 6.3 (a) as it is shifted even further. The mismatch of the NOx release temperature windows can be explained by the different CO exposure conditions. In the presence of CO, NO_2 will be reduced to NO, therefore the data shown in **Figure 7.3** were obtained in the absence of NO_2 until complete CO oxidation. This means that NO_2 was not present to influence NOx adsorption due to the presence of CO and therefore, the influence only occurs during the desorption. In order to mimic the PNA+DOC integrated system in the absence of CO, we would have to ramp the NO_2 concentration during the temperature ramp, which is experimentally challenging.

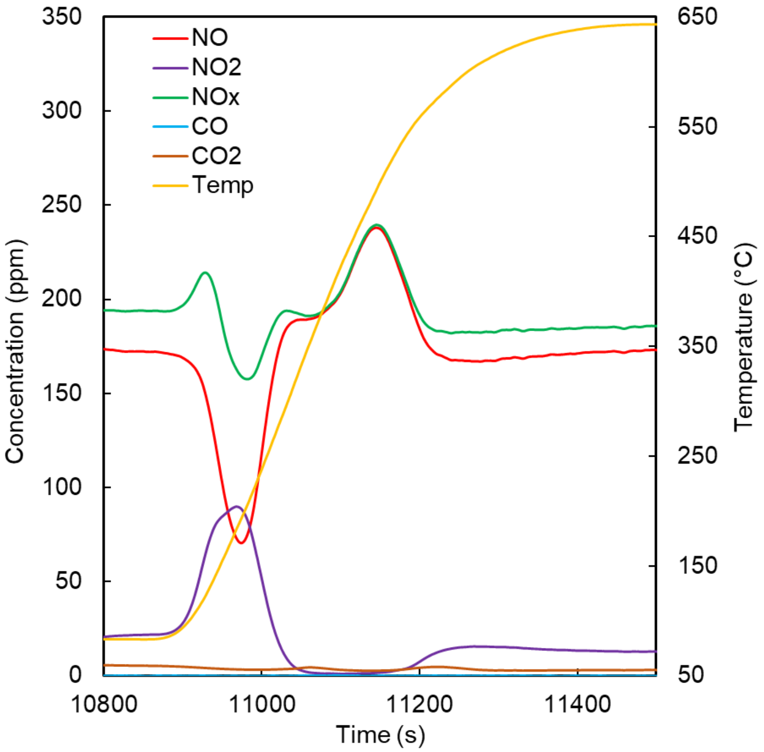

Figure 7.5 Concentration profiles of NOx (green), NO (red), NO_2 (purple), CO (light blue) and CO_2 (orange), and temperature profiles (yellow) during the temperature ramp in the presence of 30 ppm of NO_2. Data collected on Pd/SSZ-13 PNA. Feed composition: 170 ppm NO, 30 ppm NO_2, 4.5% H_2O, 10% O_2 and N_2 balance.

However, at the other extreme, we can remove CO from experiment described in Figure 6.3 for the PNA+DOC integrated system. This is expected to decrease the NO oxidation light off temperature and therefore provide NO_2 exposure at lower temperature as is discussed with **Figure 7.3** in section 3.2. **Figure** 7.**6** shows the NOx release and NO_2 profiles from the PNA+DOC integrated system during the temperature ramp, both in the presence and absence of CO. We observed a 10 °C difference in the onset of NO_2 formation and overall more NO_2 formation at temperatures below 550 °C as a result of the absence of CO, which supports the existence of the competition between NO and CO oxidation that is similar to the competition between NO and C_3H_6 oxidation observed over a Pd/BEA PNA.[59] Additionally, the slightly higher amount of NO_2 formed at low temperature led to the shift in NOx desorption profile from the high temperature feature (400 °C) to the low temperature feature (220 °C). Note, there is a slight increase in total NOx stored likely due to a subtle increase in nitrate formation on the DOC in the absence of CO,[50] which is released at around 200 °C and captured by a 0.04 difference in $R_{NOx:Pd}$. This can also be visualized in the differences between the secondary NOx adsorption feature at around 150 °C and the low temperature NOx release feature at around 220 °C reported in **Figure** 7.**6.** Although the increase in peak intensity at 220 °C could be convoluted by nitrate decomposition, the decrease in peak intensity at 400 °C proves that the early onset of NO oxidation leads to the evolution of the low temperature NOx release feature. These results clearly suggest that the NOx desorption temperature window is sensitive to the onset of NO_2 formation, and the observed evolution of the low temperature NOx release feature (220 °C) with PNA+DOC integrated system is mainly due to the early formation of NO_2 as a result of enhanced oxidation activity. Moreover, the overall higher NOx desorption temperature of the PNA before integrating with the DOC can also be rationalized by the limited NO oxidation activity as indicated by both **Figures 7.3 (c)** and 7.**4 (b)**.

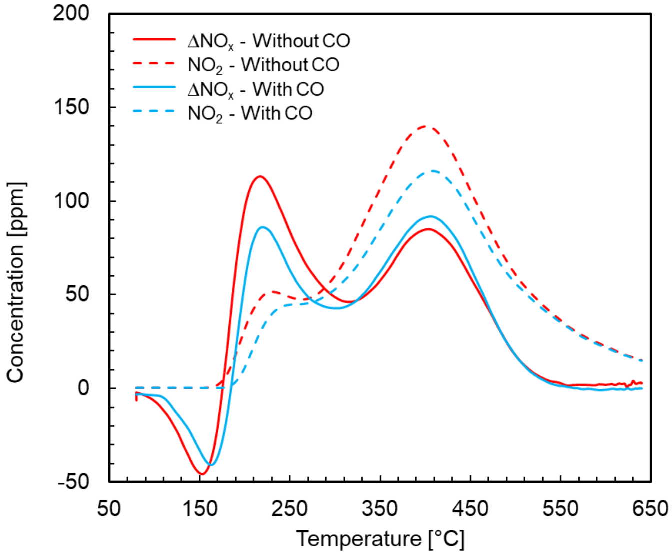

Figure 7.6 Concentration profiles of NO_2 (dashed lines) and released NOx (solid lines) during the temperature ramp in the presence of 200 ppm of CO (blue) and absence of CO (red). Data collected on the PNA+DOC integrated system. Feed composition with CO: 200 ppm NO, 200 ppm CO, 4.5% H_2O, 10% O_2 and N_2 balance. Feed composition without CO: 200 ppm NO, 4.5% H_2O, 10% O_2 and N_2 balance.

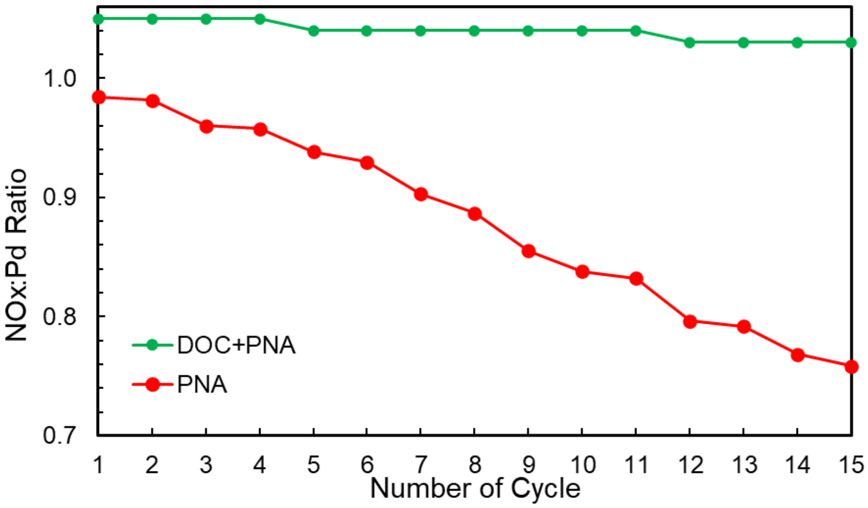

Figure 7.7. NOx-to-Pd ratios of Pd/SSZ-13 PNA(red) and Pd/SSZ-13 PNA integrated with Pt/Al_2O_3 DOC (green) as a function of number of cycles.

7.3.4 Enhancement of Degradation Resistance

As is discussed in the literature and demonstrated in section 3.1, CO exposure leads to an irreversible loss of PNA NOx storage capacity. Therefore, another impact of DOC integration with the PNA is the enhanced resistance against CO induced degradation by eliminating high temperature CO exposure. Here we plot the $R_{NOx:Pd}$ of the PNA+DOC integrated system as a function of cycle number together with the $R_{NOx:Pd}$ of the PNA in **Figure 7.7** for comparison. We also report the consecutive NOx-TPD profiles and the simultaneous CO oxidation light off curves of the PNA+DOC integrated system over the first 6 cycles in **Figure 7.8**. Although a slow decrease in $R_{NOx:Pd}$ is still observed, **Figure 7.7** clearly demonstrates that the PNA+DOC integrated system is significantly more durable as the $R_{NOx:Pd}$ remains as high as 1.03, only decreasing from 1.05 even after 15 cycles in the presence of CO as opposed to the continuous drop of $R_{NOx:Pd}$ from 0.98 to 0.75 observed on the PNA without a DOC being integrated. The initial difference in total NOx storage capacity is, again, due to the minor formation of nitrate species on the DOC, as is discussed in section 3.2. As is shown in **Figure 7.8 (b)** and consistent with **Figure 7.3 (b)**, the integrated PNA + DOC exhibits the most active CO oxidation, where the CO conversion reaches 100% at around 200 °C. Although the temperature requirement for CO induced degradation is currently not well-understood, the integration with the DOC leads to the absence of CO in the downstream PNA at any temperatures above 200 °C. Hence, it is reasonable to conclude that the durability of the PNA+DOC integrated system is achieved by the PNA component avoiding CO exposure at temperatures above 200 °C.

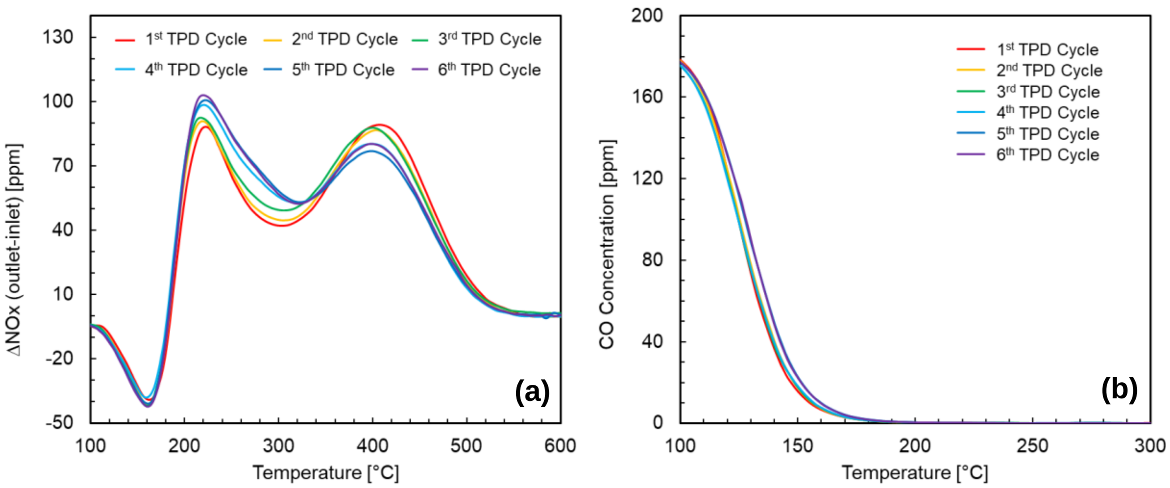

Figure 7.8. Consecutive NOx-TPD profiles (a) and the simultaneous CO oxidation light-off curves (b) of Pd/SSZ-13 integrated with Pt/Al_2O_3 over the first six cycles.

Although the total NOx storage capacity remains relatively stable, as the number of cycles increase, **Figure 7.8 (a)** shows a decrease in NOx desorbed at 400 °C and an increase in NOx desorbed at 220 °C, similar to what was discussed for **Figure 7.5**. In section 3.3 we attribute the same trend to the change in the onset of NO_2 formation, which was due to the absence of CO. CO oxidation experiments performed on the Pt/Al_2O_3 DOC reported in the supporting information **Figure S2** demonstrate that there should be no changes in CO oxidation activity over the DOC with cycling under these conditions. However, the results shown in **Figure 7.8 (b)** suggest a 5 °C difference at 50% conversion after 6 cycles which must be attributed to the changes in the PNA. Based on these results we speculate that Pd migration from one ion-exchange position to another is responsible for the observed differences in the amount of NOx desorbed at the two temperatures, and the slight shift in CO oxidation light-off curves is due to their intrinsic difference in Pd oxidation activities. As is discussed in section 3.3, there are two NOx desorption events, which we propose are associated with two types of Pd cations. Integration with the DOC protects the PNA Pd cations from CO induced detachment from the zeolite and the formation of PdO particles.

However, Pd can migrate from one ion-exchange position to another, which is widely observed in Cu ion-exchanged zeolite systems and leads to different mechanistic consequences.[60–63] We speculate an analogous mechanism as Cu migration during hydrothermal aging to be the chemistry behind this phenomenon,[61,62] although more mechanistic insights are needed.

Although the integration with a DOC slowed the degradation, the slight but non-zero decrease in NOx storage capacity with an increasing number of cycles remains a concern, since any small irreversible loss of NOx storage capacity will accumulate. These results suggest that we need to better understand the temperature dependence of CO degradation such that we can define a temperature range where no degradation will occur. Finally, the results also suggest that successful PNA commercialization can be enabled by a superior low temperature CO oxidation catalyst under realistic exhaust conditions.

7.4 Conclusions

Pd/zeolite based PNAs are vulnerable to CO induced degradation leading to an irreversible loss of their NOx storage capacities over consecutive cold start adsorption and desorption cycles. The NOx release temperature window of Pd/SSZ-13 is 350 - 550 °C, which is too high to be independently applied to diesel exhaust after-treatment systems due to the potential of insufficient NOx storage capacity regeneration under pseudo-steady state operating conditions. Our results show that integrating a Pd/SSZ-13 PNA with a Pt/Al_2O_3 oxidation catalyst leads to enhanced resistance against CO induced degradation and a more reasonable NOx release temperature window. The lower CO oxidation light-off temperature of the PNA+DOC integrated system is responsible for the enhanced durability by mitigating PNA CO exposure at temperatures above 200 °C. We observed a 0.02 drop in NOx-to-Pd ratio after 15 cycles using the PNA+DOC integrated system, versus 0.23 with no DOC integrated, and conclude that complete CO oxidation at even lower temperature could further protect the PNA from degradation. The enhanced oxidation activity of the PNA+DOC integrated system also leads to NO_2 formation at a significantly lower temperature, which triggers NOx desorption at around 220 °C. This evolution shows that at least two NOx storage mechanisms exist, one of which is relatively more sensitive to NO_2 exposure and can be destabilized by NO_2. Over the 15 TPD cycles on the PNA+DOC integrated system we observed a change in the distribution of NOx desorbed at 220 and 400 °C indicating Pd migration between two cation sites, similar to what has been observed with Cu/SSZ-13 systems.

7.5 References

[1] J. Wang, H. Chen, Z. Hu, M. Yao, Y. Li, A review on the Pd-based three-way catalyst, Catal. Rev. - Sci. Eng. 57 (2015) 79–144.

[2] P. Granger, V.I. Parvulescu, Catalytic NOx abatement systems for mobile sources: From three-way to lean burn after-treatment technologies, Chem. Rev. 111 (2011) 3155–3207.

[3] W.S. Epling, L.E. Campbell, A. Yezerets, N.W. Currier, J.E. Parks, Overview of the Fundamental Reactions and Degradation Mechanisms of NOx Storage/Reduction Catalysts, Catal. Rev. 46 (2004) 163–245.

[4] A.M. Beale, F. Gao, I. Lezcano-Gonzalez, C.H.F. Peden, J. Szanyi, Recent advances in automotive catalysis for NOx emission control by small-pore microporous materials, Chem. Soc. Rev. 44 (2015) 7371–7405.

[5] C. Paolucci, A.A. Parekh, I. Khurana, J.R. Di Iorio, H. Li, J.D. Albarracin Caballero, A.J. Shih, T. Anggara, W.N. Delgass, J.T. Miller, F.H. Ribeiro, R. Gounder, W.F. Schneider, Catalysis in a Cage: Condition-Dependent Speciation and Dynamics of Exchanged Cu Cations in SSZ-13 Zeolites, J. Am. Chem. Soc. 138 (2016) 6028–6048.

[6] C. Paolucci, I. Khurana, A.A. Parekh, S. Li, A.J. Shih, H. Li, J.R. Di Iorio, J.D. Albarracin-Caballero, A. Yezerets, J.T. Miller, W.N. Delgass, F.H. Ribeiro, W.F. Schneider, R. Gounder, Dynamic multinuclear sites formed by mobilized copper ions in NOx selective catalytic reduction, Science (80-.). 357 (2017) 898–903.

[7] R.J. Farrauto, M. Deeba, S. Alerasool, journey to cleaner air, Nat. Catal. 2 (2019) 603–613.

[8] M.P. Harold, NOx storage and reduction in lean burn vehicle emission control: A catalytic engineer's playground, Curr. Opin. Chem. Eng. 1 (2012) 303–311.

[9] P. Zelenka, W. Cartellieri, P. Herzog, Worldwide diesel emission standards, current

experiences and future needs, Appl. Catal. B Environ. 10 (1996) 3–28.

[10] M. V. Twigg, Progress and future challenges in controlling automotive exhaust gas emissions, Appl. Catal. B Environ. 70 (2007) 2–15.

[11] B.T. Johnson, Diesel Engine Emissions and Their Control, Platin. Met. Rev. 52 (2008) 23–37.

[12] H.C. Frey, Trends in onroad transportation energy and emissions, J. Air Waste Manage. Assoc. 68 (2018) 514–563.

[13] S.K. Grange, N.J. Farren, A.R. Vaughan, R.A. Rose, D.C. Carslaw, Strong Temperature Dependence for Light-Duty Diesel Vehicle NOx Emissions, Environ. Sci. Technol. 53 (2019) 6587–6596.

[14] T. Selleri, I. Nova, E. Tronconi, V. Schmeisser, S. Seher, The impact of light and heavy hydrocarbons on the NH3-SCR activity of commercial Cu- and Fe-zeolite catalysts, Catal. Today. 320 (2019) 100–111.

[15] G.D. Neely, D. Mehta, J. Sarlashkar, Diesel Cold-Start Emission Control Research for 2015-2025 LEV III Emissions - Part 2, SAE Int. J. Engines. 7 (2014) 2014-01–1552.

[16] A.K. Datye, M. Votsmeier, Opportunities and challenges in the development of advanced materials for emission control catalysts, Nat. Mater. (2020).

[17] V. Schmeisser, M. Weibel, L. Sebastian Hernando, I. Nova, E. Tronconi, M.P. Ruggeri, Cold Start Effect Phenomena over Zeolite SCR Catalysts for Exhaust Gas Aftertreatment, SAE Int. J. Commer. Veh. 6 (2013) 2013-01–1064.

[18] C.K. Lambert, Current state of the art and future needs for, Nat. Catal. 2 (2019).

[19] C.K. Lambert, Perspective on SCR NOx control for diesel vehicles, React. Chem. Eng. 4 (2019) 969–974.

[20] H.-Y. Chen, J.E. Collier, D. Liu, L. Mantarosie, D. Durán-Martín, V. Novák, R.R. Rajaram, D. Thompsett, Low Temperature NO Storage of Zeolite Supported Pd for Low Temperature Diesel Engine Emission Control, Catal. Letters. 146 (2016) 1706–1711.

[21] H.Y. Chen, S. Mulla, E. Weigert, K. Camm, T. Ballinger, J. Cox, P. Blakeman, Cold start concept (CSC^{TM}): A novel catalyst for cold start emission control, SAE Tech. Pap. 2 (2013) 372–381.

[22] H.-Y. Chen, D. Liu, E. Weigert, L. Cumaranatunge, K. Camm, P. Bannon, J. Cox, L. Arnold, Durability Assessment of Diesel Cold Start Concept (dCSC^{TM}) Technologies, SAE Int. J. Engines. 10 (2017) 2017-01–0955.

[23] R.F. Ilmasani, J. Woo, D. Creaser, L. Olsson, Influencing the NOxStability by Metal Oxide Addition to Pd/BEA for Passive NOx Adsorbers, Ind. Eng. Chem. Res. 59 (2020) 9830–9840.

[24] Y. Zheng, L. Kovarik, M.H. Engelhard, Y. Wang, Y. Wang, F. Gao, J. Szanyi, Low-Temperature Pd/Zeolite Passive NOx Adsorbers: Structure, Performance and Adsorption Chemistry, J. Phys. Chem. C. (2017) 121 (29), 15793-15803

[25] Y. Gu, W.S. Epling, Passive NOx adsorber: An overview of catalyst performance and reaction chemistry, Appl. Catal. A Gen. 570 (2019) 1–14.

[26] Porta, A., Pellegrinelli, T., Castoldi, L., Matarrese, R., Morandi, S., Dzwigaj, S., & Lietti, L. (2018). Low temperature NOx adsorption on Pd-promoted zeolites. In 11th International Congress on Catalysis and Automotive Pollution Control, CAPoC 11 (pp. 15-15).

[27] Y. Ryou, J. Lee, S.J. Cho, H. Lee, C.H. Kim, D.H. Kim, Activation of Pd/SSZ-13 catalyst by hydrothermal aging treatment in passive NO adsorption performance at low temperature for cold start application, Appl. Catal. B Environ. 212 (2017) 140–149.

[28] J. Lee, Y. Ryou, S. Hwang, Y. Kim, S.J. Cho, H. Lee, C.H. Kim, D.H. Kim, Comparative study of the mobility of Pd species in SSZ-13 and ZSM-5, and its implication for their activity as passive NO x adsorbers (PNAs) after hydro-thermal aging, Catal. Sci. Technol. 9 (2019) 163–173.

[29] J.R. Theis, C.K. Lambert, An assessment of low temperature NOx adsorbers for cold-start NOx control on diesel engines, Catal. Today. 258 (2015) 367–377.

[30] Y. Ryou, J. Lee, Y. Kim, S. Hwang, H. Lee, C.H. Kim, D.H. Kim, Effect of reduction treatments (H2 vs. CO) on the NO adsorption ability and the physicochemical properties of Pd/SSZ-13 passive NOx adsorber for cold start application, Appl. Catal. A Gen. 569 (2019) 28–34.

[31] Y. Ryou, J. Lee, H. Lee, C.H. Kim, D.H. Kim, Effect of various activation conditions on the low temperature NO adsorption performance of Pd/SSZ-13 passive NOx adsorber, Catal. Today. (2017).

[32] A. Vu, J. Luo, J. Li, W.S. Epling, Effects of CO on Pd/BEA Passive NOx Adsorbers, Catal. Letters. 147 (2017) 745–750.

[33] K. Khivantsev, N.R. Jaegers, L. Kovarik, J.C. Hanson, F. (Feng) Tao, Y. Tang, X. Zhang, I.Z. Koleva, H.A. Aleksandrov, G.N. Vayssilov, Y. Wang, F. Gao, J. Szanyi, Achieving Atomic Dispersion of Highly Loaded Transition Metals in Small-Pore Zeolite SSZ-13: High-Capacity and High-Efficiency Low-Temperature CO and Passive NO x Adsorbers, Angew. Chemie Int. Ed. 57 (2018) 16672–16677.

[34] A. Gupta, S.B. Kang, M.P. Harold, NOx uptake and release on Pd/SSZ-13: Impact Of Feed composition and temperature, Catal. Today. (2020).

[35] M. Ambast, K. Karinshak, B.M.M. Rahman, L.C. Grabow, M.P. Harold, Passive NOx

adsorption on Pd/H-ZSM-5: Experiments and modeling, Appl. Catal. B Environ. 269 (2020) 118802.

[36] K. Mandal, Y. Gu, K.S. Westendorff, S. Li, J.A. Pihl, L.C. Grabow, W.S. Epling, C. Paolucci, Condition-Dependent Pd Speciation and NO adsorption in Pd/Zeolites, ACS Catal. (2020).

[37] J.R. Theis, C. Lambert, The Effects of CO, C_2H_4, and H_2O on the NOx Storage Performance of Low Temperature NOx Adsorbers for Diesel Applications, SAE Int. J. Engines. 10 (2017) 2017-01–0942.

[38] Y. Gu, R.P. Zelinsky, Y.-R. Chen, W.S. Epling, Investigation of an irreversible NOx storage degradation Mode on a Pd/BEA passive NOx adsorber, Appl. Catal. B Environ. 258 (2019) 118032.

[39] J.R. Theis, J.A. Ura, Assessment of zeolite-based Low temperature NOx adsorbers: Effect of reductants during multiple sequential cold starts, Catal. Today. (2020)

[40] O. Mihai, L. Trandafilović, T. Wentworth, F.F. Torres, L. Olsson, The Effect of Si/Al Ratio for Pd/BEA and Pd/SSZ-13 Used as Passive NOx Adsorbers, Top. Catal. 61 (2018) 2007-2020.

[41] D. Mei, F. Gao, J. Szanyi, Y. Wang, Mechanistic insight into the passive NOx adsorption in the highly dispersed Pd/HBEA zeolite, Appl. Catal. A Gen. 569 (2019) 181–189.

[42] J. Lee, Y. Kim, S. Hwang, E. Lee, H. Lee, C.H. Kim, D.H. Kim, Deactivation of Pd/Zeolites passive NOx adsorber induced by NO and H_2O: Comparative study of Pd/ZSM-5 and Pd/SSZ-13, Catal. Today. (2020).

[43] Q. Yu, X. Chen, A. Bhat, X. Tang, H. Yi, X. Lin, J.W. Schwank, Activation of passive NOx adsorbers by pretreatment with reaction gas mixture, Chem. Eng. J. 399 (2020) 125727.

[44] H. Zhao, X. Chen, A. Bhat, Y. Li, J.W. Schwank, Understanding the chemistry during the preparation of Pd/SSZ-13 for the low-temperature NO adsorption: The role of NH_4-SSZ-13 support, Appl. Catal. B Environ. (2020) 119611.

[45] J.R. Theis, J.A. Ura, Assessment of zeolite-based Low temperature NOx adsorbers: Effect of reductants during multiple sequential cold starts, Catal. Today. (2020).

[46] S.A. Malamis, M.P. Harold, Optimizing the lean hydrocarbon NO trap: Sequential and dual-layer configurations, Catal. Today. (2020).

[47] A. Wang, K. Xie, A. Kumar, K. Kamasamudram, L. Olsson, Layered Pd/SSZ-13 with Cu/SSZ-13 as PNA − SCR dual-layer monolith catalyst for NOx abatement, Catal. Today. (2020).

[48] K. Chilumukuru, A. Gupta, M. Ruth, M. Cunningham, G. Kothandaraman, L. Cumaranatunge, H. Hess, Aftertreatment Architecture and Control Methodologies for Future Light Duty Diesel Emission Regulations, SAE Int. J. Engines. 10 (2017) 2017-01–0911.

[49] A. Wang, K. Lindgren, M. Di, D. Bernin, P.A. Carlsson, M. Thuvander, L. Olsson, Insight into hydrothermal aging effect on Pd sites over Pd/LTA and Pd/SSZ-13 as PNA and CO oxidation monolith catalysts, Appl. Catal. B Environ. 278 (2020) 119315.

[50] A. Russell, W.S. Epling, Diesel oxidation catalysts, Catal. Rev. - Sci. Eng. 53 (2011) 337–423.

[51] J. Lee, J. Kim, Y. Kim, S. Hwang, H. Lee, C.H. Kim, D.H. Kim, Improving NOx storage and CO oxidation abilities of Pd/SSZ-13 by increasing its hydrophobicity, Appl. Catal. B Environ. 277 (2020) 119190.

[52] P. Boutikos, A. Žák, P. Kočí, CO and hydrocarbon light-off inhibition by pre-adsorbed NOx

on Pt/CeO2/Al2O3 and Pd/CeO_2/Al_2O_3 diesel oxidation catalysts, Chem. Eng. Sci. 209 (2019).

[53] A. Boubnov, S. Dahl, E. Johnson, A.P. Molina, S.B. Simonsen, F.M. Cano, S. Helveg, L.J. Lemus-Yegres, J.D. Grunwaldt, Structure-activity relationships of Pt/Al_2O_3 catalysts for CO and NO oxidation at diesel exhaust conditions, Appl. Catal. B Environ. 126 (2012) 315–325.

[54] A.A. Kroupnov, M.J. Pogosbekian, DFT calculation-based study of the mechanism for CO_2 formation in the interaction of CO and NO_2 molecules, Chem. Phys. Lett. 710 (2018) 90–95.

[55] H.B. Palmef, H. Freund, The Reaction Between NO_2 and CO, Combust. Sci. Technol. 21 (1980) 179–180.

[56] D. Milks, T.N. Adams, R.A. Matula, Single pulse shock tube study of the reaction between nitrogen dioxide (NO_2) and carbon monoxide (CO), Combust. Sci. Technol. 19 (1979) 151–159.

[57] H. Oh, I.S. Pieta, J. Luo, W.S. Epling, Reaction kinetics of C_3H_6 oxidation for various reaction pathways over diesel oxidation catalysts, Top. Catal. 56 (2013) 1916–1921.

[58] M.J. Hazlett, W.S. Epling, Spatially resolving CO and C_3H_6 oxidation reactions in a Pt/Al_2O_3 model oxidation catalyst, Catal. Today. 267 (2016) 157–166.

[59] S.A. Malamis, M.P. Harold, W.S. Epling, Coupled NO and C_3H_6 Trapping, Release and Conversion on Pd/BEA: Evaluation of the Lean Hydrocarbon NOx Trap, Ind. Eng. Chem. Res. 58 (2019) 22912–22923.

[60] Y. Jangjou, Q. Do, Y. Gu, L.G. Lim, H. Sun, D. Wang, A. Kumar, J. Li, L.C. Grabow, W.S. Epling, Nature of Cu Active Centers in Cu-SSZ-13 and Their Responses to SO_2 Exposure,

ACS Catal. 8 (2018) 1325–1337.

[61] J. Luo, K. Kamasamudram, N. Currier, A. Yezerets, NH3-TPD methodology for quantifying hydrothermal aging of Cu/SSZ-13 SCR catalysts, Chem. Eng. Sci. 190 (2018) 60–67.

[62] D. Wang, Y. Jangjou, Y. Liu, M.K. Sharma, J. Luo, J. Li, K. Kamasamudram, W.S. Epling, A comparison of hydrothermal aging effects on NH_3-SCR of NOx over Cu-SSZ-13 and Cu-SAPO-34 catalysts, Appl. Catal. B Environ. 165 (2015) 438–445.

[63] Y. Jangjou, C.S. Sampara, Y. Gu, D. Wang, A. Kumar, J. Li, W.S. Epling, Mechanism-based kinetic modeling of Cu-SSZ-13 sulfation and desulfation for NH_3 -SCR applications, React. Chem. Eng. 4 (2019) 1038–1049.

Conclusions

Pd/zeolite passive NOx adsorbers represent a group of materials that are interesting for engine cold start NOx emission abatement. Although different strategies and technologies have been considered to address the same problem, future emission regulations that put emphasis on the reduction of regulated pollutants under non-standard driving conditions will continue to drive the advancement of low temperature catalysis. In this dissertation, we addressed several unique challenges associated with low temperature NOx trapping using Pd/zeolites, with a focus on establishing the mechanism under relatively more realistic conditions. We demonstrated that the optimization of a PNA incorporated system can be achieved via understanding the nature of Pd active sites, condition dependent NO adsorption and desorption characteristics, and the mechanism of potential degradation modes.

Pd speciation within a zeolite framework is complex and condition dependent. Our experiments demonstrate that the population of chabazite ion-exchange sites by Pd cations largely depends on the aluminum arrangement due to different thermodynamic drive forces and is a function of zeolite composition and Pd loading. H_2O solvation at low temperatures leads to the detachment of Pd cations from the chabazite framework, which is a general phenomenon of all Pd zeolites and has consequences on their adsorption and reaction energetics. The NO adsorption mechanism in the presence of H_2O differs significantly from that under dry conditions due to the formation of these H_2O solvated Pd cations. The presence of CO kinetically affects NO adsorption but does not influence the ultimate formation of H_2O solvated Pd-nitrosyl species. NO adsorption and desorption characteristics of a commercial Pd/ZSM PNA and the influence of CO are significantly affected by temperature and H_2O concentration due to the solvated nature of Pd cations. NO adsorption in the presence of H_2O and CO follows different reaction paths and with different rates depending on temperature and gas composition.

NO desorption in the presence of H_2O and CO as temperature increases is accompanied with the occurrence of several competing processes which lead to the eventual degradation of Pd/zeolite based PNAs due to Pd migration from ion-exchanged domain to the particle domain. Pd reduction by CO and the immediate reoxidation by O_2 were identified and represent two key reactions taking place during desorption. Although the reducibility of solvated Pd cations is not influenced by temperature or zeolite topology, the oxidative regeneration of metallic Pd particles formed as a reduction product exhibits clear temperature dependency due to particle agglomeration. Higher temperature leads to the formation of larger Pd particles after reduction because of accelerated Pd agglomeration, and therefore the irreversible formation of large PdO particles upon reoxidation. The regeneration of large PdO particles is less thermodynamically favored at the temperatures they are formed, thus the irreversible loss of NOx storage capacity observed during NO adsorption and desorption cycles.

The integration of an oxidation catalyst with Pd/zeolite based PNAs significantly enhances the system durability and also leads to an overall lower NOx desorption temperature. The avoidance of PNA CO exposure at high temperatures due to complete CO oxidation by an upstream oxidation catalyst protects Pd cations from being reduced, thus minimizing the irreversible formation of PdO particles during desorption. The enhanced oxidation activity of the integrated system also leads to the early onset of NO_2 formation during a temperature ramp which leads to the occurrence of NO desorption at a reasonably lower temperature. Although a slow degradation was still observed over NO adsorption and desorption cycles, we demonstrate that the system performance and durability can be further improved by integrating with a great CO oxidation catalyst.

Chapter 8. Appendix A - Passive NOx Adsorber: An Overview of Catalyst Performance and Reaction Chemistry

This chapter is published in Applied Catalysis A: General and can be found as: Y. Gu, W.S. Epling, Passive NOx adsorber: An overview of catalyst performance and reaction chemistry, Appl. Catal. A Gen. 570 (2019) 1–14.

8.1 Introduction

Regulated engine exhaust emissions can be mitigated using three-way catalysts for stoichiometric-burn gasoline engines, or using a combination of catalysts, including an oxidation catalyst, a NOx reduction catalyst and a particulate filter, for lean-burn diesel engines. For both though, cold start emissions are problematic. Cold start occurs when the engine is started, and the engine block, tailpipe and catalysts warm up from ambient temperature. Hence, the exhaust after-treatment system is at low temperature and therefore less effective due to kinetic limitations. With emission regulations becoming progressively more stringent and the engine exhaust temperature decreasing as a result of increasing fuel efficiency, cold start will become more problematic[1–5]. This is especially true in the case of lean burn diesel engines where an excessive amount of air exists[2,5–7]. Overall, cold start emissions abatement remains a challenge and will become more challenging[3,8]. The US EPA Urban Dynamometer Driving Schedule (FTP-72 and FTP-75), as examples of typical test cycles for light-duty gasoline engines, consist of a 505 second cold start phase with a 0.43 weighing factor, whereas the counterpart for heavy-duty diesel engines (Heavy-Duty FTP transient cycle) is run with both cold and hot start tests with a weighing factor of 1/7 and 6/7 for the cold start and hot start, respectively, to address the significance of cold start in testing procedures.

NOx emissions are widely regulated due to their toxicity and detrimental effects on health and the environment. An NH_3-SCR system with a state-of-the-art catalyst can effectively reduce NOx generated from a lean burn engine once the exhaust temperature exceeds 200 °C[9–11]. Similarly, lean NOx traps (LNTs) and three-way catalysts (TWCs) with optimized formulations are highly effective in reducing NOx[10,12–15]. However, with kinetic limitations at low temperature, neither system can remediate NOx emissions effectively during cold start. Arguably, LNT and TWC low temperature activity can be further improved to minimize NOx emitted during cold start, but the inability of decomposing the currently required aqueous urea solution at low temperature (<180 °C) makes application of NH_3-SCR systems prohibitive[16].

To address NOx emitted during cold start, a device with the ability to temporarily store NOx and thermally release NOx has been proposed. A series of patents from the automobile and catalyst manufacturing industries indicate that this technology has been conceptually established for some time[17–19], but due to the rapid development of a variety of other deNOx technologies it apparently did not attract the same attention as it has more recently. Over the last few years there has been renewed interest in this approach with publications in the open literature by Johnson Matthey Inc., specifically referring to nitric oxide adsorbents that can be thermally regenerated as part of a cold-start concept[19,20]. Since then, different groups of materials have been extensively evaluated for NOx adsorption and release. To date, this approach has been developed into one of the most promising technologies for cold start NOx emission control, and the systems are often referred to as passive NOx adsorbers or PNAs[21–30].

8.1.1 Functionality

As a supplemental device for currently existing after treatment systems, PNAs are designed to reduce NOx emissions during the cold start period[30]. Notably, cold start is a transient process with a relatively fixed time duration, therefore, the amount of NOx generated within such a period is finite. And because of this unique behavior, PNAs are able to overcome the catalytic reduction reaction challenge by simply adsorbing NOx at low temperatures instead of converting them immediately. The exhaust gas temperature will eventually exceed 200 °C, where NOx reduction catalysts are efficient, and ideally in the time to reach 200 °C, all the NOx from the engine will adsorb on the PNA.

Furthermore, again ideally, as soon as the exhaust gas temperature reaches 200 °C all the NOx that adsorbed during cold start would be released, the driving force of desorption will be nothing but the higher exhaust temperature. However, instead of generating a sharp NOx pulse in the after-treatment system that might be hard to handle, several factors that will be covered in later sections could elongate the NOx release process, but desorption temperatures around 200 °C are favored[11]. An immediate release after warm up takes advantage of a downstream highly active NH_3-SCR catalyst, because by the time NOx desorbs from the PNA, the minimum temperature for aqueous urea decomposition has been reached. However, too high of a NOx desorption temperature could possibly make the device inefficient since an adsorption-desorption cycle cannot be completed.

8.1.2 Overview of Key factors

PNA efficacy and application should be evaluated based on the following factors:

a. Low temperature NOx storage capacity
b. Rate of adsorption
c. NOx desorption temperature
d. Real exhaust compatibility
e. Degradation resistance

f. Cost

PNA storage capacity is normally calculated as the maximum amount of NOx molecules adsorbed per unit mass of the catalyst at a certain temperature[20]. Although when a PNA is operating under real exhaust conditions where the gas phase temperature increases rapidly, NOx uptake measured at a temperature typically lower than 100 °C could still be a good indicator. In considering application, a high low-temperature NOx storage capacity is desired in order to minimize the amount of the catalyst that is required for cold start NOx storage.

The rate of the adsorption also needs to be evaluated when comparing different PNA candidates. For simplicity, the rate of adsorption here is not defined as how fast a gas phase NO molecule near the surface adsorbs onto the catalyst, instead, when a rate of adsorption is measured, the diffusion within the gas phase, the diffusion within the porous catalyst support as well as the adsorption and desorption on/from the storage sites are all considered. To ensure the maximum utilization of the storage capacity, NOx adsorption and cold start duration need to at least be on the same time scale.

NOx desorption is key to not only the regeneration of PNAs but also subsequent NOx adsorption in a later cold start. Desorption temperature is usually reported as the gas-phase temperature when NOx concentration peaks during a temperature programmed desorption (TPD) experiment. In most cases there are several NOx desorption peaks, and thus binding strengths. Unlike adsorption capacity or rate of adsorption, the optimal NOx desorption temperature may vary from case to case, however, for an exhaust after-treatment system consisting of an NH_3-SCR unit, NOx release should at least start no lower than 200 °C. And as noted above, a too high desorption temperature will make the catalyst too hard to regenerate, as too high of a desorption temperature could result in incomplete desorption and less effective storage in a subsequent cold start cycle.

In addition to the low temperature NOx storage capacity and NOx desorption temperature, efficiency under real exhaust conditions is obviously important. As most of the preliminary experiments evaluating PNA candidates have been conducted under simulated exhaust conditions, the difference between simulated and real exhaust conditions needs to be considered to make sure the performance evaluation results are translatable. This usually means a more complicated gas mixture, rapid warm up and fluctuations in space velocity, temperature and gas concentrations.

Analogous to most after-treatment catalysts, PNAs can be subject to severe thermal aging and poisoning. When evaluating catalyst performance, this degradation can be reflected by a decrease in low temperature NOx storage capacity, and/or a shift in desorption temperature into a non-optimal range. Degradation resistance is crucial for catalyst longevity. Therefore, a fundamental understanding of how material changes occur during aging and poisoning can contribute to improvement of overall performance over time.

Lastly, cost is another important factor. PNAs to date typically contain precious metals as storage sites, meanwhile, the synthesis process can also be energy intensive. Therefore, after evaluating the technical viability, the cost of different synthesis methods and the precious metal selection need to be compared to ensure cost efficiency.

8.1.3 Experimental Specifications

The literature reviewed here consists mostly of NOx adsorption and desorption experiments performed in a laboratory with the purpose of either performance evaluation or mechanism identification. Though goals of these experiments are identical, the methodology and the actual procedure may vary, which gives rise to seeming inconsistency.

Low temperature NOx storage experiments are performed by exposing the PNA to NOx-containing gas mixtures. Theis et.al provided a schematic diagram where a three way valve was placed upstream of the reactor, and by doing so, simply switching the valve from a bypass line to the reactor begins NOx exposure[31]. It is worth noticing that a bypass line is necessary for such a setup to perform a step change in the reactor gas environment, especially when the addition of a sequence of gas species significantly effects PNA performance. Zheng et al. showed another setup with a similar methodology[32]. However, they used two four-way valves to perform the switching from bypass to the reactor, such that whichever side was not exposed to simulated exhaust could always be purged by an inert gas or air, or any other mixture. In general, a setup with the ability to create a step change in the reactor gas environment is the basis of low temperature NOx storage experiments with consideration to dead volume critical for accurate measurement.

NOx desorption is often performed after adsorption saturation, which is usually achieved by waiting until the outlet NOx concentration reaches the inlet concentration after a long enough NOx exposure. Set NOx adsorption times can also be used. Temperature programmed desorption (TPD) is usually used, i.e. the temperature of the catalyst increases linearly before a target temperature is reached such that temperature and time can be correlated, and thus, provides additional information about the desorption kinetics[33]. During TPD, NOx and any other exhaust gas components should be flowing to better simulate real conditions, as gas composition significantly impacts NOx release[32,34,35]. Meanwhile, ramp rate could also shift the apparent desorption temperature[33]. **Fig. 1** details a typical transient NO adsorption and TPD experiment procedure, more details about the effect of ramp rate and gas composition will be discussed in a later section.

8.2 Performance evaluation

As discussed in the previous section, there are, at least, six key factors to consider when evaluating the performance of PNAs and determining whether a novel material can be a good PNA candidate. None of these factors can be neglected, and each needs to be analyzed and evaluated systematically. In this section, literature results will be compared in terms of these performance criteria when studied, and to highlight several promising materials that standout. The performance evaluation of potential PNAs will rely on evaluating low temperature NO adsorption and TPD results as discussed previously. This section will mainly focus on studies that provide both adsorption and desorption results.

8.2.1 NO adsorption

When NOx is generated during cold start, it is mainly present as NO in the exhaust. Hence, low temperature NO adsorption specifically is often considered. Since the actual formulation of a PNA, or its integration onto the exhaust after-treatment system is not yet clear, it is possible that precious metals as part of the formulation or an integrated oxidation catalyst such as a diesel oxidation catalyst (DOC) may change the NO/NO_2 ratio along the monolith-supported PNA. Indeed, it has been reported that precious-metal containing PNAs exhibit non-negligible NO oxidation activity even at low temperature [20,32,36]. This section mainly focuses on low temperature NO adsorption, i.e. with NO in the feed. The following subsections provide insights on typical parameters that are reported to affect low temperature NO adsorption behavior. Unresolved issues related to low temperature NOx storage capacity will also be reviewed.

8.2.1.1 NOx storage capacity and rate of adsorption

Among the existing PNA studies, there are three material groups that have been well studied: Pt/Pd/Al_2O_3, Pt/Pd/ceria and Pd/zeolites. Chen et al. reported a Pt/Pd/CeO_2 PNA with a loading of 100 g/ft^3 for both Pt and Pd and a cold start concept catalyst composed of 50 g/ft^3 of Pt and 90 g/ft^3 of Pd[20]. Both showed significant low temperature NOx storage capacity, and the cold start concept catalyst seemed to trap and reduce the most NOx during cold start. Crocker et al. investigated Pt/Pd-based catalysts supported on both alumina and ceria, as well as the effect of rare earth oxide addition and a blended support[37–40]. More recently, in a paper published by Ryou et al., Pd supported on alumina and ceria were evaluated. Although bare ceria without noble metal addition trapped NOx at low temperature, Pd/CeO_2 performed better relative to Pt/CeO_2 and Pt/Pd based catalysts. Oxygen or a highly oxidative environment assists Pd in storing NO, while maintaining the NOx storage capability of the CeO_2 support[41]. However, this group of materials exhibit a severe loss of NOx storage capacity due to sulfur poisoning[42], though Yaying ji et al. reported a slight regeneration of NOx storage capacity on Pd/Mn-Ce(Pr)-Zr mixed oxides after lean desulfations at 760°C , 790°C and 815°C[43]. Chen et al. reported low temperature NOx storage capacities on Pd-SSZ-13, Pd-ZSM-5 and Pd-BEA. The performance evaluation of these catalysts was conducted under relatively more practical exhaust conditions, in the presence of CO, H_2O and n-$C_{10}H_{22}$. More importantly, the NOx storage capacities of sulphated catalysts were also measured. In contrast to Pd/CeO_2, the NOx storage capacities of all the zeolite supported Pd catalysts remained almost unaffected by sulfur poisoning[36]. Zheng et al. provided more insight into the same group of catalysts with detailed characterization results[32]. From their work, the zeolite supported Pd catalysts shared similar adsorption performance after a few NOx adsorption and desorption cycles, however, there were differences in response to aging and the nature of Pd within the different zeolite structures. In other work, Vu et al. evaluated NOx storage capacity of

Pd-BEA[44]. NOx storage capacities of Pd-SSZ-13 catalysts synthesized via different methods after hydrothermal aging were reported by Ryou et al.[45]. Murata et al. reported low temperature NOx storage ability of a Pd-ZSM-5 containing so called N-TWC catalyst[46], a series of Pd-ZSM-5 catalysts were made and evaluated by Lee et al. in an attempt to deduce the active sites[47], and Ag based PNAs were also reported to be able to store NOx at low temperatures under rich conditions[48,49]. As shown, several PNA candidate materials have been studied and characterized.

Although the three materials groups are able to store NOx at low temperatures, it appears that there is convergence towards Pd as the precious metal choice. However, when NOx storage capacities are reported, the amount of Pd varies depending on the washcoat loading and Pd loading. Therefore, NOx storage capacities normalized to the amount of Pd can be meaningful in providing information of not only the storage capacity but also the atomic utility of Pd, which is an important indicator of cost. Similarly, in the case of Pt and Pd being used simultaneously, NOx storage capacities can be normalized to moles of platinum group metals (PGM) yielding a NOx to PGM ratio. **Fig. 2** summarizes some of the reported stored NOx-to-PGM ratios from the papers discussed in this section. Zeolite supported Pd catalysts show high NOx-to-PGM ratios when the Pd weight percentage is less than or equal to ~1 wt.%. In almost all cases, doubling the amount of Pd decreased the NOx-to-PGM ratio. The same trend can be observed among the ceria and alumina supported Pd catalysts as well, while in general these materials store slightly less NOx at relatively lower rates. Simply considering NOx storage capacity, it is still debatable whether introducing PGM is beneficial or not when ceria is used as the catalyst support, because ceria is consistently reported able to store NOx without Pd or Pt addition[50]. However, the advantage of PGM addition becomes apparent when more realistic gas compositions are applied and severe aging as well as adsorption rates are considered[39].

In terms of complete adsorption and time to breakthrough, for Pd-based zeolites, reported values range from 30 s to more than 60 s [20,32,34,51]. Such results indicate that this is a process with small or almost zero activation energy, hence, unlike NOx storage capacities, rates of adsorption have not been quantitatively reported. Arguably, if NO adsorption is a process with a low activation energy barrier, the overall rate of adsorption is very likely to be limited by related mass transfer steps. Therefore, instead of a material formulation dependency, the rate of adsorption would depend on optimization of conditions such as space velocity and washcoat properties. However, for CeO_2 supported or CeO_2/ZrO_2 supported Pd catalysts, two adsorption modes were observed, one of which was relatively slow though it traps significantly more NOx given long enough time[37,39,41]. Despite this interesting phenomenon, it is unlikely to be useful under real conditions, since cold start period usually ends in less than 2-3 minutes.

8.2.1.2 Effects of exhaust species

Apart from NOx, lean burn engine exhaust normally consists of at least N_2, O_2, CO, H_2O, CO_2 and unburned and partially oxidized HCs. N_2, as an inert species, has no effect on NOx storage capacity. O_2 exists in almost all reported transient NOx adsorption tests, as most have focused on lean-burn engine exhaust conditions. Though the air-to-fuel ratio is reported to have an impact on the desorption efficiency of a N-TWC catalyst, the effect of O_2 on NOx storage capacity was otherwise proven to be negligible[46]. However, when it comes to the Pd-zeolite system, especially Pd-SSZ-13, O_2 is key to efficient passive NOx storage. This was further confirmed via an IR study, which suggested that the existence of O_2 activates another NO adsorption route via nitrate formation[52].

CO_2 is a fuel combustion product and has long been reported to have a significant impact on the NOx storage behavior of Pt/Ba/Al_2O_3 NSR catalysts[53]. Ji et al. measured the passive NOx storage capacity of Pt-Al_2O_3 with and without CO_2 and H_2O, and severe inhibition was observed when both CO_2 and H_2O were present[38]. CO_2 inhibition was due to carbonate formation, which is expected to compete with NOx adsorption on Pt-Al_2O_3. This also suggested to happen within Pd-zeolite system by Mihai et al. in their recent published work[54]. However, the addition or the removal of CO_2 from the gas environment has no impact on the NOx storage capacity of a zeolite supported Pd or Pt catalyst. In a series of experiments conducted by Vu et al. 5% of H_2O and around 200 ppm of NO were chosen as the base gas components, and upon the addition of 2.5% $CO_{2,}$ both NOx adsorbed and released remain unaffected[44].

Zheng et al. studied the effect of H_2O and CO with Pd-zeolite systems. Transient NO adsorption tests under dry and wet conditions suggest that the presence of H_2O severely suppresses NOx trapping efficiency at 100 °C[32], similar effect was also observed at a lower adsorption temperature[55]. Chen et al. used DRIFTS to study this phenomenon and concluded that the negative effect of NOx storage capacity caused by water is a result of Brønsted acid sites being blocked[36], Porta et al. however attributed the negative effect to the inhibition of water on NO oxidation[55]. However, this inhibition was proven to have temperature and gas composition dependencies for a Pd-CeO_2/ZrO_2 system[35]. When the adsorption temperature was lower than 100 °C and C_2H_4 was present in the gas feed, the inhibition caused by H_2O becomes even more severe whereas it has less effect on NOx storage when CO or a CO/H_2 mixture was the reductant. With this distinct behavior, Theis et al. proposed a mechanism comprised of three different surface intermediates that are believed to respond differently with respect to H_2O exposure. They are NCO on PdOx, alkyl nitrites or alkyl nitrates (i.e., R-NO_2 or R-NO_3) and adsorbed HNO_2* species, which forms upon CO, C_2H_4 and H_2 exposure respectively[34,35]. The effect of water on Pd speciation and Pd associated surface intermediates within Pd-zeolite systems are not well understood, beyond the loss of Brønsted sites for NOx adsorption, and neither is the observed positive effect caused by water in other cases.

Additionally, when CO was introduced into a gas feed that also contained H_2O, it recovered part of the NOx storage capacity inhibited by H_2O addition in the absence of CO. This general trend was observed over three different Pd-zeolite systems, and is consistent with the Pd-BEA result reported by Vu. et al. (shown in **Fig. 3**)[32,44]. Transient CO_2 formation and DRIFTS results suggest that a change of Pd oxidation state with the addition of CO led to higher NOx storage capacity. Theis et al. observed a similar effect of CO on Pd-CeO_2/ZrO_2 catalysts, more interestingly, reductants such as C_2H_4 and H_2 were also found to induce a higher uptake in their transient NOx adoption tests[34,35]. Additionally, according to their proposed mechanism, the formation of NOx and reductants containing surface intermediates is believed to be a more reasonable explanation since a simple surface reduction reaction cannot differentiate their distinct behavior. However, they also reported that, when reducing agents are present, even a trace amount could cause a gradual degradation of NOx storage capacity over time though the chemistry behind this phenomenon is not clear (shown in **Fig. 4**). Ryou et al. investigated the difference between H_2 and CO as the reductant and how they would negatively affect the NOx storage capacity of Pd-SSZ-13.[56]

8.2.1.3 Effects of adsorption temperature

Low temperature PNA experiments can be challenging due to condensable exhaust gas components[57], one typical issue is the condensation of water. Moreover, from a thermodynamic perspective, the temperature chosen determines the equilibrium extent of NOx adsorption and water impact. And because cold start is transient, NOx storage at different temperatures needs to be evaluated to better understand the NOx storage efficiency under more realistic conditions.

Large pore Pd-BEA loses NOx storage capacity with an increase in adsorption temperature, whereas small pore Pd-MFI and Pd-CHA are less susceptible to loss, until 170 °C, due to stronger NO-Pd binding[32]. Non-zeolite based Pt/La-Al_2O_3 adsorbed similar amounts of NOx at 80 °C, 120 °C and 160 °C, however, without La, adsorption decreased with increasing temperature as desorption commenced at temperatures below 160 °C[38]. Interestingly, when CeO_2 was used as the catalyst support, NOx storage capacity of both Pt- and Pd-based catalysts show strong adsorption temperature dependence, more specifically, with an increase in adsorption temperature this group of catalysts traps significantly more NOx within an 80 - 160 °C temperature range. This improvement was associated with the release of adsorbed H_2O[37,39,41]. Notably, the enhanced NOx storage contributes mostly to a lower temperature desorption feature, which indicates that adsorption temperature is selectively affecting NOx storage on a certain site while the others remain unaffected.

8.2.1.4 Effects of hydrothermal aging

Hydrothermal aging stability is a general concern for zeolite supported exhaust after-treatment catalysts. High temperature and H_2O content can cause a series of problems such as particle sintering and zeolite dealumination. Though exhaust temperatures are expected to decrease in the future with advances in combustion technology, high temperature excursions are still possible, especially during particulate filter regeneration. Therefore, hydrothermal aging is still needed to evaluate long-term durability.

Pd-SSZ-13 model PNAs, regardless of synthesis methods, store significantly more NOx after a 25-hour hydrothermal aging protocol at 750 °C. Ryou et al. provided strong evidence of Pd migration during this hydrothermal aging process[45]. More specifically, Pd was believed to be primarily in the form of particles when the catalysts were first made, due to pore size limited Pd diffusion. After hydrothermal aging, Pd re-dispersed which resulted in more Pd being ion-exchanged and thus the overall dispersion significantly increased, evidenced by the appearance of a new NOx desorption feature. The existence of well dispersed Pd cationic species was proven by H_2-TPR, providing insight about how Pd migrates during a hydrothermal pretreatment[45]. Hydrothermal aging conditions have been studied, including duration, temperature and H_2O concentration[58]. A similar enhancement with Pd-ZSM-5 model PNAs was reported[47]. More interestingly, Lee et al. found that an NH_4NO_3 ion-exchange treatment could selectivity remove the ionic Pd content and the Pd particles could replenish the ion-exchange sites via a subsequent high temperature oxidative pretreatment. Though hydrothermal aging on Pt/Pd-CeO_2/ZrO_2 model PNAs does not increase the NOx storage significantly, it is still worth noting that this group of materials exhibited reasonable hydrothermal stability[39].

8.2.1.5 Effect of promoters

The addition of metal promoters in TWC and LNT systems has been widely reported. However, promoters that have been added to the three model PNA systems have not been extensively investigated. Crocker's group is an exception, where they investigated promotors on the Pt/Pd/metal oxide systems. Lanthanum group metal dopants were reported to be beneficial for Pd-CeO_2, Pt-CeO_2 and Pt-Al_2O_3 systems. Ji et al. added La to Pd-Al_2O_3, and NOx storage capacities at temperatures lower than 160 °C initially increased, but then degraded with NOx adsorption and desorption cycles. In a recent study performed by Jones et al., a series of lanthanum group metals were added to Pt-CeO_2 and Pd-CeO_2 and the improvement of NOx storage capacity followed the order Pr>Nd>Sm>Y in the Pt-CeO_2 case. Notably, as shown in **Fig. 5**, adding Pr helped both Pt-CeO_2 and Pd-CeO_2 store more NOx and release more below 350 °C. The highest NOx adsorption efficiency was achieved at 20% Pr doping. This effect was attributed to the increased amount of CeO_2 vacancies, assumed to be responsible for the majority of the NOx storage. However, they also reported that this group of PNAs was not tolerant to high temperature aging, although Pt/Pr-CeO_2 was able to store a reasonable amount of NOx post thermal treatment[38,39].

8.2.1.6 Summary of unresolved issues

Sufficient evidence in the literature suggests that certain Pt- and Pd-based catalysts store NOx at low temperatures, with different studies demonstrating performance characteristics under different exhaust conditions. These findings, however, lead to further questions:

- H_2O inhibition and promotion have both been observed. H_2O competition for active sites, changing the metal oxidation state, and how these change over a range of temperatures are not quite clear. What is the role of H_2O?
- Reducing gas species seem to induce changes in storage capacity, as well as desorption temperatures (as noted below). They can also cause degradation in NOx storage. They lead initially to higher levels of NOx storage, but the performance after numbers of cycles of adsorption and desorption seems to be inconsistent. Overall, there is a lack of understanding of reductant impact.
- There is inconsistency in how hydrothermal aging impacts the NOx storage capacity of different catalysts, what is the key factor determining such an effect.
- How is the rate of adsorption influenced by washcoat properties and the morphology of support materials?

- To ensure a general lack of sulfur poisoning, or a significant extent of, sulfur exposure should be further investigated, under a variety of conditions.

8.2.2 NOx desorption characteristics

In most laboratory experiments, after NOx is adsorbed for some period of time under isothermal conditions, a TPD is initiated to monitor NOx desorption. Under real-world conditions, the temperature begins to increase immediately, with adsorption occurring initially, and then desorption once higher temperatures are reached. NOx desorption is of course critical, as it regenerates the adsorption sites to ensure capacity for the next cold start. Furthermore, NOx release needs to occur at or higher than the temperature at which the downstream NOx reduction catalyst becomes sufficiently active. This temperature varies depending on the exhaust after-treatment system configuration. However, as discussed earlier, for any that rely on an NH_3-SCR system, 200 °C is the target acceptable NOx desorption temperature[10,16]. As is shown in **Fig. 6** NOx release at lower temperatures leads to some remaining unreduced, whereas too high of a desorption temperature might not allow storage capacity recovery. Note, **Fig. 6** does not consider urea decomposition for NH_3 generation, which is usually assumed to be efficient enough around 200 °C. This section summarizes the reported desorption profiles of a wide range of PNA candidates that currently exist in the literature and discusses what known factors influence release.

8.2.2.1 Desorption temperature and NO2/NOx ratio

Thus far, three groups of Pd or Pd/Pt based PNAs (zeolites, CeO_2 and Al_2O_3 supported Pd or Pd/Pt catalysts) have attracted most attention because of their significant low temperature NOx storage capacities and sufficient hydrothermal stability. Desorption features of PNAs that were discussed in the previous section are listed in **Table 1**. Hydrothermal aging temperatures prior to the tests are noted if available, gas compositions and ramp rates of each set of corresponding TPD experiments are also listed. Most of the desorption features fall into a temperature window between 200 to 400 °C, and the NOx desorption temperature from the same material may shift due to different synthesis methods, gas compositions, aging conditions and ramp rates.

Low temperature NOx storage efficiency is usually evaluated without differentiation between NO and NO_2, as both coexist in the feed gas. And since both can be adsorbed at low temperatures, thus it is not necessary to measure the uptake of each species separately[20,32,44]. However, NO_2 formation is observed in both the transient uptake phase and at steady state, and was reported as an alternative route of NOx storage. More specifically, at least for ZSM-5 as an example, NO can be oxidized into NO_2 before it interacts with the zeolite and forms relatively thermally stable surface nitrate species[59]. Although NOx storage via surface nitrate formation may not be purely considered passive NOx adsorption, due to the fact it is an activated process and relies on NO oxidation activity, it enhances low temperature NOx storage capacity and provides extra flexibility of tuning a NO_2/NOx ratio[32,60]. In terms of desorption, surface nitrate decomposes giving rise to a mixture of NO and NO_2 during desorption, and since an equimolar ratio of NO and NO_2 is well known to facilitate fast SCR[61], the NO_2 to NOx ratio during desorption is worth noting. In the work published by Chen et al., both Pt/Pd-CeO_2 catalysts (PNA and CSC) gave rise to NO_2 desorption at around 400 °C, though the majority of released NOx comes from NO desorption at 250 °C[20]. In contrast to this result, their later work on zeolite supported Pd catalysts showed almost zero NO_2 release during TPD[32], however, by no means is this evidence of low NO oxidation activity, or that NO_2 is not a sorbed species decomposition product, because CO and decane were present in both cases, and both can react with NO_2 to form NO. In other words, the absence of CO or decane could significantly affect the NO_2-to-NOx ratio during TPD. This behavior was captured by Zheng et al. in one set of their TPD results without CO. They observed that when CO was absent, Pd-SSZ-13, Pd-ZSM-5 and Pd-BEA released NO_2 at around 150 °C, with Pd-SSZ-13 releasing the most. As expected, as soon as CO was added to the feed gas, the NO_2 concentration was lower than the background NO_2 level until CO oxidation lit off[32]. Only when the decomposition temperature of nitrate species is higher than the temperature of complete CO oxidation will NO_2 desorption be detected.

8.2.2.2 Effects of exhaust species

Gas composition during TPD has been reported to impact NOx desorption temperatures, as is shown in **Table 1**. CO_2 and H_2O seem to have no effect on desorption characteristics. Thus far, observations about how CO influences NOx desorption behavior over zeolite supported Pd catalysts are relatively consistent. Vu et al. performed TPD experiments on Pd-BEA with CO concentrations ranging from 0 to 225 ppm and found that with an increase in CO concentration, more NOx was released in the higher temperature regime, and the total amount of NOx released increased. A desorption feature at 180 °C was unaffected by CO addition, however a 100 °C feature diminished and a 260 °C feature increased, even at low CO concentrations[44]. Similarly, this effect was also observed over unaged Pd-SSZ-13 and Pd-ZSM-5 samples[32]. Via reactor and IR studies, the authors concluded that CO reduced Pd to a lower oxidation state, which is responsible for the increased NOx desorption temperature on Pd-BEA due to the strengthening of NOx and Pd bond[44]. A OC-Pd (II)-NO type surface intermediate is formed upon NO and CO exposure to Pd-SSZ-13 which is more thermally stable[52]. A similar improvement in NOx desorption temperature upon CO exposure was also observed with Pd-CeO_2/ZrO_2 systems[34,35]. IR results indicate the formation of an NCO type surface intermediate which is more thermally stable and easier to oxidize in the absence of either CO or NO. Interestingly, as shown in **Fig. 7** and **Fig. 8**, reductants such as H_2 and C_2H_4 can shift the NOx desorption temperature by forming HNO_2* and alkyl nitrite on the surface correspondingly, therefore, NOx desorption temperatures vary due to the different surface species thermal stabilities[34,35].

8.2.2.3 Effects of ramp rate

During TPD experiments, a varying ramp rate is known to shift the temperature at which peak desorption is observed. This phenomenon has long been used to measure activation energy. As discussed by Falconer et al., with the increase in heating rate, desorption peaks shift to higher temperature and become more significant in terms of amplitude[33]. This effect inevitably introduces NOx desorption temperature differences between TPD experiments that use different ramp rates, and thus leads to some inconsistency in measured peak desorption temperatures. **Table 1** lists a number of ramp rates that have been used during TPD, and it is obvious that a relatively slower ramp rate of 10 °C /min is used in most of the experiments. A slower ramp rate is preferred for kinetic studies, especially when multiple desorption features coexist such that better resolution between desorption peaks can be achieved. However, 10 °C/min is approximately an order of magnitude lower than the rate of change in exhaust temperatures during cold start, therefore the reported desorption temperature will be lower than those under real conditions. Such peak desorption temperature changes do not indicate a change in surface NOx species thermal stability, the desorption feature will still be comprised of the same kinetic information. But for exhaust application predictions, a faster ramp rate is preferred. Confounding effects, Yakerson et al. experimentally proved that the effect of ramp rate on desorption temperature is not a simple linear relationship. More specifically, if the ramp rate is slow (<10 °C /min) a significant change in peak desorption temperature can be observed with a small ramp rate variation, but in the fast ramp rate regime (>50 °C /min), only when ramp rates are orders of magnitude different is there a significant peak shift[62]. This again strongly supports using a relatively faster ramp rate when conducting NOx TPD experiments, to improve comparability. By comparing the Pd-BEA NOx TPD results provided by Vu et al. and Chen et al[36,44], where Vu et al. chose 63 °C/min and Chen et al. chose 100 °C/min, their ramp rates resulted in similar NOx desorption temperatures.

8.2.2.4 Effects of hydrothermal aging

Hydrothermal treatment induced Pd migration was observed for a Pd-SSZ-13 system, with evidence stemming from H_2-TPR experiments. This migration enhanced the ion-exchange level and resulted in higher NOx storage capacity[45,58]. This effect is also reflected by the appearance of a new desorption feature during TPD as is shown in **Fig. 9** Before hydrothermal aging, only one desorption feature was observed, at around 400 °C in the absence of any reductants. Notably, when CO is absent in both adsorption and desorption phases, the new desorption feature peaks at a more applicable temperature, 250 °C. According to the authors, the low temperature desorption feature is more likely to be a cationic Pd related NO surface intermediate which does not exist before hydrothermal aging due to the hydrolysis of the Pd ion and the small pore size of SSZ-13, hence, the desorption temperature of the new feature mainly depends on the NO-Pd cation interaction. Pt/Pd-CeO_2/ZrO_2 has been reported to be hydrothermally stable. Before aging, two desorption features are evenly distributed at around 200 and 350 °C, whereas the high temperature desorption feature dominates after hydrothermal aging with a slight shift to lower temperature and a wider peak width. As a result, the amount of NOx released below 350 °C was the same. However, after hydrothermal aging, significantly more NOx release below 200 °C was also observed[58].

8.2.2.5 Summary of unresolved issues

NOx release temperatures from a wide range of PNA candidates are reported to be “appropriate” and significant progress in assessing NOx desorption characteristics has been achieved. However, there are still several questions remaining, including:

- There appears to be debate as to how reductants affect NOx desorption temperature, and thus the actual mechanism.
- NO and NO_2 are both observed, but it is not well understood how NO oxidation competes with NO adsorption and desorption.
- How does CO and hydrocarbon oxidation affect NOx desorption characteristics?
- Though different desorption features are observed, their actual identities related to storage sites and thermal stabilities are not quite clear, i.e. neither is the desorption mechanism.
- Despite the fact that different porous supports were used, there seems to be a lack of information about how micropore geometry affects desorption temperature. The mass transfer behavior within such a system is not well understood, especially when condensable gas compositions are involved.

8.3 Adsorption chemistry

Understanding the NOx adsorption mechanism is key to designing optimized PNAs. In this section the proposed NO adsorption mechanism within different PNA systems will be summarized, with emphasis on NOx storage sites and competing surface reactions in zeolite supported Pd catalysts. There is abundant literature unravelling the NOx storage mechanism in CeO_2 based PNAs since they have historically been well investigated as key component for lean NOx traps[63]. Among these literatures, nitrate and nitrite formation on or CeO_2 are the essential to NOx storage capability[40,50,64–69] Although it is used for a different application, the operating conditions of NOx trapping step in LNTs and PNAs are very similar, hence, the NOx adsorption mechanism of CeO_2 based PNAs can be derived from previous mechanistic LNT studies. However, when it comes to PNA applications, NO desorption happens under lean conditions whereas an LNT needs a rich phase to reduce the nitrite and nitrate, otherwise their thermal decomposition happens at elevated temperatures[70]. Additionally, due to the currently inevitable sulfur exposure, sulfite and sulfate formation occurs as an analogy to nitrite and nitrate formation on CeO_2, which severely suppresses the NOx storage capacity[71–74]. Meanwhile, these sulfate species are much more stable relative to nitrate species so a reactant-rich gas environment and an even higher temperature are needed to decompose them[70,74].

Based on results to date, zeolite supported Pd catalysts seem to be much more resistant against sulfur poisoning relative to CeO_2 or CeO_2/ZrO_2 based catalysts and are easier to recover storage capacity under lean conditions, thus will be more suitable for lean burn engine PNA application[36]. However, PGM added to the zeolite-based catalysts does not seem to be well controlled during catalyst synthesis, with hydrothermal treatments subsequent to synthesis leading to better performance[45,58]. Speciation and noble metal distribution have not been clearly identified in most cases, because of which, NO adsorption mechanism is not as well understood as CeO_2 catalysts. Therefore, the discussion of the storage sites and competing surface reactions mainly focuses on this group of materials and the adsorption chemistry of other PNA candidates will only be briefly compared.

8.3.1 Storage sites

Atomically dispersed Pd cationic species have been frequently mentioned as the most efficient NOx storage site in terms of atomic utility, as well as having the most appropriate binding energy such that NOx desorption occurs at a desirable temperature[32,36,45,75]. The conventional solution phase ion-exchange method has been reported to successfully maximize cationic metal species in similar metal-zeolite systems[52]. Well dispersed Pd cations, i.e. a high ion-exchange level, is hard to achieve especially when Pd weight loadings are higher than 1wt.%[32,45]. PNA materials usually undergo a pretreatment or aging protocol before use, and these pretreatments are reportedly able to redistribute the precious metals, form bigger particles or cause damage to the support, all of which could affect NOx storage. Although there is still some debate as to whether Pd cations are the most efficient sites for NOx storage, metal distribution and speciation are of course essential to identify NOx storage sites.

8.3.1.1 Metal speciation and distribution

The precious metal dispersion within a heterogeneous catalyst contributes to its catalytic activity or adsorption capacity, although this dispersion does not directly correlate to speciation of the impregnated precious metals. Different size nanoparticles as well as atomically dispersed ionic species form, and these species can further transform depending on the synthesis methods and post treatment conditions, all of which can change the metal dispersion.

For zeolite supported PNA catalysts, the speciation usually identifies clusters, nanoparticles and ion-exchanged metal sites[60,76–81]. Clusters are typically larger than the pore size of the support material and exist on the external surface of the zeolite such that they can easily be captured by electron microscopy, as is shown in **Fig. 10** [32,54]. Smaller nanoparticles (< 2 nm) can exist both on the external surface and inside the micropores, assuming their particle sizes are smaller than the zeolite pore size, and can also be seen in microscopy[52]. Meanwhile, due to the interaction between the Brønsted acid sites and metal oxide particles or the direct ion-exchange between a proton from the Brønsted acid sites and a cationic metal species, ion-exchange can happen, forming atomically dispersed metal ion-exchange sites[82]. Ion-exchanged sites can be characterized via several techniques, though hard to visualize directly with electron microscopy. Apart from their size difference, sites can also be categorized by metal oxidation state, such that a system can be a combination of metallic particles and their oxide counterparts, and it has been reported that the oxidation state of these precious metals, especially Pd, is rather sensitive to the environment, switching states during NOx adsorption and desorption cycles.

IR studies have shown that the direct coordination of NO onto ionic Pd^{2+} species is responsible for the bulk of low temperature NOx storage[51], and the co-adsorption of CO and NO on the same Pd^{2+} site seems beneficial, leading to desorption temperatures in the appropriate range[44,52]. The actual identity of the storage sites is, however, not quite clear because Pd^{2+} can be hydrated and form $Pd^{2+}(H_2O)_n$ type species[60,83]. It has also been reported that exposure to NO will reduce Pd^{2+} to Pd^{+}, and further reduction to Pd metal can occur with exposure to CO or a stronger reductant[62]. NOx storage on PdOx clusters can occur, as it has been reported that PdO_2 oxidizes NO to NO_2 and subsequently stores another NO molecule[32]. Small Pd or PdOx nanoparticles are relatively more mobile compared to larger clusters or ion-exchange sites, and their mobility can be further promoted by high temperature thus causing particle agglomeration[32,84]. In contrast to particle agglomeration, protonalysis of PdOx nanoparticles can also occur when the nanoparticles locate inside the zeolite pores and neighbor the Brønsted acid sites, which results in enhanced ion-exchange levels[82].

8.3.1.2 Catalyst synthesis and aging

The selection of precursor, the support material, and the metal deposition technique are basics in catalyst synthesis, all of which determine the final state of a freshly prepared catalyst, i.e. the speciation and the distribution of storage sites. Thus far, four techniques have been extensively used to disperse PGM into zeolite supported PNA catalysts: incipient wetness impregnation (IWI), wet impregnation (WI), solution ion-exchange (IE), and solid-state ion-exchange (S-S)[32,45]. Though they share the same idea in terms of dispersing PGM, due to their different metal dispersing mechanisms, the initial metal distribution varies. Solution ion-exchange in most cases is believed to be the best synthesis method, providing the highest initial ion-exchange level[76,77]. However, it has also been reported that when Pd is dispersed into the SSZ-13 zeolite structure, there seems to be no difference among catalysts prepared from the different synthesis methods, and due to the transport limitation caused by small pore size most of the Pd exists on the external surface as PdOx clusters[36]. This suggests that the micropore geometry of the zeolite structure would also play an important role during catalyst synthesis. Meanwhile, the counter ion and silica to alumina ratio (SAR) of the parent zeolite have also been reported to affect catalyst performance by changing the site distribution[58][54,58]. Precursors used are mostly nitrates, chlorides and aminol nitrates [32,36,39,44,45]. Research on the direct impact of precursor selection among PNA catalysts has not been reported.

Synthesis of a fresh PNA catalyst usually ends with a calcination process that is performed at around 500 °C in air or an oxygen and nitrogen mixture to decompose the residual metal precursors. After calcination, an initial distribution of different metal sites exists. However, as the catalysts undergo more aging and testing cycles, the distribution shifts and a relatively more stable distribution of storage sites will eventually be reached[45,58].

Zeolites are well known for their hydrothermal stabilities and the metal speciation within different systems are somewhat similar, however, it seems that different morphologies respond differently to hydrothermal aging. As high temperature and water content hydrate and mobilize metal species, hydrothermal aging is also able to change the metal distribution. During the aging process, dealumination, sintering and ion-exchange can happen simultaneously, but, an optimized hydrothermal aging condition is reported to improve the NOx storage capacity of Pd-SSZ-13 significantly[45,58]. H_2O is a key component to help facilitate ion-exchange within SSZ-13 system, and when it is absent during thermal aging, ion-exchange is limited. With H_2O present, the migration of Pd from the particle phase to Pd ionic species occurs at temperatures over 600 to 650 °C, and reaches an equilibrium in less than 10h[58]. For Pd-ZSM-5, an oxidative thermal treatment without H_2O allows ion exchange, and the same trend was observed whereas the optimum temperature falls between 750 to 800 °C. Interestingly, apart from the NOx TPD experiments, the ion-exchange levels of samples thermally treated at different temperatures have been measured by comparing the residual Pd content before and after ion-exchanging with NH_4NO_3, and provided strong evidence of metal migration during high temperature treatment[47].

8.3.1.3 Effects of pretreatment methods

Prior to NOx adsorption experiments, a high temperature pretreatment is usually performed to remove residual NOx, which can influence the PGM oxidation state. This pretreatment, in the majority of cases, contains a mixture of oxygen and nitrogen or air, and sometimes water. Although not relevant to lean-burn application, a reductive pretreatment with CO or H_2 can also be performed to study the nature of the storage sites and help understand the mechanism of site migration[32,80].

Hydrogen, as a strong reductant, can readily reduce PdOx particles at sub-ambient temperature, and also form PdH which thermally decomposes at temperatures slightly higher than room temperature[85–89]. The reduction of Pd ionic species occurs at higher temperatures[45,82]. CO is not as strong a reductant for Pd oxide reduction, but in many studies has been reported to be able to reduce PdOx as well as Pd ionic species at higher temperatures[79,80]. A higher relative mobility of the reduced Pd species has been observed[79,82]. Therefore, reduction of ionic species and particle agglomeration are the main processes that change the metal distribution during a reductive pretreatment. However, under real exhaust conditions O_2 is present, so the actual reduction temperature or whether reduction can happen is questionable. It has also been reported that a reoxidation pretreatment can regenerate the Pd ionic species via surface oxidation followed by protonalysis even after severe reduction, though the reversibility of this process depends on the particle size and zeolite pore geometry, and thus may vary from case to case[82].

8.3.1.4 Summary of unresolved issues

Obvious progress has been made in understanding NOx storage sites within different PNA catalysts, and several mechanisms have been proposed to explain how storage sites evolve. However, there are still questions that need to be answered:

- The distribution between particles and ion-exchange sites varies with synthesis and changes during reaction and pretreatment. Their evolution, distribution and chemical states need to be better understood.
- The surface intermediates that form during NO adsorption in the presence of CO, HCs and H_2O are not well understood, and neither is the actual chemical environment of ionic metal species.
- Hydrothermal aging seems to affect storage site distribution differently among zeolite supported PNA catalysts.
- Pd appears to be mobile, especially at high temperature or with high water content, but the chemistry behind the mobility and the role of water are not well understood.
- The reversibility of site migration induced by high temperature oxidation or reduction needs further assessment.

8.3.2 Surface intermediates and reactions

Low temperature NOx storage begins as soon as the exhaust mixture contacts the PNA, however, due to the different responses of storage sites to different conditions, NO has been reported to undergo multiple adsorption pathways, forming different surface intermediates and subsequently exhibiting various desorption characteristics. This section summarizes the possible routes for NOx storage, and introduces a proposed adsorption mechanism as well as surface intermediates.

While NO is being adsorbed, surface reactions including CO oxidation, and NO oxidation and reduction can occur simultaneously. Activities of these reactions on similar materials have been extensively reported, and their corresponding products are observed during low temperature NOx storage. Although PNAs are not intentionally designed to facilitate these side reactions, there will be competition for active sites and potential inhibition of low temperature NOx storage capacity. Moreover, as they occur throughout the cold start period, it is also important to understand their characteristics so that they can be de-coupled for more accurate performance evaluation and robust kinetic modeling.

8.3.2.1 NO adsorption pathways

Surface intermediates formed upon NO exposure over a Pd ion-exchanged ZSM-5 catalyst were found to be mainly NO adsorbed on Pd cations. Under dry conditions and without O_2, NO first directly binds with ionic Pd(II)$(OH)_x$ and reduces Pd(II) forming NO_2, meanwhile, reduced Pd(I) coordinates with NO and forms a Pd(I)NO complex[84,90,91]:

$$2[Pd(II)(OH)]^+Z^- + NO \rightarrow 2[Pd(I)]^+Z^- + NO_2 + H_2O \quad (1)$$

$$2[Pd(I)]^+Z^- + 2NO \rightarrow 2[Pd(I)NO]^+Z^- \quad (2)$$

$* Z^- = [Al - O - Si]^-$

More interestingly, the coordination between Pd(I)NO and another NO_2 or H_2O was proposed and supported by IR evidence[60,92].

$$[Pd(I)NO]^+Z^- + NO_2 \rightarrow [NO_2Pd(I)NO]^+Z^- \text{ (3)}$$

NO_2 and NO were found to weakly interact with Brønsted acid sites under dry conditions[79,93] forming NO^+, NO_2+ species[91,94–97] as well as interacting with cation defect sites to form more thermally stable nitrate species ($NO3^-$)[60,95] :

$$NO + NO_2 + 2H^+Z^- \rightarrow\ 2NO^+Z^- + H_2O \text{ (4)}$$

$$NO_2 + H^+Z^- \rightarrow\ [NO_2H]^+Z^- \text{ (5)}$$

$$M - O^- + NO_2 \rightarrow M - {NO_3}^- \text{ (6)}$$

Following these findings, Zheng et al. pointed out that the mobility of $[Pd(II)(OH)]^+$ is key to facilitating reaction 1 due to the fact that two $[Pd(II)(OH)]^+$ sites are needed to oxidize one NO molecule, and the solvation effects of water may increase the probability of reaction 1. They also proposed different pathways for NO oxidation on a dimeric Pd ionic species as well as NO oxidation/adsorption on PdOx clusters[32]:

$$Z^-[Pd(II) - O - Pd(II)]^{2+}Z^- + NO \rightarrow NO_2 + 2Pd(I)Z^- \quad \text{(7)}$$

$$PdO_2 + 2NO \rightarrow NO_2 + NO - PdO \quad \text{(8)}$$

According to Zheng et al., reaction 1 together with reactions 7 and 8 are responsible for the reduced oxidation state of Pd upon NO exposure observed with both IR and XPS, but the bulk of NO adsorption is assumed to happen on Pd clusters i.e. reaction 8, based on the detected 2:1 ratio between NO consumed and NO_2 formed. However, there is no strong evidence to differentiate the NO adsorption and oxidation behavior of Pd^{2+} species i.e. $[Pd(II)(OH)]^+$ and $[Pd(II)\text{-}O\text{-} Pd(II))]^{2+}$, so the direct coordination of NO and Pd^{2+} species cannot be eliminated though oxidation-adsorption is a possible pathway for NOx storage.

$$Z^{-}[Pd(II)(OH)_x]^{(2-x)+}Z^{-} + NO \rightarrow Z^{-}[Pd(II)(NO)(OH)_x]^{(2-x)+}Z^{-} \quad (9)$$

Catalytic NO oxidation over Pd-SSZ-13 was found to be significant only at high temperatures[32]. Moreover, it has also been proposed that the presence of H_2O inhibits NO trapping via reaction 8, whereas reactions related to monomeric ionic Pd species remained unaffected, this is consistent with the quantification results from NaCl titration.[32] Another explanation for H_2O inhibition is the formation of a neutral $[Pd(II)(OH)_2(H_2O)_2]$ complex due to the hydrolysis of zeolitic Pd cations when PdOx particles are not present, such that reaction 8 is not significant and H_2O molecules occupy NOx storage sites due to strong hydration/hydrolysis of Pd^{2+} species. Additionally, as is shown in **Fig. 12**, Chen et al. reported that H_2O could strongly interact with Brønsted acid sites making them inaccessible for NO^+/NO_2 adsorption, which seems to be consistent for all three zeolite systems[36].

Besides the direct coordination of NO and Pd^{2+} species, NO oxidation-adsorption and NO adsorption on PdOx clusters, and the co-adsorption of NO and CO over Pd-ZSM-5 have been observed[32,36,60,62]. Similar to the mechanism of NO exposure, ionic Pd species can readily be reduced to lower oxidation state upon exposure to CO, forming Pd^{+} and eventually Pd^{0}. These Pd species with different oxidation states are all considered to be able to strongly interact with CO[83,98], however, only Pd^{2+} contributes to NO storage via $Pd^{2+}(NO)(CO)$ formation.

$$Z^{-}[Pd(II)(OH)_x]^{(2-x)+}Z^{-} + NO + CO \rightarrow Z^{-}[Pd(II)(NO)(CO)(OH)_x]^{(2-x)+}Z^{-} \quad (10)$$

In addition to the formation of different surface intermediates, the overall NOx storage capacity can increase in the presence of CO[52], which is believed to be the direct contribution of

Pd^{2+}(NO)(CO) formation. Moreover, NOx desorption temperature shifts to a higher region which indicates a strengthened binding energy between NO and its storage site. IR studies of NO and CO co-adsorption support not only the formation of Pd^{2+}(NO)(CO) type surface intermediates but also the strengthened NO-Pd(II) binding energies[83]. When CO and H_2O simultaneously exist in the gas phase, the NOx storage capacity of Pd-SSZ-13 also improved, due to the desorption of water between 100 and 150 °C and subsequent Pd^{2+}(NO)(CO) formation. This is evidenced by the second NOx adsorption feature with increasing temperature and a shifted NOx desorption temperature[52].

In summary, there are 6 proposed existing NO adsorption pathways: weak interaction between NO/NO_2 and Brønsted acid sites, nitrate formation on extra-framework alumina, NO direct coordination with Pd^{2+}, NO/NO_2 adsorption on Pd^+, NO adsorption on PdOx clusters, and NO and CO co-adsorption on Pd^{2+}. However, under realistic conditions, high water content inhibits the weak interaction between NO/NO_2 and Brønsted acid sites, and NO adsorption on PdOx clusters. CO improves the overall NOx storage uptake via reaction 10, thus Pd^{2+}(NO)(CO) type surface intermediates seem consistently present.

8.3.2.2 CO and NO oxidation over PNA

CO oxidation is believed to be a redox reaction between CO and higher oxidation state ionic Pd species[83]. Transient CO_2 formation suggests that the reduced Pd ionic species cannot be oxidized immediately at low temperatures after being reduced by CO, hence, a complete catalytic cycle is not accomplished. This phenomenon, however, provides unique information about the quantity of reducible Pd ionic species and could possibly be used to quantify the number of storage sites if the actual coordination number was known. Similarly, transient NO_2 formation indicates the oxidation of NO which has been discussed as one of the NO storage pathways[32,60,91,92].

During TPD, catalytic CO oxidation is observed and typically lights off at temperatures below 200 °C[20]. CO oxidation follows normal light off behavior, but is coupled with CO desorption. Although the origin of CO desorption feature is very likely from the dissociative desorption of Pd^{2+}(NO)(CO) type surface intermediates, as is shown in **Fig. 13**, CO and NO desorption temperatures do not perfectly match for Pd-SSZ-13 and Pd-ZSM-5, whereas they do for Pd-BEA[36]. Knowing that CO oxidation activities of different Pd species are by no means identical, the comparison between NO desorption profile and CO light off behavior could provide information to help understand the kinetics. Catalytic NO oxidation is significant at temperatures above 300 °C[99,100], but NO_2 is not observed before CO lights off[32,101]. NO light off curves are somewhat similar and related to Pd loadings[32].

8.3.2.3 NO reduction over PNA

Reduction of NO over Pd-based PNA catalysts can occur via CO or the unburned HCs as reductants. Murata et al. proposed a schematic where HCs co-adsorb with NO onto Pd-ZSM-5 at low temperatures with NOx reduction by HCs during subsequent warm up. They also investigated the potential of using such a unique property to perform PNA and TWC on the same catalyst for stoichiometric-burn engines and found that NO reduction is strongly favored under slightly rich or stoichiometric conditions[46]. Chen et al. reported low temperature NOx reduction activity over PNA and CSC catalysts, even under lean conditions[20]. Furthermore, as an incomplete reduction product, N_2O has been observed during the temperature ramp after exposing Pd/Pt/Al_2O_3 and Pd-rich-bimetallic NOx adsorber catalysts to NO and HCs by Chen et al. and Theis et al. respectively[20,34]. Theis et al. also compared the N_2O formation on a Pd/CeO_2/ZrO_2 catalyst when different reductants were introduced. C_2H_4 led to the most N_2O formed, at around 300 °C, while a much smaller amount was detected at lower temperatures when CO or H_2 was used as the reductant[34,35].

However, for lean burn engine exhaust, with increasing temperature, HC and CO combustion dominate, and NO reduction over the PNA becomes insignificant. Although it is not anticipated that the PNA will act as a highly active NOx reduction catalyst at high temperatures, or low temperatures, these studies help provide important information about NO adsorption and reduction mechanisms and can be helpful in PNA mechanistic studies. As an example, the Pd^{2+} cation is believed to be responsible for NO_2 reduction with CH_4 and therefore, NO_2 reduction via CH_4 might be used as a good indicator to quantify isolated Pd^{2+} cations[34].

8.3.2.4 Summary of unsolved issues

According to the proposed NO adsorption pathways and surface intermediates, ionic Pd species are often proposed as the primary NO trapping site, but overall, low temperature NO adsorption is relatively complicated. Although surface intermediates identified and Pd oxidation states have been tracked, questions about how these surface intermediates evolve remain unresolved. In particular:

- Among all the NO adsorption pathways, the dominating route under realistic exhaust conditions needs to be confirmed.
- It is not clear whether the reduction of Pd^{2+} to Pd^{+} or Pd^{0} is reversible or not, neither is the relationship between the reversibility and the zeolite geometry.
- Binding strengths of proposed surface intermediates need to be quantitatively compared.

- The effect of H_2O on NOx storage capacity at different temperatures, or overall the coordination of H_2O or hydroxyl groups on Pd cations is not well understood.
- The coordination number of NO on each site and the chemical structure of the surface intermediates under realistic conditions are not clear, hence, the most beneficial storage site or surface intermediate is not yet fully agreed upon.
- The NO adsorption mechanism, still remains unresolved.

8.4 Conclusions

Low temperature NOx trapping via passive NOx adsorbers can be realized under simulated lean-burn exhaust conditions as well as more realistic exhaust conditions. Among a series of materials studied for PNA application, zeolite supported Pd catalysts are highly effective. However, due to the complexity of exhaust compositions, the uniqueness of the transient cold start process and the lack of understanding of the potential PNA materials, NOx storage and release characteristics still need further investigation. Meanwhile, the effects of different exhaust components are inconsistent over a series of PNAs which raises extra complexity when integrating PNA with current lean-burn engine aftertreatment systems. In general, this technology can be used to decrease NOx emissions during cold start, but real exhaust compatibility, catalyst aging, sulfur poisoning and NOx storage capacity degradation still need to be addressed. In order to provide rational guidelines for catalyst design, better predict the long-term performance of PNAs and optimize the PNA containing exhaust aftertreatment system, more mechanistic studies need to be carried out under realistic conditions.

PNA adsorption chemistry is complex, consisting of multiple adsorption and reaction pathways as well as multiple active sites. PNA-related and unrelated literature have characterized the NO interaction with Pd dispersed in a zeolite framework as well as NO and CO co-adsorption.

These studies have laid the foundation for structure-performance relationships. Despite the fact that these works provide valuable information to help understand PNA adsorption chemistry, the understanding of the PNA mechanism under more realistic conditions is insufficient. High water content, complex gas compositions, synergistic effects between different side reactions and the mobility of Pd within the zeolite structures under these conditions are the current obstacles towards the complete mechanistic understanding.

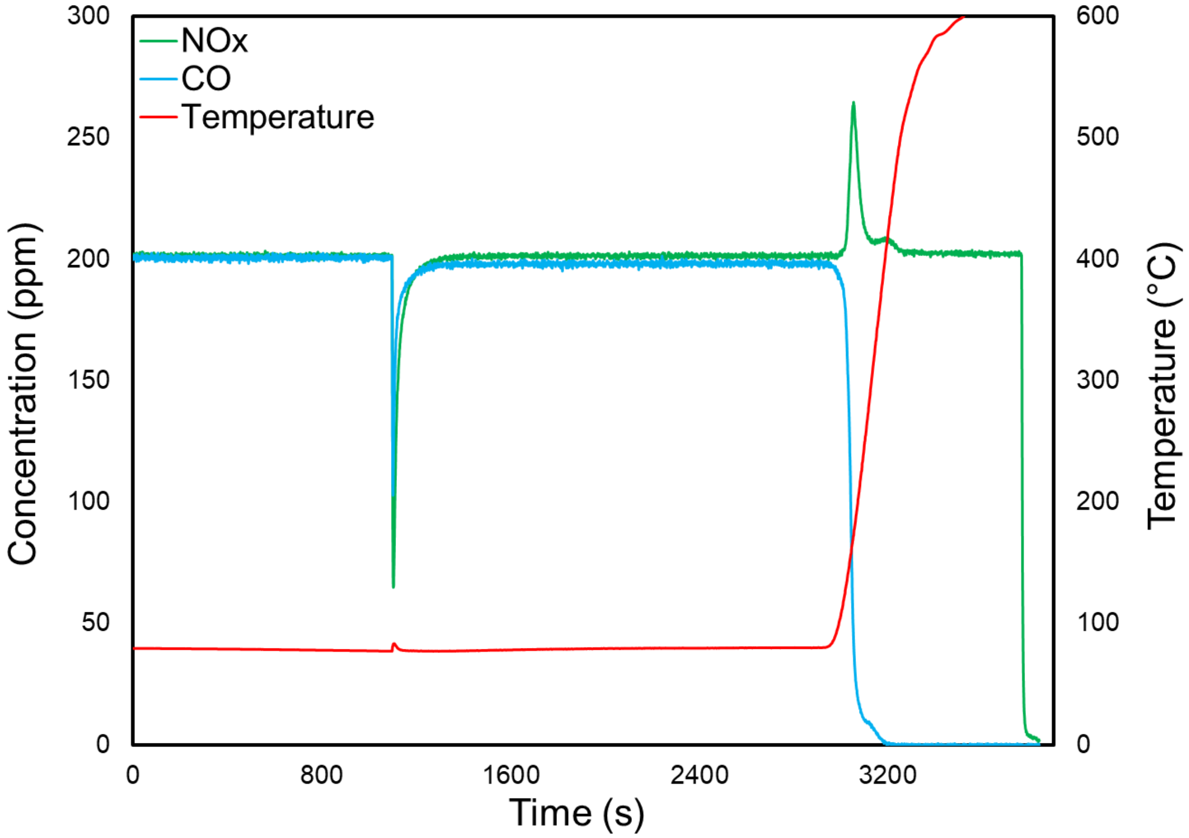

Figure 8.1 Transient NO adsorption and temperature programmed desorption

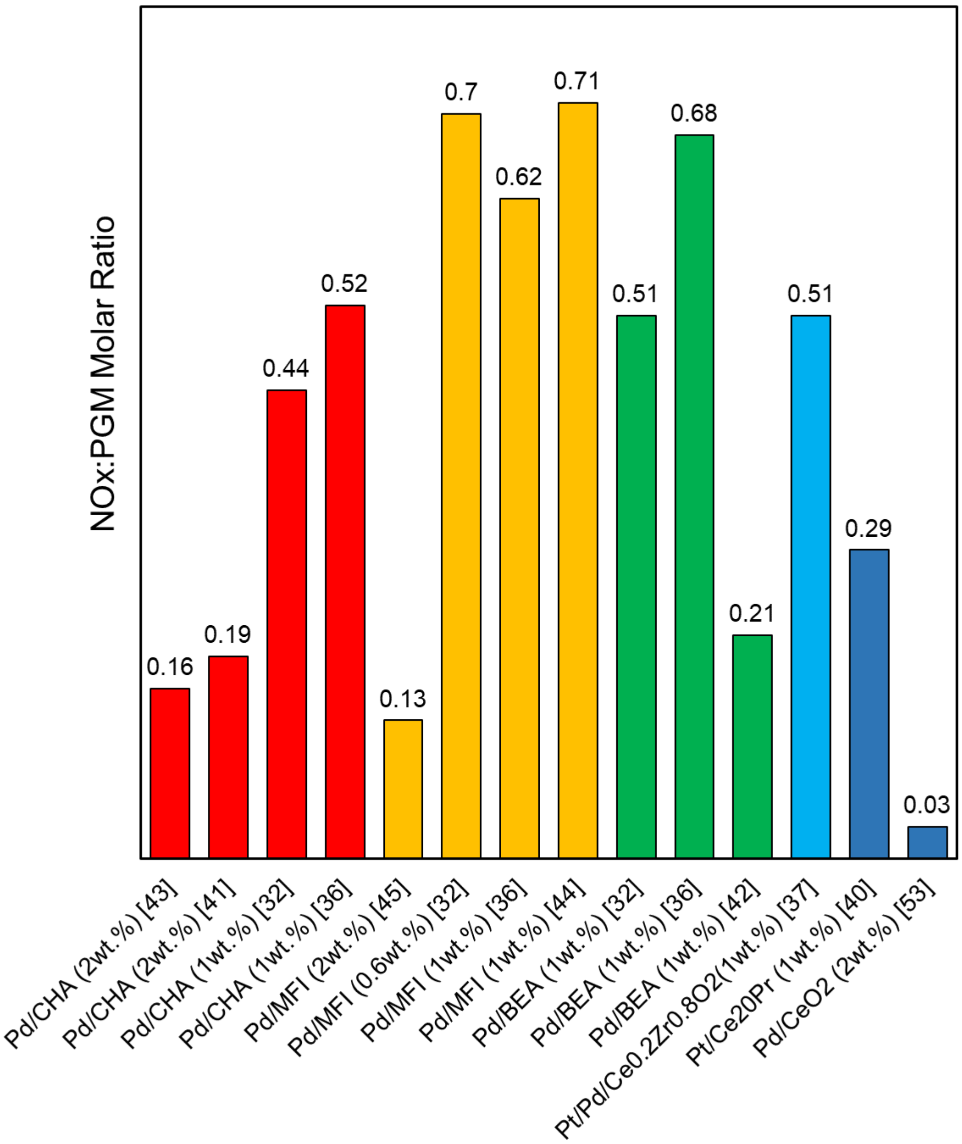

Figure 8.2 NOx: PGM ratios of reported PNA

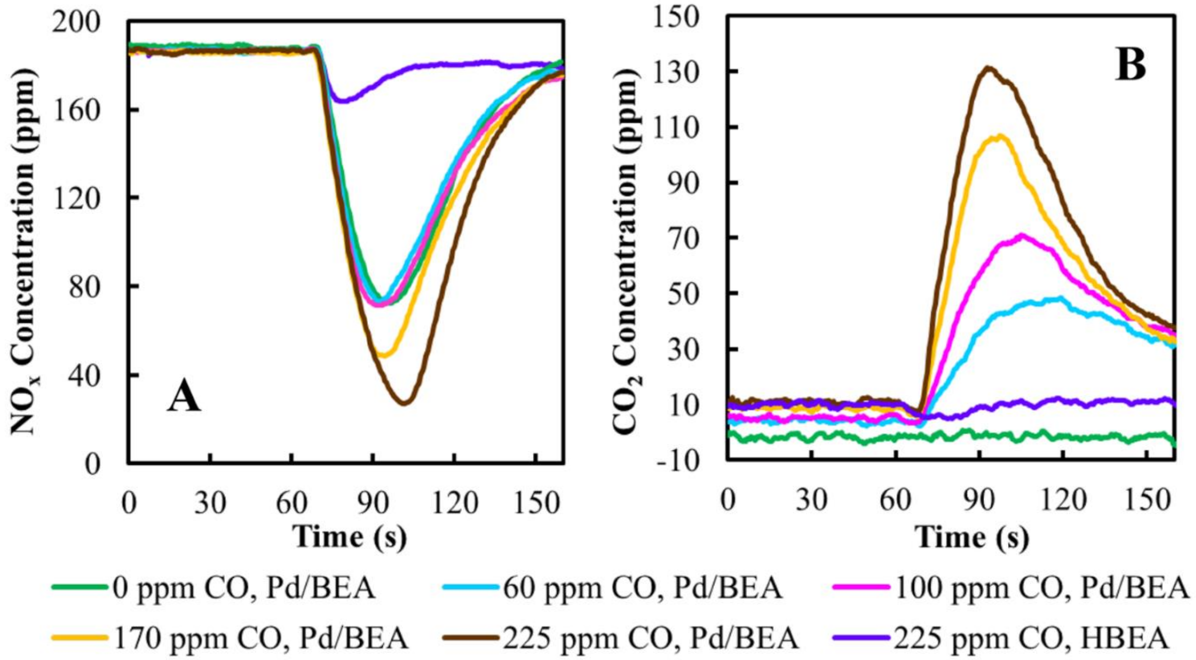

Figure 8.3 A. Effect of CO on NOx uptake and **B.** CO2 detected. Reprinted by permission from Springer Nature: Catalysis Letters, “Effects of CO on Pd/BEA Passive NOx Adsorbers.” Vu, Anh, Jinyong Luo, Junhui Li, and William S. Epling, ©2017.

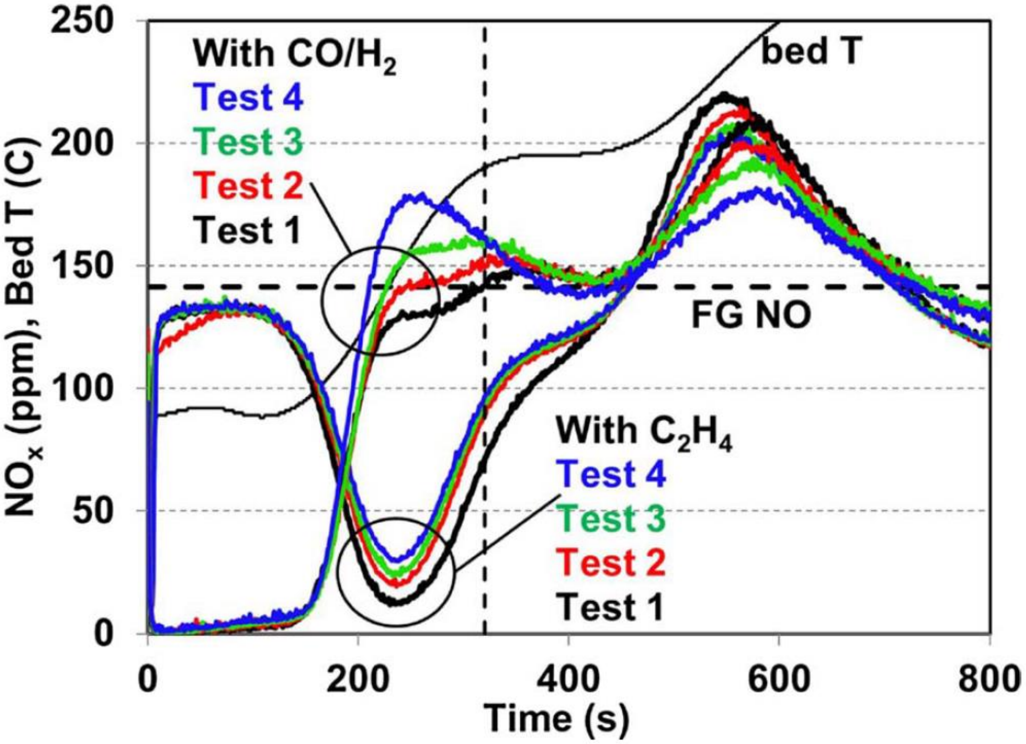

Figure 8.4 NOx slip during 4 consecutive transient tests with 140 ppm NO, 10%O_2, 5%H_2O&CO_2, with 250 ppm C_2H_4 or with 1300 ppm CO +430 ppm H_2. Reprinted from Catalysis Today, Theis, Joseph R, and Christine K Lambert, "Mechanistic Assessment of Low Temperature NOx Adsorbers for Cold Start NOx Control on Diesel Engines", In press ©2015, with permission from Elsevier.

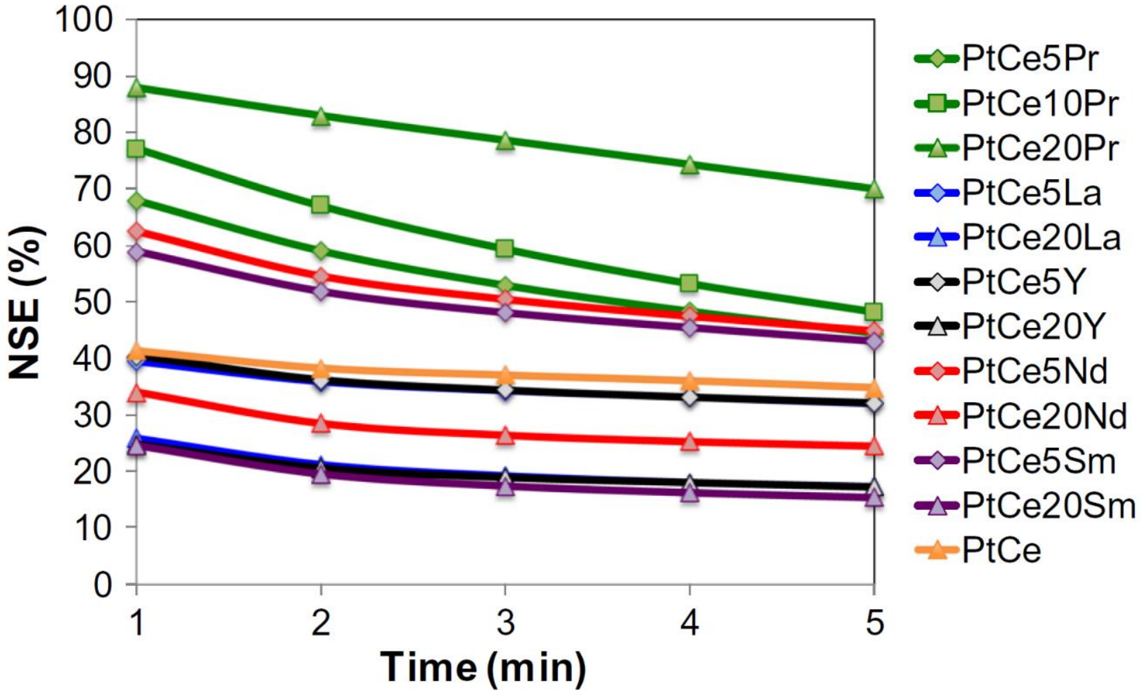

Figure 8.5 Comparison of NOx storage efficiency for Pt-CeO_2/M_2O_3 samples. Feed: 300 ppm NO, 5% O_2, 5% CO_2, and 3.5% H_2O and He balance. Reprinted by permission from Springer Nature: Emission Control Science and Technology, Jones, Samantha et al. 2017. “CeO2-M2O3 Passive NO x Adsorbers for Cold Start Applications.” S. Jones, Y. Ji, A. Bueno-Lopez, Y. Song, and M. Crocker ©2017.

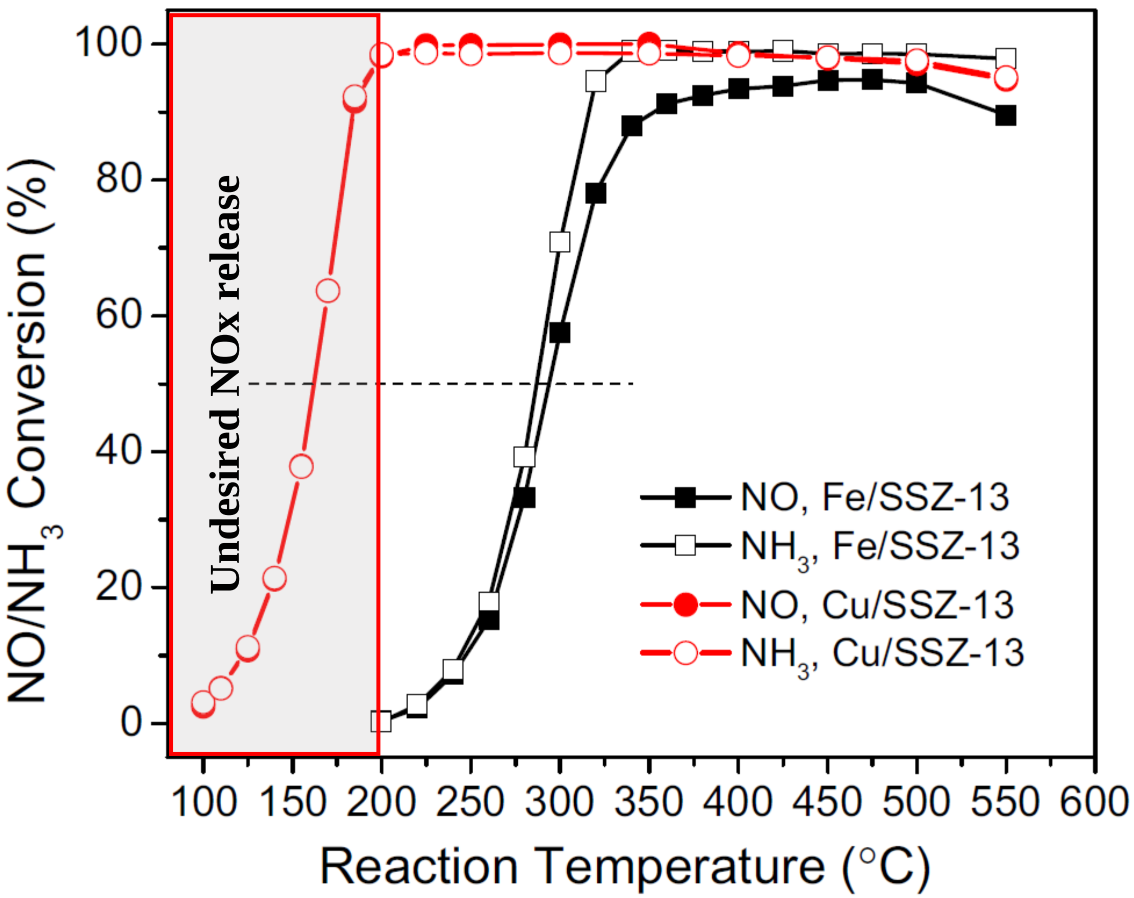

Figure 8.6 NO/NH3 conversion as a function of temperature during standard SCR for the fresh Cu- and Fe/SSZ-13 samples. Reprinted from Catalysis Today, vol. 258, F. Gao, Y. Wang, M. Kollár, N. M. Washton, J. Szanyi, and C. H. F. Peden "A comparative kinetics study between Cu/SSZ-13 and Fe/SSZ-13 SCR catalysts," pp. 347–358 ©2015, with permission from Elsevier. (Red text box with black text added)

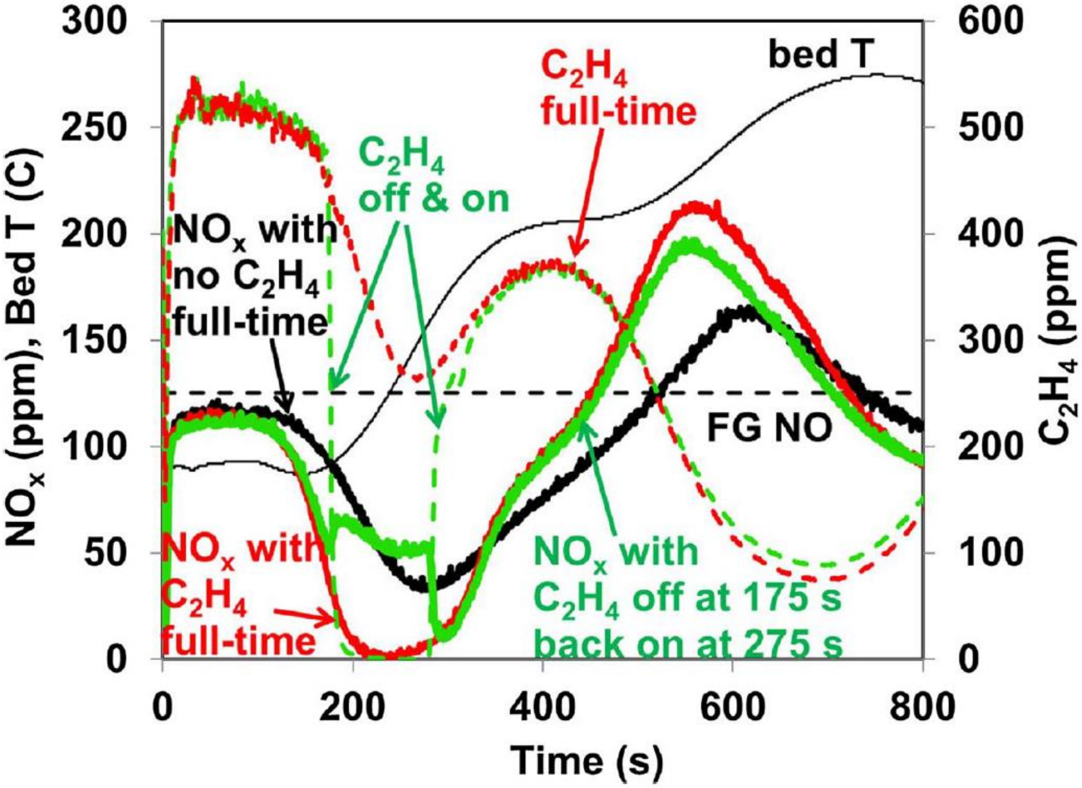

Figure 8.7 NOx and C_2H_4 slip on test with 125 ppm NO, 10%O_2, 5% H_2O & CO_2 and (1) no C_2H_4 full-time; (2) 250 ppm C_2H_4 full-time; and (3) 250 ppm C_2H_4 on initially, off at 175 s, back on at 275 s. Reprinted from Catalysis Today, Theis, Joseph R, and Christine K Lambert, "Mechanistic Assessment of Low Temperature NOx Adsorbers for Cold Start NOx Control on Diesel Engines", In press ©2015, with permission from Elsevier.

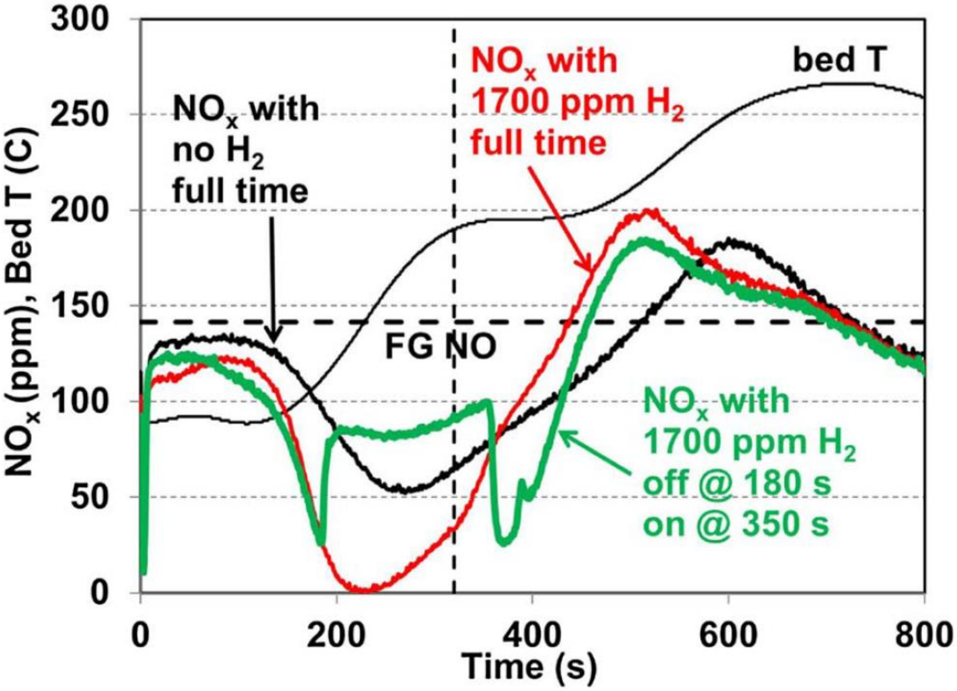

Figure 8.8 140 ppm NO, 10% O_2, 5% H_2O & CO_2 and (1) no H_2 full-time; (2) 1730 ppm H_2 full-time; and (3) 1730 ppm H_2 on initially. Reprinted from Catalysis Today, Theis, Joseph R, and Christine K Lambert, "Mechanistic Assessment of Low Temperature NOx Adsorbers for Cold Start NOx Control on Diesel Engines", In press ©2015, with permission from Elsevier.

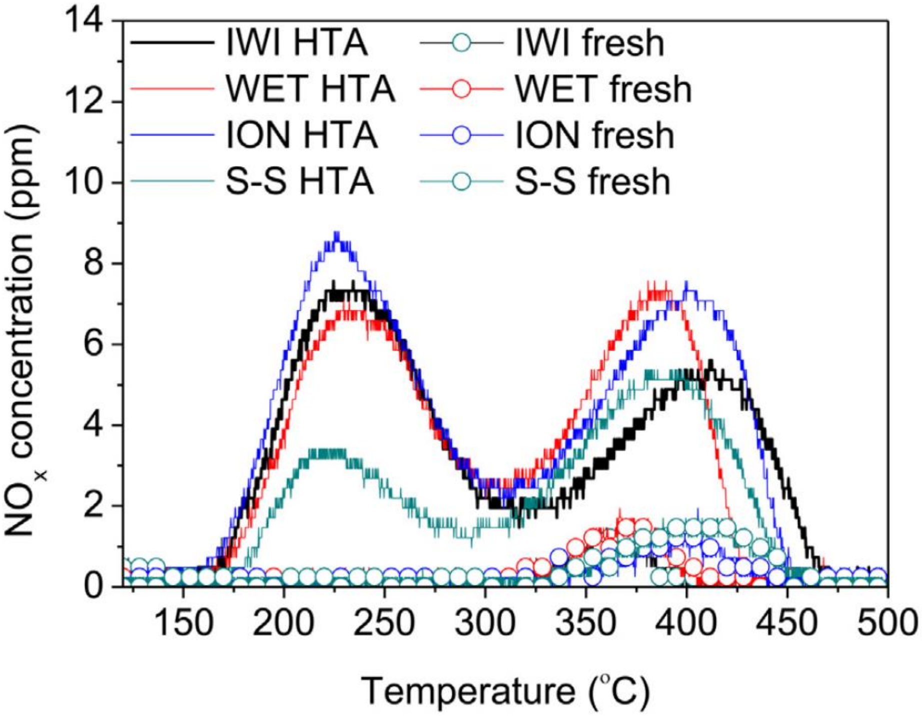

Figure 8.9 NOx desorption profiles of fresh and hydrothermally aged Pd(2)-SSZ-13 IWI,WET,S-S, and ION catalysts. Reprinted from Applied Catalysis B Environmental, vol. 212, Y. Ryou, J. Lee, S. J. Cho, H. Lee, C. H. Kim, and D. H. Kim, “Activation of Pd/SSZ-13 catalyst by hydrothermal aging treatment in passive NO adsorption performance at low temperature for cold start application,” pp. 140-149 ©2017, with permission from Elsevier.

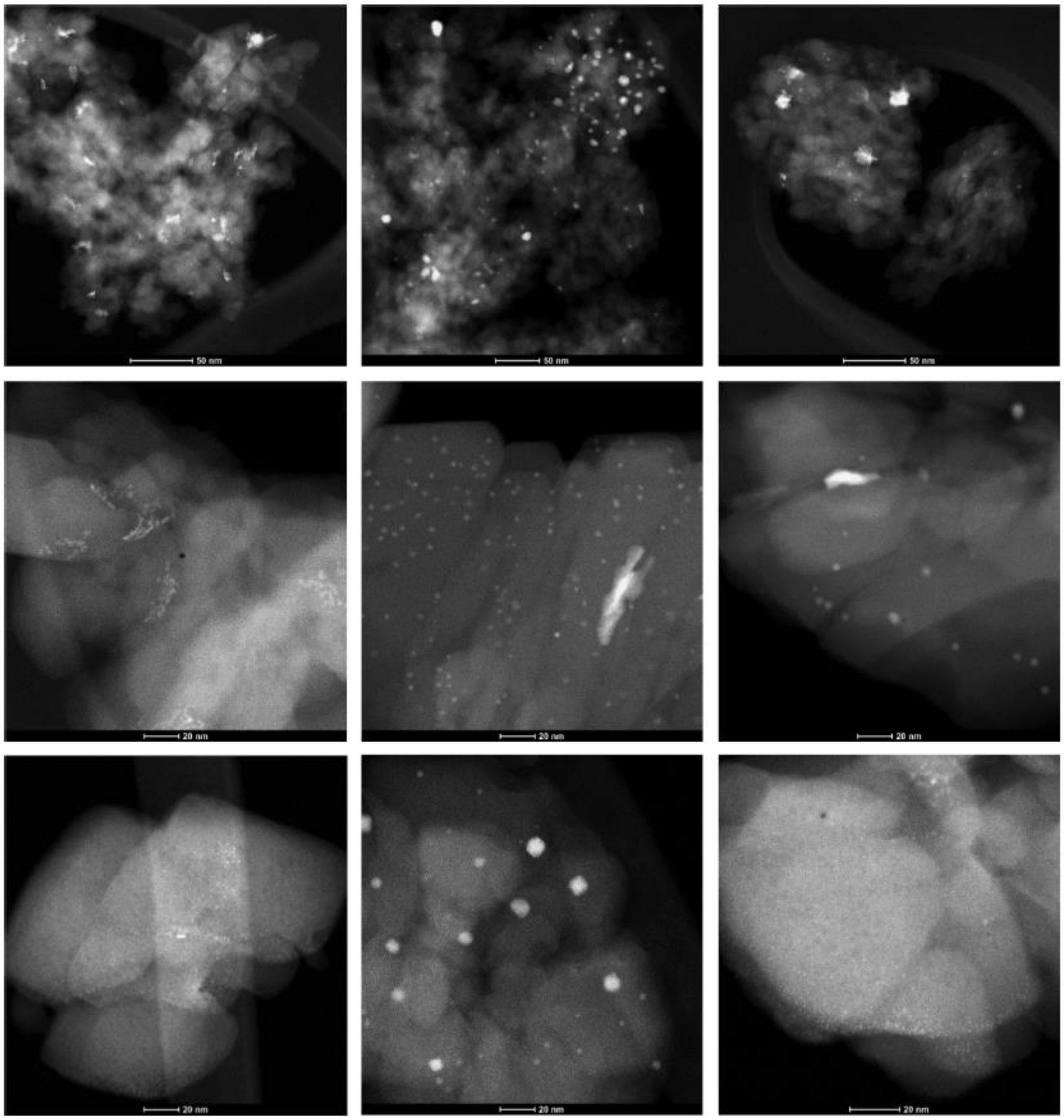

Figure 8.10 STEM images of the freshly calcined (left), reduced (by 1% H_2/He at 400 C for 30 min, middle), and reoxidized (by 10% O_2/He for 1 h, right) Pd-zeolite samples, where the upper, middle and lower rows are images for Pd-BEA (0.92%), Pd-ZSM-5 (0.62%), and Pd-SSZ-13 (0.88%). Reprinted with permission from Y. Zheng *et al.*, “Low-Temperature Pd/Zeolite Passive NO x Adsorbers: Structure, Performance, and Adsorption Chemistry,” *J. Phys. Chem. C*, vol. 121, no. 29, pp. 15793–15803, Jul. ©2017. Copyright 2017 American Chemical Society.

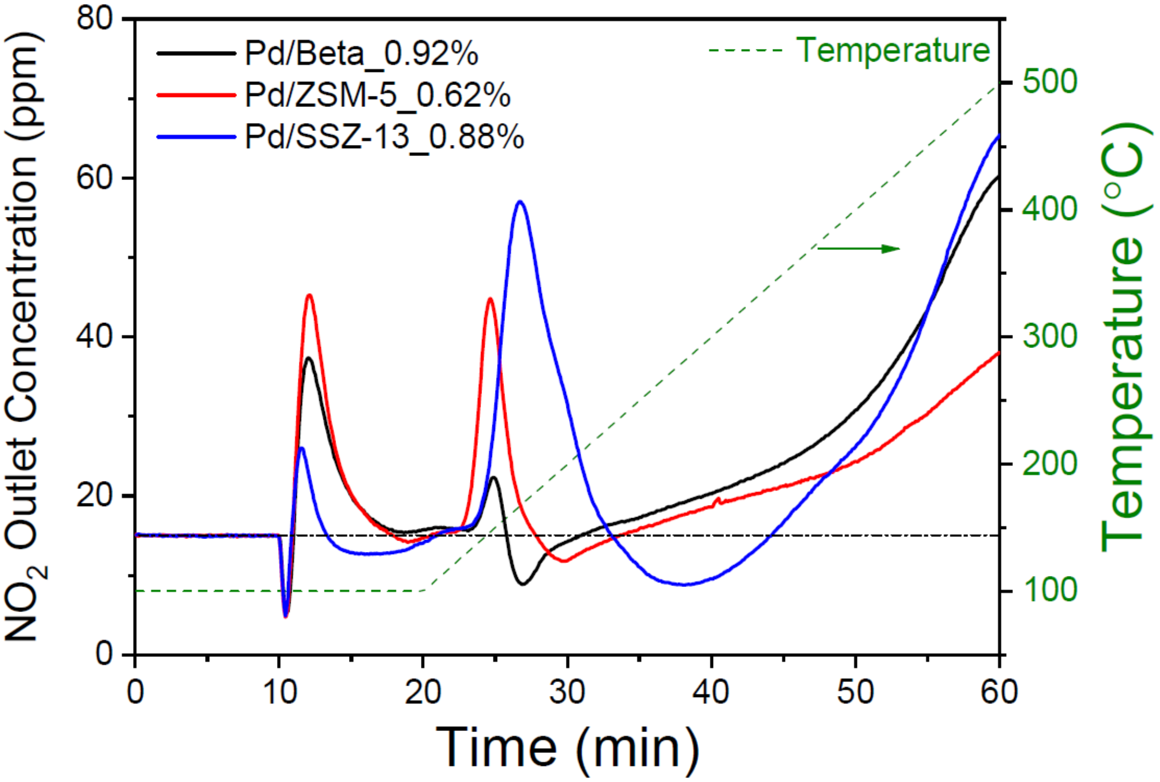

Figure 8.11 NO_2 adsorption and release profiles on the three Pd/zeolites in the presence of H_2O but absence of CO in the feed. Reprinted with permission from Y. Zheng *et al.*, "Low-Temperature Pd/Zeolite Passive NO x Adsorbers: Structure, Performance, and Adsorption Chemistry," *J. Phys. Chem. C*, vol. 121, no. 29, pp. 15793–15803, Jul. ©2017. Copyright 2017 American Chemical Society.

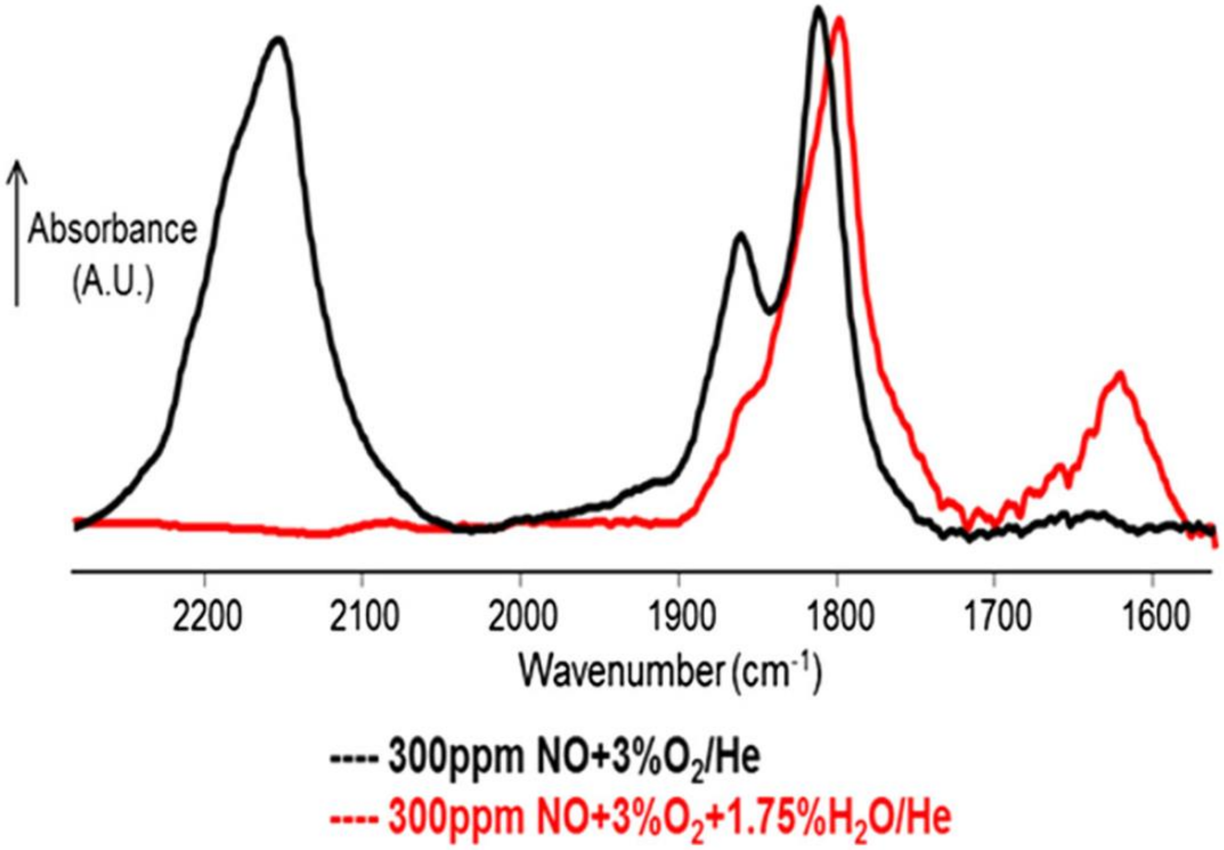

Figure 8.12 DRIFTS spectra recorded at 100 for Pd-CHA after exposure to (NO+O_2) with or without H_2O in the gas mixtures. Reprinted by permission from Springer Nature: Catalysis Letters, “Low Temperature NO Storage of Zeolite Supported Pd for Low Temperature Diesel Engine Emission Control,” H.-Y. Chen, J.E. Collier, D. Liu, L. Mantarosie, D. Durán-Martín, V. Novák, R.R. Rajaram, D. Thompsett, ©2016.

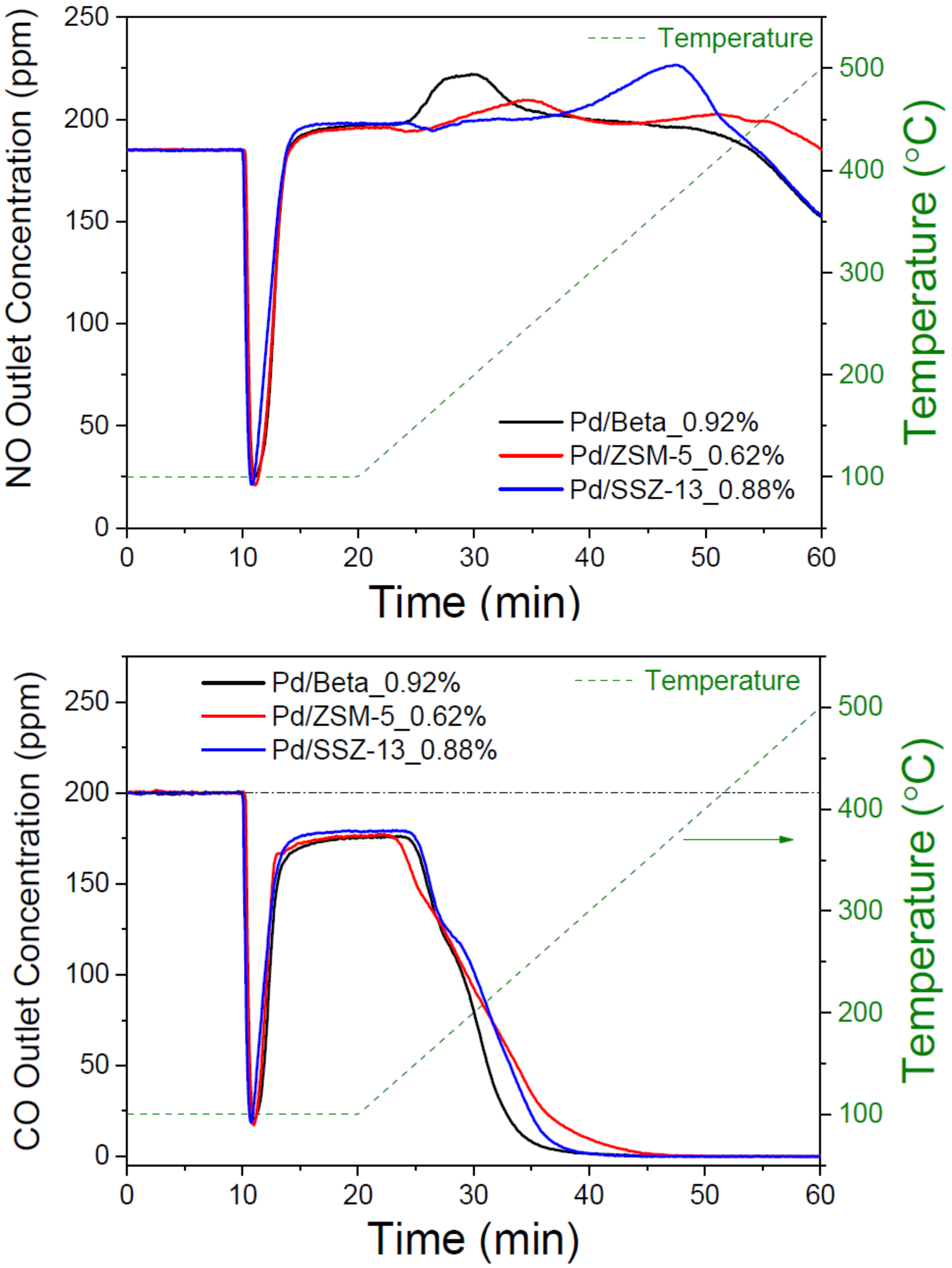

Figure 8.13 NO and CO adsorption and release profiles on the three Pd/zeolites in the presence of both H_2O and CO in the feed. Reprinted with permission from Y. Zheng *et al.*, "Low-Temperature Pd/Zeolite Passive NO x Adsorbers: Structure, Performance, and Adsorption Chemistry," *J. Phys. Chem. C*, vol. 121, no. 29, pp. 15793–15803, Jul. ©2017. Copyright 2017 American Chemical Society.

Table 8.1 NOx desorption features and desorption conditions of reported PNA candidates.

Material	Desorption temperature (°C)	Hydrothermal aging temperature (°C)	Gas composition besides O2	Ramp rate (°C /min)
Pd/CHA (2wt.%) [43]	250, 400	750	5%H_2O	10
Pd/CHA (2wt.%) [41]	230, 420	750	5% H_2O and 5% CO_2	10
Pd/CHA (1wt.%) [32]	360	None	2.5% H_2O and 200 ppm CO	10
Pd/CHA (1wt.%) [36]	360	750	5%H_2O, 200 ppm CO and 50 ppm n-$C_{10}H_{22}$	100
Pd/MFI (2wt.%) [45]	200,450	None	5%H_2O	10
Pd/MFI (0.6wt.%) [32]	250,400	None	2.5% H_2O and 200 ppm CO	10
Pd/MFI (1wt.%) [36]	275	750	5% H_2O, 200 ppm CO and 50 ppm n-$C_{10}H_{22}$	100
Pd/MFI (1wt.%) [44]	300	None	1000 ppm CO	20
Pd/BEA (1wt.%) [32]	210	None	2.5% H_2O and 200 ppm CO	10
Pd/BEA (1wt.%) [36]	260	750	5% H_2O, 200 ppm CO and 50 ppm n-$C_{10}H_{22}$	100
Pd/BEA (1wt.%) [42]	150, 260	750	5% H_2O 200 ppm CO	63
Ag/Al_2O_3 (1.3wt.%) [47]	430	650	6% H_2O, 6% CO_2, 1000 ppm CO 90 ppm C_3H_6/30 ppm C_3H_8, 40 ppm n-dodecane, 25 ppm m-xylene, 500 ppm H_2	10
Pt/Pd/Ce0.2Zr0.8O_2 (1wt.%) [37]	200, 350	750	3.5% H_2O and 5% CO_2	10
Pt/Ce20Pr (1wt.%) [40]	150, 400	None	3.5% H_2O and 5% CO_2	10
Pd/CeO_2 (2wt.%) [53]	300, 450	750	5% H_2O	10
Pt/Pd/Al_2O_3 (140g/ft^3) [20]	250, 400	750	5% H_2O, 200 ppm CO and 500 ppm decane	100
Pd/CeO_2/ZrO_2 (1.5wt.%) [34]	240	700	5% H_2O, 5% CO_2 and 500 ppm C_2H_4	10
Pt/10La/Al_2O_3 (1wt.%) [38]	150, 450	None	3.5% H_2O and 5% CO_2	10

8.5 References

[1] M.P. Harold, Curr. Opin. Chem. Eng. 1 (2012) 303–311.

[2] H.C. Frey, J. Air Waste Manage. Assoc. 68 (2018) 514–563.

[3] C. Sharp, C.C. Webb, S. Yoon, M. Carter, C. Henry, SAE Int. J. Engines 10 (2017) 2017-01–0956.

[4] A. Solouk, M. Shakiba-herfeh, K. Kannan, H. Solmaz, P. Dice, M. Bidarvatan, N.N.T. Kondipati, M. Shahbakhti, in: SAE 2016 Int. Powertrains, Fuels Lubr. Meet., SAE International, 2016.

[5] B.T. Johnson, Platin. Met. Rev. 52 (2008) 23–37.

[6] T. Johnson, SAE Int. J. Engines 9 (2016) 2016-01–0919.

[7] V. Schmeisser, M. Weibel, L. Sebastian Hernando, I. Nova, E. Tronconi, M.P. Ruggeri, SAE Int. J. Commer. Veh. 6 (2013) 2013-01-1064.

[8] G.D. Neely, D. Mehta, J. Sarlashkar, SAE Int. J. Engines 7 (2014) 2014-01-1552.

[9] K. Kamasamudram, N.W. Currier, X. Chen, A. Yezerets, Catal. Today 151 (2010) 212–222.

[10] P. Forzatti, I. Nova, E. Tronconi, Ind. Eng. Chem. Res. 49 (2010) 10386–10391.

[11] F. Gao, Y. Wang, M. Kollár, N.M. Washton, J. Szanyi, C.H.F. Peden, Catal. Today 258 (2015) 347–358.

[12] W.S. Epling, L.E. Campbell, A. Yezerets, N.W. Currier, J.E. Parks, Catal. Rev. 46 (2004) 163–245.

[13] S. Matsumoto, Catal. Today 90 (2004) 183–190.

[14] M. V. Twigg, Appl. Catal. B Environ. 70 (2007) 2–15.

[15] R.M. Heck, R.J. Farrauto, Appl. Catal. A Gen. 221 (2001) 443–457.

[16] V. Schmeisser, M. Weibel, L. Sebastian Hernando, I. Nova, E. Tronconi, M.P. Ruggeri, SAE Int. J. Commer. Veh. 6 (2013) 190–199.

[17] Jarvis, M., and Adams, K.M., US Patent US6182443

[18] Feeley, J. S., Farrauto, R.J., and Deeba, M., US Patent US6471924

[19] Melville, J.E., Brisley, R.J., Keane, O., Phillips, P.R., and Mountstevens, E.H., US Paternt US8105559

[20] H.-Y. Chen, S. Mulla, E. Weigert, K. Camm, T. Ballinger, J. Cox, P. Blakeman, SAE Int. J. Fuels Lubr. 6 (2013) 2013-01–0535.

[21] Ancimer, R.J., Geveci, M., Haas, M., Joshi, A., and Kamasamudram, K., US Patent US9512761

[22] Qi, G., Schmieg, S.J., Ren, S., Li, and Li, W., US Patent US9597635

[23] Rajaram, R.R., Chen, H., and Liu, D., US Patent US20150158019

[24] Kearl, B., Yin, Q., Qi, X., and Biberger, M.A., US Patent US20160045867

[25] Collier, J.E. and Yang, S., US Patent US20170001169

[26] Janssens, T.V.W., and Vennestrom, P.N.R., US Patent US20170095804

[27] Chiffey, A.F., Corps, J., Mitchell-Downie, L., Moreau, F., and O'brien, M., US Patent US20170096923

[28] Chen, H., and Mulla, S., US Patent US20170128922

[29] Biberger, M.A., Kearl, B., Yin, Q., and Qi, X., US Patent US20180093249

[30] H.-Y. Chen, D. Liu, E. Weigert, L. Cumaranatunge, K. Camm, P. Bannon, J. Cox, L. Arnold, SAE Int. J. Engines 10 (2017) 2017-01–0955.

[31] J.R. Theis, C.K. Lambert, Catal. Today 258 (2015) 367–377.

[32] Y. Zheng, L. Kovarik, M.H. Engelhard, Y. Wang, Y. Wang, F. Gao, J. Szanyi, J. Phys.

Chem. C 121 (2017) 15793–15803.

[33] J.L. Falconer, J. a. Schwarz, Catal. Rev. 25 (1983) 141–227.

[34] J.R. Theis, C.K. Lambert, Catal. Today (2017).

[35] J.R. Theis, C. Lambert, SAE Int. J. Engines 10 (2017) 2017-01–0942.

[36] H.-Y. Chen, J.E. Collier, D. Liu, L. Mantarosie, D. Durán-Martín, V. Novák, R.R. Rajaram, D. Thompsett, Catal. Letters 146 (2016) 1706–1711.

[37] Y. Ji, D. Xu, S. Bai, U. Graham, M. Crocker, B. Chen, C. Shi, D. Harris, D. Scapens, J. Darab, Ind. Eng. Chem. Res. 56 (2017) 111–125.

[38] Y. Ji, S. Bai, M. Crocker, Appl. Catal. B Environ. 170–171 (2015) 283–292.

[39] S. Jones, Y. Ji, A. Bueno-Lopez, Y. Song, M. Crocker, Emiss. Control Sci. Technol. 3 (2017) 59–72.

[40] S. Jones, Y. Ji, M. Crocker, Catal. Letters 146 (2016) 909–917.

[41] Y. Ryou, J. Lee, H. Lee, C.H. Kim, D.H. Kim, Catal. Today 307 (2018) 93–101.

[42] Y. Ryou, J. Lee, H. Lee, C.H. Kim, D.H. Kim, Catal. Today 297 (2017) 53–59.

[43] Y. Ji, D. Xu, M. Crocker, J.R. Theis, C. Lambert, A. Bueno-Lopez, D. Harris, D. Scapens, Appl. Catal. A Gen. 567 (2018) 90–101.

[44] A. Vu, J. Luo, J. Li, W.S. Epling, Catal. Letters 147 (2017) 745–750.

[45] Y. Ryou, J. Lee, S.J. Cho, H. Lee, C.H. Kim, D.H. Kim, Appl. Catal. B Environ. 212 (2017) 140–149.

[46] Y. Murata, T. Morita, K. Wada, H. Ohno, SAE Int. J. Fuels Lubr. 8 (2015) 2015-01-1002.

[47] J. Lee, Y. Ryou, S.J. Cho, H. Lee, C.H. Kim, D.H. Kim, Appl. Catal. B Environ. 226 (2018) 71–82.

[48] S. Ren, S.J. Schmieg, C.K. Koch, G. Qi, W. Li, Catal. Today 258 (2015) 378–385.

[49] S. Tamm, S. Andonova, L. Olsson, Catal. Letters 144 (2014) 674–684.

[50] B. Azambre, L. Zenboury, A. Koch, J.V. Weber, J. Phys. Chem. C 113 (2009) 13287–13299.

[51] H.-Y. Chen, J.E. Collier, D. Liu, L. Mantarosie, D. Durán-Martín, V. Novák, R.R. Rajaram, D. Thompsett, Catal. Letters 146 (2016) 1706–1711.

[52] K. Khivantsev, F. Gao, L. Kovarik, Y. Wang, J. Szanyi, J. Phys. Chem. C 122 (2018) 10820–10827.

[53] W.S. Epling, G.C. Campbell, J.E. Parks, Catal. Letters 90 (2003) 45–56.

[54] O. Mihai, L. Trandafilović, T. Wentworth, F.F. Torres, L. Olsson, Top. Catal. (2018).

[55] A. Porta, T. Pellegrinelli, L. Castoldi, R. Matarrese, S. Morandi, S. Dzwigaj, L. Lietti, Top. Catal. (2018).

[56] Y. Ryou, J. Lee, Y. Kim, S. Hwang, H. Lee, C.H. Kim, H.K. Do, Appl. Catal. A Gen. (2018).

[57] N. Garrido Gonzalez, R. Baar, J. Drueckhammer, C. Kaeppner, SAE Int. J. Engines 10 (2017) 1411–1421.

[58] Y. Ryou, J. Lee, H. Lee, C.H. Kim, D.H. Kim, Catal. Today 320 (2019) 175–180.

[59] I. PERDANA, D. CREASER, O. OHRMAN, J. HEDLUND, J. Catal. 234 (2005) 219–229.

[60] C. Descorme, P. Gelin, M. Primet, C. Lecuyer, Catal. Letters 41 (1996) 133–138.

[61] M. Colombo, I. Nova, E. Tronconi, Catal. Today 197 (2012) 243–255.

[62] V.I. Yakerson, V. V Rozanov, A.M. Rubinshtein, Surf. Sci. 12 (1968) 221–246.

[63] A. Filtschew, C. Hess, Appl. Catal. B Environ. 237 (2018) 1066–1081.

[64] X. Wang, L. Lv, Q. Zhang, Y. Zhang, J. Wang, M. Shen, Catal. Sci. Technol. 3 (2013)

200–207.

[65] M. Nolan, S.C. Parker, G.W. Watson, J. Phys. Chem. B 110 (2006) 2256–2262.

[66] A. Martínez-Arias, J. Soria, J.C. Conesa, X.L. Seoane, A. Arcoya, R. Cataluña, J. Chem. Soc. Faraday Trans. 91 (1995) 1679–1687.

[67] B. Levasseur, A.M. Ebrahim, T.J. Bandosz, Langmuir 27 (2011) 9379–9386.

[68] M.Y. Mihaylov, E.Z. Ivanova, H.A. Aleksandrov, P.S. Petkov, G.N. Vayssilov, K.I. Hadjiivanov, Appl. Catal. B Environ. 176–177 (2015) 107–119.

[69] I. Atribak, B. Azambre, A. Bueno López, A. García-García, Appl. Catal. B Environ. 92 (2009) 126–137.

[70] W.S. Epling, in: RSC Catal. Ser., 2018, pp. 104–126.

[71] C. Shi, Y. Ji, U.M. Graham, G. Jacobs, M. Crocker, Z. Zhang, Y. Wang, T.J. Toops, Appl. Catal. B Environ. 119–120 (2012) 183–196.

[72] Y. Ji, T.J. Toops, M. Crocker, Catal. Letters 119 (2007) 257–264.

[73] F.A. Lafossas, C. Manetas, A. Mohammadi, M. Kalogirou, G. Koltsakis, Z. Samaras, M. Iida, M. Inoue, Int. J. Engine Res. 16 (2015) 197–212.

[74] J.H. Kwak, D.H. Kim, J. Szanyi, C.H.F. Peden, Appl. Catal. B Environ. 84 (2008) 545–551.

[75] K. Khivantsev, N.R. Jaegers, L. Kovarik, J.C. Hanson, F.F. Tao, Y. Tang, X. Zhang, I.Z. Koleva, H.A. Aleksandrov, G.N. Vayssilov, Y. Wang, F. Gao, J. Szanyi, Angew. Chemie (2018).

[76] S. HOMEYER, J. Catal. 117 (1989) 91–101.

[77] S.T. Homeyer, W.M.H. Sachtler, Appl. Catal. 54 (1989) 189–202.

[78] B.J. Adelman, W.M.H. Sachtler, Appl. Catal. B Environ. 14 (1997) 1–11.

[79] A.W. Aylor, L.J. Lobree, J.A. Reimer, A.T. Bell, J. Catal. 172 (1997) 453–462.

[80] M. Ogura, M. Hayashi, S. Kage, M. Matsukata, E. Kikuchi, Appl. Catal. B Environ. 23 (1999) 247–257.

[81] A. Baylet, P. Marécot, D. Duprez, P. Castellazzi, G. Groppi, P. Forzatti, Phys. Chem. Chem. Phys. 13 (2011) 4607–4613.

[82] B.J. Adelman, W.M.H. Sachtler, Appl. Catal. B Environ. 14 (1997) 1–11.

[83] K. Chakarova, E. Ivanova, K. Hadjiivanov, D. Klissurski, H. Knözinger, Phys. Chem. Chem. Phys. 006 (2004) 3702–3709.

[84] B. Pommier, P. Ge´lin, Phys. Chem. Chem. Phys. 1 (1999) 1665–1672.

[85] M. BOUDART, J. Catal. 39 (1975) 44–52.

[86] J. BENSON, J. Catal. 30 (1973) 146–153.

[87] M.W. Tew, J.T. Miller, J.A. van Bokhoven, J. Phys. Chem. C 113 (2009) 15140–15147.

[88] S. LADAS, J. Catal. 53 (1978) 356–365.

[89] N.K. Nag, J. Phys. Chem. B 105 (2001) 5945–5949.

[90] K. Okumura, J. Amano, N. Yasunobu, M. Niwa, J. Phys. Chem. B 104 (2000) 1050–1057.

[91] B. Pommier, P. Gelin, Phys. Chem. Chem. Phys. 3 (2001) 1138–1143.

[92] C. Hess, E. Ozensoy, C.-W. Yi, D.W. Goodman, J. Am. Chem. Soc. 128 (2006) 2988–2994.

[93] C.-C. Chao, J.H. Lunsford, J. Am. Chem. Soc. 93 (1971) 6794–6800.

[94] K. Hadjiivanov, J. Saussey, J.L. Freysz, Catal. Letters 52 (1998) 103–108.

[95] C. Sedlmair, B. Gil, K. Seshan, A. Jentys, J.A. Lercher, Phys. Chem. Chem. Phys. 5 (2003) 1897–1905.

[96] J. Szanyi, J.H. Kwak, C.H.F. Peden, J. Phys. Chem. B 108 (2004) 3746–3753.

[97] J.A. Loiland, R.F. Lobo, J. Catal. 325 (2015) 68–78.

[98] K. Honkala, P. Pirilä, K. Laasonen, Surf. Sci. 489 (2001) 72–82.

[99] J.A. Loiland, R.F. Lobo, J. Catal. 311 (2014) 412–423.

[100] B.M. Weiss, E. Iglesia, J. Catal. 272 (2010) 74–81.

[101] E. Ozensoy, D. Wayne Goodman, Phys. Chem. Chem. Phys. 6 (2004) 3765.

Chapter 9. Appendix B - Supporting Information of Chapter 3: Condition-Dependent Pd Speciation and NO Adsorption in Pd/ Zeolites

9.1 Energies of 210 Z_2Pd structures computed using GGA-PBE functional

We used the 210 Z_2Cu structures from Li et al.,[1] substituted Cu with Pd, and then optimized the geometry of all structures using the GGA-PBE functional. For the 25 possible Al-Al configurations in a 36 T-site supercell, there were 12 initial Pd^{II} positions for each of the 10 asymmetric Al pairs and 6 Pd^{II} positions for the 15 symmetric pairs. A convergence criterion of 10^{-6} eV and 0.03 eV/Å for self-consistent-field (SCF) electronic energies and atomic forces respectively was used. The lowest energy Z_2Pd structure, 3NN 6MR, was set as the zero of energy, and all other energies were calculated relative to it.

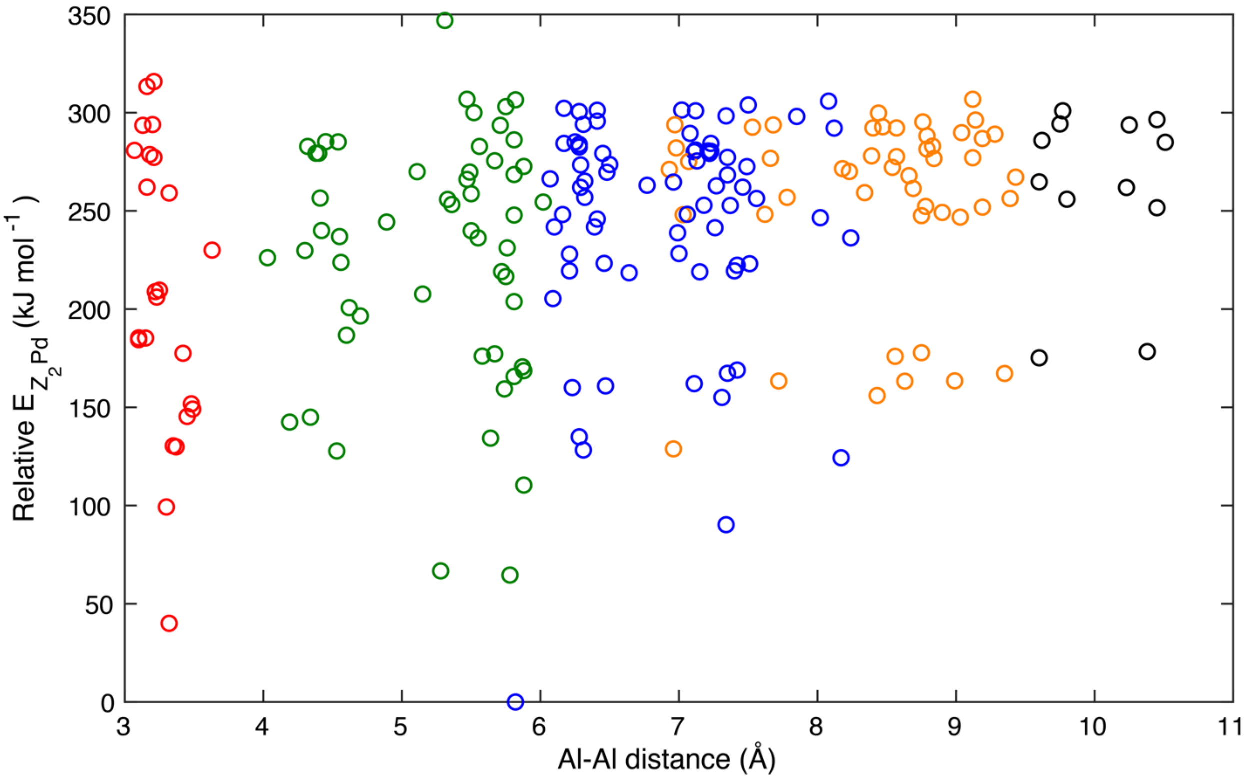

Figure S1. Z_2Pd energy vs Al-Al distance for all possible 210 structures of Z_2Pd. The nearest neighbor configurations are color-coded as: red-1NN, green-2NN, blue-3NN, orange-4NN, and black-5NN. The 1NN (red circles) denote Al configurations in violation of Löwenstein's rule.[2,3]

9.2 Energies of Z_2Pd structures computed using the HSE06 functional

We optimized the lowest energy structure from the PBE calculations (**Figure 2**) for each of the 25-symmetry distinct Al-Al configurations using the HSE06 functional with a convergence criterion of 10^{-6} eV and 0.03 eV/Å for self-consistent-field (SCF) electronic energies and atomic forces respectively. Energy trends were analogous to the PBE calculations, with the 3NN 6MR as the lowest energy configuration. Energies of other structures have been reported relative to it.

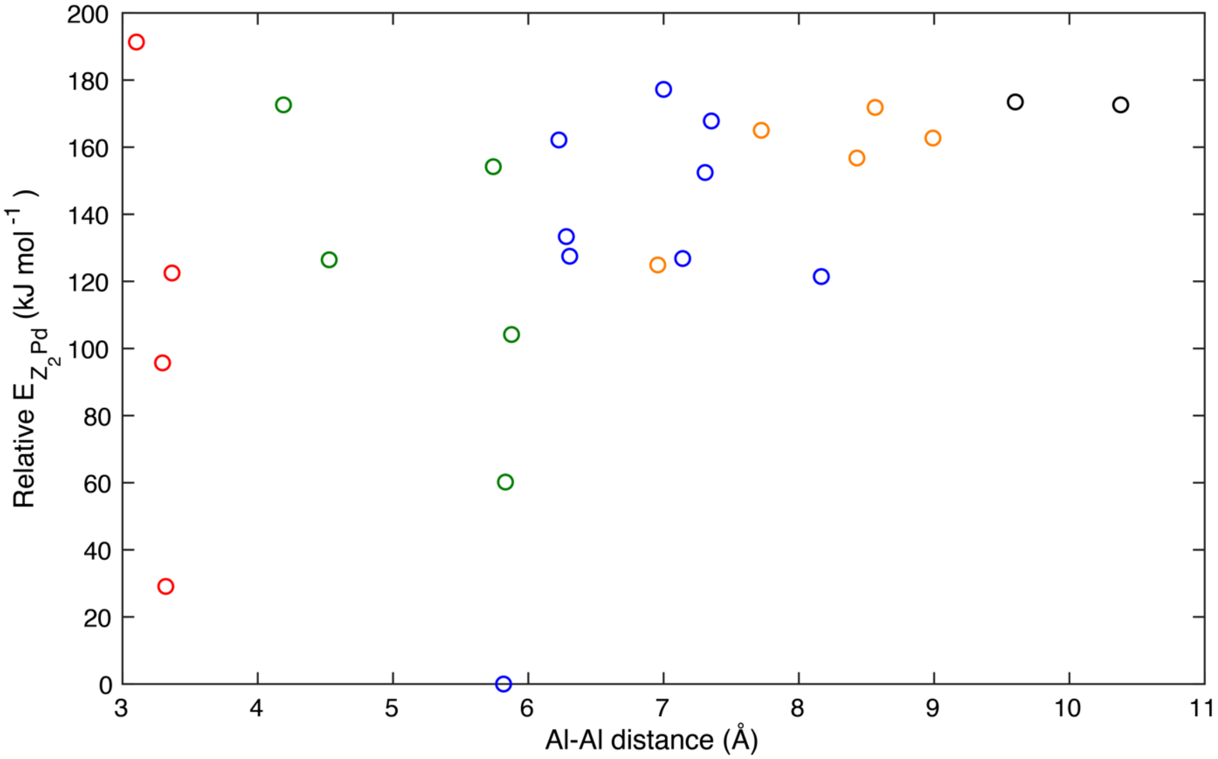

Figure S2. Z_2Pd energy vs Al-Al distance for the lowest energy structure in each of the 25 Al-Al configurations of Z_2Pd. The nearest neighbor configurations are color-coded as: red-1NN, green-2NN, blue-3NN, orange-4NN, and black-5NN. The 1NN (red circles) denote Al configurations in violation of Löwenstein's rule.[2,3]

9.3 1Al and 2Al T-sites exchange reaction energies

Different mechanisms to transfer a Pd cation between 1Al and 2Al sites were considered in 12- and 24 T-site supercells, with Z_2 and Z sites in the same (represented by forward slash), and separate (denoted by +), supercells using PBE and HSE06 functionals. Optimized structures of all reactants and products have been provided in the CONTCARS attachment.

$$[\mathrm{Z_2Pd^{II}(H_2O)}] \rightarrow [\mathrm{ZPd^{II}OH}]/[\mathrm{ZH}], \tag{1}$$

	ΔE (kJ mol^{-1})	
	PBE	HSE06
12 T-site	+85	+79
24 T-site	+100	+101

$$[\mathrm{Z_2Pd^{II}(H_2O)}] + [\mathrm{ZH}] \rightarrow [\mathrm{ZPd^{II}OH}] + [\mathrm{ZH}]/[\mathrm{ZH}], \tag{2}$$

	ΔE (kJ mol^{-1})	
	PBE	HSE06
24 T-site	+111	+91

$$[\mathrm{Z_2Pd^{II}}] + \frac{1}{2}\mathrm{H_2O} - \frac{1}{4}\mathrm{O_2} \rightarrow [\mathrm{ZH}]/[\mathrm{ZPd^{I}}], \tag{3}$$

	ΔE (kJ mol^{-1})	
	PBE	HSE06
12 T-site	+82	+28
24 T-site	+87	+30

9.4 DRIFTS spectra for Pd/SSZ-13

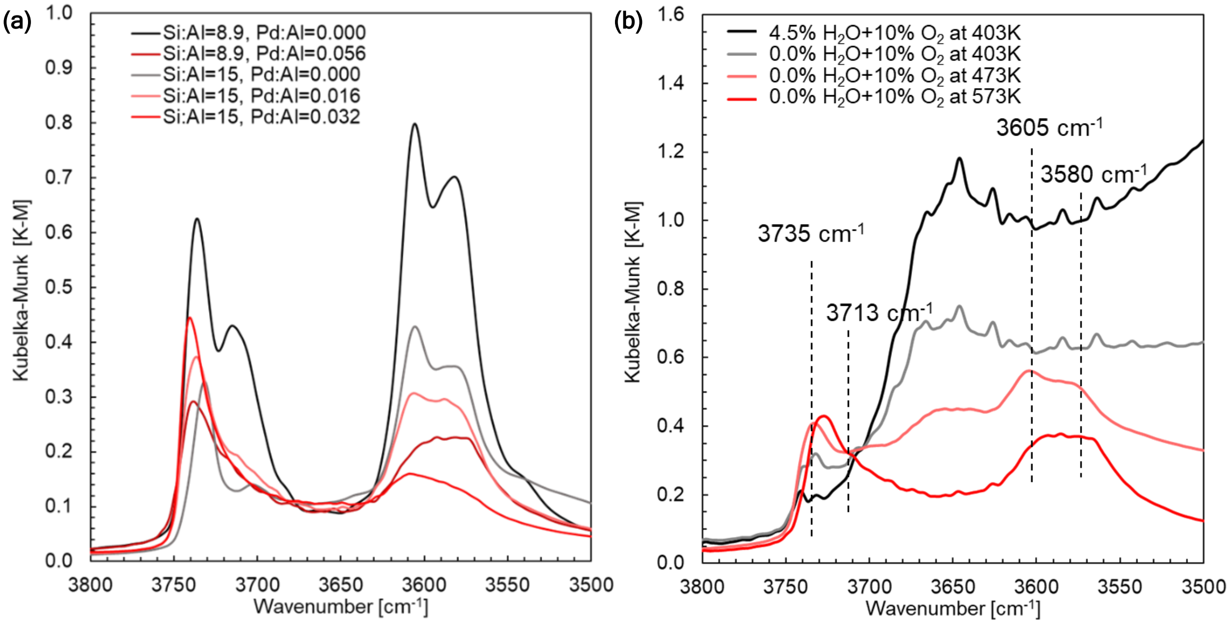

Figure S3. (a) Ex-situ DRIFTS spectra of Pd/SSZ-13 samples with different Si/Al and Pd/Al ratios (ICP-OES confirmed) collected at 473 K in 10% O_2 after a 45 min 773 K 10% O_2 pretreatment. **(b)** In-situ DRIFTS spectra of Pd/SSZ-13 collected at: 403 K with 10% O_2 and 4.5% H_2O (black); 403 K with10% O_2 after 10% O_2 and 4.5% H_2O exposure at 403 K (gray); 473 K with 10% O_2 after 10% O_2 and 4.5% H_2O exposure at 403 K (pink); 573 K with 10% O_2 after 10% O_2 and 4.5% H_2O exposure at 403 K (red). 75 mg of powder sample were pressed into a pellet for each test, and the total flow rate through the IR cell was maintained at 60 standard cubic centimeters per minute (sccm).

*Absence of [ZPd^{II}OH] is observed among all synthesized samples in **Figure S3a**

Figure S3b shows the in-situ DRIFTS characterization on a Pd/SSZ-13 sample (Si/Al = 9, Pd/Al = 0.056) at 403 K, 473 K and 573 K in the absence of H_2O after an exposure to 4.5% H_2O at 403 K. After exposure to 10% O_2 and 4.5% H_2O at 403 K, we observe the perturbation of O-H stretching features associated with Brønsted acid sites at 3730 cm^{-1} and 3600 cm^{-1}, and silanol at 3580 cm^{-1} due to hydrogen bonding.[34,90,92] The adsorption of H_2O is also captured by the significant increase in intensity of a broad O-H stretching band from 3500 cm^{-1} to 3700 cm^{-1}. The same characteristics are captured in the spectrum obtained at 403 K after H_2O is turned off. As temperature increases, the intensity of the O-H stretching band spanning 3500 cm^{-1} to 3700 cm^{-1} decreases, and O-H stretching features associated with Brønsted acid sites at 3730 cm^{-1} and 3600 cm^{-1}, and silanol at 3580 cm^{-1} restore. The spectrum collected at 573 K after the 403 K H_2O exposure is identical to the spectrum obtained after the 773 K pretreatment suggesting complete dehydration at 573 K. These results agree well with the DFT computed free energy plots in **Figure 4a**, where $Z_2[Pd^{II}(H_2O)_4]$ and $[Z_2Pd^{II}]$ are predicted to be the lowest free energy species under condition 1 (298 K, 4.5% H_2O, and 10% O_2) and condition 2 (773 K, 3.1% H_2O, and 10% O_2), respectively, and the complete dehydration in 4.5% H_2O is predicted to occur at 575 K according to the phase diagram shown in **Figure 4b**.

9.5 Functional accuracy

9.5.1 PBE *vs* HSE06 Adsorption Energies of xH_2O (x = 1- 6)

For [ZPd^{I}] and [$ZPd^{II}OH$] we used a 12 T-site supercell. To maintain a uniform Si/Al ratio across the 1Al and 2Al site models, we constructed a 24 T-site supercell for [Z_2Pd^{II}].

Table S1. Comparison of Adsorption Energies (ΔE_{ads}) of H_2O Molecules (x = 1 - 6) on Pd Sites Calculated Using PBE-D3(BJ)vdw and HSE06-D3(BJ)vdw.

	$+xH_2O$		1	2	3	4	5	6
ZPd	ΔE_{ads} (kJ mol^{-1})	PBE	-104	-75	-83	-59	-73	-68
		HSE06	-105	-76	-77	-63	-67	-70
	Pd oxidation state		1.0	1.0	1.0	1.0	1.0	1.0
ZPdOH	ΔE_{ads} (kJ mol^{-1})	PBE	-145	-61	-116	-75	-94	-69
		HSE06	-147	-53	-126	-71	-95	-46
	Pd oxidation state		2.0	2.0	2.0	2.0	2.0	2.0
Z_2Pd	ΔE_{ads} (kJ mol^{-1})	PBE	-42	-118	-93	-77	-130	-78
		HSE06	-52	-127	-88	-87	-124	-81
	Pd oxidation state		2.0	2.0	2.0	2.0	2.0	2.0

9.5.2 HSE06-computed Energies and Bader Charges of 1Al and 2Al Pd-exchanged Sites

Bader charges for the $Z_*PdH_xO_y$ species were normalized by setting ZPd as 1.00 (raw Bader charge = 9.32) and Z_2Pd as 2.00 (raw Bader charge = 8.89).

Table S2. Calculated Total Energies and Normalized Bader Charges for the HSE06-D3(BJ)vdw Optimized Structures of $Z_*PdH_xO_y$ Species at 1Al and 2Al Sites.

Species	Energy (eV)	Bader Charge
ZPd	-356.801	1.00
ZPd.1H_2O	-375.383	1.08
ZPd.2H_2O	-393.668	1.12
ZPd.3H_2O	-411.959	1.04
ZPd.4H_2O	-430.102	1.03
ZPdOH	-369.362	1.97
ZPdOH.1H_2O	-388.384	1.90
ZPdOH.2H_2O	-406.430	1.94
ZPdOH.3H_2O	-425.232	1.98
ZPdO	-363.190	2.16
$ZPdO_2$	-371.558	1.64
$ZPdO_2$.1H_2O	-389.813	1.84
$ZPdO_2$.2H_2O	-407.828	1.84
$ZPdO_2$.3H_2O	-426.574	1.94
Z_2Pd	-708.299	2.00
Z_2Pd.1H_2O	-726.328	2.04
Z_2Pd.2H_2O	-745.144	2.05
Z_2Pd.3H_2O	-763.551	2.10
Z_2Pd.4H_2O	-781.942	2.18
Z_2PdO	-713.079	2.61
Z_2PdO_2	-722.446	2.01

9.5.3 HSE06-computed Thermodynamic Phase Diagrams

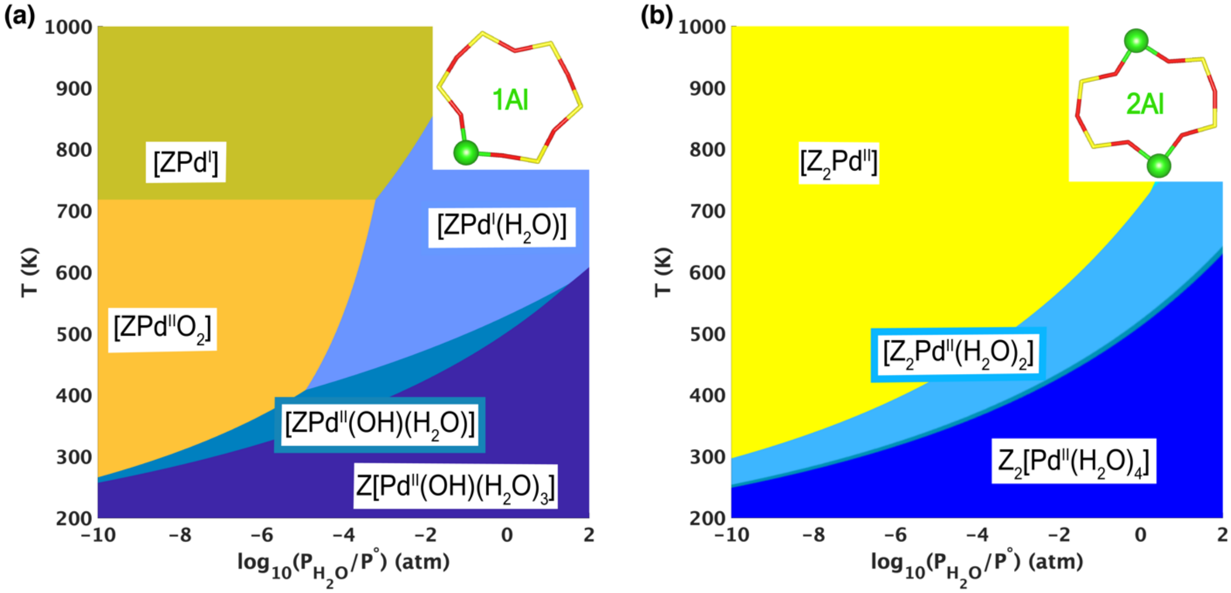

Figure S4. Thermodynamic phase diagrams of $Z_*PdH_xO_y$ species for individual **(a)** 1Al and **(b)** 2Al Pd-exchanged sites based on HSE06-D3(BJ)vdw calculated energies. Vibrational contributions to free energy are not included in these diagrams.

9.6 X-Ray absorption experiments

9.6.1 EXAFS Characterization

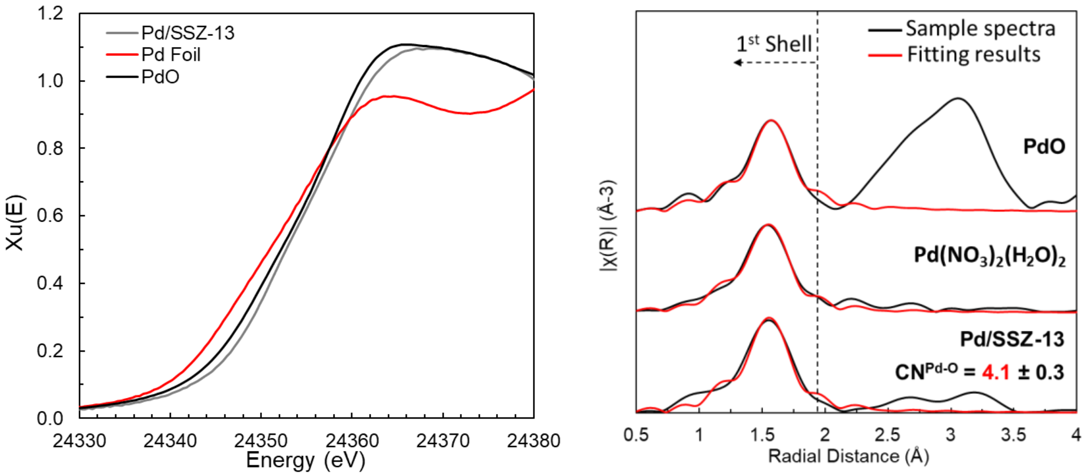

Figure S5. XANES spectra (left) of an ambient exposed Pd/SSZ-13 sample (Si/Al = 8.9, Pd/Al = 0.056), PdO and Pd foil. EXAFS spectra and fitting (right) of fist shell Pd-O scattering (red) using PdO and $Pd(NO_3)_2(H_2O)_2$ as Pd^{II} standards (black). 180 mg of powder sample with particle sizes between 250 to 425 μm were loaded into the in-situ reactor cell, and the total flow rate used was 250 sccm.

Table S3. Fitting parameters and results of EXAFS spectra shown in **Figure S5**

Temp. [K]	Scattering path	Coordination number	Distance (Å)	σ^2 (Å^2)	ΔE_0 (eV)	R-factor
298	Pd-O	4.1 ± 0.3	2.01	0.006 ± 0.00078	-1.3 ± 0.6	0.001

S_0^2 was fixed at 0.8934. fitting of Pd/SSZ-13 Sample spectrum was performed in R-space for $2.5 < k < 10$ Å-1 and $1.0 < R < 2.0$ Å. Combined k^1-k^2-k^3 weighted fits.

*Absence of significant second shell scattering indicates that all Pd cations are hydrated and there is no significant nanoparticle formation.

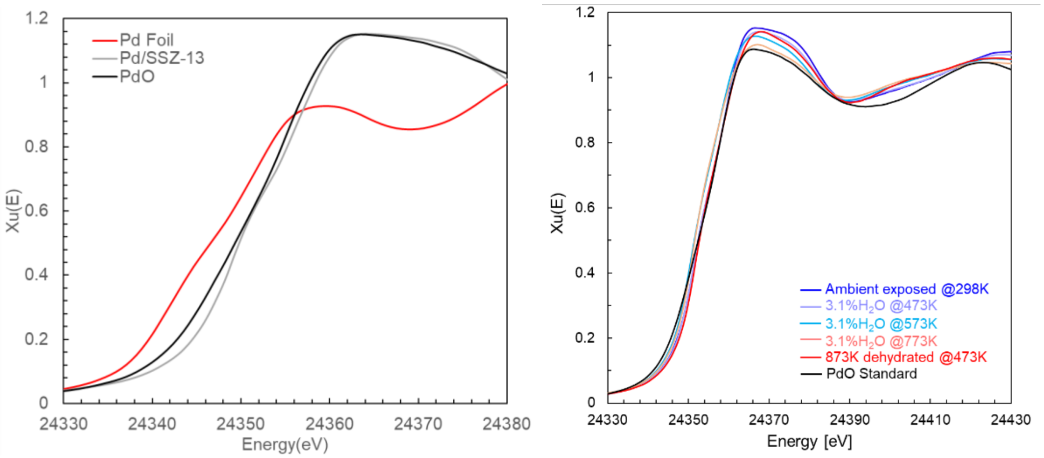

Figure S6. XANES spectra (left) of an ambient exposed Pd/SSZ-13 sample (Si/Al = 17, Pd/Al = 0.046), PdO and Pd foil. XANES spectra (right) of all the states studied by EXAFS. 30 - 45 mg of powder sample were pressed into the sample holder for testing.

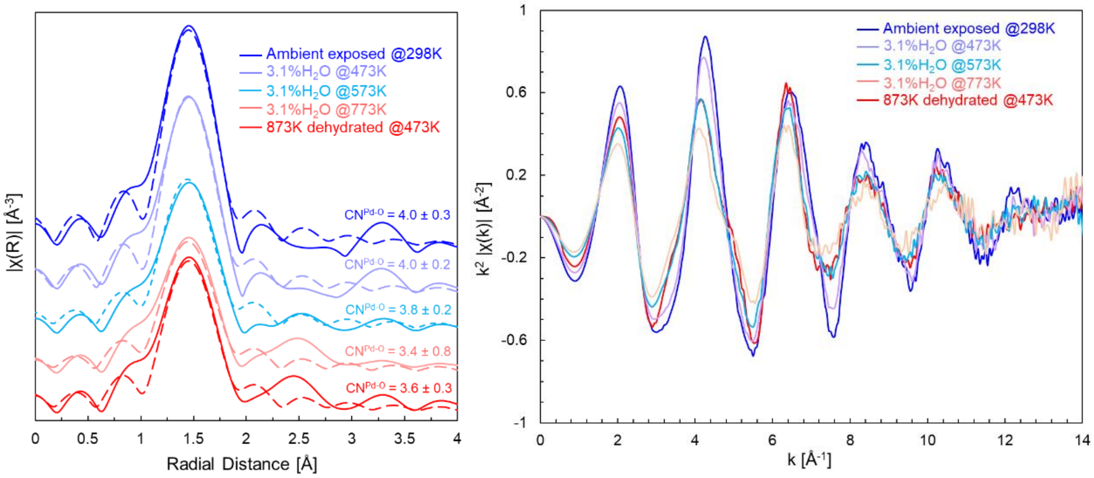

Figure S7. First shell Pd-O single path scattering fitting results, dashed lines show the single scattering path fit (left). The corresponding chi(k) (right).

Table S4. Fitting parameters and results of EXAFS spectra shown in **Figure 3b**.

Temp. [K]	Scattering path	Coordination number	Distance (Å)	σ^2 (Å^2)	ΔE_0 (eV)	R-factor
298	Pd-O	4 ± 0.3	2.01	0.006 ± 0.00085	-4.3 ± 0.6	0.001
473	Pd-O	4 ± 0.2	2.01	0.008 ± 0.00091	-4.1 ± 0.7	0.001
573	Pd-O	3.8 ± 0.2	2.01	0.011 ± 0.00108	-3.9 ± 0.8	0.006
773	Pd-O	3.4 ± 0.8	2.01	0.017 ± 0.00121	-3.8 ± 0.9	0.012
473	Pd-O	3.6 ± 0.3	2.01	0.007 ± 0.00083	-3.9 ± 0.6	0.003

*S_0^2 was fixed at 0.8913. Fits were performed in R-space for $2.5 < k < 10$ Å^{-1} and $1.0 < R < 2.0$ Å. Combined k^1-k^2-k^3 weighted fits.

9.7 NO adsorption energetics

9.7.1 PBE and HSE06 Adsorption Energies of NO

Bader charges for the $Z_*PdH_xO_yN_z$ species were normalized by setting ZPd as 1 (raw Bader charge = 9.32) and Z_2Pd as 2 (raw Bader charge = 8.89).

Table S5. Adsorption Energies (ΔE_{ads}) of NO on Pd Sites in the Absence and Presence of H_2O Molecules (x = 0 - 3) Calculated Using PBE-D3(BJ)vdw and HSE06-D3(BJ)vdw.

	$+xH_2O$		0	1	2	3
ZPd-NO	ΔE_{ads} (kJ mol^{-1})	PBE	-272	-239	-240	-224
		HSE06	-175	-142	-141	-146
	Pd Bader Charge		1.38	1.52	1.41	1.56
ZPdOH-NO	ΔE_{ads} (kJ mol^{-1})	PBE	-195	-126	-157	-99
		HSE06	-140	-58	-103	-37
	Pd Bader Charge		2.05	2.12	2.18	2.09
Z_2Pd-NO	ΔE_{ads} (kJ mol^{-1})	PBE	-123	-150	-120	-123
		HSE06	-70	-106	-60	-68
	Pd Bader Charge		2.07	2.13	2.18	2.15

9.7.2 Adsorption of a Second NO molecule

Adsorption of the second NO molecule was calculated in the absence and presence of H_2O as per the following reactions:

1Al: $\mathrm{ZPd(NO)(H_2O)}_x + \mathrm{NO} \xrightarrow{\Delta E_{\mathrm{ads}}} \mathrm{ZPd(NO)_2(H_2O)}_x$

(4) $\mathrm{ZPd^{II}(OH)(NO)(H_2O)}_x + \mathrm{NO} \xrightarrow{\Delta E_{\mathrm{ads}}} \mathrm{ZPd^{II}(OH)(NO)_2(H_2O)}_x$

(5)

2Al: $\mathrm{Z_2Pd^{II}(NO)(H_2O)}_x + \mathrm{NO} \xrightarrow{\Delta E_{\mathrm{ads}}} \mathrm{Z_2Pd^{II}(NO)_2(H_2O)}_x$

(6)

The computed energy was compared to the energy for adsorbing a H_2O molecule on the same sites as follows:

1Al: $\mathrm{ZPd(NO)(H_2O)}_x + \mathrm{H_2O} \xrightarrow{\Delta E_{\mathrm{ads}}} \mathrm{ZPd(NO)(H_2O)}_{x+1}$

(7)

$\mathrm{ZPd^{II}(OH)(NO)(H_2O)}_x + \mathrm{H_2O} \xrightarrow{\Delta E_{\mathrm{ads}}} \mathrm{ZPd^{II}(OH)(NO)(H_2O)}_{x+1}$ (8)

2Al: $\mathrm{Z_2Pd^{II}(NO)(H_2O)}_x + \mathrm{H_2O} \xrightarrow{\Delta E_{\mathrm{ads}}} \mathrm{Z_2Pd^{II}(NO)(H_2O)}_{x+1}$

(9)

Table S6. Adsorption Energies (ΔE_{ads}) of the Second NO Molecule on Pd Sites Compared to Adsorption Energies (ΔE_{ads}) of H_2O on the Same Sites Calculated Using PBE-D3(BJ)vdw and HSE06-D3(BJ)vdw.

Adsorption Site	+NO ΔE_{ads} (kJ $\mathrm{mol^{-1}}$)		+H_2O ΔE_{ads} (kJ $\mathrm{mol^{-1}}$)	
	PBE	HSE06	PBE	HSE06
ZPd(NO)	-89	-65	-71	-73
$\mathrm{ZPd(NO)(H_2O)_2}$	-77	-45	-66	-82
ZPdOH(NO)	-127	-44	-76	-66
$\mathrm{ZPdOH(NO)(H_2O)}$	-123	-29	-92	-98
$\mathrm{Z_2Pd(NO)}$	-110	-35	-70	-88
$\mathrm{Z_2Pd(NO)(H_2O)_2}$	-71	+6	-69	-95

9.7.3 PBE *vs* HSE06 Thermodynamic Phase Diagrams for 1Al and 2Al Pd-exchanged Sites

Exchange Reaction 1: $[Z_2Pd^{II}(H_2O)] \rightarrow [ZPd^{II}OH]/[ZH]$

PBE HSE06

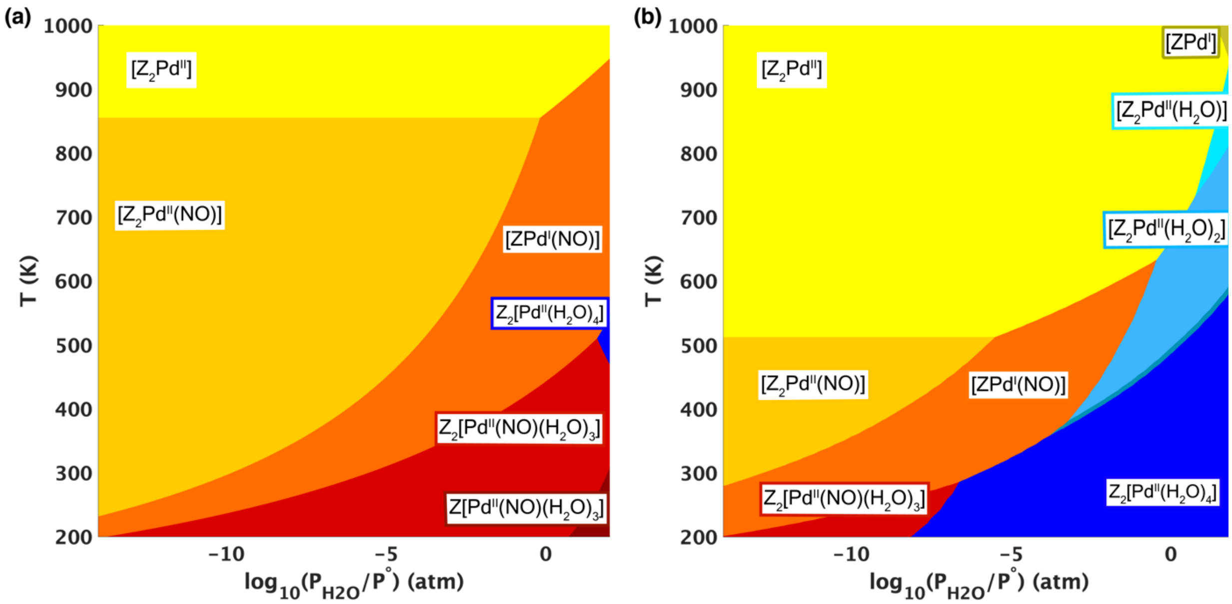

Exchange Reaction 2: $[Z_2Pd^{II}] + \frac{1}{2}H_2O - \frac{1}{4}O_2 \rightarrow [ZH]/[ZPd^{I}]$

PBE HSE06

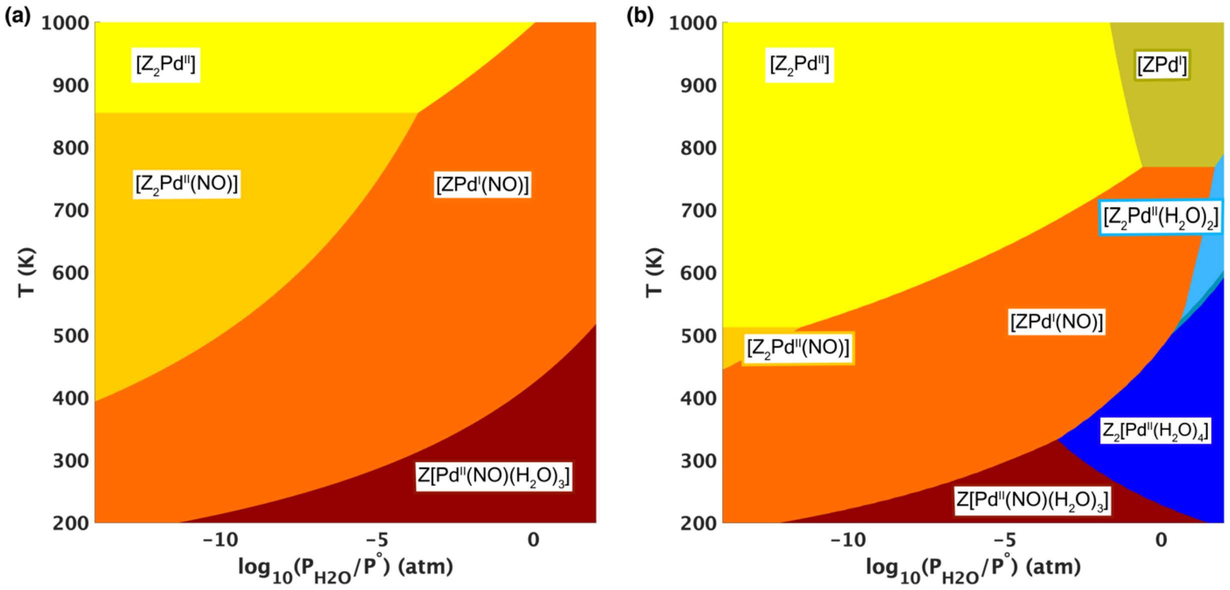

Figure S8. Thermodynamic phase diagrams of $Z_*PdH_xO_yN_z$ species for 1Al and 2Al sites represented on a common energy scale based on **(a)** GGA-PBE-D3(BJ)vdw, and **(b)** HSE06-D3(BJ)vdw calculated energies for two exchange reaction routes. Vibrational contributions to free energy are not included in these diagrams.

9.8 Pd-nitrosyl complexes

9.8.1 Frequencies of Pd-nitrosyl complexes

The NO vibrational frequencies for the structures considered in the H_2O-solvated Pd-, and zeolite cluster models were computed using B3LYP/def2-TZVPP method in Gaussian 16.[4] We then scaled the raw frequencies with a scale factor of 0.963.[5] This reported scale factor (*c*) was obtained from 310 calculations of different molecules and considering 3508 computed vibrations (ω_i), along with experimentally observed frequencies (ν_i) as follows:

$$c = \Sigma (\nu_i \times \omega_i) / \Sigma (\omega_i^2)$$

(10) $u_r^2 = (\Sigma (\omega_i^2 \times (c - \nu_i / \omega_i)^2)) / (\Sigma (\omega_i^2))$

(11)

u_r represents the relative uncertainty which was ±0.044 for NO.

Table S7. Vibrational Frequencies Computed Using B3LYP/def2-TZVPP for a NO Molecule Adsorbed on Pd Sites Using the Zeolite Cluster, and H_2O-solvated Pd Models. All the Reported Frequencies are in cm^{-1}.

	B3LYP NO Frequency	Scaled NO Frequency
NO gas phase	1977	1904
[ZPd(NO)]	1903	1848
[ZPdOH(NO)]	1920	1833
$[Z_2Pd(NO)]$	1937	1866
$Z[Pd(NO)(H_2O)_3]$	1867	1798
$Z[PdOH(NO)(H_2O)_2]$	1950	1878
$Z_2[Pd(NO)(H_2O)_3]$	2062	1986

9.8.2 NBO Analyses on H_2O-solvated Pd Model

Table S8. Full NBO populations of Pd-NO moieties on B3LYP optimized structures. NBO populations obtained through NBO 3.1[6] as implemented in Gaussian 16.

	Pd-N	N LP1	N-O (1)	N-O (2)	N-O (3)	O LP1	O LP2
$Z_2[PdNO(H_2O)_3]$	0.99	1.89	2.00	2.00	1.00	1.99	0.98
$Z[PdNO(H_2O)_3]$	1.99	1.92	2.00	2.00	0.00	1.99	1.81
$Z[PdOH(NO)(H_2O)_2]$	1.95	0.99	2.00	2.00	1.00	1.99	0.99

9.8.3 Calculation of Zero-Point Energy (ZPE) and Vibrational Free Energies

For the H_2O-solvated Pd and H_2O-solvated Pd-nitrosyl complexes all frequencies were used for subsequent calculations of ZPE and S_ν. For the zeolite cluster model calculations, we considered only frequencies of the adsorbates.

ZPE and vibrational free energies were calculated for all the $Z_*PdH_xO_y(NO)_z$ species considered in **Figure 7** from the vibrational frequencies (ν) computed using B3LYP/def2-TZVPP in Gaussian 16 as follows:[7]

$$\mathrm{ZPE} = \frac{1}{2}\Sigma_K h\nu_K \tag{12}$$

ΔZPE was evaluated as the difference between the zero-point energies of the adsorbate bound site and the clean site and gas species:

$$\Delta\mathrm{ZPE}\left(\mathrm{Z_*PdH_xO_y(NO)_z}\right) = \mathrm{ZPE}\left(\mathrm{Z_*PdH_xO_y(NO)_z}\right) - \mathrm{ZPE}\left(\mathrm{Z_*Pd}\right) - \frac{x}{2}\left(\mathrm{ZPE(H_2O)} - \frac{1}{2}\mathrm{ZPE(O_2)}\right) - \frac{y}{2}\mathrm{ZPE(NO)} \tag{13}$$

The entropy contributions from the harmonic vibrational partition function were calculated as:[7]

$$\mathrm{S}_\nu = R\Sigma_K\left(\frac{\Theta_{\nu,K}/\mathrm{T}}{e^{\Theta_{\nu,K}/\mathrm{T}}-1} - \ln\left(1 - e^{\frac{-\Theta_{\nu,K}}{\mathrm{T}}}\right)\right) \tag{14}$$

where $\Theta_{\nu,K}$ represents the vibrational temperatures.

The thermodynamic phase diagram and formation free energies of $Z_*PdH_xO_y(NO)_z$ species were then calculated by incorporating these terms as per the equation:

$$\Delta\mathrm{G}^{\mathrm{form}}_{x,y,z}\left(\mathrm{T},\, \Delta\mu_{O_2},\, \Delta\mu_{H_2O}, \Delta\mu_{\mathrm{NO}}\right) = \Delta\mathrm{E}^{\mathrm{form}}_{x,y,z} + \Delta\mathrm{ZPE} - \mathrm{T}\Delta\mathrm{S}^{\mathrm{ST}}_{x,y,z}(\mathrm{T}) - \mathrm{T}\Delta\mathrm{S}_\nu(\mathrm{T}) - \frac{x}{2}\left(\Delta\mu_{H_2O} - \frac{1}{2}\Delta\mu_{O_2}\right) - \frac{y}{2}\Delta\mu_{O_2} - z\Delta\mu_{\mathrm{NO}} \tag{15}$$

9.8.4 NO$_x$-TPD Profiles

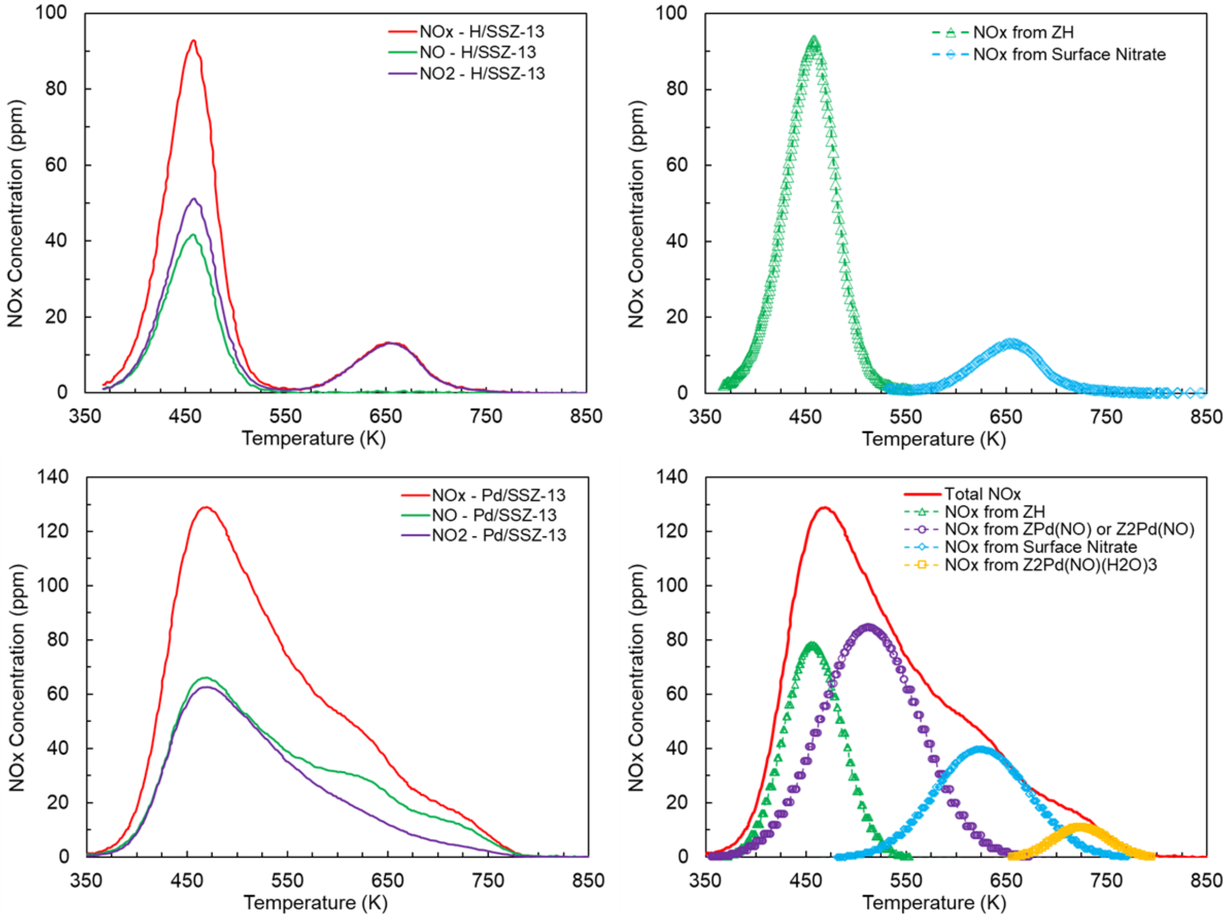

Figure S9. NO$_x$-TPD profiles (left) of Pd/SSZ-13 (bottom left) and H/SSZ-13 (top left) in the absence of H_2O and peak deconvolution results (right) using H/SSZ-13 Si/Al = 8.9 (top right) to subtract the zeolite contribution from Pd/SSZ-13 (bottom right). 45 mg of powder sample with particle sizes from 250 - 425 µm were loaded into the reactor for testing, and the total flow rate used was 550 sccm.

9.9 In situ DRIFTS experiments

9.9.1 NO Adsorption DRIFTS Spectra of Pd/SSZ-13

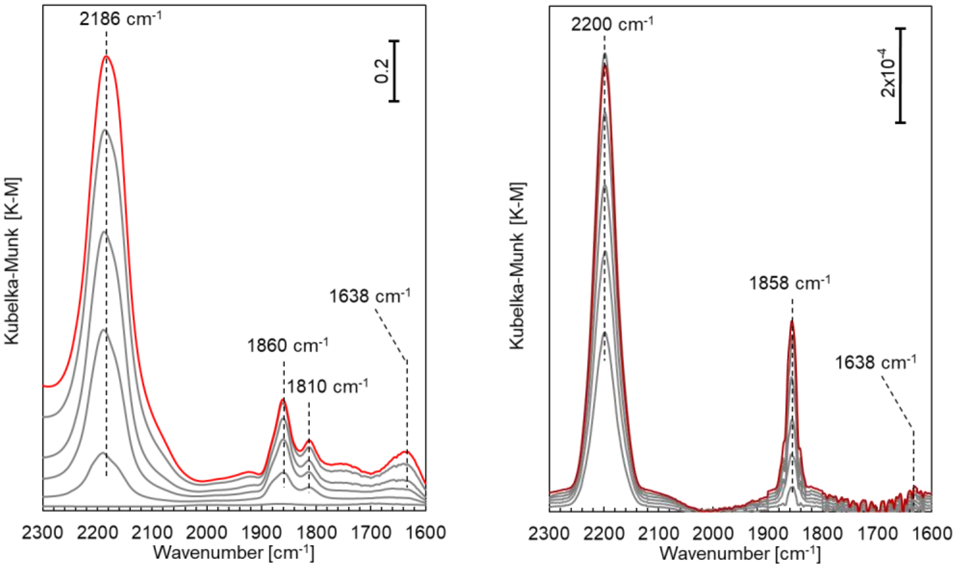

Figure S10. In-situ DRIFTS spectra collected during NO adsorption experiments with 200 ppm NO, 10% O_2 at 353 K while bypassing the moisture trap and cold trap (left), and at 473 K using the moisture trap and cold trap (right). For the spectra on the left, a downstream IR analyzer was used to measure the H_2O concentration and it equaled 20 ppm. 75 mg of powder sample were pressed into a pellet for each test, and the total flow rate through the IR cell was 60 sccm.

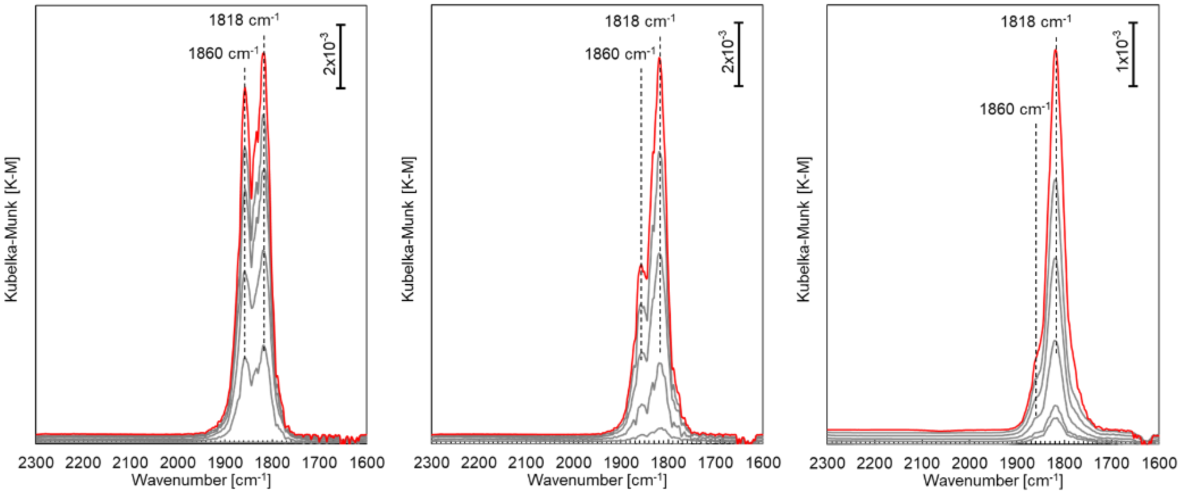

Figure S11. In-situ NO adsorption DRIFTS spectra of Pd/SSZ-13 (Si/Al = 9, Pd/Al = 0.056) collected at: (left) 473 K with 200 ppm NO, 10% O_2 and 1.3% H_2O; (middle) 403 K with 200 ppm

NO, 10% O_2 and 1.3% H_2O; (right) 403 K with 200 ppm NO, 10% O_2 and 4.5% H_2O. The same spectra shown in **Fig. 9** with nitrate region included.

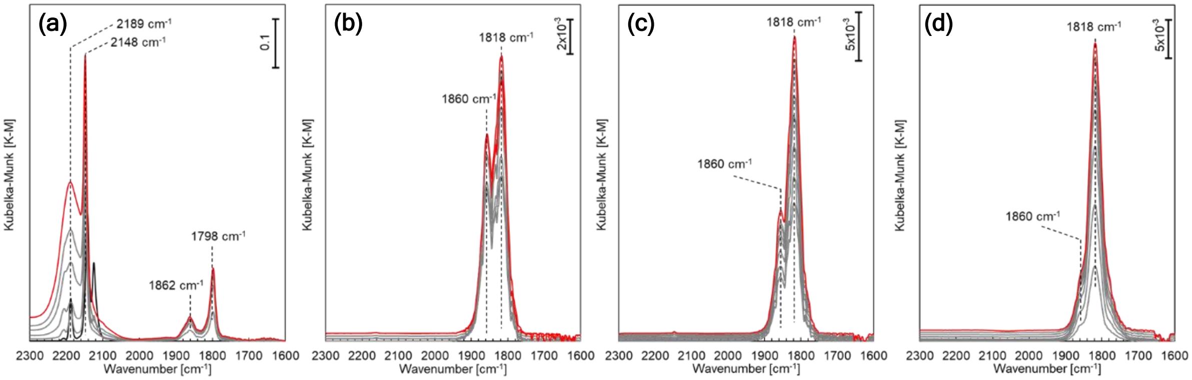

Figure S12. In-situ DRIFTS spectra of Pd/SSZ-13 (Si/Al = 9, Pd/Al = 0.056) collected at: (**a**) 353 K during 200 ppm NO addition after exposure to 10% O_2, 20 ppm H_2O and 200 ppm CO; (**b**) 403 K during 200 ppm CO addition after exposure to 10% O_2, 1.3% H_2O and 200 ppm NO; (**c**) 473 K during 200 ppm CO addition after exposure to 10% O_2, 1.3% H_2O and 200 ppm NO; (**d**) 403 K during 200 ppm CO addition after exposure to 10% O_2, 4.5% H_2O and 200 ppm NO. Background spectra were collected at (**a**) 353 K with 10% O_2 and 20 ppm H_2O; (**b**) 403 K with 10% O_2 and 1.3% H_2O; (**c**) 473 K with 10% O_2 and 1.3% H_2O; (**d**) 403 K with 10% O_2 and 4.5% H_2O. The same spectra shown in **Fig. 10** with nitrate region included.

9.10 NO and CO co-adsorption

9.10.1 HSE06-computed CO *vs* NO Adsorption Energies

The energy required to exchange a H_2O molecule with CO (or NO) at the $\mathrm{Z_*PdH_xO_y}$ sites was calculated as per the following reactions:

$$1\text{Al: } \mathrm{ZPd^{I}(H_2O)_{\mathit{x}} + CO \xrightarrow{\Delta \mathit{E}_{ads}} ZPd(CO)(H_2O)_{\mathit{x}-1} + H_2O}$$

(16) $$\mathrm{ZPd^{II}(OH)(H_2O)_{\mathit{x}} + CO \xrightarrow{\Delta \mathit{E}_{ads}} ZPd^{II}(OH)(CO)(H_2O)_{\mathit{x}-1} + H_2O}$$

(17)

$$2\text{Al: } \mathrm{Z_2Pd^{II}(H_2O)_{\mathit{x}} + CO \xrightarrow{\Delta \mathit{E}_{ads}} Z_2Pd^{II}(CO)(H_2O)_{\mathit{x}-1}H_2O}$$

(18)

$$1\text{Al: } \mathrm{ZPd^{I}(H_2O)_{\mathit{x}} + NO \xrightarrow{\Delta \mathit{E}_{ads}} ZPd(NO)(H_2O)_{\mathit{x}-1} + H_2O}$$

(19) $$\mathrm{ZPd^{II}(OH)(H_2O)_{\mathit{x}} + NO \xrightarrow{\Delta \mathit{E}_{ads}} ZPd^{II}(OH)(NO)(H_2O)_{\mathit{x}-1} + H_2O}$$

(20)

$$2\text{Al: } \mathrm{Z_2Pd^{II}(H_2O)_{\mathit{x}} + NO \xrightarrow{\Delta \mathit{E}_{ads}} Z_2Pd^{II}(NO)(H_2O)_{\mathit{x}-1}H_2O}$$

(21)

Table S9. HSE06-D3(BJ)vdw Computed Energies Required to Exchange one H_2O at 1Al and 2Al Sites with CO *vs* NO.

	+CO ΔE_{ads} (kJ mol^{-1})	+NO ΔE_{ads} (kJ mol^{-1})
$\mathrm{Z[Pd^{I}(H_2O)_4]}$	-59 (Eqn. 16)	-80 (Eqn. 19)
$\mathrm{Z[Pd^{II}(OH)(H_2O)_3]}$	-16 (Eqn. 17)	+14 (Eqn. 20)
$\mathrm{Z_2[Pd^{II}(H_2O)_4]}$	+20 (Eqn. 18)	+12 (Eqn. 21)

We also evaluated the energy required to exchange a H_2O molecule with CO at the H_2O-solvated Pd-nitrosyl complexes as follows:

$$\text{1Al: } \mathrm{ZPd(NO)(H_2O)}_x + \mathrm{CO} \xrightarrow{\Delta E_{\mathrm{ads}}} \mathrm{ZPd(NO)(CO)(H_2O)}_{x-1} + \mathrm{H_2O} \quad (22)$$

$$\mathrm{ZPd^{II}(OH)(NO)(H_2O)}_x + \mathrm{CO} \xrightarrow{\Delta E_{\mathrm{ads}}} \mathrm{ZPd^{II}(OH)(NO)(CO)(H_2O)}_{x-1} + \mathrm{H_2O} \quad (23)$$

$$\text{2Al: } \mathrm{Z_2Pd^{II}(NO)(H_2O)}_x + \mathrm{CO} \xrightarrow{\Delta E_{\mathrm{ads}}} \mathrm{Z_2Pd^{II}(NO)(CO)(H_2O)}_{x-1}\mathrm{H_2O} \quad (24)$$

Table S10. HSE06-D3(BJ)vdw Computed Energies Required to Exchange H_2O with CO at 1Al and 2Al Sites.

	ΔE_{ads} (kJ mol^{-1})
$\mathrm{Z[Pd^{II}(NO)(H_2O)_3]}$	+44 (Eqn. 22)
$\mathrm{Z[Pd^{II}(OH)(NO)(H_2O)_2]}$	+23 (Eqn. 23)
$\mathrm{Z_2[Pd^{II}(NO)(H_2O)_3]}$	+81 (Eqn. 24)

9.10.2 CO Oxidation kinetics of Pd/SSZ-13

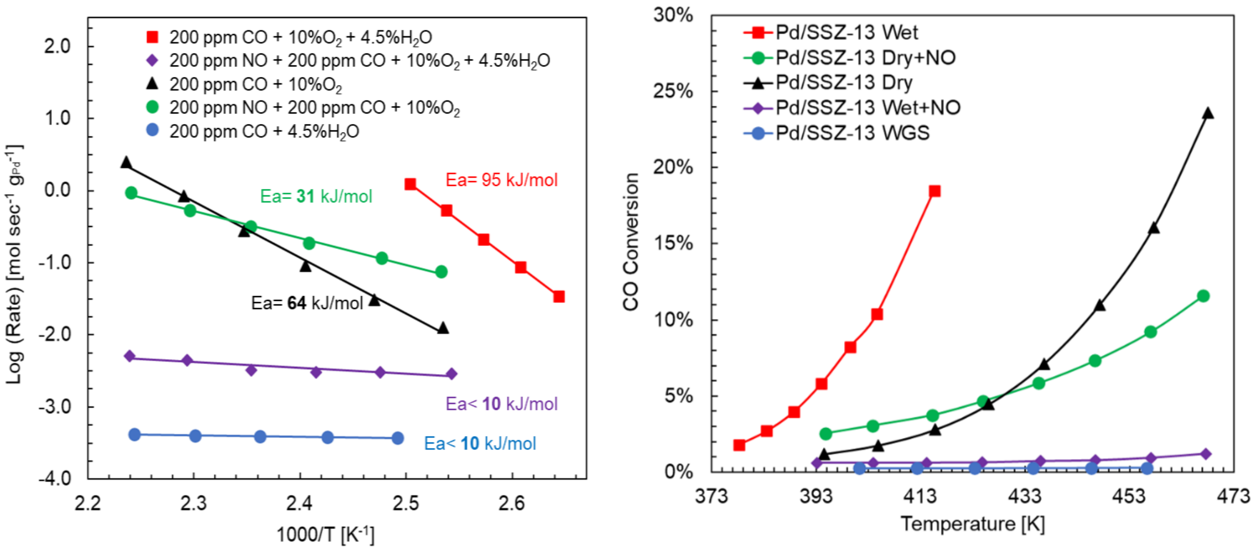

Figure S13. CO oxidation rates measured on Pd/SSZ-13 (Si/Al = 9, Pd/Al = 0.056) in the presence of: 200 ppm CO, 10% O_2 and 4.5% H_2O (red square); 200 ppm NO, 200 ppm CO, 10% O_2 and 4.5% H_2O (purple diamond); 200 ppm CO and 10% O_2 (black triangle); 200 ppm NO, 200 ppm CO and 10% O_2 (green circle). Water gas shift rates measured on Pd/SSZ-13 (Si/Al = 9, Pd/Al = 0.056) in the presence of 200 ppm CO and 4.5% H_2O (blue circle). 45 mg of powder sample with particle sizes from 250 - 425 μm were loaded into the reactor for testing, and the total flow rate used was 550 sccm.

We performed steady-state CO oxidation experiments between 373 K to 473 K in the presence and absence of 4.5% H_2O, where 200 ppm CO was present at all times**.** **Figure S13** shows that calculated apparent activation energies are 95 kJ mol^{-1} in the presence of H_2O (red squares) and 64 kJ mol^{-1} in the absence of H_2O (black triangles). We also measured water gas shift (WGS) activity on the same catalyst to eliminate a possible change in activation energy due to the onset of the WGS reaction (blue circles). Results show that WGS plays no role in the activation energy calculations. CO oxidation rates measured in the presence of 4.5% H_2O are significantly higher than those measured in the absence of H_2O. The different CO oxidation activation energies further highlight the distinction between H_2O-solvated and dehydrated Pd, herein catalyzing CO oxidation.

We also performed steady-state CO oxidation experiments in the presence of NO, with and without 4.5% H_2O, with 200 ppm CO, 200 ppm NO and 10% O_2. When both H_2O and NO are present (purple diamonds), CO oxidation is inhibited.

9.10.3 CO Temperature programmed reduction of Pd/SSZ-13

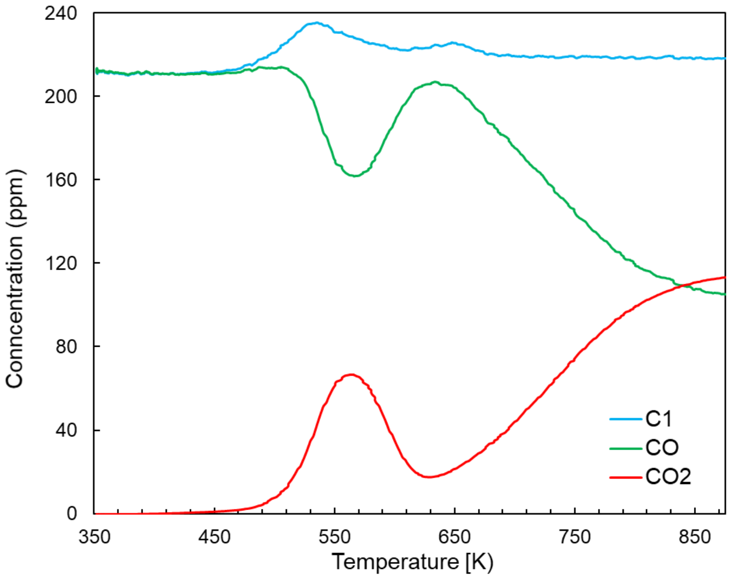

Figure S14. CO Temperature programmed reduction profile of Pd/SSZ-13 (Si/Al = 9, Pd/Al = 0.056) in the presence of : 200 ppm CO and 4.5% H_2O; Pretreatment: 873 K with 10% O_2 for 45 min, and N_2 purge at 353 K for 2 hr. 45 mg of powder sample with particle sizes from 250 - 425 µm were loaded into the reactor for testing, and the total flow rate used was 550 sccm.

We observed the transient reduction of Pd^{II} by CO in the presence of 4.5% H_2O at around 573 K, which leads to the formation of Pd particles indicated by the onset of the water-gas shift reaction after Pd^{II} is reduced.

9.11 12 *vs* 24 T-site supercells for 1Al Pd-exchanged sites

We evaluated the reaction energies for [ZPd^{I}] and [ZPd^{II}OH] in 12 and 24 T-site supercells in the presence of the four maximum ligands that can absorb on the Pd cation.

Table S11. Comparison of Reaction Energies at 1Al Pd-Exchanged Sites Calculated Using PBE-D3(BJ)vdw

	ΔE (kJ mol^{-1})	
	12 T-site	24 T-site
$[ZPd^{I}] + 4H_2O \rightarrow Z[Pd^{I}(H_2O)_4]$	-358	-354
$[ZPd^{I}] + 3H_2O + NO \rightarrow Z[Pd^{I}(NO)(H_2O)_3]$	-513	-503
$[ZPd^{II}OH] + 4H_2O \rightarrow Z[Pd^{II}(OH)(H_2O)_3] + H_2O$	-398	-398
$[ZPd^{II}OH] + 3H_2O + NO \rightarrow Z[Pd^{II}(OH)(NO)(H_2O)_2] + 2H_2O$	-422	-421

9.12 Sample characterization

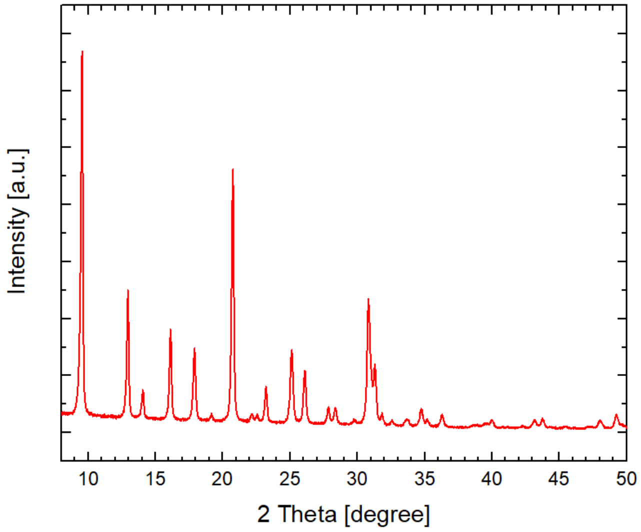

Figure S15. X-ray diffraction pattern of Pd/SSZ-13 (Si/Al = 8.9, Pd/Al = 0.056)

*CHA zeolite structure remains intact after the introduction of Pd and the following calcination.

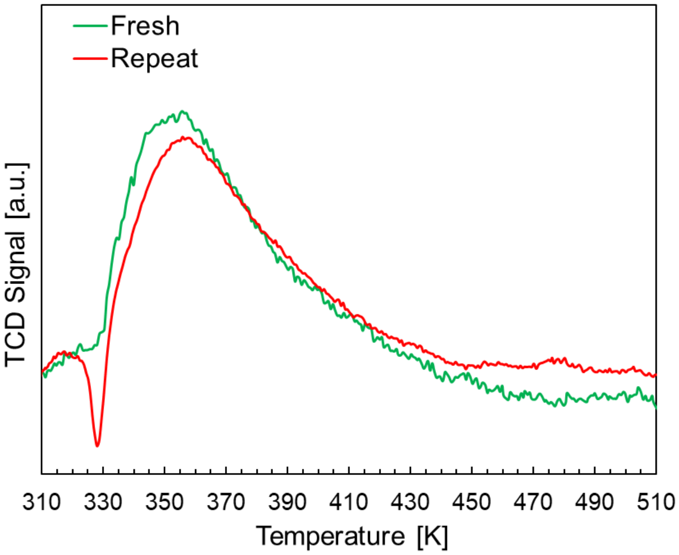

Figure S16. H_2-TPR profiles from a fresh Pd/SSZ-13 (green) sample and the same sample after the TPR to 873 K and a subsequent pretreatment in 873 K in 10% O_2 (red). 60 mg of powder sample were loaded into the reactor for each test, and the total flow rate used was 30 sccm.

*Absence of a PdH decomposition peak at around 330 K indicates the absence of Pd nanoparticles bigger than 3 nm,[8] which is consistent with EXAFS characterization results. The reduction feature around 350 K corresponds to Pd^{II} cations indicating that Pd is ion-exchanged into the zeolite.

9.13 References

(1) Li, S.; Li, H.; Gounder, R.; Debellis, A.; Müller, I. B.; Prasad, S.; Moini, A.; Schneider, W. F. First-Principles Comparison of Proton and Divalent Copper Cation Exchange Energy Landscapes in SSZ-13 Zeolite. *J. Phys. Chem. C* **2018**, *122* (41), 23564–23573.

(2) Loewenstein, W. The Distribution of Aluminum in the Tetrahedra of Silicates and Aluminates. *Am. Mineral.* **1954**, *39* (1–2), 92–96.

(3) Bell, R. G.; Jackson, R. A.; Catlow, C. R. A. Löwenstein's Rule in Zeolite A: A Computational Study. *Zeolites* **1992**, *12* (7), 870–871.

(4) Frisch, M. J.; Trucks, G. W.; Schlegel, H. B.; Scuseria, G. E.; Robb, M. A.; Cheeseman, J. R.; Scalmani, G.; Barone, V.; Petersson, G. A.; Nakatsuji, H.; Li, X.; Caricato, M.; Marenich, A. V.; Bloino, J.; Janesko, B. G.; Gomperts, R.; Mennucci, B.; Hratchian, H. P.; Ortiz, J. V.; Izmaylov, A. F.; Sonnenberg, J. L.; Williams; Ding, F.; Lipparini, F.; Egidi, F.; Goings, J.; Peng, B.; Petrone, A.; Henderson, T.; Ranasinghe, D.; Zakrzewski, V. G.; Gao, J.; Rega, N.; Zheng, G.; Liang, W.; Hada, M.; Ehara, M.; Toyota, K.; Fukuda, R.; Hasegawa, J.; Ishida, M.; Nakajima, T.; Honda, Y.; Kitao, O.; Nakai, H.; Vreven, T.; Throssell, K.; Montgomery Jr., J. A.; Peralta, J. E.; Ogliaro, F.; Bearpark, M. J.; Heyd, J. J.; Brothers, E. N.; Kudin, K. N.; Staroverov, V. N.; Keith, T. A.; Kobayashi, R.; Normand, J.; Raghavachari, K.; Rendell, A. P.; Burant, J. C.; Iyengar, S. S.; Tomasi, J.; Cossi, M.; Millam, J. M.; Klene, M.; Adamo, C.; Cammi, R.; Ochterski, J. W.; Martin, R. L.;

Morokuma, K.; Farkas, O.; Foresman, J. B.; Fox, D. J. *Gaussian 16 Rev. C.01*; Wallingford, CT, 2016.

(5) NIST Computational Chemistry Comparison and Benchmark Database, NIST Standard Reference Database Number 101. Release 20, August 2019, Editor: Russell D. Johnson III.

(6) Glendenning, E. D.; Reed, A. E.; Carpenter, J. E.; Weinhold, F. NBO Version 3.1. **2001**.

(7) McQuarrie, D. A.; Simon, J. D. *Molecular Thermodynamics*; University Science Books: Sausalito, California, 1999.

(8) Nag, N. K. A Study on the Formation of Palladium Hydride in a Carbon-Supported Palladium Catalyst. *J. Phys. Chem. B* **2001**, *105* (25), 5945–5949.

Chapter 10. Appendix C - Supporting Information of Chapter 5: Investigation of An Irreversible NOx Storage Degradation Mode on Pd/BEA as A Model Catalyst for Passive NOx Adsorption

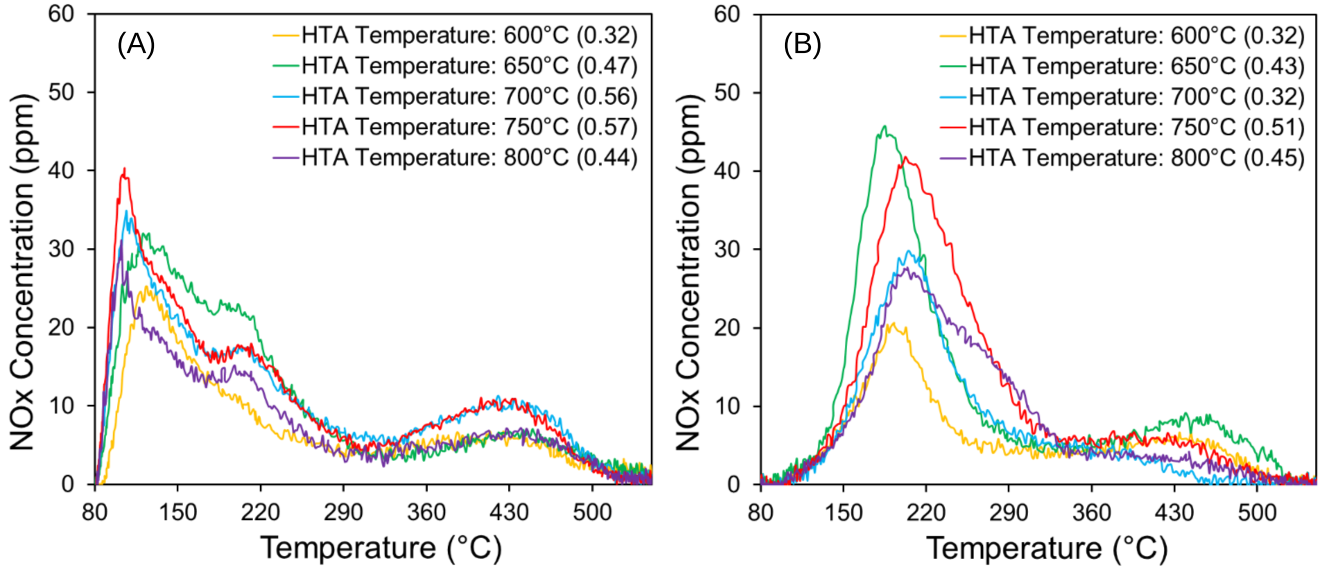

Fig.S.1 NOx TPD profiles of samples hydrothermally aged at different temperatures. Gas phase composition **A**: 200 ppm NO, 5% H_2O and 10% O_2; **B**: 200 ppm CO, 200 ppm NO, 5% H_2O and 10% O_2

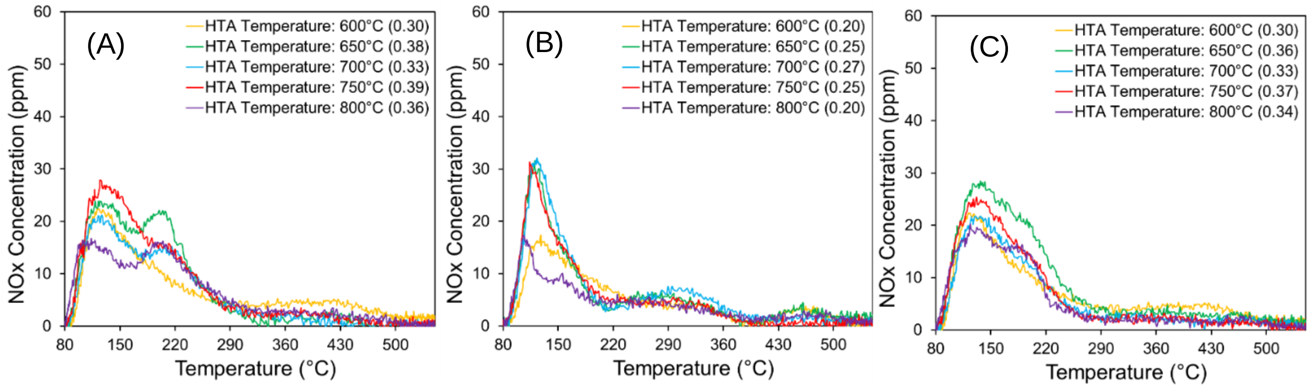

Fig.S.2 NOx TPD profiles of samples hydrothermally aged at different temperatures. **A**: After NO and CO co-adsorption and TPD; **B**: After reduction pretreatment; **C**: After reoxidation pretreatment. Gas phase composition: 200 ppm NO, 5% H_2O and 10% O_2

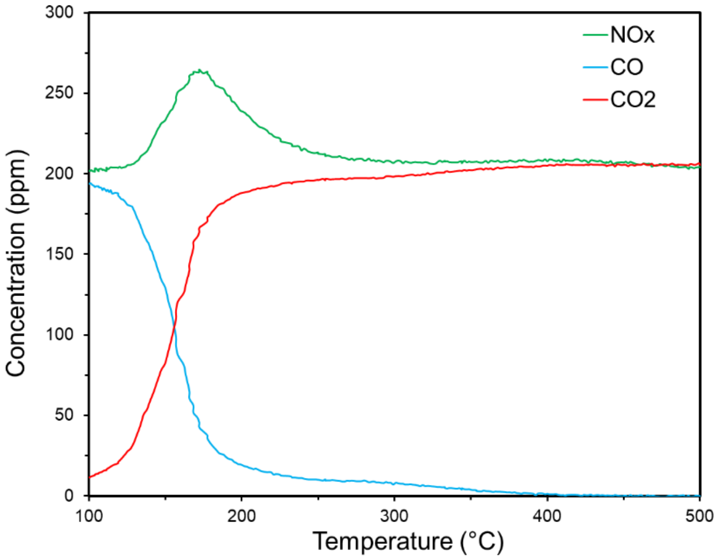

Fig.S.3 NOx, CO and CO_2 concentrations during a TPD experiment with the Pd/BEA-750HTA sample. Gas phase composition: 200 ppm CO, 200 ppm NO, 5% H_2O and 10% O_2

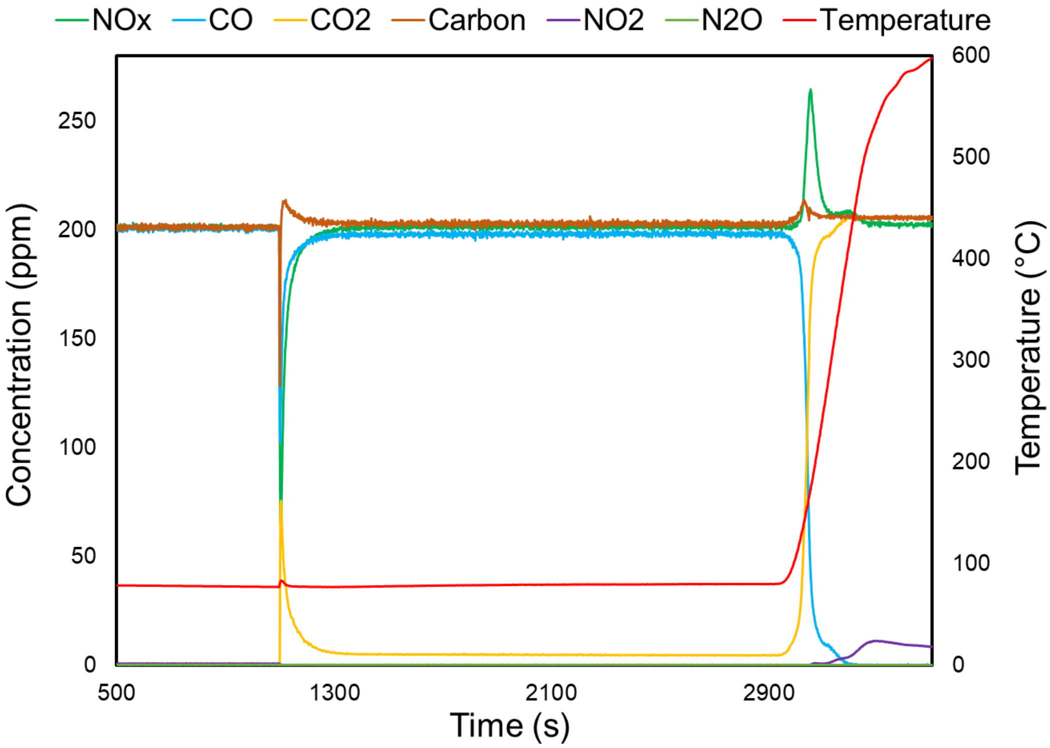

Fig.S.4 Full concentration profiles during low temperature the NO adsorption and TPD experiment with a Pd/BEA-750HTA sample. Gas phase composition: 200 ppm CO, 200 ppm NO, 5% H_2O and 10% O_2

Chapter 11. Appendix D - Supporting Information of Chapter 6: Integration of an Oxidation Catalyst with Pd/Zeolite-Based Passive NOx Adsorbers: Impacts on Degradation Resistance and Desorption Characteristics

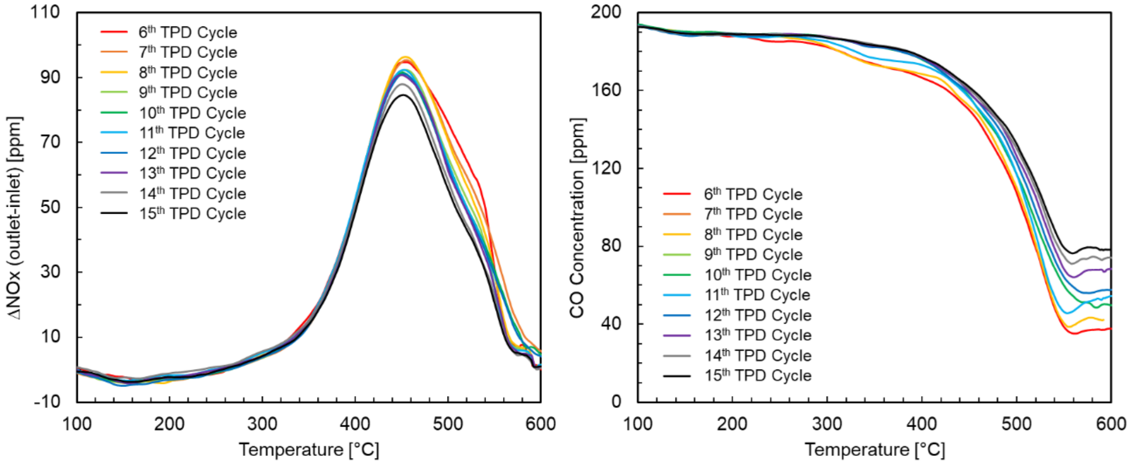

Figure S1. Consecutive NOx-TPD profiles (a) and the simultaneous CO oxidation light-off curves (b) of Pd/SSZ-13 PNA over the last 10 cycles. Feed composition: 200 ppm NO, 200 ppm CO, 4.5% H_2O, 10% O_2 and N_2 balance.

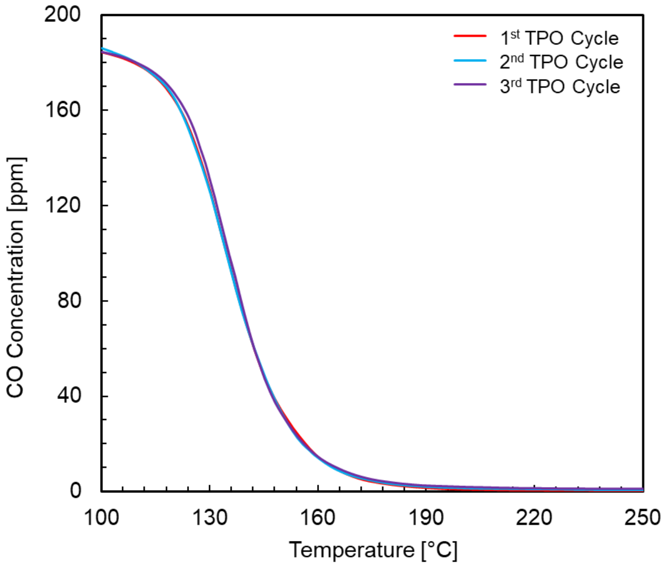

Figure S2. Consecutive CO oxidation light-off curves of Pt/Al_2O_3 over 3 cycles. Feed composition: 200 ppm CO, 4.5% H_2O, 10% O_2 and N_2 balance.